UNIVERSITÀ DEGLI STUDI DI PALERMO

Corso di Dottorato di Ricerca in Scienze Molecolari e Biomolecolari
Dipartimento di Scienze e Tecnologie Biologiche Chimiche e Farmaceutiche (STEBICEF)
Curriculum scienze chimiche CHIM/06

SYNTHESIS, CHARACTERIZATION, AND STUDY OF NEW NANOSTRUCTURED MATERIALS

IL DOTTORE
CARMELO GIUSEPPE COLLETTI

IL COORDINATORE
Prof. PATRIZIA DIANA

TUTOR
Prof. RENATO NOTO
Prof. FRANCESCA D'ANNA

CO TUTOR

Dr. SERENA RIELA

CICLO IXX
ANNO 2018

SYNTHESIS, CHARACTERIZATION, AND STUDY OF NEW NANOSTRUCTURED MATERIALS

Index

Chapter 3 - Halloysite Nanotubes

Chapter 4 - Halloysite Nanotubes Modifications

Chapter 7 - Modified Halloysite Nanotubes for Pollutant Removal

Chapter 8 - Conclusions

Chapter 9 - Experimental Details

Preface

Inspired by the issues addressed since my graduation and studied in the research group where I did my thesis work, in my PhD, I dealt with the synthesis, characterization, and study of new nanostructured materials.

The theme of nanostructured materials is one of the most studied by the contemporary scientific world. The great potential and the wide fields of application, make it one of the main themes of contemporary interests.

Among many, halloysite nanotubes have unique properties that make them excellent candidates for nanomaterials applications.

In the following chapters, I will discuss the theme of nano materials with particular attention to the development and application of natural materials such as clays used for centuries by humanity.

Introduced the halloysite I will expose the path that led me to use this innovative material in various areas, exposing the methodologies used and the results obtained in what has been a research path between two worlds, between the hallways of the building 17 of the University of Palermo and the Institute for Micromanufacturing of Louisiana Tech University, U.S.A.

My true job, that one I studied at school and gave me to live until today, is the chemist.
I do not know if you have a clear idea about, but it looks a little like yours:

just that we assemble and dismantle very small buildings*.*

We divide ourselves into two main branches, those that mount and those that
disassemble, and both of us are like blind people with sensitive fingers[...].

Those who disassemble, the analyst chemists, must be able to dismantle a structure
piece by piece without damaging it too much [...].

However, I have always done the builder chemist, one of those who makes the
synthesis, those who build customized structures...

Primo Levi - The Monkey's Wrench

Chapter 1

A Nanometric World

1. *"There's Plenty of Room at the Bottom"*

The 29th December 1959, the physicist Richard Feynman gave a lecture at an American Physical Society meeting at Caltech, talking about the futuristic idea of atomic control of the matter and the creation of nanodevices.

That lecture is usually considered the milestone and the born day of nanotechnologies. In that occasion, Feynman did not use the name nanotechnologies. This was first used by Norio Taniguchi, from Tokyo University, in 1974 and independently by Eric Drexler, from MIT, in 1986 in his book "Engines of Creation: The Coming Era of Nanotechnology".

From that day, the term "nano" became a popular label commonly adopted in the scientific community, and it is being used in a lot of words such as nanoscale, nanotechnology, nanometer, nanoscience, nanotube, nanostructure, and so on.

In his "futuristic" lecture Feynman hypothesized two main challenges: i) the construction of a tiny motor and ii) the possibility to assemble letters small enough to write the entire Encyclopedia Britannica on the head of a pin. Although those challenges were soon won, the interest in the nanometric world did not stop and led to an ever-growing development.

In this context, a crucial turning point occurred in 1989 when a scientist of IBM demonstrated the possibility of manipulating individual atoms. This was possible by a scanning tunneling microscope, that thanks to thirty-five individual xenon atoms arranged on a solid surface can write the IBM acronym. This moment represents the first time where an atom or group of atoms can be positioned on a flat surface.

Demonstration of the great interest in this topic by the international scientific community was the awarded of the Nobel Prize in Chemistry 2016 to Jean-Pierre Sauvage, Sir J. Fraser Stoddart and Bernard L. Feringa "for the design and synthesis of molecular machines".

Today we know that the nano level build and manipulation is possible and real. Our fringes of knowledge are continually extended and it is possible to think that prefiguring like the possibility of injectable nanorobots that can repair internal damage to the human body at the molecular level, will be realized.

As Feynman foresaw, there's an infinite, fantastic universe at the Bottom. Our job is to learn to know it and to use it.

1.1. *Nanostructured materials and nanotechnologies*

It is well known that in the past there has been an unconscious use of some micro and nanotechnology. The colored glasses of the Gothic cathedrals, for example, contain gold nanoparticles whose color depends on their size.

After Feynman, the development of nanotechnologies and their applications has become greater and greater. This trend has involved the most diverse fields, from physics to biology as well as medicine, computer science, chemistry and materials sciences in general.

It is known the term "nano" refers to something on a very small scale: larger than atoms but smaller than a breadcrumb; despite this the definition of the term nanotechnology is still debate and usually it is considered as the study and use of structures and phenomena with dimensions ranging from 1 nanometer (nm) and 100 nanometers.[1]

At atomic, molecular and macromolecular scales, the properties differ significantly from those at bulk scale.

In some aspects, nanomaterials should be considered almost a distinct state of matter with unique chemical, physical, mechanical, electronic, or mechanical properties, due, in particular, to the surface effects. Indeed, nanomaterials possess a great number of atoms on their surface with respect to the bulk ones or to particles on the micrometric scale. This is due to a higher surface area of the nanomaterial compared to other particles. For example, considering carbon particles both on micro and nanometric scale, it is noteworthy that the nano presents a greater surface area despite its smaller dimensions (11.3 mm^2 for a diameter of 60 nm nanoparticles and 0.01 mm^2 and a 60 m in diameter for microparticles).

In addition, since atoms in a nanomaterial are not so close to each other, they possess a lower binding energy which involves a reduction in the melting point with a decreasing of dimensions, according to Gibbs Thomson equation.

An added value in the use of nanosize systems is related to the fact that their chemical reactivity tends to increase with decreasing of the particles size. Therefore, it is possible to envisage several kinds of functionalizations such as covalent or not covalent modifications, surface coating, layer by layer assembly and so on, which allow to obtain appealing materials with tunable properties for several applications.[2]

It is possible to classify the different nanoparticles according to their characteristic, the most commonly adopted for this purpose are, among others, size, composition,

morphology, agglomeration, and uniformity. A general classification of them is listed below:

Table 1. General classification of nanoparticles.

Classification	Dimension	Type	Example
0D	dot shape	dots	metal nanoparticles
1D	predominantly, in one dimension	fibers and wire	nanotubular structures, nanofibers, wire and nano necklace
2D	planar extension	sheets and lamellar structures	nanometric tin films
3D	tridimentional extension	organized 3D structures	proteins, enzymes complexes

1.1.1 From / To down

The synthesis of nanomaterials should seem simple, however because of their small size, the preparation methods are more complexes and this represents the main limitation on the use of nanoparticles. Therefore, it is crucial the development of techniques and equipment that allow to overcome the aforementioned drawbacks. Up to now, two main techniques of synthesis of nanomaterials are employed: the top down and the bottom up approaches.

The first one consists in devices made from macroscopic materials by accurate high control of a miniaturization process to the atomic level.

The top-down method is currently in use to manufacture computer chips as well as other products you use every day. Much of the early progress in nanotechnology has relied on this approach in which the nanoscale components of interest are fabricated by cutting down larger precursors, as by some kind of lithographic techniques.

The latter approach represents the most adopted and interesting one for the chemical society. [3]

In the bottom-up approach, the materials and devices are made by self-assembly aggregation of molecular building blocks drove by chemical bonds and supramolecular interactions.

In the dream of Feynman, the bottom up techniques were crucial. A world were new materials and devices are build atom by atom or nanostructure by nanostructure. The importance of this approach is highlighted by the possibility to build the tiniest computer chip possible by placing each atom, one-to-one in their correct position and in this way, one can build the entire circuit.

Another aspect of the bottom-up approach deals with the arrangement of atoms and molecules in a specific way in order to create the final material: this takes the name of self-assembly and it is the technique that, in the last few years, is been adopted more and more by chemists.

In the near future, the improvement of the current nanotechnologies and the development of novel ones will permit to create sophisticated nanostructures which could manufactured genes directly inside the DNA or some kind of nanosurgery for healing wounds on the cellular level.[1]

These aspects represent the main challenges of the modern scientific society.

1.2. Tubular nanomaterials

After years of research and study in the field of nanotechnology, a lot of different nanostructured materials have been made.

Among them, nanotubes consist in one of the main appealing and studied sector. This great interest is due to structural versatility, which delineates interesting chemical and physical properties with consequent applications in various fields, such as electronics, optics, catalysis and biological systems.

Different kind of nanotubular structures have been finding out in the years, made by different atoms and techniques. Every composition gives to them unique properties and infinite field of potential application.

1.2.1. Carbon nanotubes

A carbon atom can form various types of allotropes. In 3D structures, diamond and graphite are the allotropes of carbon. Carbon also forms low-dimensional (2D, 1D or 0D) allotropes collectively known as carbon nanomaterials. Examples of such nanomaterials are 1D carbon nanotubes (CNTs) and 0D fullerenes. In the list of carbon nanomaterials, graphene is known as 2D single layer of graphite.[4]

Carbon nanotubes (CNTs) were observed for the first time in 1991 by S. Iijima.[5]

They are made by rolling up of a sheet of graphene into a cylinder. The central part consists of carbon atoms whit sp^2 hybridization, arranged in hexagonal rings, which with the appropriate curvature, is a degree of generating the tubular structure. The ends of the tubes could be close by and half fullerene structure.
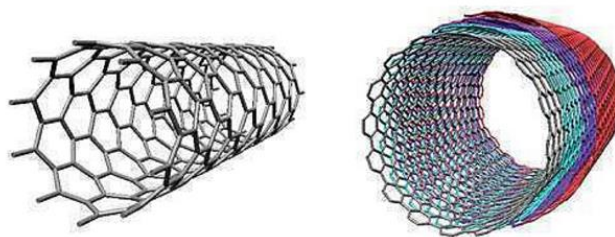
Figure 1. Representations of single- and multi-walled carbon nanotubes.

Nanotubes come in two types: single-walled nanotubes (SWNTs) and multi-walled nanotubes (MWNTs). The SWNT forms a single layer cylinder and is the most commonly used type of nanotube. The MWNT is made up of multiple cylinders tucked into each other.[1]

SWNTs have dimensions between 0.7 nm and 2 nm, instead, MWNTs could have diameter up to 100 nm. Depended on the rolling direction and radius, CNTs can have different properties, in particular, metallic or semi-conductive behavior.

There are many synthesis methods of CNTs, but the most common are, electric-arc technique, laser ablation and chemical vapor deposition.[6–8]

The ability of production is in order of grams. One of the bigger limitation in the application of CNT is the low solubility in aqueous and organic solvents media.

To solve this problem and for modulating the properties of tubes, several studies are carried out. Two different methodologies for the functionalization of CNTs have been exploited, the covalent approach and the supramolecular one. The first mainly consists in

oxidative processes to create new chemical groups on tubes available for further functionalization by grafting suitable compounds. This kind of approach, however, has the disadvantage of destroying the network of carbon atoms affecting the electric properties of the tubes.

Supramolecular functionalization, instead, occurs using not covalent bonds and weak intermolecular forces and represents a valid alternative to the covalent one.[9–11]

1.2.2. Boron-nitride nanotubes

Boron-nitride nanotubes (BNT) were predicted in 1994 and experimentally discovered in 1995. They are a polymorph form of boron nitride, similar to carbon nanotubes, composed of boron atoms covalently bonded to nitrogen atoms to form hexagons to give hollow cylinders.[12] These nanotubes show electrical properties similar to that of CNT. In addition, they can give strong, but light-weight, composites materials, flame resistant and with tunable properties by doping with metal atoms via sputtering.

Toxicological investigations are still in progress.

The most common synthesis methods of BT are the high-temperature N_2-H_2 plasma synthesis, laser ablation, and chemical vapor deposition. Unlikely, these techniques, like for CNT, are able to give tubes in a tens of grams scale.[1,13–17]

1.2.3. A natural way

In the recent years, among the tubular nanostructures, that based on silicon structures have attracted a great interest. Representative examples of this class of materials are imogolite and halloysite. They come from a larger family of nanostructured materials used by human being since the beginning of the history: clay minerals.

References

(1) Booker, R.; Boysen, E. *Nanotechnology for dummies*; Wiley, 2005.

(2) Buzea, C.; Pacheco, I. I.; Robbie, K. *Biointerphases* **2007**, *2* (4), MR17.

(3) Steed, J.; Atwood, J. *Supramolecular Chemistry*; 2006.

(4) Kaushik, B. K.; Majumder, M. K. *Carbon Nanotube Based VLSI Interconnects*; SpringerBriefs in Applied Sciences and Technology; Springer India: New Delhi, 2015.

(5) Iijima, S. *Nature* **1991**, *354* (6348), 56.

(6) Ivanov, V.; Nagy, J. B.; Lambin, P.; Lucas, A.; Zhang, X. B.; Zhang, X. F.; Bernaerts, D.; Van Tendeloo, G.; Amelinckx, S.; Van Landuyt, J. *Chem. Phys. Lett.* **1994**, *223* (4), 329.

(7) Thess; Lee; Nikolaev; Dai; Petit; Robert; Xu; Lee; Kim; Rinzler; Colbert; Scuseria; Tomanek; Fischer; Smalley. *Science* **1996**, *273* (5274), 483.

(8) Journet, C.; Maser, W. K.; Bernier, P.; Loiseau, A.; de la Chapelle, M. L.; Lefrant, S.; Deniard, P.; Lee, R.; Fischer, J. E. *Nature* **1997**, *388* (6644), 756.

(9) Massaro, M.; Riela, S.; Cavallaro, G.; Saladino, M. L.; Agnello, S.; Noto, R. *Int. J. Org. Chem.* **2013**, *3* (1), 26.

(10) Star, A.; Liu, Y.; Grant, K.; Ridvan, L.; Stoddart, J. F.; Steuerman, D. W.; Diehl, M. R.; Boukai, A.; Heath, J. R. *Macromolecules* **2003**, *36* (3), 553.

(11) Tuci, G.; Vinattieri, C.; Luconi, L.; Ceppatelli, M.; Cicchi, S.; Brandi, A.; Filippi, J.; Melucci, M.; Giambastiani, G. *Chem. - A Eur. J.* **2012**, *18* (27), 8454.

(12) Rubio, A.; Corkill, J. L.; Cohen, M. L. *Phys. Rev. B* **1994**, *49* (7), 5081.

(13) Yu, D. P.; Sun, X. S.; Lee, C. S.; Bello, I.; Lee, S. T.; Gu, H. D.; Leung, K. M.; Zhou, G. W.; Dong, Z. F.; Zhang, Z. **1998**, *72* (16), 1966.

(14) Lee, C. H.; Qin, S.; Savaikar, M. A.; Wang, J.; Hao, B.; Zhang, D.; Banyai, D.; Jaszczak, J. A.; Clark, K. W.; Idrobo, J.-C.; Li, A.-P.; Yap, Y. K. *Adv. Mater.* **2013**, *25* (33), 4544.

(15) Ciofani, G.; Danti, S.; Genchi, G. G.; Mazzolai, B.; Mattoli, V. *Small* **2013**, *9* (9–10), 1672.

(16) Chen, H.; Chen, Y.; Li, C. P.; Zhang, H.; Williams, J. S.; Liu, Y.; Liu, Z.; Ringer, S. P. *Adv. Mater.* **2007**, *19* (14), 1845.

(17) Schimmenti, R.; Cortese, R.; Duca, D.; Mavrikakis, M. *ChemCatChem* **2017**, *9* (9), 1610.

Chapter 2

Clays and Natural Compounds

2. *Clays and natural compounds*

"Then the Lord God formed a man from the dust of the ground… Gen. 2:7"

The importance of clays in human life and culture has solid roots until the dawn of the first civilizations, maybe enough to attribute to them the origin of the same human beings.

With the term "clay", we usually refer to a natural material with particles of very fine size, plastic properties and mineral fragments or particles composed mostly of hydrous-layer silicates of aluminum. In particular these minerals are composed, essentially, of silica, alumina or magnesia or both, and water. Appreciable quantities of iron, potassium, sodium, and calcium are frequently present as well.[1]

Clays are perhaps the oldest materials from which humans have manufactured various artifacts. Indeed, more than 5,000 years ago, primitive men used clays to fabricate bricks and this was the second main activities of the time after agriculture. In the years, the use of clays (probably with the smectite structure) was extended to fabricate soaps and absorbents as the Roman author Pliny the Elder reported in Natural History. In the years, the kaolinite clay was also used for the manufacture of whiteware, refractories, and porcelain. Clay materials were used by the ancient Mayas and other Mesoamerica's people, from at least the 8[Th] century, as pigments to decorate murals. At the present, these murals preserve vivid blue color, and the pigment that characterized this vibrant color was namely "Maya blue" and it was considered to be an inorganic pigment. Several years later it was discovered as an example of organic-inorganic nanohybrid material in which the organic molecules, indigo molecules, responsible for the blue color of the clay, are encapsulated within the nanosize tunnels of clays.

Beside the use of clay minerals for ceramic products, they have been also used, since ancient time, for medical purposes. There are traces that minerals have been used for curative applications since prehistory; *homo erectus* used ochres mixed with water and different type of mud in order to cure wounds.

More than half century ago, Irish physicist Bernal and Swiss geochemist Gold Shimidt, independently, proposed that clay minerals may have played an important role in the prebiotic synthesis, because of their ability to take up, protect, and catalyzed the polymerization of small organic molecules.

Considering all of this, it is clear the important role of clays in the industrial mineral's field. Accordingly with the recent arise of nanotechnology, clay materials have found

multiple applications. The versatility is one of the most important peculiarities of clay minerals, that give to these materials the possibility to be used in several fields, increasing the interest by the scientific community.

2.1. Clays and Clay Minerals

Often the terms clay and clay minerals are used as one and the same, but they are not exactly synonymous. The meaning of "clay" indicates a rock, a sedimentary deposit, and the alteration products of primary silicate minerals. The definition of clay, according to *Joint Nomenclature Committees, Association Internationale Pour l'Etude des Argille and Clay Mineral Society* is "…a naturally occurring material composed primarily of fine-grained minerals, which is generally plastic at the appropriate water contents and will harden with dried and fired". The plasticity, in general, is a property of all materials which can deform irreversibly without breaking.

Instead, clay mineral are phyllosilicate minerals and minerals which give plasticity to clay, have the tendency to harden upon drying or firing and can be also be defined as the major constituents of clay, being responsible for their primary characteristic.

2.1.1. Origin and terminology

The origin of clay materials, in nature, is due to weathering and hydrothermal and diagenetic actions. Physical and chemical weathering interaction with the rocks forms silica, alumina and other rocks materials (primary minerals) that can develop in secondary minerals after a recrystallization process.

For example, the CO_2 gas dissolves easily in water forming carbonic acid, which hydrolyzes in hydrogen and bicarbonate ions making the water slightly acidic. Then the acidic water reacts with the rock's surfaces dissolving the potassium ions and silica to form feldspar, a potassium aluminosilicate. After that, the feldspar is transformed into kaolinite.

$$2KAlSi_3O_8 + 2H^+ + H_2O \rightarrow Al_2Si_2O_5(OH)_4 + 2K^+ + 4SiO_2$$

The assembly of the particles brings the formation of aggregates that can provide the assembly of aggregation. Accordingly, we may distinguish between interlayers, interparticle and interoperate cavities. All clays minerals are porous, containing pores of varied size and shapes: the pores act as sites of a host that can interact with a guest.

Several different arrangements of particles can be achieved: dispersed (No face to face association of clay particles), aggregates (face to face association of several clay particles), flocculated (Edge to edge or edge to face association), deflocculated (No association between aggregates).

Kaolinite is known with the commonly used name kaolin, which is a corruption of the Chinese *Gaoling*, meaning "high ridge," the name of a hill near Jingdezhen where the occurrence of the mineral is known as early as the 2nd century BC. Montmorillonite and nontronite are named after the localities Montmorillon and Nontron, located in France where these minerals were first found. The name of Celadonite is from the French *céladon* (meaning grayish yellow-green) in allusion to its color. Sepiolite is a light and porous material, and its name is based on the Greek word for cuttlefish, the bone of which is similar in nature. The name saponite comes from the Latin *sapon* (meaning soap), because of its appearance and cleaning ability. Vermiculite derived from the Latin *vermiculari* ("to breed worms"), related to the physical characteristic of exfoliation upon heating, which causes the mineral to exhibit a spectacular volume change, from small grains to long wormlike threads. Baileychlore, brindleyite, corrensite, sudoite, and tosudite are instead examples of clay minerals that were named after distinguished clay mineralogists—Sturges W. Bailey, George W. Brindley, Carl W. Correns, and Toshio Sudō, respectively.[1]

2.1.2. Delamination and Exfoliation

Delamination denotes the process of separation of the individual layers of the particles. In aqueous dispersion, intercalated water molecules lead to increasing separations between two successive layers. The possibility to split clay layers into isolated units is the process of delamination. Delaminated clay minerals layers present: higher surface areas, much smaller particles size, the ability to form much more stable colloidal dispersion as nondelaminated ones, due to the much higher interaction with the liquid phase.

The exfoliation phenomenon is a process in which no further interaction occurs between two or more delaminated units that become independently mobile in the liquid phase. In other words, is the decomposition of large aggregates into smaller particles. Exfoliation mostly involves the mechanical disruption of the solid, which can be achieved by grinding, extruding or similar process. On the other hand, the mechanical process may not be efficient enough to separate the individual layers of the clay minerals in structure

with strong interlayer interactions like kaolinite. In these cases, exfoliation must involve chemical process, which influences the interlayer cohesive forces.

2.2. Classifications

The classification of clay minerals can be made in different ways, mainly based on morphology and chemical structure (Figure 2.).

The arrangement of the particles or aggregates leads, as above mentioned, to different morphology: road-like (palygorskite), fibrous(sepiolite), tubular (Halloysite), lamellar (MTM), layer-pillared (Hydrotalcite).

Some clay minerals may be expressed using a general chemical formula as the following: $2SiO_2 \cdot Al_2O_3 \cdot 2H_2O$ (kaolinite), $4SiO_2 \cdot Al_2O_3 \cdot H_2O$ (pyrophyllite), $4SiO_2 \cdot 3MgO \cdot H_2O$ (talc), and $3SiO_2 \cdot Al_2O_3 \cdot 5FeO \cdot 4H_2O$ (chamosite).

Commonly clay mineral minerals can be classified varying the chemical composition and atomic structure, into nine groups[1]:

1. Kaolin-serpentine (kaolinite, halloysite, lizardite, chrysotile);
2. Pyrophyllite-talc;
3. Mica (illite, glauconite, celadonite);
4. Vermiculite;
5. Smectite (montmorillonite, nontronite, saponite);
6. Chlorite (sudoite, clinochlore, chamosite);
7. Sepiolite-palygorskite
8. Interstratified clay minerals; (e.g., rectorite, corrensite, tosudite);
9. Allophane-imogolite.

SILICATES

Tectosilicates
(Framework silicates)
• **Zeolites**
• **Quartz**
• **Feldspars**

Phyllosilicates
(Sheet silicates)

Other silicates

1:1 Phyllosilicates
Kaolinite-serpentine

2:1 Phyllosilicates

2:1 Inverted ribbons
• Sepiolite
• Palygorskite (attapulgite)

Kaolinite subgroup
• **Kaolinite**
• Halloysite
• Dickite
• Nacrite

Talc-Pyrophyllite

Smectites

Vermiculites

Chlorites

Micas

Serpentine subgroup
• Chysotile
• Antigorite
• Lizardite
• etc.

Dioctahedral smectites
• **Montmorillonite**
• **Beidellite**
• Nontronite

Dioctahedral micas
• **Muscovite**
• *Illite*
• **Phengite**
• etc.

Trioctahedral smectites
• Saponite
• Hectorite
• Sauconite

Trioctahedral micas
• **Biotite**
• etc.

Figure 2. Family tree of silicates.

2.3. Structures

The term phyllosilicate originates from the greek φύλλον, "*phyllon*", meaning leaf. The phyllosilicates are constituted of alumina and silica sheets combine to form layers that may condense in either 1:1 or 2:1 proportion. The 1:1 can be considered like "a biscuit with acing on top"; meanwhile the 2:1 is like "Oreo biscuit". The 1:1 group is constituted by the kaolin in which the most abundant minerals is the kaolinite, and less popular halloysite, with an interlayer space of about 7 Å. Regarding the 2:1 phyllosilicate, the most popular and used in several fields are sepiolite and montmorillonite that shows different chemical structure, and an interlayer space ranging from 10 to 20 Å.

In the 2:1 clay minerals, between the layer there are some water molecules and it is possible to observe an increase of the interlayer space. Under dry condition, cations are present in the interlayer and when clays are dispersed in water, water molecules interact with cations by the oxygen atoms and with the layer by the hydrogens. After an appropriate time, the cations are fully hydrated, which result in repulsive forces and expanding clays layers and different size of the interlayer space.

In detail, the structure of clay materials consists of two basic units: an octahedral and a tetrahedral sheet. The octahedral sheet includes a closely packed oxygen and a hydroxyl

group in which aluminum or magnesium atom are arranged in octahedral coordination (Figure 3a). When aluminum is present in the sheets, only two out of three octahedral sites are occupied by the trivalent ions, in order to balance the total charge (this type of minerals is named "dioctahedral"). Instead, when magnesium is present, all three position are filled to balance the structure and this type of mineral is named trioctahedral.
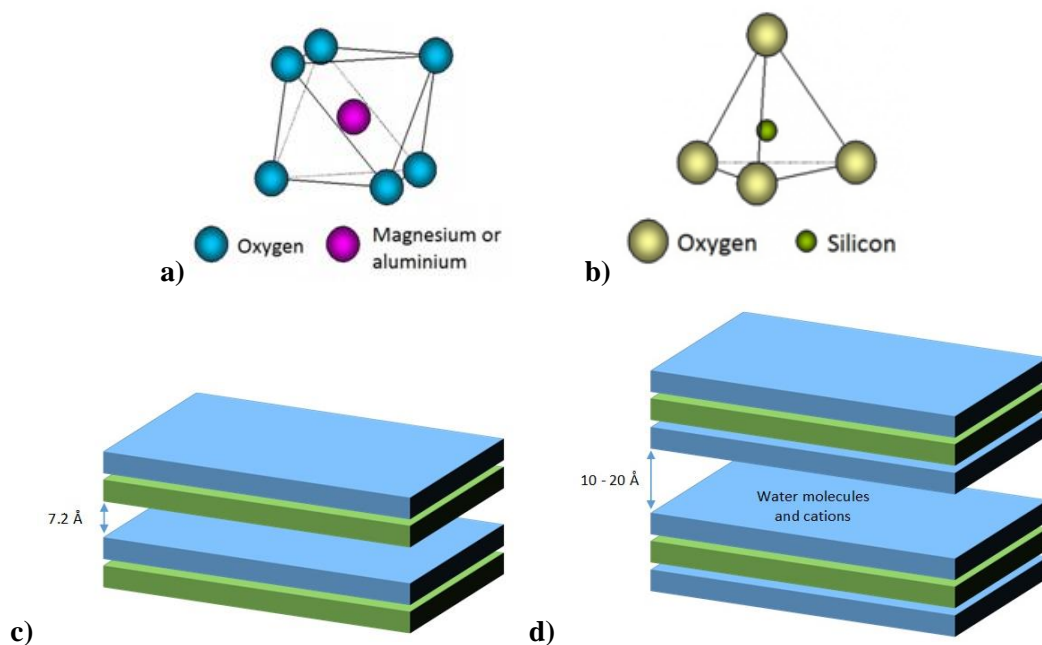
Figure 3. Representation of a) octahedral coordination; b) tetrahedral coordination c-d) building blocks of clays.

The second structural unit is the silica tetrahedral layer, in which the silicon atoms, in the center of a tetrahedral, are equidistant from four oxygens (Figure 3b). The tetrahedrons are arranged to form a hexagonal network repeated infinitely into two horizontal directions to form what is called the "silica tetrahedral sheet".

The silica tetrahedral sheet and the octahedral sheet are joined by sharing the apical oxygen or hydroxyl to form what is named the 1:1 clay materials layer or the 2:1 clay material layer (Figure 3c-d). According to this disposition, several types of surfaces are present, like the external, internal and edge surfaces.

Based on these types of disposition of the layers, clays minerals can be also classified in amorphous and crystalline, in particular, the last one includes the two-layer type, like kaolinite and halloysite, the three-layer type, like MTM, but also a regular mixed-layer type and chain-structure type.

An important feature is the possibility of substitution between cations that may occur in the tetrahedral and octahedral sheet, resulting in the different charge deficit. Consequently,

the negative charge tempts to attract cations which are inserted between the layers. Depending on this substitution, the composition of the tetrahedral and octahedral sheet changes and the resulting layer will have no charge or will have a net negative charge based on this aspect and the type of cations.

2.3.1. Structure vs Properties

The physical and chemical proprieties of clay minerals are dependent on its structure and composition. A layer structure with one dimension in the nanometric range, and the thickness increasing from 1:1 to the 2:1 clay minerals, reaching in the 2:1 type 1 to 2 nm in size. The anisotropy of the layers or particles is the property of being directionally dependent, which imply different proprieties in different directions and surfaces. As a matter of facts, as previously mentioned, clay minerals are characterized by external and edge surfaces as well as internal or interlayer surface, each one with different dimension and so different properties. Furthermore, they can be modified by adsorption, ion exchange or grafting extended the range of this properties.

An important aspect or property is about the charge of the surfaces. There are two charges: structural or permanent and pH dependent. The permanent charge is usually due to ions substations, or it can be also caused by structural imperfections. For example, the external or interlayer surface is negatively charged in general, that can interact with cation molecules and different cations to balance charge deficiencies. Whereas the edges can be positively or negatively charged pH dependent. Under acid condition we can observe the protonation of hydroxyl groups that produce, as a consequence, a positive charge; or under basic condition, we can observe a deprotonation and a negative charging. The several different charges that can be involved are the result of the hydrolysis of broken SiO- and Al-OH bonds. On top, the SiO has acid characteristic, whereas the AlOH is amphoteric.

2.4. Clays

Clays have been one of the more important industrial minerals; and with the recent advent of nanotechnology, they have found several applications and in each application, nanoclays help to improve the quality of the product, economize on the cost and saves the environment.

Between the different groups, some have a large diffusion and historical application, others, recently have been applied in new interesting applications.

2.4.1. Kaolin

The kaolin group comprises predominantly kaolinite. Usually, "kaolin" is used to replace the more accurate term of kaolinite. Indeed kaolinite is the principal mineral in kaolin clays, a 1:1 clay mineral featured by a basic unit of a 2-dimensional (2D) layer of silicate groups tightly bonded to a 2D layer of aluminate groups. As already mentioned, the interlayer space of 1:1 clay mineral is about 7.2 Å, value much lower respect to the 2:1 clay mineral, and not expandable due to the strong hydrogen bond in the interlayer space, and not allowing water molecules or ions to enter the structure. Particle size ranges from 0.2 to 2 μm and the effective surface area is limited (10-30 m^2/g) as mainly external surface (more available).

Sheets of kaolinite are arranged like pages in a book: if the book is open patch pages has surface area on the front and back, which coved be a lot of surface area; if the book is closed the pages are tightly packed, so the surface area is not available. So, the only surface that can adsorb water or cation would be the outside of the book. Furthermore, the ability to cation's exchanges is very low, which explain the low fertility of soils that are rich in kaolinite minerals.

2.4.2. Smectite group

The Smectite group belongs to the 2:1 clay mineral. Unlike kaolinite with its tetrahedral/octahedral (TO) sheet arrangement (or 1:1), these minerals have a tetrahedral/octahedral/tetrahedral (TOT) sheets structure. So, these are composed of two silica tetrahedral sheets, within the center an octahedral sheet, filled with water molecules

and cations in the space between the 2:1 layers. The main constituents of smectite group are Na^+ MTM and Ca^{++} MTM, in the general formula. This is the theoretical charge distribution in the smectite layers. MTM's morphology looks like a sponge, with an extensive isomorphous substitution for silicon and aluminum by the cations, which results in charge deficiencies of clay particles. The spacing between layers can be easily expanded: the $n \times H_2O$ and cation exist between unit layers, and the basal spacing is from 9.6 Å to infinity after swelling. During the dry season, in the soil rich in MTM it is possible to observe a contraction of soil aggregates and developments of cracks in the soil surface. This phenomenon is due to the water loss that brings to the reduction of the interlayer space.

2.4.3. Sepiolite

Another known clay mineral is the sepiolite. Sepiolite is the constituent of the already mentioned Maya blue color. The combination of the octahedral and tetrahedral sheets is different respect MTM, with the sheets linked to each other infinitely in two dimensions: in particular, the octahedral sheets are continuous in only one dimension and the tetrahedral sheets are divided into ribbons by the periodic inversion of rows of tetrahedral. This clay mineral contains two kinds of water: one coordinated to the octahedral cations, and the other loosely bonded in the channels, which is named "zeolitic water". The resulting morphology is an elongate chain, with channels that may contain exchangeable cations.

2.4.4. Imogolite

Cradwick *et al.* proposed the first model of the imogolite structure, which consisted of aluminosilicate ($Al_2SiO_7H_4$) single-walled nanotubes with 2–3 nm external diameter, and a few being hundreds of nanometers long. Imogolite is composed of a curved gibbsite layer on the outer surface and Si monomers linked to six Al inside the tube.[3]

This mineral was discovered in 1962 in a soil derived from glassy volcanic ash known as "imogo."

2.4.5. Laponite

Laponite is a synthetic hectorite clay, with chemical formula $[(Si_8Mg_{5.5}Li_{0.3})\ O_{20}$ $(OH)_4]_{0.7}$- Na^+. It consists of disk-shaped particles, of approximately 25 nm diameter and 1 nm thickness, with a 2:1 structure: an octahedral MgO sheet, sandwiched in between two tetrahedral silica sheets. The features of this particular clay are a permanent negative surface density charge, arising from isomorphic substitutions of Mg by Li in the crystal structure, and a weak positive edge charge (about 10% of the total negative charges), pH dependent, from the presence of sodium ions in the interlayer, to balance the negative charge density.[4]

These particles have the ability to spread in water, with a self-organize dispersions via face-edge aggregation, forming an open, macroporous and reversible (thixotropic) gel network. The driving force of gelation in aqueous dispersion is due to the fact that molecules of water are driven into the inter-layers of particle aggregates by osmosis, hydrating the sodium ions and delaminating them into primary particles.[5–7]

The mechanism of gel formation has been proposed by Van Olphen and Norrish to describe the nature of colloidal dispersion and the underlying particle interactions. The first one hypothesis consists in electrostatic attraction between positively charged edges and negatively charged faces, that result in a linked structure known as "house of cards", but this mechanism is favored only at high ionic strength such that more than 0.01 M sodium chloride. The second proposed mechanism is due to the effect of long-range electrostatic repulsion between interacting double layers, which is considered leads to equilibrium state.[8]

This propensity for swelling and delamination of the charged particles, gives rise to a rich selection of potential interactions between organic molecules and the clay surfaces, inter-layer pores and inter-particle spaces, involving several mechanisms including cation exchange, hydrophobic interactions, hydrogen bonding, cation bridging, anion exchange and proton transfer depending on pH, size and electrostatic properties of the interacting molecule, as shown in Figure 4.[9]
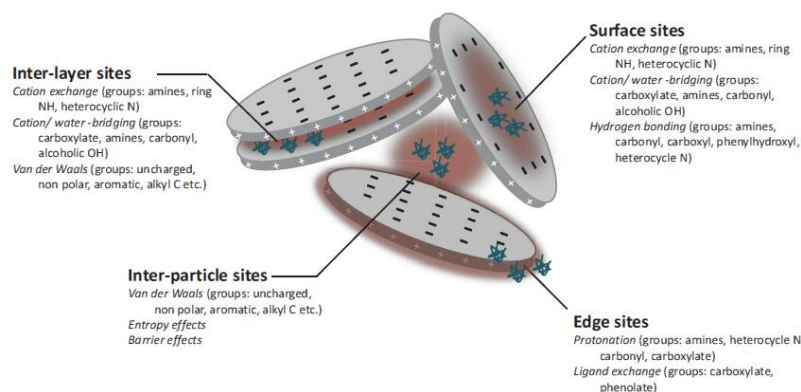
Figure 4. Representation of Laponite.

2.4.6. Halloysite

Halloysites are types of naturally occurring multiwalled aluminosilicates with 1:1 sheet arrangement. The halloysite layer structure is composed of octahedral coordinated Al_3^+ and tetrahedral coordinated Si_4^+ in a 1:1 arrangement with water molecules between the layers. Up until about 2005, the main application of halloysites had been as an alternative raw material to kaolinite for ceramics. Since then, however, there has been an exponential increase in studies aimed at applications of halloysite nanotubes. The readily available and relatively cheap nanotubular forms of halloysite have potential uses in nanocomposites with polymers, as carriers for active agents, e.g. in medicine, agriculture, cosmetics, and environmental remediation, as well as in nanotemplating, as supports for catalysts.

Since 2005, the number of patents has virtually equaled the number of papers on HNTs. These observations provide clear evidence that research on halloysite is readily translated into important new technologies, perhaps to a greater extent than the research on any other clay mineral.[10]
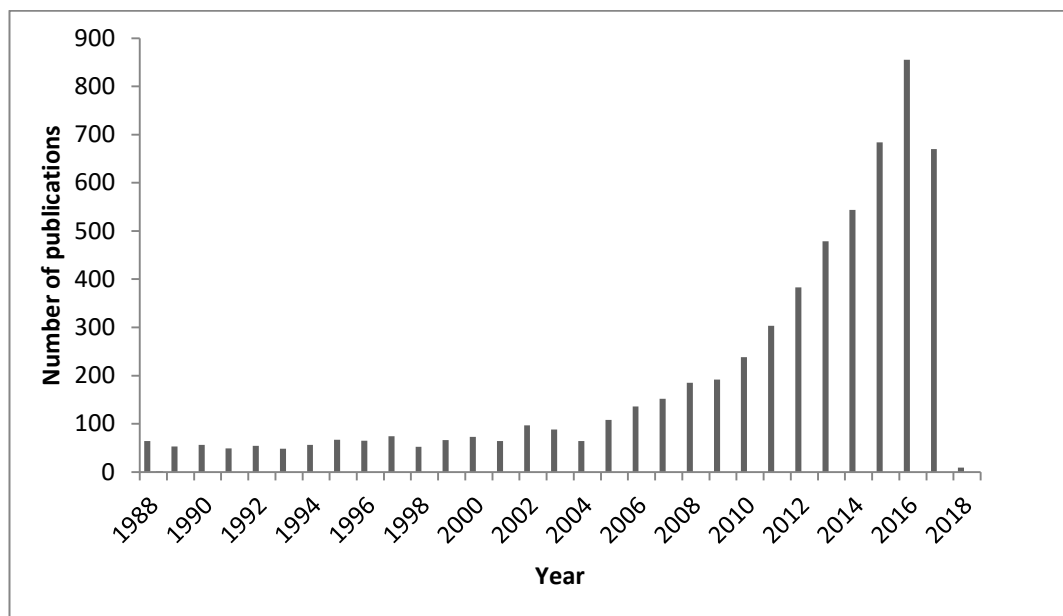
Figure 5. Trend of the number of publication in the years using the SciFinder Scholar search system with the terms «Halloysite», at November 2017.

References

1   H. Kodama and R. Grim, *Encycl. Br.*, 2014.

2   M. S. Nazir, M. H. Mohamad Kassim, L. Mohapatra, M. A. Gilani, M. R. Raza and K. Majeed, 2016, pp. 35–55.

3   E. Joussein, in *Nanosized Tubular Clay Minerals. Halloysite and Imogolite*, eds. P. Yuan, A. Thill and F. Bergaya, Elsevier, 7th edn., 2016, vol. 7, pp. 12–48.

4   J. I. Dawson and R. O. C. Oreffo, *Adv. Mater.*, 2013, **25**, 4069–4086.

5   T. Nicolai and S. Cocard, *Eur. Phys. J. E*, 2001, **5**, 221–227.

6   P. Mongondry, J. F. Tassin and T. Nicolai, *J. Colloid Interface Sci.*, 2005, **283**, 397–405.

7   J. D. . Ramsay, *J. Colloid Interface Sci.*, 1986, **109**, 441–447.

8   K. Norrish, *Discuss. Faraday Soc.*, 1954, **18**, 120.

9   G. Lagaly, *Dev. Clay Sci.*, 2006, **1**, 141–245.

10   G. Jock Churchman, P. Pasbakhsh and S. Hillier, *Clay Miner.*, 2016, **51**, 303–308.

Chapter 3

Halloysite Nanotubes

3. *Halloysite nanotubes*

Halloysite was first described as a separate mineral by P. Berthier in 1826, which discovered the mineral in Angleur, Liege, in Belgium.[1]

The name 'halloysite' was chosen in honor of Omalius d'Halloy (1783-1875) who first observed the material but it was not used until 1882.

Omalius d'Halloy was the founder of geological science in Belgium and famous for a lot of scientific papers and contributions. Member of the Belgian Royal Academy and of Academy of the Sciences of Paris, among his numerous writings, we recalled: *Description géologique des pays situés entre le Pas de Calais et le Rhin*, *Éléments de Géologie*, *Des roches considérées minéralogiquement* and *Géologie de la Belgique*.[2]

Halloysite was originally distinguished from kaolinite (in the 19th century) on the basis of a higher proportion of water associated with it than with kaolinite. In 1935, two distinct substances, both referred as halloysite were discovered by Mehmel. One of them have loosely bound water and showed a 10 Å basal reflection on an X-ray diagram, the other one none and showed a reflection approximately at 7

Figure 6. Jean Baptiste Julien d'Omalius d'Halloy (February 17, 1783 in Liège – January 15, 1875 in Brussels)

Å. Mehmel chose to use the name halloysite for the hydrous mineral, and for the product of its dehydration proposed the name "metahalloysite". Now we know that is possible to find both substances naturally. Before these clarifications, Hofmann, Endell, and Wilm suggested that the 10 Å material on dehydration at a low temperature gave kaolinite, but Mehmel showed that was wrong and that the error was due to the similarity of their X-ray diagrams. Hofmann, Mehmel, and relative co-workers assumed that the name halloysite was best to apply to the 10 Å material rather than the 7 Å.

Hendricks introduced the use of the term "halloysite" for the non-hydrated material and the term "hydrated halloysite" for the hydrated one but the two terms are still in use, with the term "halloysite" used in both senses. In an attempt to clear up the confusion, another revision of the nomenclature has been proposed, consisting in the introduction of a new

name "endellite" for the hydrated mineral, and the name halloysite being retained for the dehydrated mineral.[3]

In the years, several classification schemes for halloysite minerals have been proposed based on different properties and characteristics like hydration state, particle morphology and degree of crystalline order, but also based on relating variations in particle morphology to chemistry, structure, or environmental conditions in the formation process. For this reason, a big number of synonymous have been used for halloysite since its initial description: endellite, hydrated halloysite, hydrokaolin, hydrohalloysite, gummite, glagerite, glossecolite, indianaite, lenzinite, tithomarge, Fuller's earth, tuesite, steinmark, ablykite that is really a close mineral of halloysite.

MacEwan suggested that both the hydrated and dehydrated forms of halloysite are opposite edges of a series, differing in their degree of hydration. More precisely proposed the name "halloysite" for the material with a d_{001} spacing of 10 Å and "metahalloysite" for the dehydrated end member with 7 Å spacing. Later, Brindley and Grim proposed halloysite - (10 Å) and halloysite - (7 Å) to denote the state of hydration. These terms were also recommended by Churchman & Carr who, following MacEwan, agreed to a continuum of hydration states. Although this nomenclature is now generally accepted, the possibility of confusing halloysite - (7 Å) with kaolinite can remain. In light of this, in 2002 Hart *et al*. suggested the specific name of kaolinite for 1:1 dioctahedral clay minerals with a morphology of particle plate-like, and the name of halloysite when these particles are cylindrical or tubular. Finally, as recommended by the AIPEA, International Association for the Study of Clays, the most accepted used terms are halloysite (10 Å) for the hydrated mineral and halloysite (7 Å) for the dehydrated, and the term "endellite" was to be discarded.[4–6]

3.1. *Structure of Halloysite Nanotubes*

One of the first descriptions of halloysite was that it has an irregular shape, amorphous granules, with irregular surfaces and a sponge-like structure.

Today we know that halloysite is a phyllosilicate clay mineral of the kaolin group, which contains octahedral gibbsite $Al(OH)_3$ and tetrahedral SiO_4 sheets with chemical formula $Al_2Si_2O_5(OH)_4 \cdot nH_2O$ although usually contains minor amount of metal ions replacing aluminum in some positions.[7]
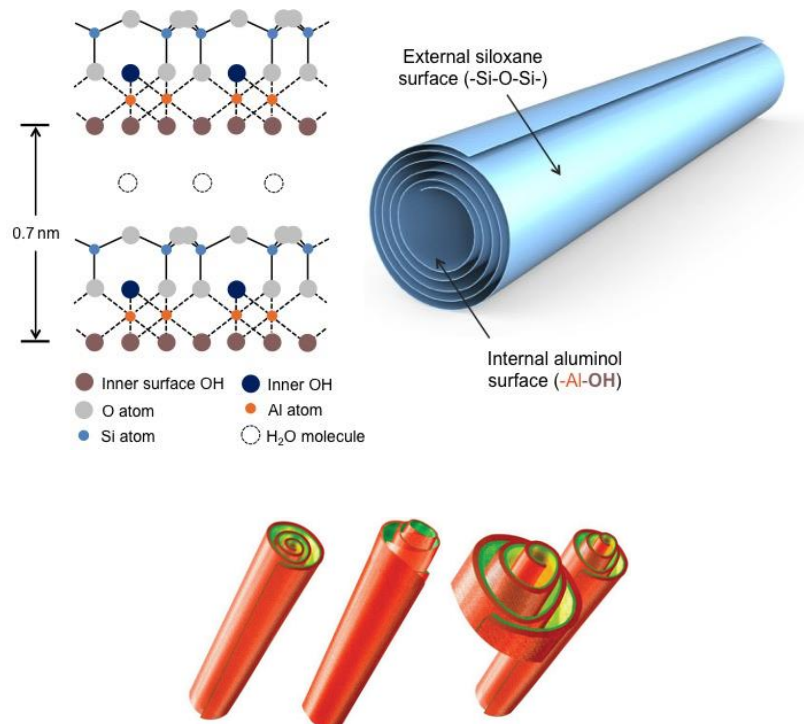
Figure 7. Schematic illustration of the crystalline structure and rolling of HNTs.[15]

Halloysite can exist in different forms, including elongated or short tubes, spheroidal, squat cylinders, and plates, but consists of predominately hollow cylinders (HNTs). These are made of multiple rolled layers composed by a sheet of corner-sharing SiO_4 tetrahedral bonded to a sheet of edge-sharing AlO_6 octahedral, making in this way a 1:1 layer silicate. In the gaps between the aluminosilicate layers of the structures, there are crystallographic water molecules and kaolinite OH groups (Figure 7).[8,9]

As previously introduced, layered halloysite occurs mainly in two different polymorphs, the hydrated form with the formula $Al_2Si_2O_5(OH)_4 \cdot 2H_2O$ and the anhydrous

form with the formula $Al_2Si_2O_5(OH)_4$, with interlayer spacing of 10 Å and 7 Å), respectively.[10,11]

Typically, 10–15 aluminum-silicate bilayers roll into the cylinder giving an external surface composed of siloxane (Si–O–Si) groups, an internal surface that consists of a gibbsite - like array of aluminol (Al–OH) groups, and Al-OH and Si–OH groups at the edges of the material.

Due to this characteristic structure, halloysite has negative charges on its external surface, positive on inner lumen surface and negative/positive charges at its edges at pH values ranging from 3 to 10. Considering the charges at the edges, the structure of the mineral clay is disrupted and bond cleavages occur at different pH values, exposing in this way the hydroxyl groups. These charges at the edges are therefore attributed to the deprotonation/ protonation of silanol and aluminol groups, which are pH-dependent.[12,13]

The hydroxyl groups at the surfaces and edges of HNTs also providing a useful opportunity for further modification with various organic compounds.[14]

Generally, HNTs have external diameter of 40–60 nm, internal diameter of 10–15 nm and length of 0.7–1 μm. These characteristics depend on many factors, such as the extraction site and purification procedures. For example, in some deposits, were observed halloysite tubes with length up to 3–5 μm but in the size distribution curve they have a minor fraction. The smaller clay nanotubes are most interesting for composites with sustained delivery chemicals or drug formulations. As a matter of fact in many cases, the halloysite tubes that are commercially available are the shorter ones (with 400–500 nm length) because of harsh milling during industrial processing.[15]

Table 2. Literature report of occurrences around the world of various morphologies of halloysite.[4]

Morphologies	Occurrences
Tubular, long and thin, short and stubby tubes	Crypto karstic sediment, volcanic glass, and pumice, feldspar and mica alteration
Pseudo spherical and spheroidal	Weathered volcanic ash and pumices, volcanic glass in marine environment, (e.g. Guatemala soils, New Zealand)
Platy or tabular	Volcanic ash soils, weathered pyroclastic, lateritic profiles, fissures within granite, hydrothermal alteration, tuff bed (e.g. Texas, Brazil, Guatemala)
Fibre	Lateritic soil, weathered granite (e.g. Australia, Brazil)
Prismatic, rolled, crinkly, walnut-meat	Volcanic ash soils, weathered granite (Japan)
Cylindrical, disk	Rhyolitic tephra (New Zealand)
Spherulitic, irregular lath with rolling edge	Weathered granite/gabbros, (Scotland)
Crumpled lamellar	Weathered pumices (Japan)
Lath, scroll	Altered volcanic glass (Japan)
Glomerular or "onion-like"	Volcanic ash (Cameroon)

The hydrated halloysite presents a water layer between two adjacent sheets, about 12% mass,[16] that evaporates under heating giving a compression of the layers and the smaller packing spacing.

The interlayer water molecules can be classified into two types: hole and associated. The hole water molecules are embedded into the ditrigonal cavities in the basal oxygen site with two main different orientations and forming hydrogen bonds with the basal oxygen. The associated ones, instead, are located at different levels in the interlayer space with an ice-like configuration, forming a network of hydrogen bonds with each other and/or with inner-surface hydroxyls with a high degree of mobility.

Because of the different stability, the hole water is lost more slowly than the associated ones. The dehydration process gives an intermediate state between a fully hydrated and fully dehydrated form whit two intermediate states of HNTs (8.6 Å) and HNT (7.9 Å). The dehydration process is irreversible,[1,3,15,17] and can have different effects on HNTs such as the reduction of particle size, unfolding or changes in diameter.[18]

Crystallographic data indicate partial tube unrolling takes place upon dehydration causing to increase tube diameter by 10–15%. The remaining strong interlayer hydrogen bonds prevent complete unrolling.[19]
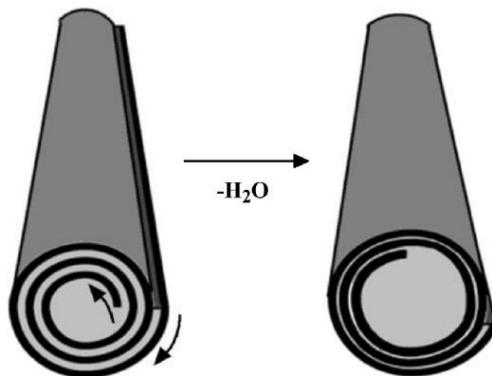
Figure 8. Scheme of the halloysite dehydration (10→ 7 Å).[19]

The reason for the curving and the rolling up of the flat kaolinite that brings to the multilayer tubes and so the formation of the halloysite tubes is still unclear and hotly debated in the literature, without any real consensus.

In principle, the formation of a such rolled structure could be due to an alteration of the flat kaolinite where part of the plate undergoes a curved and smoothly rolling up with lateral defects of the smaller octahedral sheet compared to a larger tetrahedral one in terms of iron content, direct precipitation and other characteristics.[16]

In 1966 Chukhrov *et al.* concluded that the halloysite-like structure may be the end member of such defect-type kaolinite.

In literature is also well explained the influence of Fe amount and particle morphology. The relationship between the main morphologies of halloysite and the Fe content shows some clear trends. It has been demonstrated that platy forms always contain relatively large amounts of Fe, tubular particles are relatively Fe poor, and spheroidal halloysite instead exhibit a large range of Fe contents, from almost zero up to values that are comparable to those of many tubular halloysite to quite high values.[4]

Is possible to find an explanation of this trend in the behavior of the plates after the substitution of Al^{3+} with Fe^{3+} in the octahedral position that increases the overall size of the octahedral sheet and limits the curvature effects, thus influencing the ultimate structure.

In order to obtain more detail information on the distortions of the kaolinite sheet in the process of halloysite nanotube formation, a lot of computational investigation have been also made, considering different factors as distortions of the aluminum and silicon polyhedral and the water molecules effect on stabilization of the spiral structure.[16,20]

The peculiar tubular structures allow the halloysite to show different surface chemical properties at the inner and outer sides of the tubes.

In HNTs, the silica layer is located on the outer surface of the tube, while the alumina layer is located on the inner lumen surface. Aluminum and silicon oxides have different dielectric and ionization properties, which are evident from observations of the electrical ζ-potentials of these oxide colloids in water. The peculiarity to have different charges between the inner and outer side of the halloysite nanotubes, among other things, allows for the selective loading of negatively charged molecules into their lumen. The different chemistry of the inner and outer surfaces of the halloysite nanotubes can also be exploited for selective modification.[21] By easy math counts, is possible to calculate that the lumen volume is c.a. 10% of all the all cylinder.

Unlike other tubular materials, such as boron nitride, metal oxide, clays and carbon nanotubes, halloysite is an abundantly available natural nanomaterial, which makes it very convenient for technological applications (Table 3). Furthermore, HNTs have unique properties that associate with the low cost and the biocompatible of the material make it attractive in different fields of interest.

Table 3. Comparison of main properties of halloysite, imogolite and carbon nanotubes

	Halloysite nanotubes	Imogolite nanotubes	Carbon nanotubes
Chemical formula	$Al_2Si_2O_5(OH)_4$	$Al_4Si_2O_6(OH)_8$	C
Length	0.5–2 µm	1–5 µm	1–5 µm
External diameter	50–100 nm	2–10 nm	2–10 nm
Inner diameter	10–20 nm	1–5 nm	1–3 nm
Biocompatibility	Biocompatible	Biocompatibile	Health hazard
Water wettability	Hydrophilic	Hydrophilic	Hydrophobic
Surface chemistry	SiO_2 outside $Al(OH)_3$ inside	$Al(OH)_3$ outside SiO_2 inside	Graphene sheet, both sides
Surface charge at pH 2–9	Negative	Positive	Not charged
Specific surface area, m^2/g	50–150	300–400	15–250
Price	$ 4 per kg	-	$ 500 per kg
Availability	Tons	-	Grams

3.2. Characterizations

As mentioned before, over the decades, there have been many debates on the identification of the halloysite as a unique mineral and in particular about the ability to distinguish it from the kaolinite.

The technical and technological development has enabled us to have more accurate investigation techniques, in particular, to verify the correct interaction and modification of halloysite nanotubes, with the purpose of expanding the properties and fields of potential application of them. Some of this techniques will be discussed below.

Halloysite (CAS Number 1332-58-7) has relativity low specific gravity of 2-2.6 g/cm^3, Mohs scale hardness 2-2.5 and shows white, grey, yellow-red color in depending on the presence of impurities.[14,22,23]

3.2.1. Contact Angle

Wettability describes the preference of a solid to be in contact with one fluid rather than another. It deepens on balance of surface and interfacial forces between solid and fluid giving important information about the superficial properties of a material.

In recent years, there has been an increasing interest in the study of wettability, in particular for the determination of the properties of superhydrophobic surfaces.

Wettability studies usually involve the measurement of contact angles (CA) as the primary data, which indicates the degree of wetting when a solid and liquid interact. A CA less than 90° indicates that wetting of the surface is favorable, and the fluid will spread over a large area on the surface; while CA greater than 90° generally means that wetting of the surface is unfavorable so the fluid will minimize its contact with the surface and form a compact liquid droplet. [24]

Contact angle between a certain liquid and halloysite is adopted to evaluate, especially, the change in surface properties.

To evaluate the hydrophilicity/hydrophobicity of halloysite, the water CA is usually measured by placing water drops on the surface of the molded powder. The powder surfaces were prepared by pressing it onto an adhesive paste on a silicon wafer or by dish pellets. The most widely used technique of CA measurement is a direct measurement of the tangent angle at the three-phase contact point on a sessile drop profile.

The CA of the pristine halloysite is, on average, around 10°, indicating that the pristine halloysite was hydrophilic, due to the electron donor ability of the external oxygen atoms on the siloxane surface and the formation of hydrogen bonds with water molecules. Hydrophilicity can be modulated by modification of pristine halloysite.[25]

3.2.2. Dynamic Light Scattering

Dynamic light scattering (DLS) is one of the most popular methods used to estimate the size of nanoparticles by measuring their diffusion coefficient.

Particularly for anisotropic particles, the diffusion can be expressed with a diffusion coefficient described by Stokes-Einstein equation

$$D = \frac{k_B T}{6\eta\pi R_h}$$ *Equation 1*

were

D = diffusion coefficient

η = viscosity of the medium

k$_B$ = Boltzmann's constant

R$_h$ = hydrodynamic radius of the particle

T = temperature in K

Sending a monochromatic light beam, such as a laser, towards a solution having particles in Brownian motion bring the light to hits the moving particles, causing a Doppler Shift that change the wavelength of the incoming light.

Since this change of wavelength is related to the size of the particle, it is possible to estimate the sphere size distribution. Thus it can be performed a description of the particle's motion in the medium, measuring the diffusion coefficient of the particle and using the autocorrelation function.[16,26]

An average of apparent hydrodynamic radius of individual halloysite tubes corresponds to 100–200 nm,[19] but this value may change a lot depending on the source field, extraction techniques and operating conditions of the measurement with the appearance of more than one population.

3.2.3. Energy Dispersive X-ray Spectrometry

Energy Dispersive X-ray Spectrometry (EDS) is an analytical technique that makes use of the X-ray spectrum, emitted by a solid sample bombarded with a focused beam of electrons, to obtain a localized elemental analysis.

In particular, EDS is a surface analysis technique that allowed to having information about the elemental composition of the edge part of the material, normally, in the nanometer range. This makes the technique very interesting for catalytic materials such as supported nanoparticles, and in general, for all those "surface-active" systems.
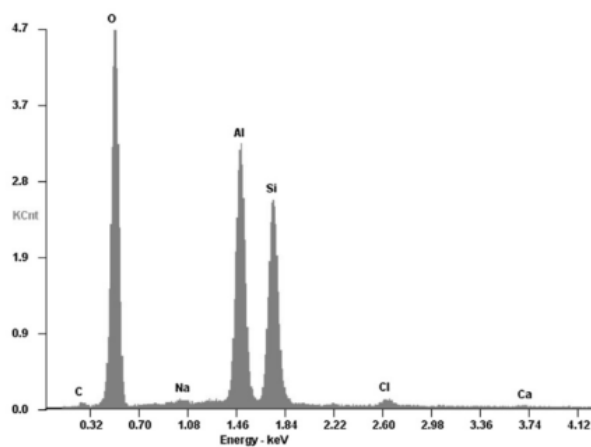
Figure 9. EDS spectrum of a halloysite sample.[27]

Beside mapping the elemental composition of a surface, a quantitative analysis is also very interesting.

Probes are often associated with scanning electron microscopy (SEM) and transmission electron microscopy (TEM) instruments.

According to the molecular formula, quantitative EDS analysis of pristine HNTs shows almost the same percentage in Al and Si, around 20%, with little difference between the picks depends on the sample's history and beam collecting position.

Very relevant is the presence of the metal impurities that could be considered as the fingerprint of the stock.

3.2.4. Infrared spectroscopy

Infrared spectroscopy (IR) is a general technique related to the vibrations of atoms in a molecule and has been widely used for the structural and compositional analysis of organic, organometallic, metalorganic, inorganic and polymeric materials.

Despite being a qualitative technique, IR is an efficient and sensitive tool for identifying minerals of the kaolin group since each mineral exhibit a specific IR spectrum. Furthermore, IR spectroscopy can show the presence of very small quantities of kaolin minerals that are not detectable by XRD.

Briefly, two characteristic bands of HNTs around 3695 and 3620 cm^{-1} are due to the stretching vibration of O–H in the inner-surface hydroxyl groups of Al–O–H. The very low intensity of OH stretching bands between these, around at 3671 and 3652 cm^{-1}, reflects a poorly ordered structure typical for halloysite samples (Figure 10).
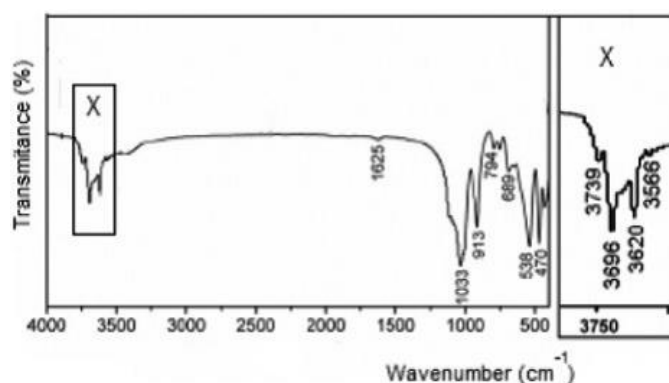
Figure 10. FT-IR spectrum of HNTs.[14]

A weak band at 1107 cm^{-1} is assigned to apical Si–O and the bands at 1030 and 690 cm^{-1} are assigned to perpendicular stretching vibrations of Si–O–Si. The Si-OH stretching vibration is observed around 3739. The bands observed at 940 and 914 cm−1 are caused by the O–H deformation of inner-surface hydroxyl groups, and O–H deformation of inner hydroxyl groups. Halloysite generally also shows a single Al_2OH bending band at about 920 cm^{-1}. Occasionally, the presence of a shoulder at 3600 cm^{-1}, coupled with a weak band at 875 cm^{-1}, is effective in Fe rich halloysite. This band is ascribed to Al-Fe^{3+}-OH vibrations and is in accordance with the presence of structural iron.[14,16,28–31]

3.2.5. Nuclear Magnetic Resonance

Nuclear Magnetic Resonance (NMR) is a spectroscopic method based on magnetic behavior data from the spin momentum of the nuclei of some isotopes.

The most commonly nuclei observed in the NMR experiments are ^{1}H, ^{13}C, ^{15}N, but also ^{27}Al and ^{29}Si, ^{11}B and others.

The NMR has the advantage of being able to be applied, with suitable technical measures, either in solution or on the solid state samples or in gases.

By NMR measurements is possible to extrapolate information on the structure of molecules. For example, great application in the chemistry area of this technique consists in the recognition of the structure of molecules and macromolecules.

Other types of measurements can give information related to the correlations between nuclei and so giving the possibility to obtain information regarding not only the structure but also the interactions, more or less away from each other, with other systems such as the formation of inclusion complexes. In fact, the NMR response of a given nucleus depends on its neighborhood. The neighborhood may consist of vicinal groups of the same molecule but also from the solvent or from the location inside or outside of a Host-Guest system.

NMR allows, furthermore, to follow the kinetics of a reaction or also observe the interaction of a substrate and an active site.

About halloysite nanotubes, the ^{29}Si CP/MAS NMR spectra show a chemical shift at -92 ppm assigned to the silicon, $Si(OSi)_3(OAl)$, of halloysite and other two signals at -68 and -61 ppm.[32]

In literature, there are some examples of the use of NMR studies concerning the halloysite. For example, Dedzo *et al.* [33] used the NMR in solid state and in solution, for the confirmation of the intercalation and graft of ionic liquids in nanotubes.

Another example is found in a paper by Zhang *et al.* who have used ^{11}B-NMR and ^{13}C-NMR to study the selective modification of HNTs with 1 - Pyrenylboronic Acid.[34]

3.2.6. Scanning Electron Microscopy

Scanning Electron Microscopy (SEM) is a powerful magnification tool to investigate nanostructures. It uses a focused electron beam to scan a sample and deliver three-dimensional images with information about the samples' topography and composition.
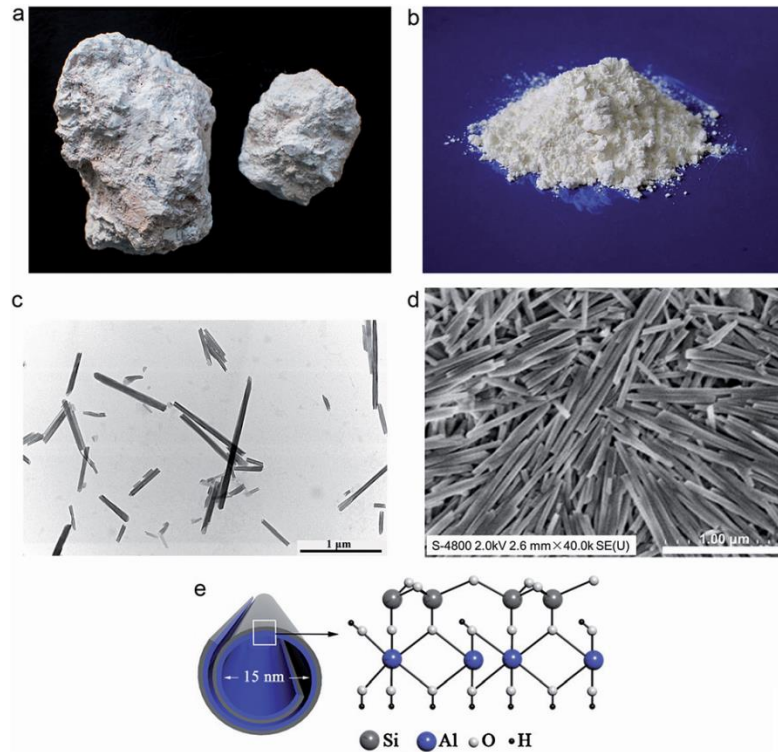
Figure 11. (a) Raw halloysite. (b) Ground halloysite; (c) TEM micrograph (d) SEM micrograph (e) schematic illustration of the crystalline structure of HNTs.[35]

About halloysite, SEM is often used to check the tubular structure of a pristine halloysite stock or for the confirmation of the keeping ore change of the morphology after uses or modification.

3.2.7. Specific Surface Area and porosity

The gas adsorption method is used to measuring the amount of gas adsorbed on the surface of a power sample as a function of the pressure of the adsorbate gas and therefore can be used to determine the specific surface area and porosity of a sample.

For this purposes, many techniques can be taken in consideration, such as Brunauer–Emmett–Teller (BET), which theory aims to explain the physical multilayer adsorption of

gas molecules on a solid surface and serves as the basis for the estimate the specific surface area of a micro/meso/macroporous material. Barrett-Joyner-Halenda (BJH), instead, is a method to determine pore size distribution of a mesoporous solid based on the Kelvin equation.

Both the methods are commonly used to determinate these halloysite properties.

Halloysite, depending on natural deposit and processing, has porosity distribution extended up to 30 nm, with most pores less than 10 nm, and the pore diameter distribution curve has a characteristic peak corresponding to the lumen diameter.[32] Its specific surface area is in the range of 50–150 m^2/g,[14,19] with a total pore volume generally in a very large range from 0.1 to less than 0.01 cm^3/g.[29,36] However, it must always be remembered that these values can change depending on the system. Furthermore, its typical for halloysite material to have both pore volume and diameter influenced by pH condition, with an increase in these at lower pH, instead the total surface area and mesopore surface area tend to decrease with increased pH.

In acidic condition, halloysite nanotubes tend to aggregate and many of the mesopores were blocked, leading to smaller pore volumes and pore size, and pore area show decreasing values according to the increasing pH. On the contrary, in basic condition halloysite nanotubes were well dispersed and the inner-space surface area increased due to the opening of mesopores of halloysite nanotubes.[16]

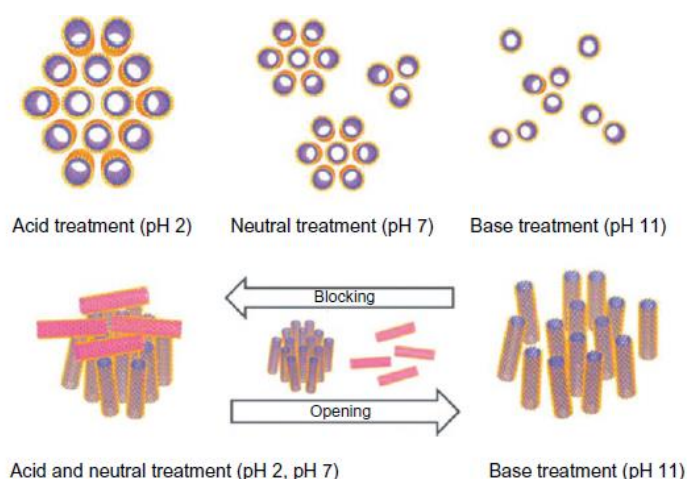**Figure 12.** Schematic illustration of the interspace between halloysite nanotubes after treatment with different pH solutions.[16]

3.2.8. Transmission Electron Microscopy

Similar in concept to SEM, transmission electron microscopy (TEM) is another microscopy technique. In this case are given two dimensions image by using an accelerated beam of electrons transmitted through a specimen, usually with an ultrathin section less than 100 nm thick or a suspension on a grid.

The TEM images enable the observation of features such as structure and morphology. In particular is possible to observed that the halloysite particles have a specific cylindrical shape and contain a transparent central area that runs longitudinally along the cylinder, indicating that the nanotubular particles are hollow and open-ended.[32]

For some tubes, is usually possible to see the packing of the alumosilicate sheets.[37]

Great value has this technique in the study of the modification of the lumen dimension and also in the determination of supported metal nanoparticles, outside, interlayer or inside the tubes.

3.2.9. Thermogravimetric Analysis

Thermogravimetry (TG) is another method of analysis, that uses the recording of the mass variations of a sample, in a controlled atmosphere, as a function of temperature or time. From the data of this analysis, usually expressed with a thermogram, is possible to achieve important information about composition and also some clues about the structure of a material.

The thermogram of halloysite depends heavily on the field of origin and in the history of the sample. Generally, an HNTs curve shows a slight decrease of the weight when the temperature reached around 50 °C to 450 °C, probably due to the loss of physically sorbbed water. This temperature ranges indicated the starting point of the thermal degradation of HNTs with a weight loss of 3% to 5%. Instead, the complete removal of the interlayer water molecules is achieved upon heating at 400 °C without dehydroxylation,[18] and the transformation into methahalloysite occurs around 470 °C.[38]

The major thermal degradation in the approximate range 450 °C to 570 °C generated a weight loss of about 10% to 15%. This mass loss is assigned to the dehydroxylation of structural AlOH groups of halloysite. However, the tubular shape is preserved up to 900 °C.[15,32,39,40]

TGA is a useful technique to determinate in a quantitative way the amount of loaded of organic substances and hybrid functionalizations.

3.2.10.   *X-ray diffraction analysis*

X-ray powder diffraction (XRD), although it is a technique that not provide a direct information on the chemical composition of a material, allows, however, to define and quantify the crystalline phases there are in a crystalline material, giving also some information on cell dimensions.

The experimental data obtained can be analyzed by the Bragg law (*Equation 2*) to obtain information about the distance between the crystalline planes (*d*).

In the formula, λ represents the x-ray wavelength used, commonly copper's Kα *(λ= 0.154 nm)*. θ is the diffraction angle.

$$n\lambda = 2dsin\theta \hspace{3cm} Equation\ 2$$

The typical X-ray powder diffraction spectra of a halloysite exhibit (001) diffraction peaks at ca. 12° in 2θ, corresponding to a basal spacing of 0.72 nm, which identifies the samples as halloysite (7 Å), consequence of its characteristic wall packing.[15] This peak is broader than the similar peak for stacked kaolinite sheets even though both of them have similar crystal lattices and usually between 7.2 and 7.6 Å. Some authors reported that preheating at 100–350 °C sharpens the basal reflection and reduces the spacing to about 7.2 Å, but never as low as 7.14 Å, which is characteristic of kaolinite.[16]
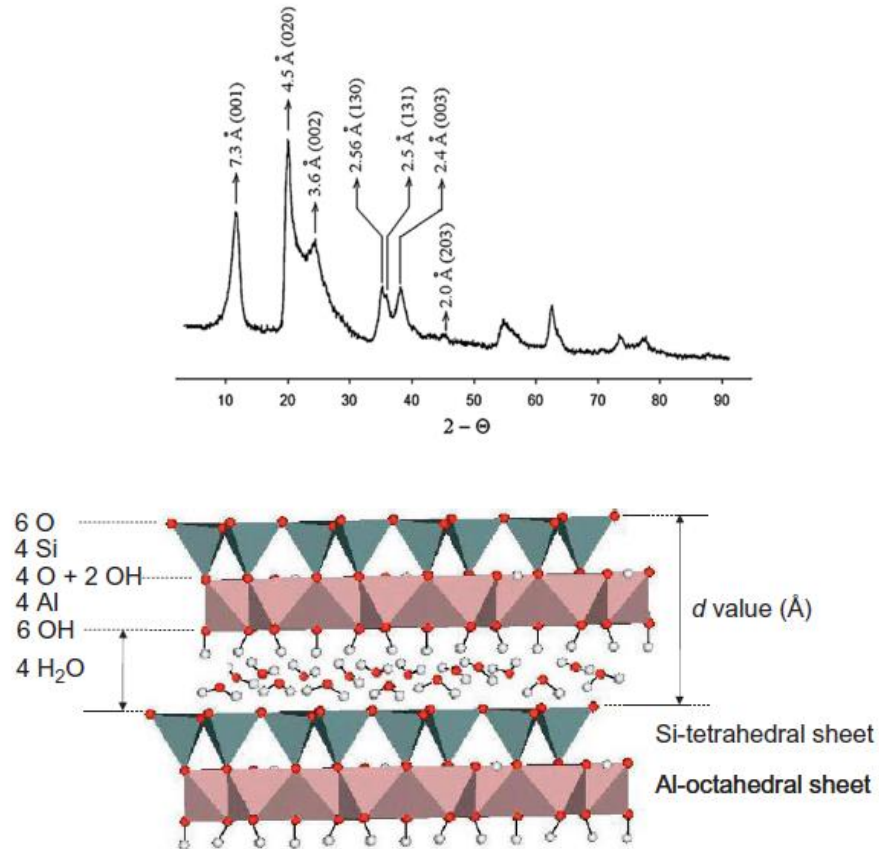
Figure 13. Typical X-ray powder diffraction spectra and representation of halloysite (10 Å) crystalline structure. [4,19]

Halloysite (10 Å), exhibit (001) diffraction peaks at ca. 8.5° in 2θ, corresponding to the (001) diffraction with basal spacing of 1.0 nm.[32]

The high intensity peak at 4.5 Å is indicative of the tubular halloysite structure, instead, the peak at 3.6 Å corresponds to the second order basal reflection.[16,19,27,42]

3.2.11. ζ-potential

Halloysite has a characteristic charge distribution in water, different between the inner and outer surface, within a range of pH from 3 to 8. This is explained and proved by the dielectric properties of aluminum and silicon oxides in the material that are different between them. They undergo to ionization in aqueous media in an opposite way leading halloysite tubes with inner and outer surfaces oppositely charged.[43]

In a practical manner, the charge separation is the result of comparing the negative and positive values for electrical □-potential of silica and alumina surfaces in water, respectively.

Shortly, ζ-potential is the potential difference between the dispersion medium and the stationary layer of fluid attached to the dispersed particle.

The contemporary presence of negative outermost silica surface with the positive alumina inner lumen makes the value of □□potential of HNTs lower than the value of pure silica particles of –50 mV.
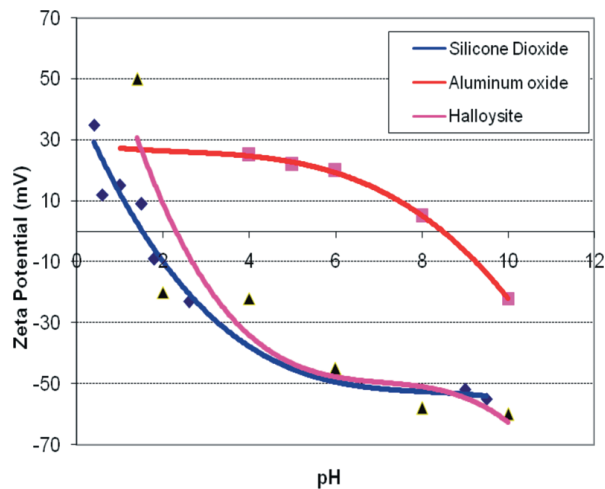
Figure 14. ξ - potential of halloysite, silica and alumina nanoparticles.[37]

The pH of a solution can substantially influence the overall charge of HNTs, in fact, is known that ζ-potentials are ca. −3.5, −33, and −45 mV at pH = 2, 7, and 11, respectively.[18]

In general, the line between the curve of stable and unstable suspensions is approximately taken at either +30 mV or -30mV, and particles with ζ–potential values more positive than +30 mV or more negative than – 30 mV are normally considered stable.

Thanks to this distinctive nanotube surface charge, halloysite presents moderate 2–3 h colloidal stability in water.

In addition, at neutral pH, in aqueous dispersions, the ζ–potential is of ca. −30 mV on the tube surface and +25 mV in the tube innermost. This property allows loading of negative molecules selectively into the lumen and positive ones to adsorb on the external surface.[7,37]

3.3. Extraction and cleaning

3.3.1. Natural Deposits

Halloysite is a worldwide mineral and compared to kaolinite ore deposits, the high purity and economically interesting deposits of halloysite are relatively rare.

Halloysite minerals are the results of pedogenesis or hydrothermal alteration of ultramafic rocks, weathering, volcanic pumice, and glass, in particular in subtropical or wet tropical regions, but it is uncommon in sedimentary deposits. In this regard, the most important deposits around the world are due to hydrothermal alteration.

Usually, halloysite's deposits are situated in the proximity of the kaolinite ones, with the exception of the two biggest deposits, Matauri Bay (New Zealand) and in Utah in the United States, that contain 90–95 wt% of tubes in raw caved. In particular, halloysite is commonly extracted from a vein or pocket in altered rock and often requires specific mining. In fact, there are a few deposits that can only be hand-extracted due to the size of the interesting pockets.[16]

The raw mined halloysite is usually white in color but it is also sometimes slight red.[35] The different colors are simply due to the common presence of impurities like associated minerals and Fe.

Chemical analysis of many halloysites reveals significant amounts, up to 12 wt%, of Fe_2O_3. This finding may partly be ascribed to associated Fe oxides such as hematite or maghemite, and partly to isomorphous substitution of Fe^{3+} for Al^{3+} in the octahedral sheet.

The isomorphous substitution of Fe^{3+} for Si^{4+} in the tetrahedral sheet has never been reported. [4]

3.3.2. Purification

Annually, the ceramic industry uses tens of thousands of tons of halloysite. In many cases, commercially available halloysite tubes are shorter (of 400–500 nm length) because of harsh milling during industrial processing.[15]

Near to the industrial procedure, dependence of the needs, sometimes, is necessary a small scale purification before the use.

The main extraction techniques include, after a first mine work, one or more successive steps of washing and crushing by mechanical or ultrasonic action. Further refinements may

include various types of intervention such as the transfer into acid or bases, or treatment with hydrogen peroxide solutions, centrifugation, dried and final calcination.[17,40,44]

A usual laboratory procedure suggests the preliminary grinding of halloysite mineral with a pestle. Then is prepared a water suspension at 10 wt% and further milled in a laboratory blender or by sonication. After, the larger particles, such as admixed quartz or kaolin, can be easily removed by sedimentation by gravity or centrifugation. The resulting halloysite nanotubes could be also washed several times with distilled water, before drying and sieved to remove aggregates that can be resulting from drying.[45–47]

Obtain a fine dispersion of single particles with halloysite is easier than other clays mineral since that clays nanotubes are not stacked together, as they are instead montmorillonite, kaolin or bentonite.[15]

The homogenization of HNTs with surfactant molecule solutions, by subsequent sediment removal, allows obtaining good quality nanotubes from the remaining supernatant.

In a typical process of this type, a 10 wt% aqueous dispersion of halloysite is mixed with 0.05 wt% of sodium hexametaphosphate under mechanical stirring for 30 min and then left to decant 20 minutes at room temperature. Following this operation the clay clusters and precipitated impurities are removed and the halloysite is obtained from the remaining supernatant after further washing and drying 80 °C in air for 5 h.[18,48]

Rong *et al.* have proposed a method for preparing homogeneous and controllable length of HNTs. This process envisaged the combination of ultrasonic treatment and uniform viscosity centrifugation using *UV–Vis* spectroscopy for faster determination of the concentration of HNTs.[49]

3.3.3. Laboratory development of a low cost and environmentally friendly post-mining procedure for the purification of halloysite

As previously explained, the post-mining procedure is crucial to obtaining a high clean and well performing halloysite stock.

For this reason, during the period at the Louisiana Institute of Technology, under the supervision of Prof. Y. Lvov, I performed many experiments in order to test the cleaning process of a sample by literature procedure and define a new low cost and environmentally

friendly post-mining procedure for the purification of raw halloysite. To reach this goal the experiments were performed by using a test stock (**E3**) of raw halloysite provided by *Applied Materials*.

The sample comes from an American deposit and was already supplied in powder and after the preliminary mining cleaning procedure.

The powder is brown in color. If it is mechanically dispersed in water and left decanted, for at least 12 hours, three sedimentation phases appear (Figure 15a). The first consists of large agglomerates, in the middle a dark brown precipitate and on the top a straw yellow one. After an ultrasound treatment of **E3** dispersion (10 mg/mL), only two precipitates are present, one brown (**E3B**) and one yellow (**E3Y**) (Figure 15b). This mixture, in order to obtain a better phase separation, was further centrifuged in presence of 0.05 wt% of sodium hexametaphosphate. In details, after sonication and mixing, followed by centrifugation for one minute at 50x, a solid precipitate of **E3B** was obtained, on the contrary, **E3Y** was still dispersed in the supernatant. After washing and dry a complete separation of the components was obtained which was further analyzed.

In order to find an efficient, low-cost alternative procedure, the behavior of the system in NaCl solutions was studied. The best results were obtained by adding to the halloysite dispersion a saturated aqueous solution of NaCl (1/8 v/v). After work-up, it was found out that this batch was composed by 47 wt% of **E3B** and 53 wt% of **E3G**.

a)   **b)**
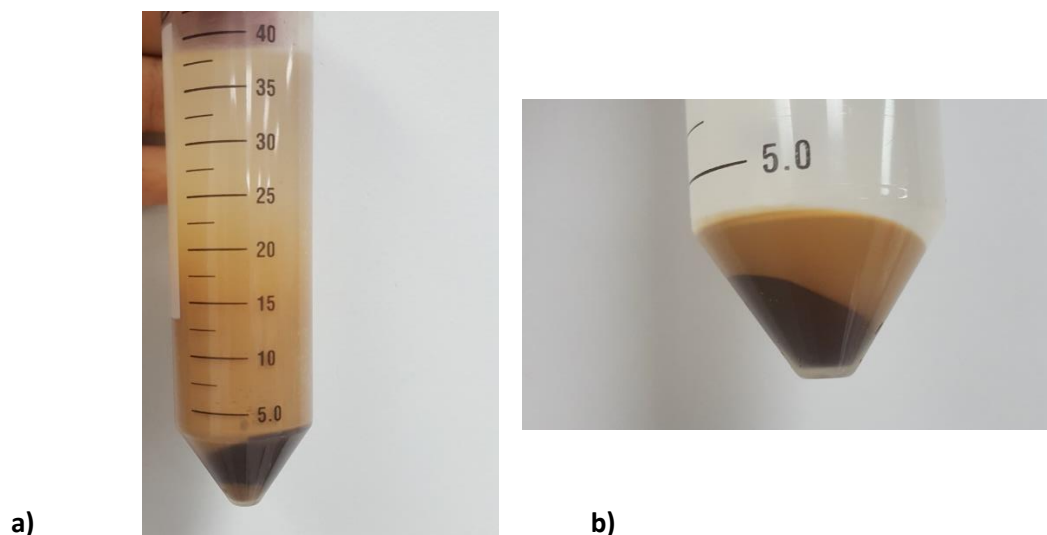
Figure 15. a) 10 mg/mL water mechanically dispersion of **E3** after partial decantation. b) precipitates, one brown (**E3B**) and one yellow (**E3Y**).

A small aliquot of **E3B**, ca. 2 wt%, also shows a discrete ability to be attracted to a magnet. This behavior is not surprising; indeed it is common to find metallic minerals, especially ferrous, mixed with clays.

The obtained powders were characterized by different techniques.

From DLS measurements it was found that **E3B** presents an apparent hydrodynamic radius of 407 ± 25 nm and a ζ-potential value of 34 ± 1 mV while **E3Y** shows an apparent hydrodynamic radius of 299 ± 18 nm and a ζ-potential value of 32 ± 2 mV.

From these values, it is possible to conclude that the **E3B** fraction presents particles with greater size than **E3Y**, that could be due to more aggregated clusters, but ζ-potential values are in both cases close to that reported in the literature for halloysite nanotubes.

The thermograms of the raw material (Figure 16a) shows one weight loss, of about 2.5%, at 300 °C and one more at 100 °C, in addition to the usual loss at around 500 °C.

After the purification steps, the weight loss at 100 °C is completely lost. Probably it was due to previous purification agents added in post-mining procedure and removed in the various washings steps.

Figures 16b and c, show the thermograms of **E3B** and **E3Y**. How is possible to see, the unwanted component from the original sample was significantly reduced, obtaining a more clean material, which can subsequently be further refined.

Figure 16. Thermograms of a) **E3** b) **E3Y** c) **E3B**.

In agreement with the data collected, SEM micrographs, which are displayed in Figure 17, show for **E3B** the presence of some clusters without any tubular morphology. Instead in **E3Y**, it is possible to observe the tubular structures typical of halloysite, even if they are not so long.
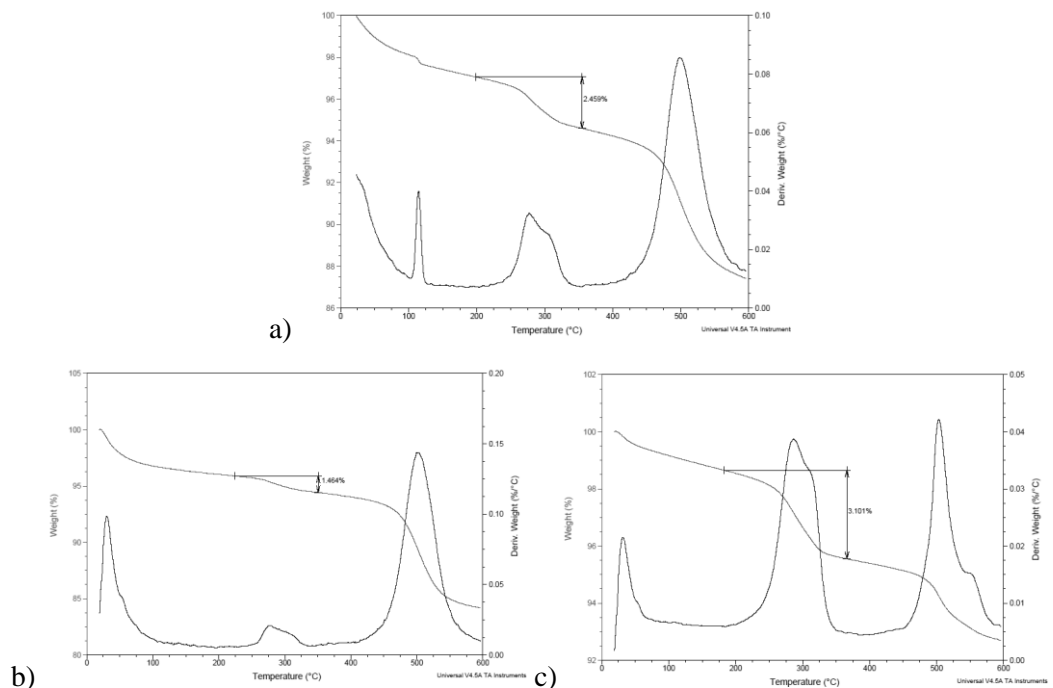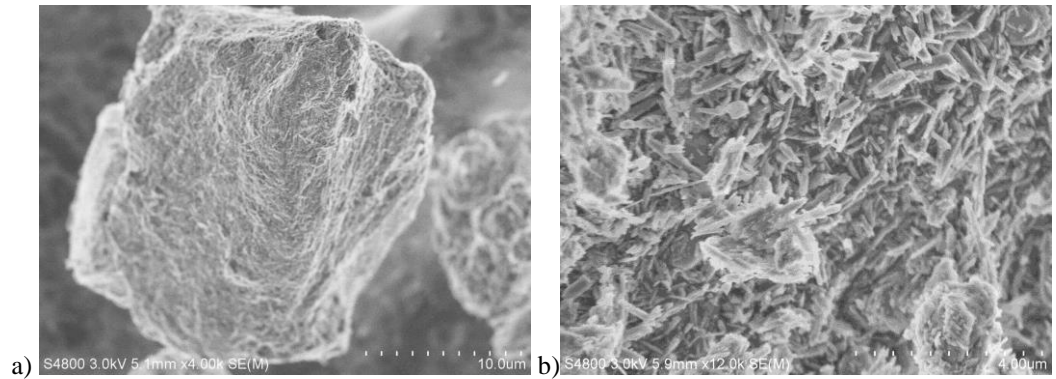

Figure 17.. SEM micrographs of a) **E3B** b) **E3Y**

References

(1) Churchman, G. J. *Clays Clay Miner.* **1975**, *23* (5), 382.

(2) Stefano Sorrentino. *Encyclopedia Italiana "Treccani";* 1935.

(3) MacEwan, D. M. C. *Mineral. Mag.* **1947**, *28* (196), 36.

(4) Joussein, E.; Petit, S.; Churchman, J.; Theng, B.; Righi, D.; Delvaux, B. *Clay Miner.* **2005**, *40* (4), 383.

(5) Deliens, M.; Daltry, V. D. C. *Ann. la Société géologique Belgique* **1993**, *116* (1), 15.

(6) Guggenheim, S.; Adams, J. M.; Bain, D. C.; Bergaya, F.; Brigatti, M. F.; Drits, V. A.; Formoso, M. L. L.; Galan, E.; Kogure, T.; Stanjek, H. *Clays Clay Miner.* **2006**, *54* (6), 761.

(7) Lvov, Y.; Aerov, A.; Fakhrullin, R. *Adv. Colloid Interface Sci.* **2014**, *207* (1), 189.

(8) White, R. D.; Bavykin, D. V.; Walsh, F. C. *Nanotechnology* **2012**, *23*, 65705.

(9) Wang, X.; Chen, Y.; Zhang, W.; He, W.; Wang, J.; Chen, B. *Korean J. Chem. Eng.* **2016**, *33* (12), 3504.

(10) Cravero, F.; Churchman, G. J. *Clay Miner.* **2016**, *51*, 417.

(11) Zhang, Y.; Tang, A.; Yang, H.; Ouyang, J. *Appl. Clay Sci.* **2016**, *119*, 8.

(12) Machado, G. S.; de Freitas Castro, K. A. D.; Wypych, F.; Nakagaki, S. *J. Mol. Catal. A Chem.* **2008**, *283* (1–2), 99.

(13) Maziarz, P.; Matusik, J. *Clay Miner.* **2016**, *51*, 385.

(14) Szpilska, K.; Czaja, K.; Kudla, S. *Polimery* **2015**, *60* (6), 359.

(15) Lvov, Y.; Wang, W.; Zhang, L.; Fakhrullin, R. *Adv. Mater.* **2016**, *28* (6), 1227.

(16) Joussein, E. In *Nanosized Tubular Clay Minerals. Halloysite and Imogolite*; Yuan, P., Thill, A., Bergaya, F., Eds.; Elsevier, 2016; Vol. 7, pp 12–48.

(17) Pasbakhsh, P.; Churchman, G. J.; Keeling, J. L. *Appl. Clay Sci.* **2013**, *74*, 47.

(18) Yuan, P.; Tan, D.; Annabi-Bergaya, F. *Appl. Clay Sci.* **2015**, *112–113*, 75.

(19) Lvov, Y.; Abdullayev, E. *Prog. Polym. Sci.* **2013**, *38*, 1690.

(20) Ferrante, F.; Armata, N.; Lazzara, G. *J. Phys. Chem. C* **2015**, *119* (29), 16700.

(21) Lvov, Y. M.; Guo, B.; Fakhrullin, R. F. *Functional Polymer Composites*, RSC Smart.; The Royal Society of Chemistry, 2016.

(22) John, Anthony, W.; Bideaux, R. A.; Bladh, K. W.; Nichols, M. C. In *Handbook of Mineralogy*; 1995; Vol. 2.

(23) Kamble, R.; Ghag, M.; Gaikawad, S.; Panda, B. K. *J. Adv. Sci. Res.* **2012**, *3* (2), 25.

(24) Bracco, G.; Holst, B. *Surface Science Techniques*; Bracco, G., Holst, B., Eds.; Springer Series in Surface Sciences; Springer Berlin Heidelberg: Berlin, Heidelberg, 2013; Vol. 51.

(25) Lvov, Y. M.; Shchukin, D. G.; Möhwald, H.; Price, R. R. *ACS Nano* **2008**, *2* (5), 814.

(26) Sartor, M. *Dynamic light scattering to determine the radius of small beads in Brownian motion in a solution*; 2003.

(27) Peixoto, A. F.; Fernandes, A. C.; Pereira, C.; Pires, J.; Freire, C. *Microporous Mesoporous Mater.* **2016**, *219*, 145.

(28) Madejová, J. *Vib. Spectrosc.* **2003**, *31* (1), 1.

(29) Słomkiewicz, P. M.; Szczepanik, B.; Garnuszek, M. *Appl. Clay Sci.* **2015**, *114*, 221.

(30) Duce, C.; Della Porta, V.; Bramanti, E.; Campanella, B.; Spepi, A.; Tiné, M. R. *Nanotechnology* **2017**, *28* (5), 55706.

(31) Rozynek, Z.; Zacher, T.; Janek, M.; Čaplovičová, M.; Fossum, J. O. *Appl. Clay Sci.* **2013**, *77–78*, 1.

(32) Yuan, P.; Southon, P. D.; Liu, Z.; Green, M. E. R.; Hook, J. M.; Antill, S. J.; Kepert, C. J. *J. Phys. Chem. C* **2008**, *112* (40), 15742.

(33) K Dedzo, G.; Ngnie, G.; Detellier, C. *ACS Appl. Mater. Interfaces* **2016**, *8* (7), 4862.

(34) Zhang, H.; Ren, T.; Ji, Y.; Han, L.; Wu, Y.; Song, H.; Bai, L.; Ba, X. *ACS Appl. Mater. Interfaces* **2015**, *7* (42), 23805.

(35) Liu, M.; Jia, Z.; Jia, D.; Zhou, C. *Prog. Polym. Sci.* **2014**, *39* (8), 1498.

(36) Wang, Q.; Zhang, J.; Wang, A. *Appl. Surf. Sci.* **2013**, *287*, 54.

(37) Vergaro, V.; Abdullayev, E.; Lvov, Y. M.; Zeitoun, A.; Cingolani, R.; Rinaldi, R.; Leporatti, S. *Biomacromolecules* **2010**, *11* (3), 820.

(38) Melo, J. D. D.; Barbosa, A. P. C.; Costa, M. C. B.; de Melo, G. N. *Adv. Compos. Mater.* **2014**, *23* (5–6), 507.

(39) Jang, S.; Jang, S.; Lee, G.; Ryu, J.; Park, S.; Park, N. *J. Food Sci.* **2017**, *82* (9), 2113.

(40) Abbasov, V. M.; Ibrahimov, H. C.; Mukhtarova, G. S.; Abdullayev, E. *Fuel* **2016**, *184*, 555.

(41) Katsuda, K.; Kohmoto, M.; Kawashima, K.; Tsunemitsu, H.; Tsuboi, T.; Eguchi, M. *Molecular typing of Mannheimia (Pasteurella) haemolytica serotype A1 isolates from cattle in Japan.*; 2003; Vol. 131.

(42) Li, Z.; Fernández Expósito, D.; Jiménez González, A.; Wang, D. Y. *Eur. Polym. J.* **2017**, *93* (June), 458.

(43) VEERABADRAN, N. G.; PRICE, R. R.; LVOV, Y. M. *Nano* **2007**, *2* (2), 115.

(44) Chen, S.; Li, J.; Zhang, Y.; Zhang, D.; Zhu, J. *J. Nat. Gas Chem.* **2012**, *21* (4), 426.

(45) Shchukin, D.; Sukhorukov, G.; Price, R.; Lvov, Y. *Small* **2005**, *1* (5), 510.

(46) Liu, M.; Guo, B.; Du, M.; Cai, X.; Jia, D. *Nanotechnology* **2007**, *18* (45), 455703.

(47) Shchukin, D. G.; Sukhorukov, G. B.; Price, R. R.; Lvov, Y. M. *Small* **2005**, *1* (5), 510.

(48) Liu, M.; Guo, B.; Du, M.; Lei, Y.; Jia, D. *J. Polym. Res.* **2008**, *15* (3), 205.

(49) Rong, R.; Xu, X.; Zhu, S.; Li, B.; Wang, X.; Tang, K. *Chem. Eng. J.* **2016**, *291*, 20.

Chapter 4

Halloysite Nanotubes Modifications

4. *Halloysite nanotubes modifications*

In recent years, the functionalization of clay minerals with organosilane has attracted considerable interests. Functionalization of clays with organosilanes has been explored as a way to modulating clay properties and expands the fields of their application. The modification of oxide surfaces by coupling with functionalized organosilanes is applicable to the fields of catalysis, adsorption, electrochemistry, chromatography and nanocomposite materials.

The molecular formula of HNTs is similar to kaolinite. Interestingly, HNTs are morphologically similar to multiwalled carbon nanotubes (MWCNTs), which are technologically demanding to produce in bulk and consequently are very expensive. However, in contrast to the walls of CNTs, the surfaces, and edges of HNTs contain hydroxyl groups, providing an opportunity for further modification with various organic compounds. Therefore, the much cheaper, natural and fully ecological HNTs with unique combination of tubular nanostructure, rich functionality, and high aspect ratio may replace the more expensive CNTs in high-performance and multifunctional polymer nanocomposites.[1,2]

4.1. *Halloysite inorganic modifications*

Inorganic modification of clays is one of the older techniques to adapt, change and use the ability of these materials. The ceramicists have done this for centuries, and more, nature have been used properties as ions exchange as fundamental property of a fertile soil.

4.1.1. *Ion exchange capacity*

Ion-exchange capacity, measure of the ability of a material to undergo displacement of ions previously attached into its structure by oppositely charged ions present in the surrounding solution.[3]

Depending on deficiency in the positive or negative charge balance of mineral structures, clay minerals can adsorb some cations and anions and retain them around the outside of the structural unit in an exchangeable state, generally without affecting the basic silicate structure. These adsorbed ions are easily exchanged by other ions. The exchange

reaction differs from simple sorption because it has a quantitative relationship between reacting ions.[4]

Halloysite shows high cation exchange capacity (CEC) ranges from 0.1 to 0.7 mol/kg and the hydrated halloysite has a larger CEC than the corresponding dehydrated form. In addition, the CEC of halloysite is higher than that of kaolinite.

The CEC of halloysite is influenced by sample purity, particle size and possibly by particle morphology, it increases with increasing Fe content the pH and the final concentration of the electrolyte solution. With the increase of the salt concentration in solution, both CEC and anion exchange capacity increased, as predicted by classical anion and cation adsorption models for variable charges.

Several halloysite rich clays show a high selectivity for poorly hydrated cations, such as NH_4^+, K^+, and Cs^+.[5–8]

4.1.2. Acid and base response

Due to its characteristic structure, halloysite has negative charges on its external surface, positive on inner lumen surface and negative/positive charges at its edges at pH values. The charges at the edges are therefore attributed to the protonation/deprotonation of silanol and aluminol groups, which are pH-dependent. The hydroxyl groups at the surfaces and edges of HNTs, also, providing an opportunity for further modification with various organic compounds.[1,9,10]

Also, as previously reported, the pore volume, pore diameter, total surface area and mesoporous surface area change depending on the pH.

Acid activation of clay minerals probably is one of the most effective methods that has been used to produce active clay materials. Many applications of halloysite are conditioned by its lumen size, ca. 10 v/v% of the nanotube. Due to the different chemical properties of the tubes inner and outer surfaces, the lumen diameter can be enlarged by acid treatment of aluminum oxides sheets. The enlarged pores allow higher amounts of active loading of chemicals with a target capacity of 40–50%.[6]

The treatment of natural halloysite with 1 mol/dm^3 NaOH for 28 days makes an increase in the average diameter of the inner pores of the nanotubes. The growth of the inner diameter of the nanotubes is caused by slow etching of the tube walls due to progressive dissolution of the aluminosilicate layers as seen in the TEM images.[11]

HNTs were corroded in quite different ways in 1 M solutions of strong acidity or basicity. In the acid-assisted corrosion of HNTs, the inner AlO_6 octahedral surface is first attacked by the acid, resulting in the release of Al^{3+} in the solution after an induction period. Further dissolution continues predominantly on the inner surface of the lumen, leading to the release of Si^{4+}, which rapidly reaches a saturated concentration and gradually precipitates in the form of amorphous SiO_2 in the lumen of the nanotubes observed via TEM.

The decomposition of Hal in 1 M NaOH solution is also initiated on the inner surface of the nanotubes, leading to the release of Si^{4+} in the solution, whose solubility in alkaline environments is greater than that of Al^{3+}. Unlike corrosion in an acid environment, the crystallization of saturated Al^{3+} occurs predominantly outside the nanotubes in the form of flat $Al(OH)_3$ nanosheets.

4.2. Supramolecular interactions with HNT surfaces

In HNTs, the silica layer is located on the outer surface of the tube, while the alumina layer is located in the inner lumen surface. Aluminum and silicon oxides have different dielectric and ionization properties, which are evident from observations of the electrical ζ-potentials of these oxide colloids in water. The ability to have different charges at the inner and outer parts of the halloysite nanotubes allows for the selective loading of negatively charged molecules into their lumen. The different chemistry of the inner and outer surfaces of the halloysite nanotubes can also be exploited for selective modification.[12]

4.2.1. Interlayer Space

Hydrated halloysite tubes can intercalate in their wall multilayers a variety of salts (potassium, ammonium and cesium acetates) and small organic compounds such as urea, formaldehyde, glycerol, dimethylsulfoxide.[9,13]

Loading and intercalation behavior of the halloysite tubes depends on the processing history: halloysite dehydrated at high temperature loses its intercalate capability due to the formation of strong hydrogen bonds between layers. In this case, adsorption of

macromolecules, such as polymers, proteins, drugs mainly takes place through loading into the inner tube lumens.[5–7]

Intercalation of organosilanes into the interlayer of halloysite or kaolinite did not occur. Most of the interlayer inner-surface AlOH groups of both halloysite and kaolinite were unavailable for grafting since they were blocked by the strong hydrogen bonds between layers.[2]

Moreover, the interlayer water could significantly influence the grafting of organosilanes on halloysite by affecting their hydrolysis.[14]

The HNTs intercalation can observe by using XRD. The dehydrated halloysite shows a characteristic first basal peak at ca. 7.2 Å, which tends to disappear when the amount of, for example, urea increases shifting to ca. 10.7 Å.[15]

4.2.2. *Functionalization of inner lumen*

The most attractive feature of halloysite is its inner lumen with a diameter capable of entrapping chemical agents such as macromolecules, including drugs, DNA, proteins, and other chemically active agents, e.g., anticorrosion for protective coating. In this context, the empty lumen of halloysite acts as a miniature container for processes which benefit from suitable molecules sustained release.

If we assume that no loading occurs between rolled layers, then maximum loading in the lumen is equal to r^2/R^2 which is ca. 10 v/v%, where R is the outer radius and r is lumen radius. This capability can easily increase by acid or alkali treatment.

The use of halloysite as nano-container for drug loading and release was firstly introduced by Price, Gaber and Lvov, who used the nanotube as carrier for oxytetracycline HCl (a water-soluble antibiotic); khellin (a lipophilic vasodilator) and nicotinamide adenine dinucleotide (NAD) (an important co-enzyme).[16] Successively, Veerabadran *et al*. reported that halloysite can load and release in controlled manner dexamethasone and furosemide.[17]

It is possible to utilize electrostatic interactions to load, into positively charged HNT lumen, protein with globule diameters of 3–8 nm. In this context, Lvov *et al*. reported the immobilization of laccase, glucose oxidase, lipase, and pepsin.[18]

Besides drug immobilization in HNT inner lumen, some inorganic salts can be loaded and released from halloysite lumen.[19] Therefore, ammonium molybdate ($NH_4 \cdot 6Mo_7O_{24}$), potassium permanganate ($KMnO_4$), sodium silicate (Na_2SiO_3) and sodium chromate (Na_2CrO_4) can be loaded into HNT from their saturated solution in water via

vacuum cycling. Complete release of the inorganic compounds from halloysite nanotubes is achieved within 1–2 h. Abdullayev *et al*. exploited the charge difference in outer and inner surfaces of halloysite for loading benzotriazole (corrosion inhibitor) and the obtained material was mixed to paint coatings in the amount of 2-10 wt%.[20]

The introduction of perfluorinated compounds in the inner lumen is another strategy to obtain advanced materials for several applications.[21] The modified HNT with perfluoroalkylated anionic surfactants formed kinetically stable aqueous dispersions due to the enhanced electrostatic repulsions exercised between the particles. This hybrid can be used as non-foaming oxygen nanocontainers in aqueous media. The gas release from supersaturated dispersions can be controlled by external stimuli and system composition. Halloysite was functionalized with dioctyl sulfosuccinate sodium salt and the obtained nanomaterials were successfully employed as stabilizing oil in water emulsions (Figure 18).[22]
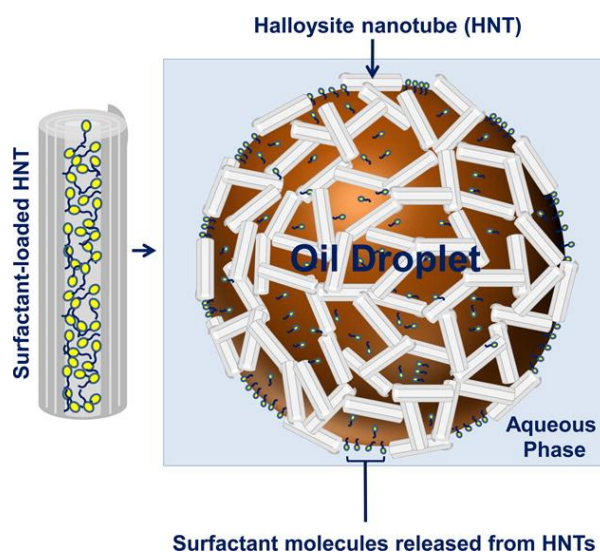
Figure 18. Halloysite nanotube stabilization of an emulsion droplet and the release of surfactant cargo.

To avoid fast release of the active agent from the HNT lumen, for example, Fakhrullin *et al*.[23] fabricated a novel drug delivery system based on HNTs loaded with brilliant green, as drug model, and coated with dextrin to clog the tube opening until the cell absorbs these nanocarriers where sugar can be cleavable by intercellular glycosyl hydrolases (Figure 19). They found that the accumulation and enzymatically induced release of drug occurred exclusively in cells prone to internalization of the nanotubes with a higher proliferation rate, which is a characteristic of tumoral cells. Therefore, the developed nanomaterial does not damage healthy cells and as a result, drug-loaded dextrin-HNTs will be accumulated selectively in tumor cells (Figure 20).
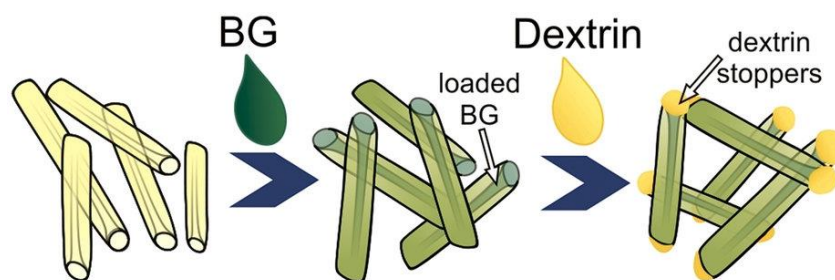
Figure 19. Fabrication of brilliant green-loaded HNTs and the subsequent coating with dextrin stoppers.
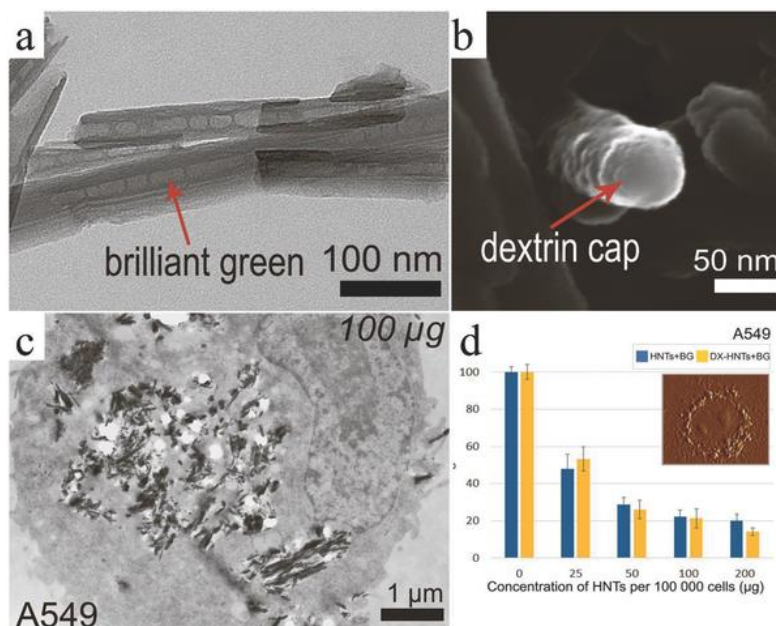
Figure 20. a) TEM image of brilliant-green-loaded halloysite; **b)** SEM image of a dextrin cap on the end of the functionalized nanotube; **c)** TEM images of A549 cell incubated with dextran-coated clay nanotubes; **d)** Resazurin assay results demonstrating the LD$_{50}$ value of BG-loaded halloysite for A549 cells. The insets show AFM images of the distribution of DX-halloysite in the A549 cells.

4.2.3. Functionalization of the external surface

The negative surface potential in a wide pH range endows the external siloxane surface of HNT to be modified by adsorbing specific cations. Lvov *et al*. adsorbed a monolayer of poly(ethyleneimine) (PEI) with a thickness of 54 nm and, then, alternately adsorbed HNT forming a thin film with approximately 14 sets of HNT-PEI monolayers. Due to the loosely packed HNT in the composite (ca. 50% is empty space), the material could be used to load and, subsequently, release guest molecules.[24]

A similar layer by layer (LBL) method was applied by Han *et al.*[25] to coat the halloysite external surface with PEI, with the final goal to apply the materials for load and release of clove bud oil, a natural insect-repellant for food packaging applications.

Emerging nanomaterials for CO_2 capture were recently obtained by impregnation of halloysite with PEI.[26] A polymer loading of 50% allows to obtain a nanocomposite that showed a CO_2 adsorption capacity of 2.75 mmol/g. Furthermore, this material showed quick kinetics and better stability on 10 cycles of CO_2 adsorption/desorption behavior (Figure 21).
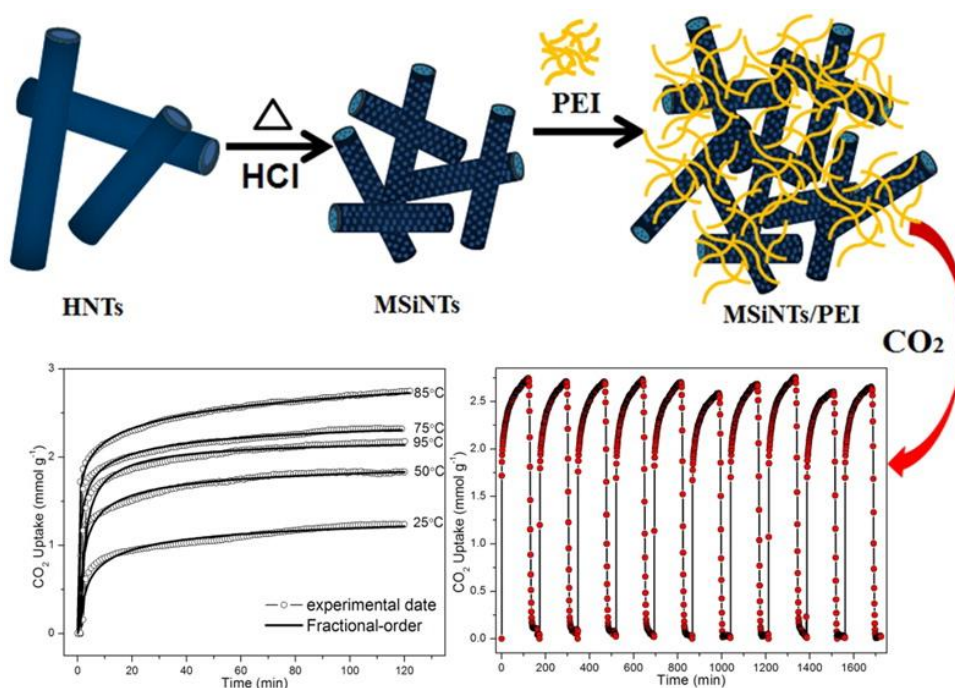
Figure 21. Halloysite nanotube stabilization of an emulsion droplet and the release of surfactant cargo.

The negative charged external surface of halloysite was used to immobilize by electrostatic interactions a positive charged thermo-responsive polymer such as a poly-(N-isopropylacrylamide)-amine terminated (PNIPAM-NH_2).[27] As a consequence of polymer introduction, it was found a strong enhancement of the colloidal stability of the nanohybrid obtained that can be properly used in aqueous phase for external-stimuli triggering solubilization and delivery of hydrophobic compounds.

It was reported that halloysite tends to adsorb organic molecules *via* electron-transferring interaction; within this issue, it was reported the functionalization of HNT outer surface with 2,5-bis(2-benzoxazolyl) thiophene (BBT), a molecule that can act as electrons donor, selected as the interfacial modifier for polypropylene (PP)/HNTs composites. The nanocomposites with BBT showed substantially enhanced tensile and flexural properties, which were attributed to better crystallinity of the nanocomposites.[28]

Veerabadran *et al.* elaborated a layer by layer assembly (LBL) by sequentially absorbing layers of polyelectrolytes of different molecular weight, with a final layer of silica nanoparticles. LBL shell assembly was applied to dexamethasone loaded halloysite to retard the drug release from the nanotubes. The loading of the drug was confirmed by porosity measurements that showed a reduction in the pore volume of the dexamethasone loaded HNT compared to the unloaded tube. The drug loading was estimated, by UV experiments, to be ca. 7 vol. which is approximately the lumen volume.[29]

Modification of the negative halloysite nanotubes external surface was successfully done through the adsorption of alkyltrimethylammonium bromides via electrostatic interactions. The as-prepared reverse inorganic micelles generated oils phase affinity, which was enhanced by the longer alkyl chain, creating rather stable non-aqueous dispersions (Figure 22). The hydrophobized nanotubes were proved to solubilize hydrophilic compounds, such as copper sulfate, into the confined water as expected for efficient water-in-oil emulsions being that copper ions were entrapped into the lumen.[30]
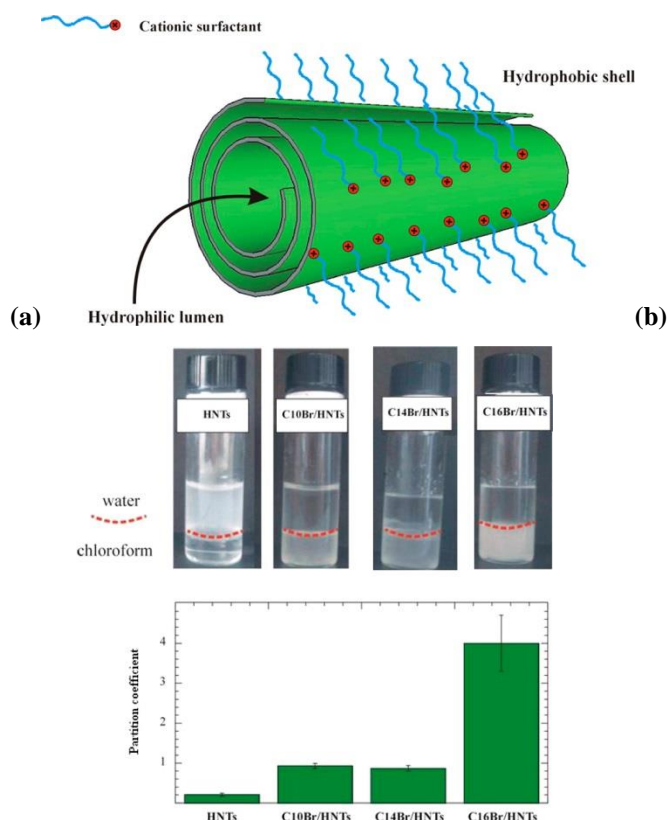

Figure 22. a) Illustration of the alkyltrimethylammonium bromide/HNTs hybrid materials; **b)** Partition coefficients of pristine and modified HNTs between the oil and the aqueous phases.

4.2.4. Functionalization of both surfaces

Noncovalent functionalization of both HNT lumen by selective adsorption of anionic and cationic surfactants as sodium dodecanoate and decyltrimethylammonium bromide was, also, reported (Figure 23). It is demonstrated that the adsorption of anionic surfactant into the HNTs lumen increases the net negative charge of the nanotubes enhancing the electrostatic repulsions and consequently the dispersion stability. On the contrary, the cationic surfactant addition enhances the precipitation of the nanomaterial. The functionalization of HNT lumen with sodium alkanoate, in addition, generates a nanohybrid with a hydrophobic lumen. Due to this structure, this material behaves like a sponge to entrap hydrophobic compounds.[31]
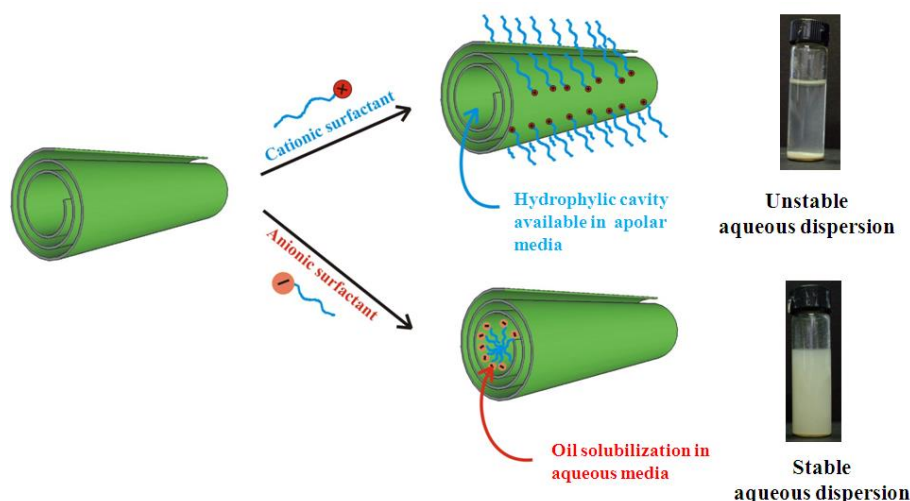
Figure 23. Illustration of the hybrid surfactant/HNTs materials.

4.3. Covalent modification of HNT

Halloysite shows, as a carrier, great potential and economic viability as a substitute for ordered mesoporous silica. However, pristine halloysite shows only weak interactions with guest molecules through hydrogen bonding or van der Waals forces,[32] which restrict the loading of guest molecules. In addition, molecules loaded into HNT lumen or adsorbed onto halloysite external surface, suffer from fast and non-controlled release. Therefore, it seems clear that the need to functionalize halloysite surfaces is crucial to solving the above mentioned drawbacks. Fortunately, the different inside/outside halloysite chemistry allows for different functionalization of both surfaces that, of course, increases HNT application fields.

Modification of halloysite outer surface, indeed, can improve clay dispersal in polymeric matrix or in solvents. In addition, the introduction of functionalized halloysite in a polymeric matrix can improve the stress-strain transfer, generate a nanocomposite with enhanced physicochemical properties. Moreover, selective lumen modification via covalent bonds of functional groups could open up new applications based on molecular recognition, such as molecular storage, molecular separation, catalysis and drug delivery.

4.3.1. Covalent modification of the HNT lumen

Although it is reported that the hydroxyl groups present in the halloysite inner lumen are thoroughly reactive towards a lot of organic compounds,[33] selective modification of interior remains, so far, a difficult task. Up to now, to the best of our knowledge, only few examples are reported in literature about the covalent modification of inner surface. All of them consider the selective hydrophobization of the halloysite inner surface by reaction with suitable organic compounds. Pioneering work of Lvov *et al*. reported the reaction of the hydroxyl aluminol groups of the inner lumen with octadecyl phosphonic acid without its bonding on the siloxane outer tube surface. In this way, they obtained inorganic tubular micelles that show the typical features of pristine halloysite presenting, at the same time, a hydrophobic core that allows for selective adsorption of hydrophobic molecules such as bisphenol-bis(diphenyl phosphate) or ferrocene.[34,35] In addition, the hydrophobic modification allows a slower release of the active agents from the lumen with respect to the unmodified halloysite.

A potential new tool for selective modification of silica-aluminum oxides materials is the covalent immobilization of catechol derivative or the reaction with arylboronic acids. In this context it was demonstrated that 2-bromo-N-[2-(3,4-dihydroxyphenyl)ethyl]-isobutyryl amide (Dopa), a catechol derivative, can be covalently linked in aqueous conditions to the alumina innermost surface but not to the silica outermost surface of halloysite.[36] Arylboronic acid is able to rapidly react with diols in mild conditions and therefore it was used for selective modification of the inner surface of halloysite clay nanotubes.[37] Phenyl boronic acid was found to bind to alumina groups into HNT lumen and did not bind the external siloxane surface (Figure 24). The tubular hybrid material, with the established Al−O−B linkage, can be used as fluorescence probe for the detection of hydrogen peroxide at low levels.
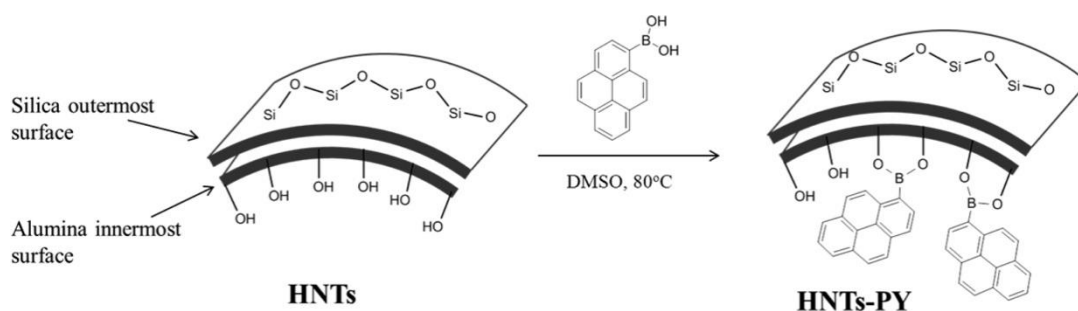
Figure 24. Selective modification of the alumina innermost surface.
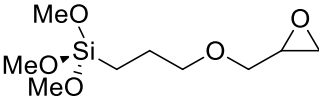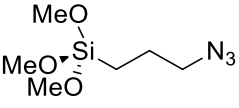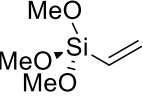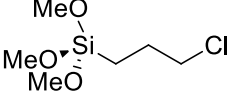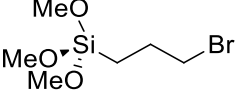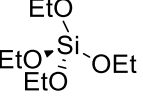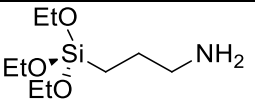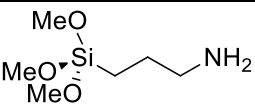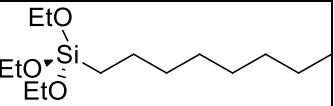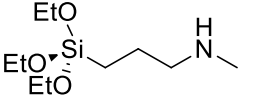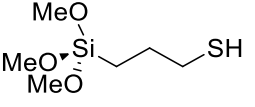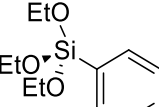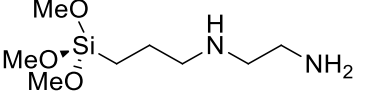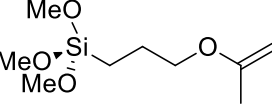
Recently, the selective modification of inner lumen is becoming attractive in metal-based catalysis. Pristine halloysite, indeed, shows some drawbacks, when used as support for metal nanoparticles, since, as a consequence of the low compatibility of the metal nanoparticles with halloysite surfaces lead to a low amount of immobilized nanoparticles. The formation of specific Al-O-C bond on HNT inner lumen ensures, above all, the localization of the metal nanoparticles on the exposed aluminol functionalized surfaces, allowing the control of the environment of the future catalytic reactions. This strategy was employed by Dedzo *et al.* that obtained an efficient catalyst for the reduction of 4-nitrophenol by functionalizing the inner lumen with an ionic liquid, which was used as immobilizing agent for palladium nanoparticles.[38]

4.3.2. Functionalization of the halloysite external surface

With regards, the covalent modification of the outer surface, the most common modification is grafting silanes via condensation between the hydrolyzed silanes and the surface hydroxyl groups of the HNTs located on the edges or on external surface defects.[2]

The grafting reactions can occur in toluene, in water/alcohol mixtures or in solvent-free conditions under microwave irradiation. In the years various silanes have been grafted onto HNTs with the aim to prepare nanomaterials with hierarchical nanostructure (Table 4).

Table 4. The chemical composition of silanes used for modification of HNTs.

γ−glicidoxypropyltrimethoxysilane[2,39]	3-azidopropyltrimethoxysilane	Vinyltrimethoxysilane[40,41]
3-Chloropropyl-trimethoxysilane[42]	3-bromopropyltrimethoxysilane[43]	Tetraethoxysilane[44]
3-aminopropyltriethoxysilane[2,44,45]	3-aminopropyltrimethoxysilane[46–48]	Octyltriethoxysilane[44,49]
[3-methylamino)propyl]trimethoxysilane[50]	3-mercaptopropyltrimethoxysilane[51,52]	Phenyltriethoxysilane[53]
[3-(2-aminoethylamino)propyl]trimethoxysilane[35,53–56]	3-(trimethoxysilyl)propyl methacrylate[57–59]	

Once attached a specific organosilane onto HNT external surface, it is possible to introduce other functionalities by modifying the terminal group formerly anchored. In this way, starting from APTES functionalized HNT, it is possible to obtain, for example, the HNT-COOH nanomaterial by reacting the amino functionality with maleic or succinic anhydride in DMF.[60–62]

In other works, amine-terminated dendritic groups were attached on the surface of HNTs by a divergent synthesis starting from HNT-APTES and methyl methacrylate (MA) as monomer, followed by reaction with ethylenediamine to obtain a third generation dendrimer functionalized halloysite.[63]

The HNT-NH$_2$ scaffolds were also used as precursor for polymer attachment on HNT external surface. Several polymers have been covalently grafted by means of simple condensation reactions, such as polyethyleneimine[64] or poly N-isopropyl acrylamide.[65]

Of course, it is possible to perform a bifunctionalization of halloysite surfaces by modifying both the external surface and the inner lumen. These functionalizations can be achieved by covalent grafting of organic moiety, for example, on the external surface and

at the same time encapsulation of chemicals in the inner lumen or, by covalent modification of both surfaces. The latter aspect was exploited by Lvov *et al.*[35] that after halloysite lumen modification through specific reaction of phosphonic acid with the alumina innermost surface, they made a consecutive treatment of the outermost silica surface through silanization (Figure 25).
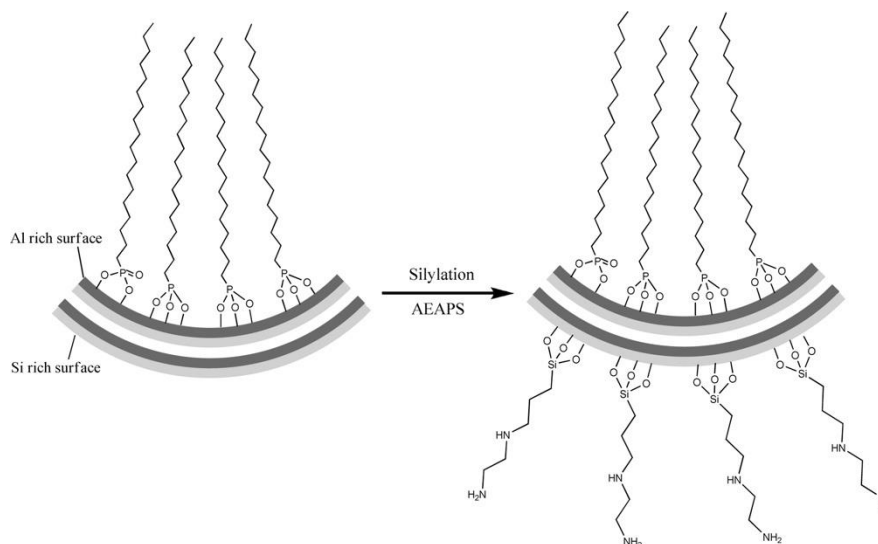
Figure 25. Schematic illustration of bifunctionalization of the silica-alumina oxide surface of halloysite by octadecylphosphonic acid and subsequent silylation with [3-(2-aminoethylamino)propyl]trimethoxysilane.

4.4.   *Modification of halloysite*

The introduction of an organosilane with the appropriate functionality, therefore, allows to increase the operating range of HNT derivatives for the development of more complex compounds. For this purpose, during my PhD, I have performed the covalent grafting of organosilanes, specifically with thiol and azide terminations, to be used as a scaffold or building block for different types of systems and application areas.

4.4.1. *Thiol derivatives synthesis*

Thiol functionalities were introduced on the external halloysite surface by the covalent grafting of 3-mercaptopropyltrimethoxysilane with the –OH groups present on HNT following a procedure reported in Scheme 1. In particular, the condensation reaction between the organosilane and the hydroxyl groups present on the HNT surface was carried

out in solvent-free conditions, under microwave irradiations at the temperature of 100 °C for an irradiation time of 1 h.
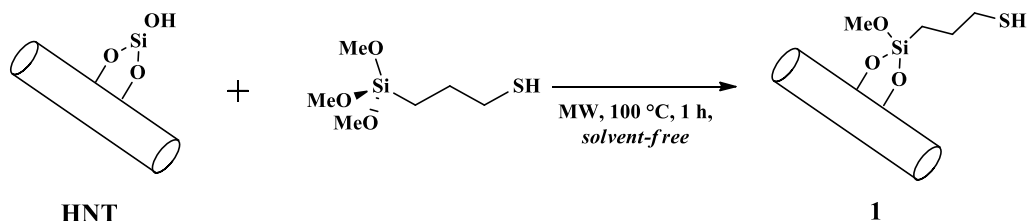
Scheme 1. Schematic synthesis of compound **1**.

Since the density of the hydroxyl group into HNT external surface is very low,[33,66,67] the covalent functionalization of HNT external surface occurs with a low percent loading and randomly. Depending on the different types of **p-HNT** used, were obtained different percentage of loading of organic moiety onto the clay. In details, the percentage of loading was estimated, 1 wt% or 2.1 wt%, respectively, by the quantitative analysis of the residual mass at 800 °C, obtained by thermogravimetric analysis. The successful loading was confirmed by TGA and FT-IR spectroscopy. In Figure 26 are reported the thermoanalytical curves of pristine halloysite and compound **1**. As it is possible to observe, besides the typical weight loss of halloysite, an additional weight loss is present, around 250 °C, relative to the degradation and volatilization of organic moiety.
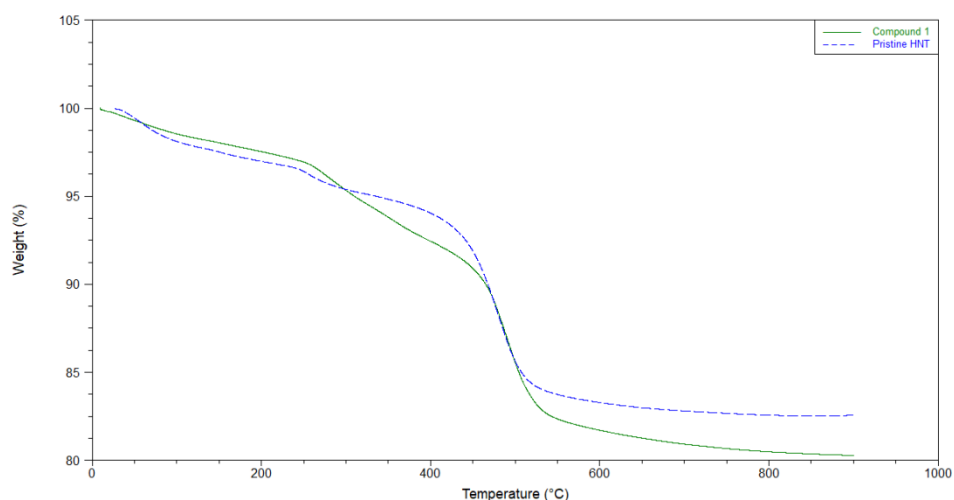
Figure 26. Thermograms of **p-HNT** and **1**.

FT-IR investigation on compound **1** shows that the vibrational bands of HNTs remain unaltered after the reactions. Compared to pristine HNT (Figure 27), **1** exhibits the vibration bands for C-H stretching of methylene groups around 2930 and 2850 cm^{-1}.
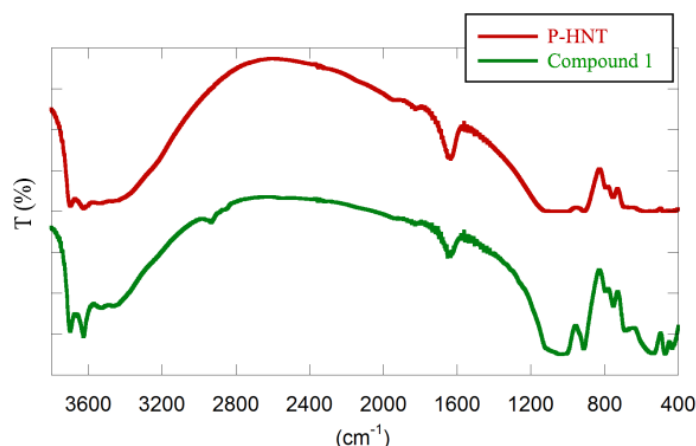
Figure 27. FT-IR spectra of **p-HNT** and compound **1**.

The compound **1** so obtained was used as scaffold for the covalent linkage of several organic compounds on halloysite external surface, which are useful for application in several fields. In particular, the thiol termination was exploited for the covalent linkage of cyclodextrin units as follow:

HNT-SH material was covalently linked to heptakis-6-(tert-butyldimethylsilyl)-2-allyloxy-β-cyclodextrin **2** synthesized by a thiol-ene reaction according to the procedure reported in the literature (Scheme 2). After work-up, the nanomaterial **3** was obtained, with a percent loading of cyclodextrin on halloysite of 4.1 wt% with respect to compound **1**.
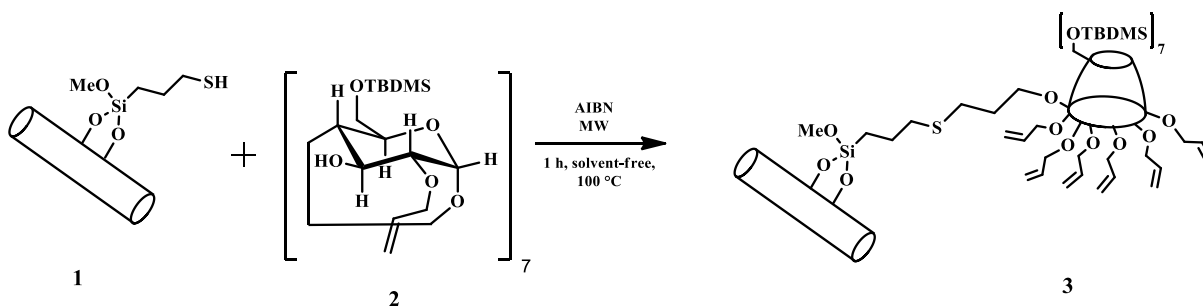
Scheme 2. Schematic representation of the synthesis of compound **3**.

Compound **3** was used, once again, as a scaffold for the covalent linkage of alkyl thiols **4(a–d)** by means of thiol–ene reactions between vinyl groups on β-CDs and –SH groups on thiols (Scheme 3). The reaction of **3** with alkyl thiols **4(a-d)** was carried out by UV irradiation, using toluene as solvent, at room temperature under an argon atmosphere. After 24 h, the compound **5(a–d)** was obtained and analyzed by TGA in order to evaluate the percentage of the loading, that was in the range among 0.6–2.9 wt% according to the thiol used (from **4a** to **4d**). It is interesting to note that, upon increasing the alkyl chain

length of thiol (from **4a** to **4d**), materials with lower percentage loading (2.9 and 0.9 wt%, respectively) were obtained, as a consequence of enhanced steric hindrance on the HNT surface. The grafting degrees provided an idea in terms of average positions substituted in the CD, namely it comes out that in **5a** and **5b** the allyl groups have been fully substituted while **5c** and **5d** have an average of two substituted allyl groups.
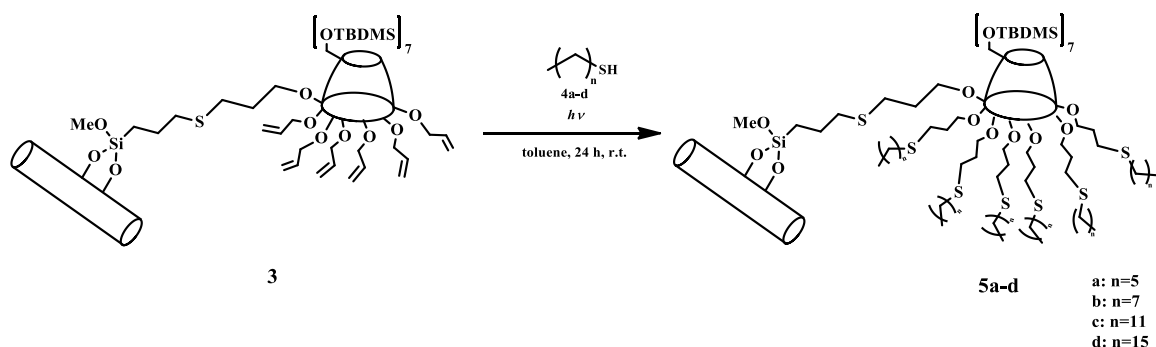
Scheme 3. Schematic representation of the linkage of alkyl thiols on compound **3**.

The new materials were characterized by FT-IR spectroscopy, TGA and SEM measurements.

FT-IR investigation of **5a–d** show that the vibrational bands of HNTs remain unaltered after the reactions. Compared to **3** compounds **5a–d** exhibit an increase in the intensity of vibration bands for C–H stretching of methylene groups at around 2960 cm^{-1} and 2865 cm^{-1} (Figure 28).
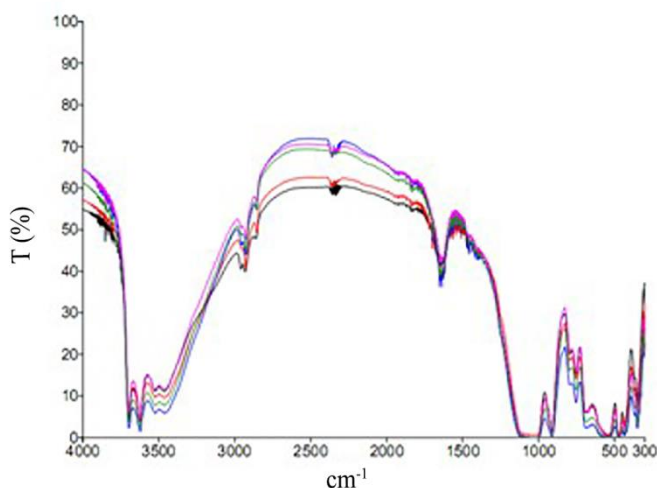
Figure 28. FT-IR spectra of compound **5a-d**.

Direct observation of the surface morphology of **5a–d** was accomplished by SEM. In all cases, the tubular shape of the nanoclay is not lost after grafting. Moreover, the lumen of the functionalized nanotubes appears empty, in agreement with the expected grafting at the external surface (Figure 29).
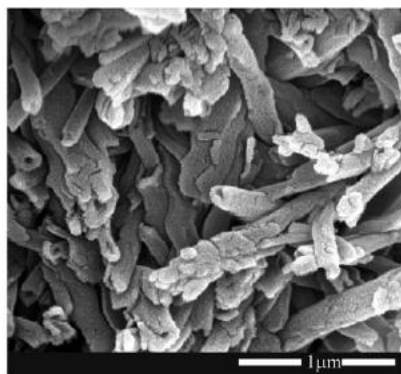
Figure 29. SEM images of **5a**.

The turbidimetric analysis was performed to highlight the influence of functionalization on the dispersion stability of HNTs in aqueous media, which might be crucial future applications. Dispersions of **5a–c** showed a lower stability in water than **3**, according to the more hydrophobic surface functionalization in **5a–b** as compared to **3** (Figure 30). In contrast, dispersions of **5d** showed higher aqueous stability (Figure 30) than **5a–b**, and, surprisingly, even than **3**. It is known[68] that the presence of the polymer and/or the surfactant at the nanoparticle surface may, generally, cause two different effects: (i) hydrophobic interactions that involve aggregation of material; (ii) steric repulsion or osmotic effects that involve an increase in repulsive interactions between nanoparticles and this generates stabilization of the dispersions. The stability of the dispersions of compounds **5a–c** is controlled by hydrophobic interactions, while for **5d** a steric stabilization.
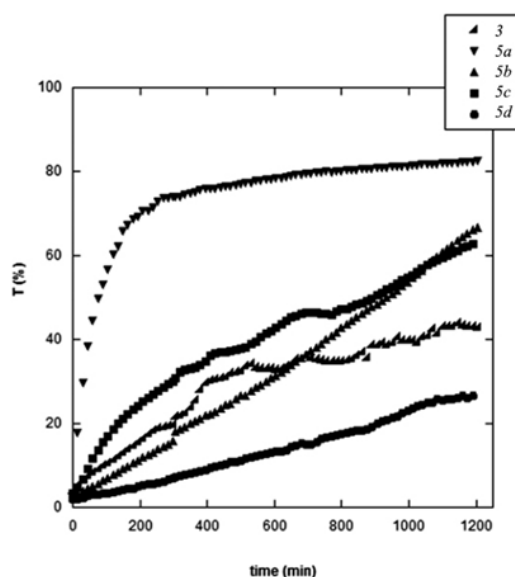
Figure 30. Optical transmittance as a function of time for **3** and **5a–d** dispersions in water. The concentration is 0.1 wt% in all cases.

The diffusion coefficient of the nanoparticles in the solvent confirmed the results obtained by turbidimetric analysis. The diffusion coefficients of **5a–d** obtained by DLS experiments are collected in Table 5. By comparing these results with the diffusion coefficient of **3** (11×10^{-13} m^2 s^{-1}) and HNTs in water (9.4×10^{-13} m^2 s^{-1}) it appears that **5a–b** form aggregates while **5c–d** show no aggregation.

With the aim of evidencing possible changes in the nanoparticle–nanoparticle electrostatic interactions, the ζ-potential in water was measured. All samples **5a–d** showed negative ζ-potential values (ca. -20 mV) close to that of **p-HNT** (-19.5 mV). Therefore, the electrostatic nanoparticle–nanoparticle repulsions are not altered by the surface functionalization, confirming that the aggregation of **5a–b** compounds are driven by van der Waals interaction and hydrophobic effects.

Table 5. Diffusion coefficients for compounds **5a-d**.

Entry	Sample	D(10^{-13} m^{2}s^{-1})
1	5a	5.57
2	5b	5.93
3	5c	9.53
4	5d	9.01

As far as the use of the HNT-CD hybrid, it is interesting to note that by combining β-CD with functionalized halloysite with different percent loading of –SH groups, it is possible to obtain different nanomaterials. In particular, starting to the scaffolds HNT-SH with a low percent loading (1 wt%) an HNT–CDs nanosponges can be obtained (compound **6**). The nanosponges were synthesized by AIBN-catalyzed polymerization of heptakis-6-(tert-butyldimethylsilyl)-2-allyloxy-β-cyclodextrin to HNT–SH **1** by means of a thiol-ene reaction (Scheme 4).

For this synthesis, the reactants were mixed in different proportions (Table 6) and the different percentage of **2** in the obtained composite materials was determined by TGA from the residual mass upon degradation (Table 6).[69] Based on the stoichiometric ratios, it should be considered that an excess of unreacted allyloxy groups could be present and they could be able to undergo further functionalizations. The polymerization was carried out in a microwave oven, for an irradiation time of 1 h at 100 °C, in solvent free conditions. Then, the obtained nanomaterials were isolated by subsequent washings with CH$_2$Cl$_2$ and CH$_3$OH, in order to remove the catalyst and some residual unreacted reagents.

Table 6. Reactant ratios and mass yields for nanosponges hybrids.

Reactants	HNT-CDs (6)	
HNT (mg)	200	200
CD (mg)	300	150
HNT:CD ratio	1:1.5	1.5:1
% Loading (CD on HNT)[a]	40	20

[a] estimated by TGA.
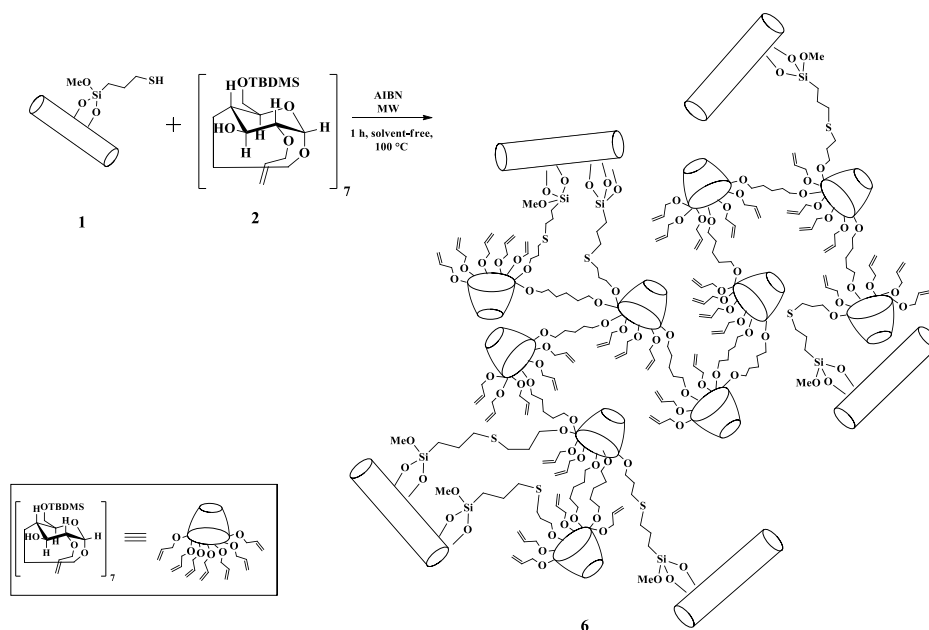
Scheme 4. Schematic representation of the synthesis of nanosponges hybrid (compound **6**).

Compared to pristine HNT,[69] compound **6** exhibits the vibration bands for C–H stretching of methylene groups around 2980 cm^{-1} and a broad and wide band around 3000 cm^{-1} due to the –OH groups of cyclodextrin (Figure 31). These findings provide evidence for the presence of organic moieties in the new material. Moreover, it is interesting to notice that little signals at ca. 1700 cm^{-1} and 1418 cm^{-1} are still present in the spectrum, indicating that not all the reactive functional groups in the starting reactants actually happened to react. This may be a consequence of the hyper-reticulated nature of the hybrid polymers obtained. Steric hindrances and strains, indeed, might prevent some of the reacting groups to achieve the minimum arrangement requirements needed for the polymerization process to occur.
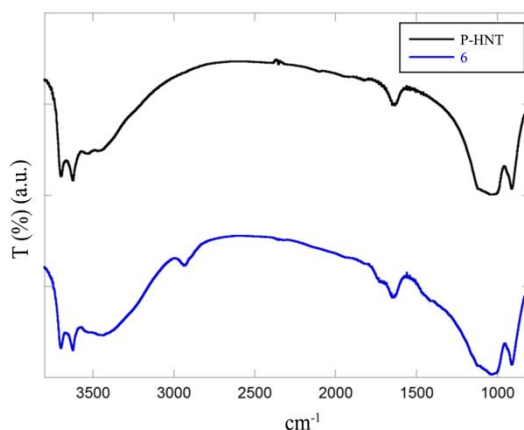
Figure 31. FTIR spectra of HNT and compound **6**.

Thermogravimetric analysis evidenced a peculiar pyrolysis process of CDs nanosponges in the presence of HNT. Namely, the organic material degraded almost completely in a single step at ca. 327 °C that is coincident with the degradation temperature of β-CD,[67] the presence of HNT generates a two-steps degradation pattern with maximum degradation rates at 265 and 360 °C, respectively. It should also be noted that the degradation at lower temperature is enhanced in the presence of larger HNT amounts (Figure 32). These findings can be explained by involving a change in the degradation mechanism of CDs nanosponges being it split into two consecutive or parallel reactions.[70] To clarify the effect of HNTs on the CDs degradation mechanism, heating rate was changed for the **6** (40 %) sample and the obtained results indicate that HNTs generate a two steps degradation mechanism rather than a catalytic degradation alternative pattern (Figure 33).
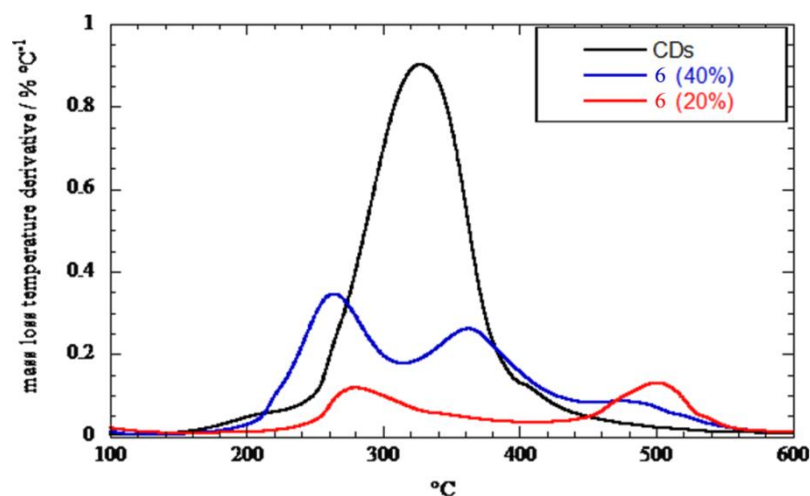
Figure 32. Differential thermal analysis curves for HNT-CD hybrid and CD polymers.
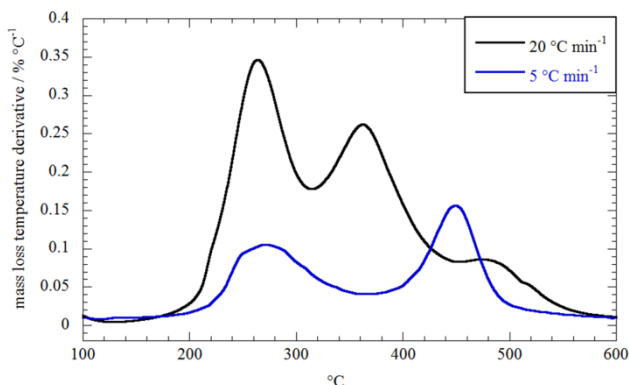
Figure 33. Differential thermal analysis curves for HNT-CD hybrid 40% at two heating rates.

The so-prepared hybrid was imagined by SEM and TEM in order to obtain some insight into the morphology.

SEM images of compound **6** are given in Figure 34a. As previously described, pristine HNTs show long-fibrous morphology with a length of 0.5–1 μm and outer diameter of about 100 nm. After functionalization, it seems clear that the tubular shape of halloysite is preserved and **6** presented a different morphology as compared with **p-HNT**. **6** still shows a long-range rod-shape with the diameter increasing to about 170 nm. Moreover, the hybrid shows a rather compact structure where the HNT seems glued together with a smooth surface that indicated the presence of an organic layer.
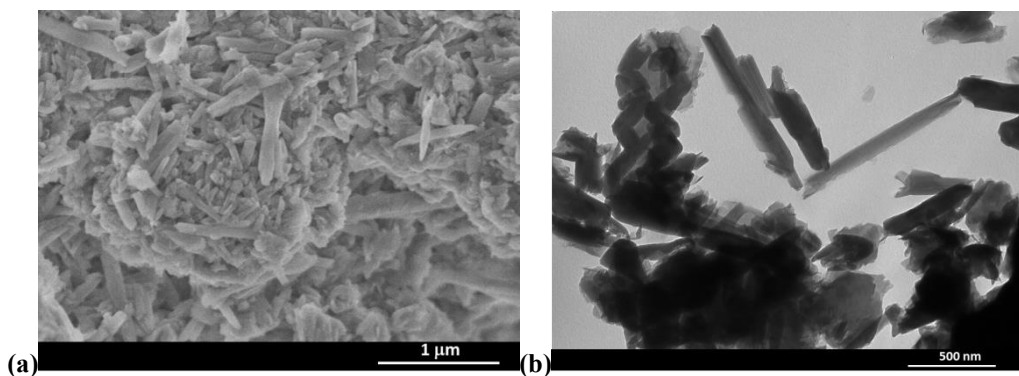
Figure 34. (a) SEM and (b) TEM images of **6**

According to the TEM images (Figure 34b), **6** shows the typical nanorod-shaped structure of HNTs. The hybrid exhibits the characteristic hollow tubular structure of halloysite as shell with a cyclodextrin core. The increased thickness of the hybrid with respect to pristine nanotubes takes into account the formation of the hyper-reticulated network after the reaction.

To confirm the formation of the hyper-reticulated structure, the diffusion dynamics in water of **6** was characterized by dynamic light scattering (DLS). Measurements of the particle size using DLS reveal a translational average diffusion coefficient of **6** of 3.24×10^{-14} m^2 s^{-1} that is smaller than the value for **p-HNT** in water (9.4×10^{-13} m^2 s^{-1}); this result is consistent with the formation of a polymer-like network where HNT are incorporated after the reaction with cyclodextrin units. Although the diffusion behavior is strongly altered, the surface charge in the hybrid is not significantly altered as expected for non-ionic functionalization (ζ-potential=-25 ± 1 mV).

The morphological properties of **6** in terms of specific surface area (BET), mean pore size distribution (BJH) and cumulative pore volume, were determined by N$_2$ adsorption/desorption measurements and are listed in Table 7. In Figure 35 is shown the absorption/desorption isotherm of **6**. The isotherm can be classified as a type II isotherm with an H3 type hysteresis loop according to the IUPAC classification.[71] Hysteresis is related to the filling and emptying of the pores by capillary condensation. At low p/p$_0$ values, the **6** shows higher microporous adsorption.

6 shows a surface area of 19.9 m$^{2\cdot}$g^{-1} slightly smaller than that of starting pristine halloysite (22.1 m$^{2\cdot}$g^{-1}). The slight decrease in the specific surface area, observed for the new polymeric hybrid, takes into account the small degree of organosilane loading on HNT surface. The pore size of **6** is greater than that of **p-HNT** as a result of the formation of a reticulated structure that could form additional channels in the hybrid polymer mesh. The porous structure makes the hybrid polymer a promising material that could act as nanosponge for dye adsorption.
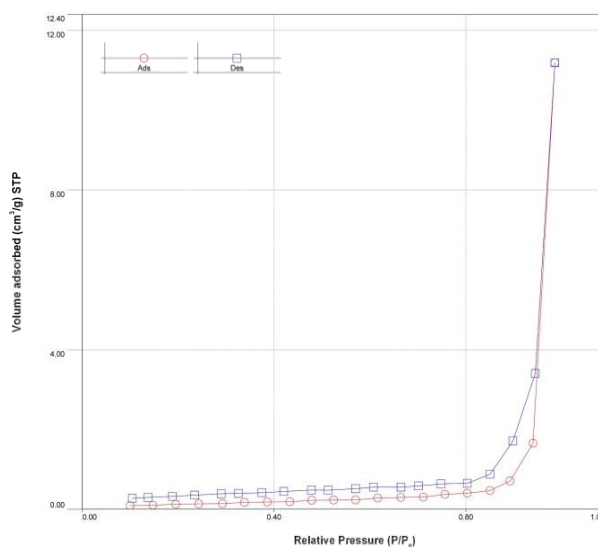
Figure 35. N$_2$ adsorption-desorption isotherm of **6**.

Table 7. Textural parameters determined by N_2 adsorption/desorption measurements for **p-HNT** and **6**.

	Surface area, S_{BET} ($m^2\ g^{-1}$)	Total pore volume ($cm^3\ g^{-1}$)	Average pore size (nm)
p-HNT	22.1	0.06	9.3
6	19.9	0.29	85.2

Since swelling provides more specific surface area for adsorption, hence wettability and swelling are presumed to facilitate the adsorption of target molecules or ions. Therefore, it is essential to measure swelling of a polymer in aqueous medium before its application as adsorbent. The swelling ratio of the **6** (40%) nanosponge hybrid is 91.2 ± 1.6 %. The reduction of swelling ratio in comparison with some previously reported cyclodextrin polymers[72] could be due to the presence of HNT that increased crosslinking density through formation of covalent bonding within the cyclodextrin; as a consequence, HNTs could make the hybrid polymer network denser, blocking the passage of water from entering in the polymer.

4.4.2. Azido derivatives

Similarly to the synthesis of thiol derivatives, azido groups were successfully introduced on the external surface of halloysite by the covalent grafting of 3-azidopropyltrimethoxysilane.

The HNTs bearing random -N_3 groups (compound **8**), were prepared according to the synthetic route shown in Scheme 5. The reaction was carried out at reflux, using toluene as solvent for a reaction time of 48 h. After workup, the N_3 group loading, estimated by TGA, was as large as 2 wt%.
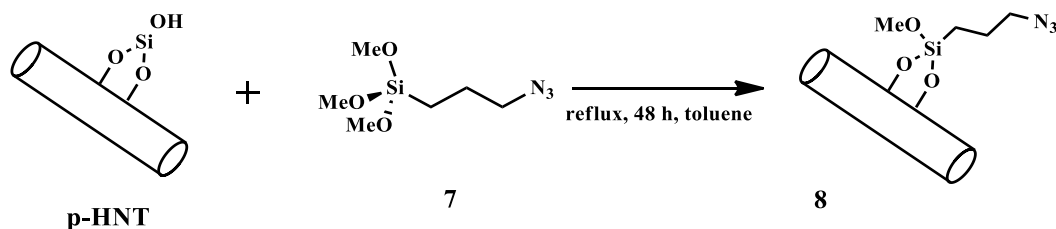
Scheme 5. Schematic representation of the synthesis of compound **8**.

In order to find a green protocol for the synthesis, several tests were performed using microwave irradiations. The obtained results are reported in Table 8.

Table 8. Experimental conditions for the synthesis of compound **8**.

Entry	Solvent	Time (h)	T (°C)	Percent loading (wt%)[a]
1	/	1	50	0.7
2	/	1	100	0.8
3	/	3	100	0.7
4	Toluene	24	100	0.5

[a] Estimated by TGA

As it is possible to note, in all cases a low percent loading of the organic moiety on halloysite surface was obtained and therefore, in this case, the best experimental conditions are the traditional method. The azido functionalized HNTs can be used as scaffold for the synthesis of HNT-bearing random triazolium salts by means of click reactions.

The concept of "Click Chemistry", was, first, introduced by K. B. Sharpless in 2001; this term describe reactions that are high yielding, wide in scope, create only byproducts that can be removed without chromatography, are stereospecific, simple to perform, and can be conducted in easily removable or benign solvents. For these reasons in the year, the click reaction has attracted enormous attention from the scientific community.

Thus, triazole rings can be easily prepared by 1,3 dipolar cycloaddition between an azido compound (compound **8**) and alkyne derivatives in the presence of Cu(I) salts as catalyst.

The HNT - triazole compounds were prepared in two synthetic steps following the procedure reported in Scheme 6. In the first step, compound **8** was reacted with propargyl alcohol **9** by cyclo-addition reaction under Huisgen conditions to afford **10**, which was purified by extensively washing with water and methanol. In the second step, the N-alkylation with iodoalcane gave the final products **11(a-b)**.
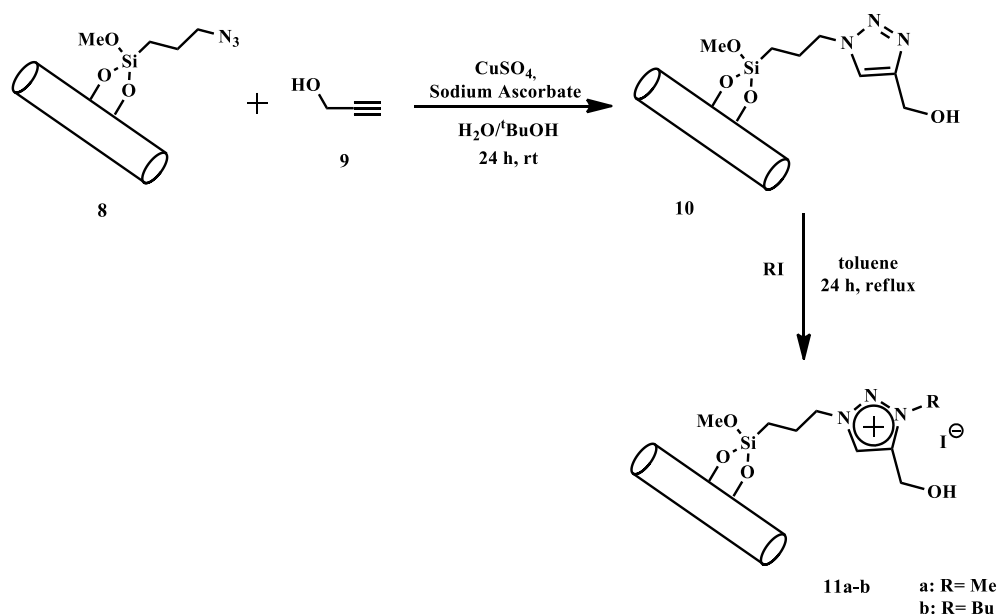
Scheme 6. Schematic representation of the synthesis of the triazolium salt modified HNT **11a-b**.

FT-IR investigation of **8**, **10** and **11** show that the vibrational bands of HNT remain unaltered after the reactions (Figure 36). Compared to **p-HNT**, **8** exhibits the vibration bands for C-H stretching of methylene groups around 2930 cm^{-1}, stretching of terminal methyl groups at 2850 cm^{-1}, the deformation of CH_2 at 1470 cm^{-1} and stretching of azido groups at 2103 cm^{-1}. In the **11a-b** compounds, the stretching of H-C=, C=N, N=N aromatic groups and C-N of triazolic groups around 3000, 1600, 1400 and 1320 cm^{-1}, respectively, are also observed. These findings evidence the presence of the silane moieties in **8** and triazolic groups in **11** and, based on the unaltered frequency of stretching bands of the OH of the inner-surface Al-OH groups, and led to conclude that grafting has taken place only on the external surface of HNT.
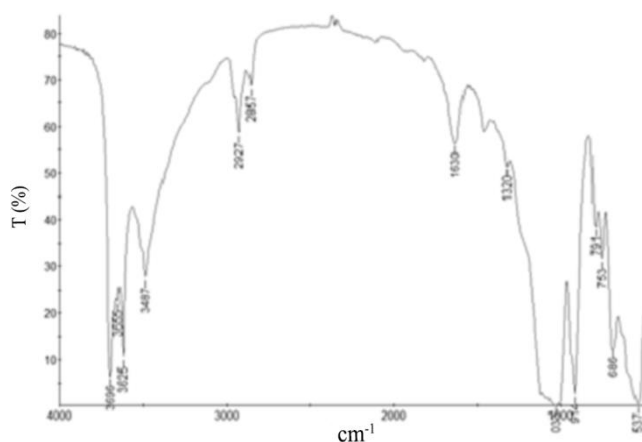
Figure 36. FT-IR spectrum of compound **11a**.

The samples **11a-b** were investigated by means of TGA to determine the grafted amount of organic moieties (Figure 37). A mass loss in three steps was observed for 11a-**b**. Based on the thermogram for **p-HNT**, one can state that besides the nanotubes dehydration at ca. 500 and 700 °C, the **11a-b** present a mass loss in the range from 200 to 400 °C due to the degradation and volatilization of the organic fractions. The grafting degree was determined by comparing the residual mass at 900 °C of each f-HNT and **p-HNT**, the obtained results are 6.1 wt% and 8.6 wt% for **11a** and **11b**, respectively.
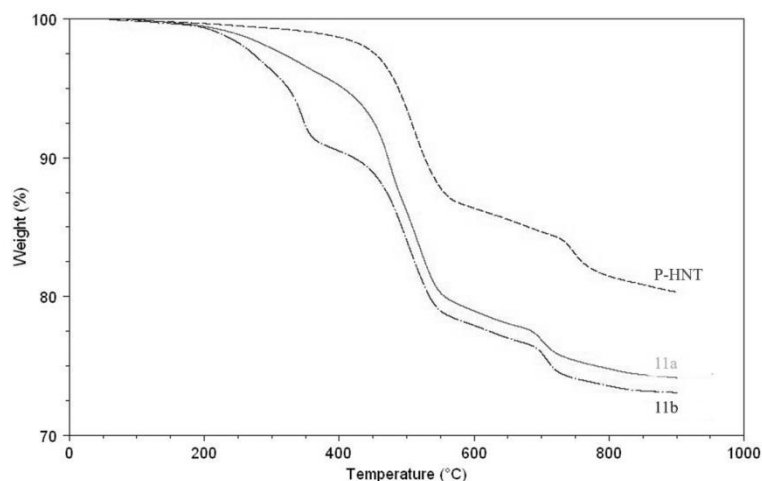
Figure 37. Thermograms of **p-HNT** and f-HNT **11a-b**.

Direct observation of the surface morphology of **11a** and **11b** was carried out by SEM measurements. As Figure 38 shows, in both cases, the tubular shape of the nanoclay is not lost upon the grafting. Moreover, the lumen of the nanotubes appears empty after functionalization in agreement with the expected grafting in the external surface. The average characteristic sizes of the functionalized nanotubes are coincident with those observed for the **p-HNT**.[73]
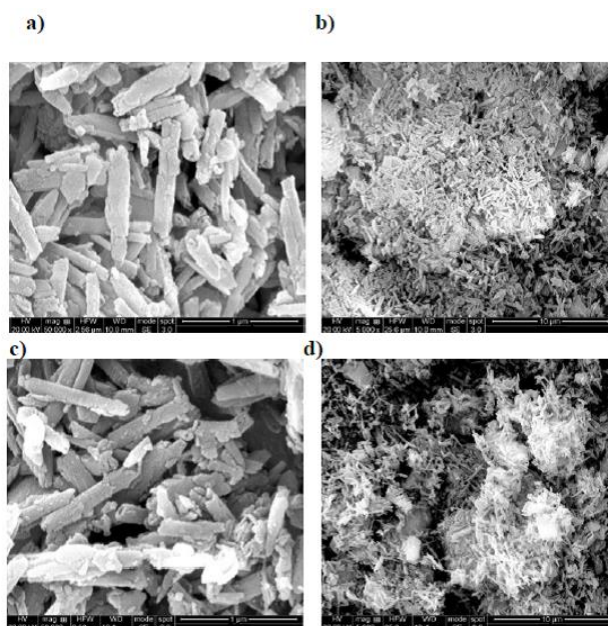
Figure 38. SEM images of **a-b) 11a**, **c-d) 11b**.

Turbidimetric analyses were performed to highlight the influence of functionalization on the dispersion stability of f-HNT in aqueous media. f-HNT **11a** dispersion showed a higher stability in water than **11b** one, this result is in agreement with the more hydrophobic surface functionalization in **11b** compared to **11a** (Figure 39).
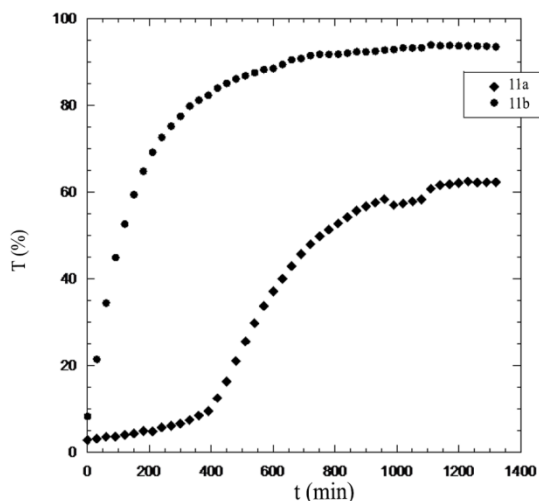
Figure 39. Transmittance values as a function of time for aqueous dispersion of **11a** and **11b**.

For better highlight the occurrence of hydrophobic interactions that affect the aqueous stability of the obtained nanomaterial, further investigations were carried out by means of dynamic light measurements (DLS) both in water and in an organic solvent such as methanol, that could be useful for future applications.

The obtained results showed that in methanol the samples show a diffusion coefficient (D) values of $(1.18 \pm 0.02) \times 10^{-12}$ and $(1.6 \pm 0.5) \times 10^{-12}$ m^2 s^{-1} for **11a** and **11b** respectively, while in water the D values are $(1.73 \pm 0.09) \times 10^{-13}$ and $(1.5 \pm 0.1) \times 10^{-13}$ m^2 s^{-1} for **11a** and **11b** respectively.

By comparing these results with the diffusion coefficient of **p-HNT** in water $(9.4 \times 10^{-13}$ m^2 s$^{-1})$[73] it appears that in methanol both **11a** and **11b** are dispersed as single nanotubes. This is not the case in water where the more hydrophobic substituent plays a role favoring the aggregation of nanotubes evidenced by the slower diffusion for **11b**. These results can be explained considering that water might be a worse solvent in the case of the more hydrophobic external modification. The reduced diffusion dynamic is obtained for **p-HNT** by hydrophobic modification of the outer surface by means of a cationic surfactant[31] and the nanotubes aggregation due to hydrophobic lateral interaction was claimed in that case. With the aim at evidencing the nanoparticle-nanoparticle interaction changes, the ζ-potential was, also, measured in water. Both samples **11a-b** showed close negative ζ-potential values (-20±2 and -24.1±0.9 mV for **11a** and **11b** respectively), similarly to that of **p-HNT** (-19±1 mV) and therefore differences in the electrostatic nanoparticle-nanoparticle repulsions are likely negligible confirming that the aggregation of **11b** is driven by π-π and van der Waals interactions.

Based on our results, it was planned to investigate the colloidal stability of **11b** in methanol/water mixed media. To this aim, the diffusion coefficient was measured in a wide range of solvent composition (Figure 40). It is straightforward to note that **11b** is rather stable in the methanol-rich regime as it is proved by a value of the diffusion coefficient close to those expected for single dispersed nanotubes. On the other hand, as the methanol concentration is lower than 8.4% (that corresponds to 9:1 methanol/water volume ratio), the diffusion is suddenly slowed down likely due to the **11b** aggregation induced by π-π and van der Waals interactions between the external moieties.
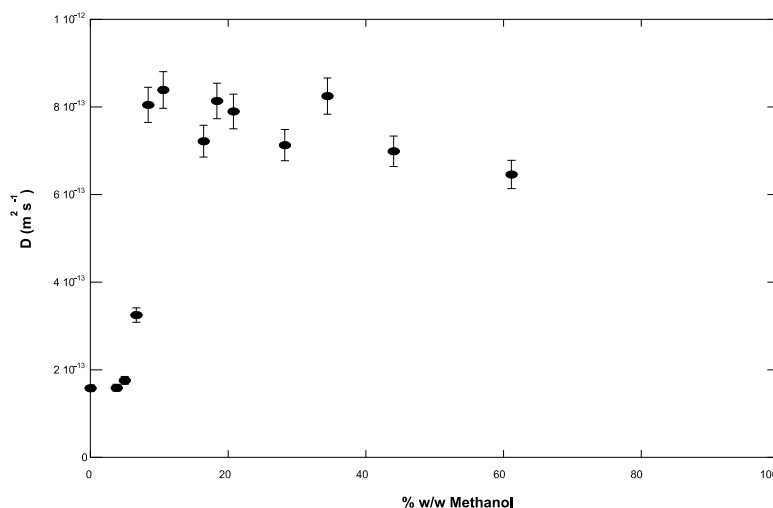
Figure 40. D values relative to **11b** compound as a function of different methanol/water mixture.

An HNT triazole material with two triazole rings (compound **17**) was prepared as a result of four-step synthetic procedure as depicted in Scheme 8. Compound **14** was synthesized following a procedure reported in literature (Scheme 7) [74]. The first alkylation of 4,4'byphenol with 2-(2-chloroethoxy) ethoxyethanol was carried out in DMF in the presence of K_2CO_3 as base. The product was purified by chromatography to yield the 4,4'bis[2-(2-hydroxyethoxy) ethoxy]-diphenyl **13** in 30% yield. The subsequent propargylation was carried out by adding propargyl bromide in DMF and in the presence of NaH to give the compound **14** in 80% yields.

Compound **14** reacts in the first step with azido-functionalized HNT **8**, in a mixture *t*-BuOH/H₂O (1:1), in the presence of catalytic amount of $CuSO_4$ and sodium ascorbate for 48 h at r.t. to give compound **15**. This material reacts in the second step with an excess of NaN_3 and finally, in the third step, by alkylation with butyl bromide, we have obtained the organic salt **17**.
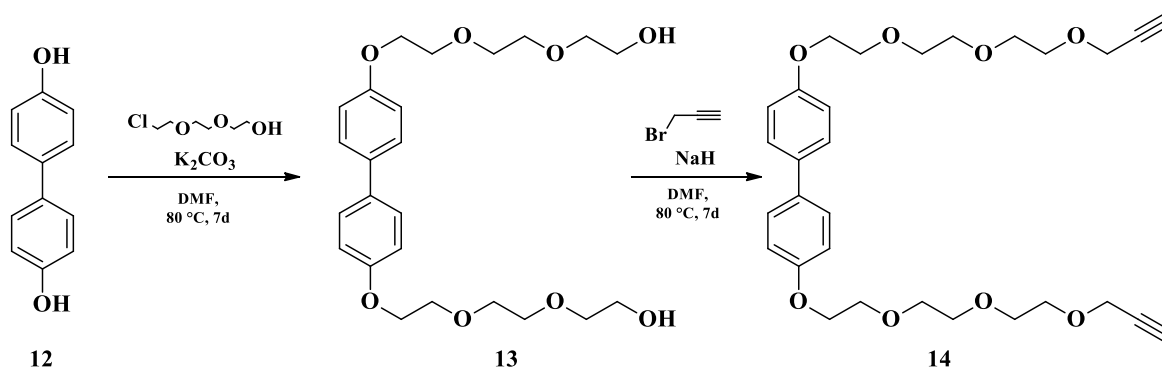
Scheme 7. Schematic representation of the synthesis of compound **14**.
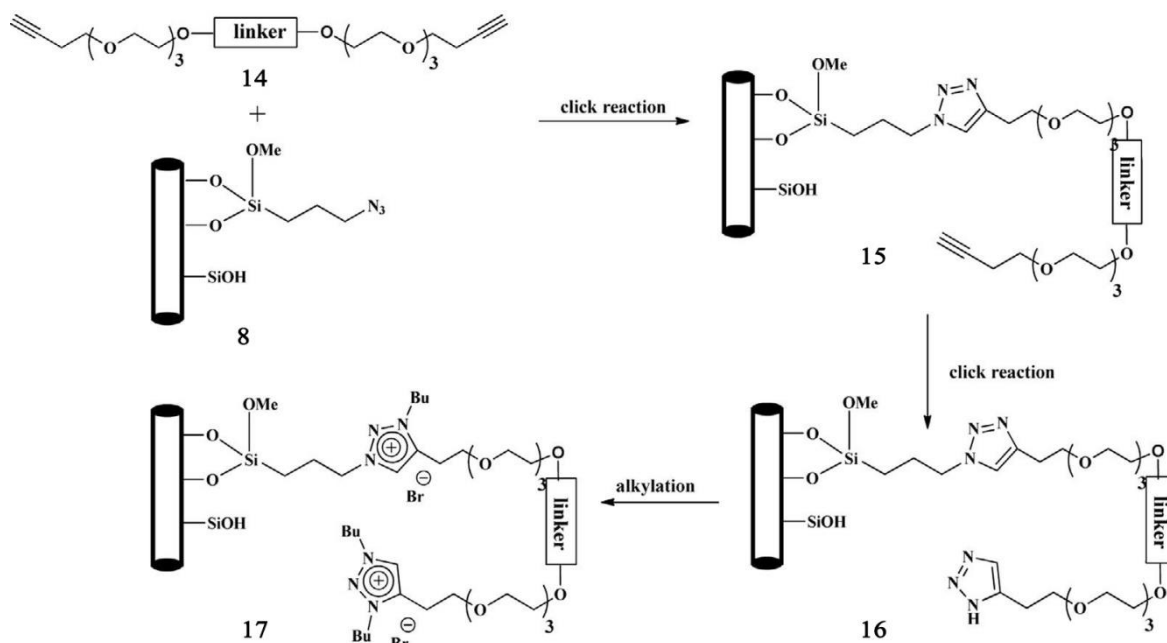
Scheme 8. Schematic representation of the synthesis of compound **17**.

The successful formation of the network of supported ionic liquids was confirmed by solid-state ^{13}C NMR spectroscopy. The characteristic signals of the carbon atoms of the triazolium ring are observed at $\delta = 168$ ppm, the signals of the aromatic moieties are observed in the range between 164 and 117 ppm, whereas the carbon atoms of ether groups resonate in the range 60–80 ppm. These data indicate that the main structure of the triazolium salts is not affected by the grafting process. The weak signals in the range 30–32 ppm are due to the aliphatic carbon atoms of triazolium salts. It is interesting to note that is not present the signal related to the silicon connected to the carbon atoms of the functionalized HNT (as confirmed from ^{29}Si NMR spectrum). This result is not surprisingly because the low loading of azido silane moiety onto HNT external surface. The presence of the triazolium salts on the HNT was, also, confirmed by FT-IR spectra (Figure 41). Compared to azido HNT **8**, compound **15** exhibited new bands around 1595 and 1348 cm^{−1}due to C=C, N=N, C-N stretching vibrations of triazolium moiety. Furthermore, **17** did not show the stretching vibration band of C≡C (2103 cm^{−1}) group, which was observed for compound **15**. The FTIR spectrum of **17** was also characterized by the OH stretching vibrational bands of halloysite.[51] The frequencies of these bands were not altered in the functionalized nanotubes. Specifically, we observed the broad peak of the water OH stretch as well as the OH stretching vibration bands of the Al-OH and Si-OH groups. From these data, one can state that **17** were synthesized. These findings were confirmed by TG studies. In fact, the precursor of **17** (compound **16**) exhibited the typical

halloysite weight losses occurring at ca. 550 °C attributed to the expulsion of interlayer water molecules and the mass losses due to the thermal degradation of the organic moiety on HNT external surface (300–400 °C). After the alkylation, the degradation at 300–400 °C is absent and the organic moiety results stable up to 700 °C when a new degradation step is observed for **17** (Figure 42). Such a stabilization effect is expected for a dicationic salt. The catalyst support could benefit from increased thermal stability, which makes it ideally suited for several applications. TG experiments allowed us to calculate the degree of HNT functionalization to be as ca. 25%.
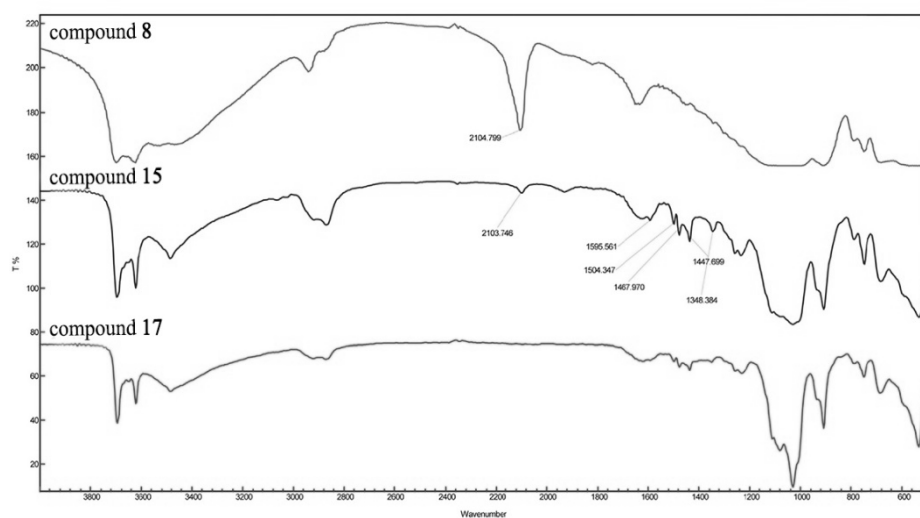
Figure 42. FT-IR spectra of compounds **8**, **15** and **17**.
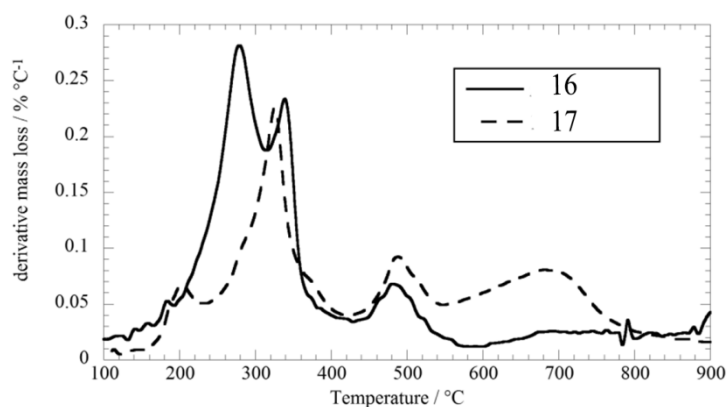
Figure 42. Derivate mass loss of **compounds 16** and **17**.

Although the rather high experimental error, EDX measurements confirmed the loading amount as from the N/Al weight ratio a loading of 36 ± 20 % was calculated. The surface morphology of **17** was investigated by SEM. As Figure 43 shows, the general feature of a tubular structure is preserved in the composite material but there is a change on the surface properties. In particular, a smooth surface is observed in comparison to pristine

HNT This peculiarity can be explained by considering the high loading of the organic moiety on HNT outer surface and the strong $\pi-\pi$ interactions between aromatic rings.
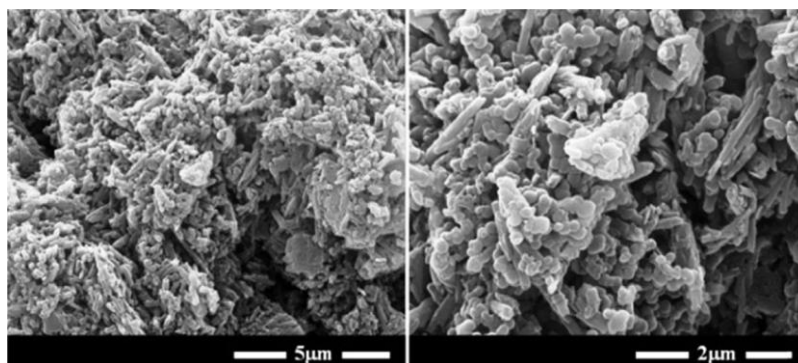
Figure 43. SEM images of **17**.

4.5. Non-covalent modification

As aforementioned, the HNT/CB[8] (compound **18)** nanosponge hybrids were obtained by the non-covalent functionalization of pristine halloysite nanotubes. In details, the supramolecular complex was prepared by mixing halloysite with an aqueous saturated (highly-concentrated) CB[8] solution. Then, the obtained suspension was stirred and kept under vacuum for 3−5 min resulting in light fizzling which indicated that air is removed from the tubes. Once that the vacuum was removed, solution entered into the lumen and the loaded compound condensated within the tube. This procedure was repeated 2–3 times to improve the loading efficiency. The obtained nanomaterial was washed several times with water to remove free CB[8] and dried under vacuum at 70 °C (Figure 44).
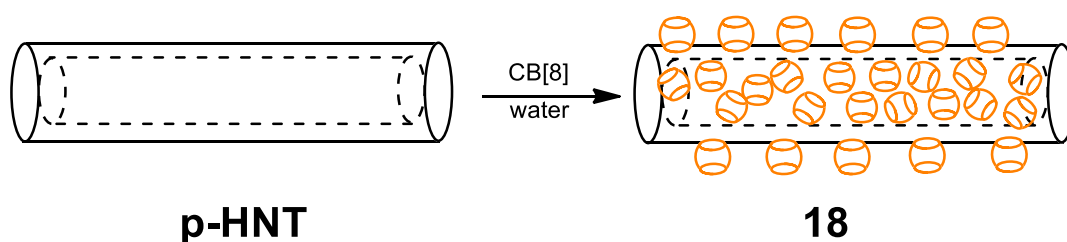
Figure 44. Schematic representation of the preparation of compound **18**.

The functionalization was confirmed by FT-IR spectroscopy, differential scanning calorimetry, and thermogravimetric analysis. In Figure 45 the FT-IR spectrum of the **18** is reported. For comparison, it is also reported the FT-IR spectrum of pristine cucurbituril.
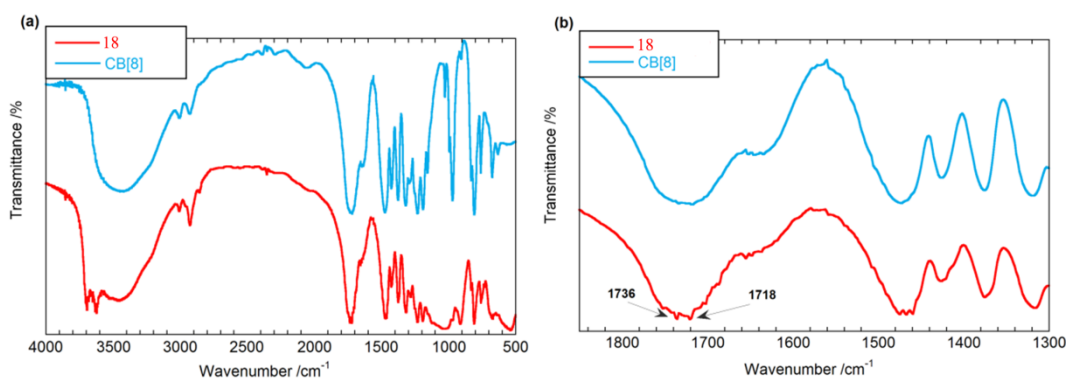
Figure 45. FTIR spectra of the **a) 18** and pristine CB[8] **b)** Magnification in the carbonyl stretching region.

The spectrum for **18** shows the characteristic vibration bands of halloysite and some new FT-IR peaks; namely, the CH_2 stretching vibration bands (at ca. 2933 and 2863 cm^{-1}) and C=O stretching vibration bands at ca. 1750 cm^{-1} of CB[8] are evident. Moreover, all stretching bands of CB[8] (Figure 45b) and the vibration bands of -OH inner surface groups of HNT are also shifted toward lower values compared to the pristine compounds that indicate a more constricted vibration of CB[8] groups inside the confined spaces of halloysite lumen. The C=O stretching vibration bands splitting was also observed for alkanoates adsorption within the HNT lumen.[75]

The DSC thermograms (Figure 46) showed endothermic peaks due to the dehydration of pristine CB[8] occurring within two steps (at 80 and 130 °C) and a peak at ca. 420 °C due to the degradation of the organic molecule that is in agreement with literature findings.[76] In the case of **18**, the CB[8] dehydration takes place within three steps (at 80, 130 and 170 °C) in agreement with a different situation of the hydrated hybrid.
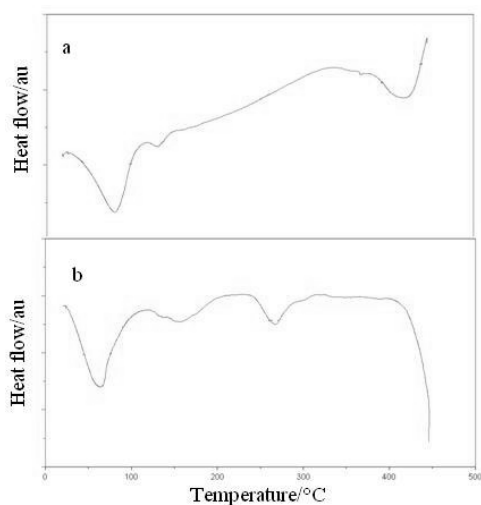
Figure 46. DSC thermograms of a) CB[8] and b) **18**.

TGA studies allowed us to determine the amount of CB[8] loaded and the thermal stability of the new nanomaterial. Figure 47 illustrates the TGA curves for **18**, HNT and CB[8]. The thermogravimetric curves exhibited features of both HNT CB[8] (Figure 47). Namely, the weight loss occurring to ca. 100 °C reveals the moisture content of the pristine CB[8]; the weight loss over the range comprised between 400 and 550 °C may be ascribed to the presence of both HNT and CB[8]. Accordingly, the shoulder present at ca. 360 °C for pristine CB[8] is still present in the curve of the composite material which exhibits an additional weight loss for temperatures larger than 550 °C. The degradation temperature of 487 °C for **18** is equal to the value of the pristine HNT (487 °C) and larger than that of pristine CB[8] (438 °C). The shift of degradation temperature of CB[8] towards a larger value as well as the degradation temperature at 639 °C is consistent with the interactions with the nanotubes.
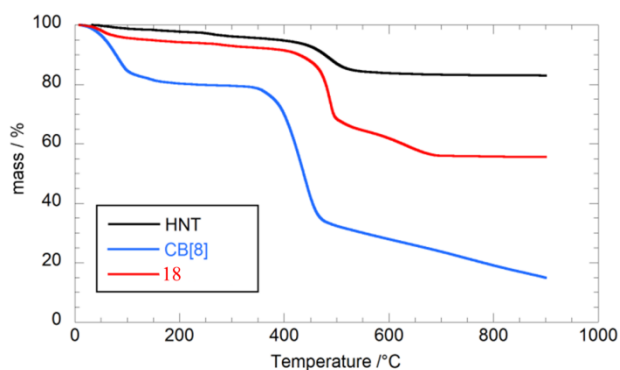
Figure 47. TG curves of pristine HNT and CB[8] and **18** supramolecular complex.

The enhanced thermal stability of CB[8] may be due to the barrier effect towards the mass transport of the volatile species due to their encapsulation into the nanotubes cavity. The formation of the hybrid nanomaterial is corroborated by the residual content at 700 °C from which we evaluated the degree of HNT functionalization that was 25 wt%.

Being that from the geometric of the nanotube cavity, one expects a maximum of incorporation of 10% one may conclude that the organic molecules were incorporated not only into the HNT lumen, as already evidenced by FTIR spectrum, but also onto the HNT external surface. Therefore the peaks at 487 °C and at 639 °C may represent two kinds of CB[8] populations present into the supramolecular structure. This hypothesis is in line with the nature of cucurbit[n]urils[77,78] that are highly symmetric structures featured by negatively charged carbonyl rims and hydrophobic internal surface while the outer surface is to some extent electrostatically positive.

Recently, self-assemblies formed as a consequence of outer-surface interactions of cucurbit[n]urils with different materials like aromatic molecules, calixarenes, inorganic ions, polyoxometalates were reported.[76] Aesthetic structures were provided honey–comb like, fiber-like, linear supramolecular chains assemblies. The different chemistry of the inner and the outer surfaces of HNT provides several sites of interactions. The external and the internal surfaces are composed of silica and alumina groups, respectively, that, under certain experimental conditions, undergo dissociations. Thus, the large amount of CB[8] loaded into the nanohybrid might be explained in terms of interactions between portal carbonyl groups and the positively charged alumina groups of the HNT internal surface (*via* hydrogen bonds formation Al-OH---O=C-) and electrostatic forces between the negatively siloxane groups of HNT outer surface and the partial dipole of carbonyl groups of CB[8]. On this basis, nanocylinders decorated with pumpkin-shaped containers are obtained (Figure 48).
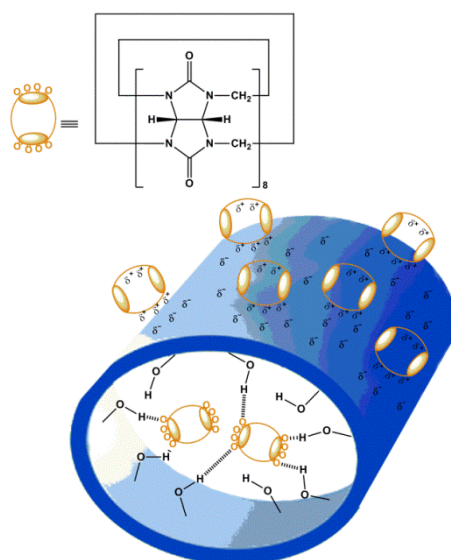
Figure 48. Schematic representation of interactions between cucurbit[8]uril and HNT.

In order to prove the validity of this interpretation we have investigated the local mobility of CB[8] into the **18** by means of solid state variable contact time, cross polarization, magic angle spinning (VCT-CP-MAS) NMR experiments. Cross polarization, indeed, is based on heteronuclear dipolar interactions and therefore it is sensitive to internuclear distances and mobility of the functional groups involved. A series of spectra at various contact times (τ) were recorded for **18** complex under proton pulse cross-polarization conditions (Figure 49a).

Under these circumstances, signal intensities depend on τ according to the relationship[79]

$$I_t = I_0 \cdot \left(1 - \frac{T_{CH}}{T_{1\rho}^1}\right)^{-1} \cdot \left[\exp\left(-\frac{\tau}{T_{1\rho}^1}\right) - \exp\left(\frac{\tau}{T_{CH}}\right)\right] \qquad \textit{Equation 3}$$

where I_0 is the maximum observable signal intensity and $T^1_{1\rho}$ is the proton longitudinal relaxation time in the rotating frame associated with each group resonating. T_{CH} depends on the number of nuclei involved in cross polarization and on their disposition.

The single exponential function (Equation 3) was applied to the interpolation of the variable contact time data from the CP-MAS ^{13}C-NMR experiments on **18** and on CB[8] (Figure 49b). The value of T_{CH} obtained for the carbonyl carbon of pristine CB[8] and in the hybrid **18** are 1.40±0.08 ms and 1.11±0.07 ms respectively. It is interesting to note that T_{CH} value in the complex is shorter than the CB[8] one as a consequence of a stable aggregation of CB[8] with HNTs. Presumably due to the heteronuclear dipolar interactions between oxygens on carbonyl groups of CB[8] and hydroxyl groups on both HNT surfaces. It is known that the T_{CH} value decreases with a number of hydrogen atoms bound to the carbon atom under observation;[80] such a trend is registered for our systems because of the specific interaction with HNT inner surface that is rich in hydrogen bond donating groups.
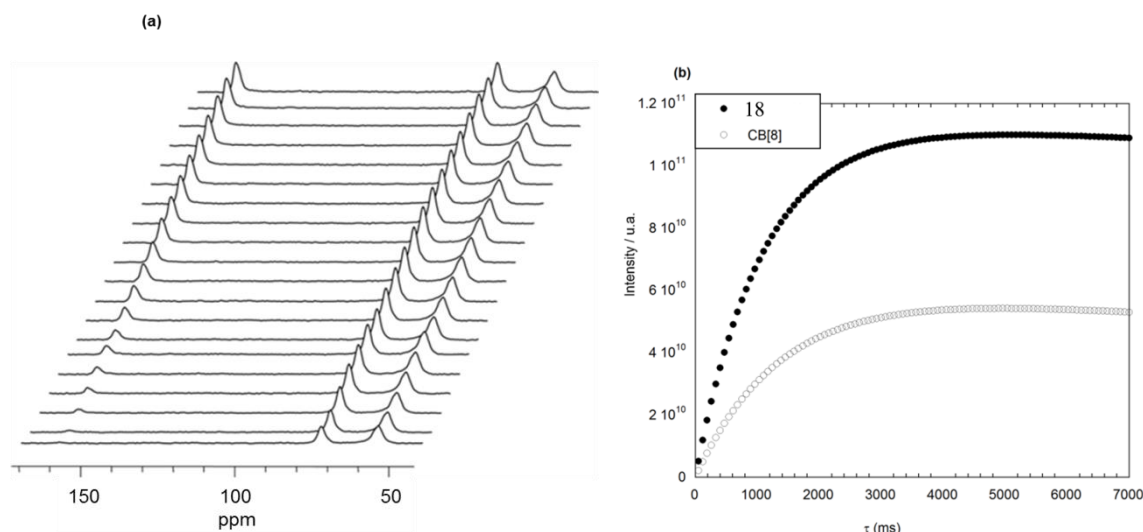
Figure 49. a) The spectra of **18** recorded at various CP contact-time (in ms); **b)** ^{1}H-^{13}C CP/MAS variable-contact data for the carbonyl carbon of CB[8] and **18**.

The translational average diffusion of **18** (3.4±0.2) $\times$ 10^{-13} m^2 s^{-1} is three times smaller than the value[81] for pristine HNTs in water (9.4$\times$10^{-13} m^2 s^{-1}); this result is consistent with the increase of the HNT size generated by the adsorption of the organic molecule onto the external surface but also by the HNTs aggregation as a consequent effect of the CB[8] total loading. Accordingly, the adsorption of the organic molecule onto the HNT causes the increase of the ζ-potential value (-3.1±0.2 mV) compared to the value of

pristine HNT (-19.4 mV). Such an increment provides further light on the sites of CB[8] anchoring. In fact, in case CB[8] is selectively entrapped into the lumen a more negative ζ-potential value is expected according to literature findings. Namely, loading of alkanoates[81] and perfluoroalkanoates[21] into the HNT cavity enhanced the negative ζ-potential value and did not modify the HNT translational average diffusion. On the contrary, sodium decyltrimetylammonium bromide adsorbed onto the external negative surface allowed positive ζ-potential value and a reduced translational average diffusion.

In conclusion, the reduced translational average diffusion of the new nanohybrid is due not only to the layer of the adsorbed CB[8] onto the external surface but also to the enhancement of the attractive forces between the modified HNT being that the electrostatic repulsions are less important. The dried composite material imaged by SEM (Figure 50) evidence that the **18** has a rather compact structure where the HNT seems glued together in agreement with DLS results.
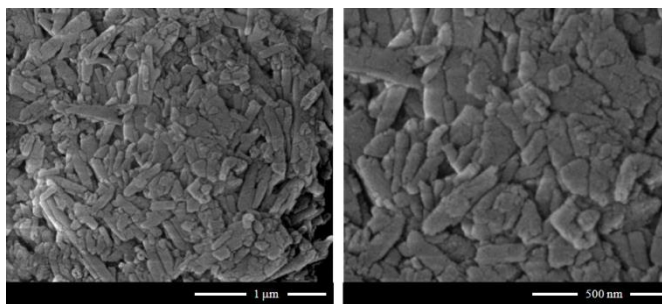
Figure 50. SEM images of **18**.

References

(1) Szpilska, K.; Czaja, K.; Kudla, S. *Polimery* **2015**, *60* (6), 359.

(2) Yuan, P.; Southon, P. D.; Liu, Z.; Green, M. E. R.; Hook, J. M.; Antill, S. J.; Kepert, C. J. *J. Phys. Chem. C* **2008**, *112* (40), 15742.

(3) Editors, B. *Encyclopedia Britannica*; 2016.

(4) Kodama, H.; Grim, R. *Encyclopedia Britannica*; 2014.

(5) Joussein, E.; Petit, S.; Churchman, J.; Theng, B.; Righi, D.; Delvaux, B. *Clay Miner.* **2005**, *40* (4), 383.

(6) Joussein, E. In *Nanosized Tubular Clay Minerals. Halloysite and Imogolite*; Yuan, P., Thill, A., Bergaya, F., Eds.; Elsevier, 2016; Vol. 7, pp 12–48.

(7) Lvov, Y.; Abdullayev, E. *Prog. Polym. Sci.* **2013**, *38*, 1690.

(8) Kamble, R.; Ghag, M.; Gaikawad, S.; Panda, B. K. *J. Adv. Sci. Res.* **2012**, *3* (2), 25.

(9) Machado, G. S.; de Freitas Castro, K. A. D.; Wypych, F.; Nakagaki, S. *J. Mol. Catal. A Chem.* **2008**, *283* (1–2), 99.

(10) Maziarz, P.; Matusik, J. *Clay Miner.* **2016**, *51*, 385.

(11) White, R. D.; Bavykin, D. V.; Walsh, F. C. *Nanotechnology* **2012**, *23*, 65705.

(12) Lvov, Y. M.; Guo, B.; Fakhrullin, R. F. *Functional Polymer Composites*, RSC Smart.; The Royal Society of Chemistry, 2016.

(13) Churchman, G. J. *Clays Clay Miner.* **1990**, *38* (6), 591.

(14) Yuan, P.; Tan, D.; Annabi-Bergaya, F. *Appl. Clay Sci.* **2015**, *112–113*, 75.

(15) Nicolini, K. P.; Fukamachi, C. R. B.; Wypych, F.; Mangrich, A. S. *J. Colloid Interface Sci.* **2009**, *338* (2), 474.

(16) R. Price, B. P. G. Y. L. R. *J. Microencapsul.* **2001**, *18* (6), 713.

(17) VEERABADRAN, N. G.; PRICE, R. R.; LVOV, Y. M. *Nano* **2007**, *2* (2), 115.

(18) Tully, J.; Yendluri, R.; Lvov, Y. *Biomacromolecules* **2016**, *17* (2), 615.

(19) Lvov, Y. M.; Shchukin, D. G.; Möhwald, H.; Price, R. R. *ACS Nano* **2008**, *2* (5), 814.

(20) Abdullayev, E.; Price, R.; Shchukin, D.; Lvov, Y. *ACS Appl. Mater. Interfaces* **2009**, *1* (7), 1437.

(21) Cavallaro, G.; Lazzara, G.; Milioto, S.; Palmisano, G.; Parisi, F. *J. Colloid Interface Sci.* **2014**, *417*, 66.

(22) Owoseni, O.; Nyankson, E.; Zhang, Y.; Adams, S. J.; He, J.; McPherson, G. L.; Bose, A.; Gupta, R. B.; John, V. T. *Langmuir* **2014**, *30* (45), 13533.

(23) Dzamukova, M. R.; Naumenko, E. a.; Lvov, Y. M.; Fakhrullin, R. F. *Sci. Rep.* **2015**, *5*, 10560.

(24) Lvov, Y.; Price, R.; Gaber, B.; Ichinose, I. *Colloids Surfaces A Physicochem. Eng. Asp.* **2002**, *198–200*, 375.

(25) Kim, J.; Park, N.; Na, J. H.; Han, J. *J. Food Sci.* **2016**, *81* (8), E1956.

(26) Niu, M.; Yang, H.; Zhang, X.; Wang, Y.; Tang, A. *ACS Appl. Mater. Interfaces* **2016**, *8* (27), 17312.

(27) Cavallaro, G.; Lazzara, G.; Milioto, S.; Parisi, F. *J. Colloid Interface Sci.* **2016**, *461*, 346.

(28) Liu, M.; Guo, B.; Zou, Q.; Du, M.; Jia, D. *Nanotechnology* **2008**, *19* (20), 205709.

(29)	Veerabadran, N. G.; Mongayt, D.; Torchilin, V.; Price, R. R.; Lvov, Y. M. *Macromol. Rapid Commun.* **2009**, *30* (2), 99.

(30)	Cavallaro, G.; Lazzara, G.; Milioto, S.; Parisi, F. *Langmuir* **2015**, *31* (27), 7472.

(31)	Cavallaro, G.; Lazzara, G.; Milioto, S. *J. Phys. Chem. C* **2012**, *116* (41), 21932.

(32)	Aguzzi, C.; Cerezo, P.; Viseras, C.; Caramella, C. *Appl. Clay Sci.* **2007**, *36* (1–3), 22.

(33)	Yuan, P.; Tan, D.; Annabi-Bergaya, F. *Appl. Clay Sci.* **2015**, *112–113*, 75.

(34)	Jing, H.; Higaki, Y.; Ma, W.; Wu, H.; Yah, W. O.; Otsuka, H.; Lvov, Y. M.; Takahara, A. *Chem. Lett.* **2013**, *42* (2), 121.

(35)	Yah, W. O.; Takahara, A.; Lvov, Y. M. *J. Am. Chem. Soc.* **2012**, *134* (3), 1853.

(36)	Yah, W. O.; Xu, H.; Soejima, H.; Ma, W.; Lvov, Y.; Takahara, A. *J. Am. Chem. Soc.* **2012**, *134* (29), 12134.

(37)	Zhang, H.; Ren, T.; Ji, Y.; Han, L.; Wu, Y.; Song, H.; Bai, L.; Ba, X. *ACS Appl. Mater. Interfaces* **2015**, *7* (42), 23805.

(38)	K Dedzo, G.; Ngnie, G.; Detellier, C. *ACS Appl. Mater. Interfaces* **2016**, *8* (7), 4862.

(39)	Nakhaei Pour, A.; Housaindokht, M. *Catal. Letters* **2013**, *143* (12), 1328.

(40)	Albdiry, M. T.; Yousif, B. F. *Mater. Des.* **2013**, *48*, 68.

(41)	Peixoto, A. F.; Fernandes, A. C.; Pereira, C.; Pires, J.; Freire, C. *Microporous Mesoporous Mater.* **2016**, *219*, 145.

(42)	Cao, X. T.; Showkat, A. M.; Kim, D. W.; Jeong, Y. T.; Kim, J. S.; Lim, K. T. *J. Nanosci. Nanotechnol.* **2015**, *15* (11), 8617.

(43)	Li, H.; Zhu, X.; Zhou, H.; Zhong, S. *Colloids Surfaces A Physicochem. Eng. Asp.* **2015**, *487*, 154.

(44)	Lun, H.; Ouyang, J.; Yang, H. *RSC Adv.* **2014**, *4* (83), 44197.

(45)	Tan, D.; Yuan, P.; Annabi-Bergaya, F.; Liu, D.; Wang, L.; Liu, H.; He, H. *Appl. Clay Sci.* **2014**, *96*, 50.

(46)	Li, C.; Liu, J.; Qu, X.; Guo, B.; Yang, Z. *J. Appl. Polym. Sci.* **2008**, *110* (6), 3638.

(47)	Li, C.; Liu, J.; Qu, X.; Yang, Z. *J. Appl. Polym. Sci.* **2009**, *112* (5), 2647.

(48)	Zhang, J.; Zhang, D.; Zhang, A.; Jia, Z.; Jia, D. *Iran. Polym. J.* **2013**, *22* (7), 501.

(49)	Bischoff, E.; Daitx, T.; Simon, D. A.; Schrekker, H. S.; Liberman, S. A.; Mauler, R. S. *Appl. Clay Sci.* **2015**, *112–113*, 68.

(50)	Carli, L. N.; Daitx, T. S.; Soares, G. V; Crespo, J. S.; Mauler, R. S. *Appl. Clay Sci.* **2014**, *87*, 311.

(51)	Massaro, M.; Riela, S.; Cavallaro, G.; Gruttadauria, M.; Milioto, S.; Noto, R.; Lazzara, G. *J. Organomet. Chem.* **2014**, *749*, 410.

(52)	Massaro, M.; Riela, S.; Lo Meo, P.; Noto, R.; Cavallaro, G.; Milioto, S.; Lazzara, G. *J. Mater. Chem. B* **2014**, *2* (44), 7732.

(53)	Peixoto, A. F.; Fernandes, A. C.; Pereira, C.; Pires, J.; Freire, C. *Microporous Mesoporous Mater.* **2016**, *219*, 145.

(54)	Zhang, Y.; Chen, Y.; Zhang, H.; Zhang, B.; Liu, J. *J. Inorg. Biochem.* **2013**, *118*, 59.

(55)	Luo, P.; Zhang, J.; Zhang, B.; Wang, J.; Zhao, Y.; Liu, J. *Ind. Eng. Chem. Res.* **2011**, *50* (17), 10246.

(56)	Barrientos-Ramirez, S.; de Oca-Ramirez, G. M.; Ramos-Fernandez, E. V; Sepulveda-Escribano, A.; Pastor-Blas, M. M.; Gonzalez-Montiel, A.

Appl. Catal. A Gen. **2011**, *406* (1–2), 22.

(57) Pasbakhsh, P.; Ismail, H.; Fauzi, M. N. A.; Bakar, A. A. *Appl. Clay Sci.* **2010**, *48* (3), 405.

(58) Guo, B.; Zou, Q.; Lei, Y.; Jia, D. *Polym. J* **2009**, *41* (10), 835.

(59) Zhang, J.; Zhang, D.; Zhang, A.; Jia, Z.; Jia, D. *J. Reinf. Plast. Compos.* **2013**, *32* (10), 713.

(60) Liu, M.; Chang, Y.; Yang, J.; You, Y.; He, R.; Chen, T.; Zhou, C. *J. Mater. Chem. B* **2016**, *4* (13), 2253.

(61) Zargarian, S. S.; Haddadi-Asl, V.; Hematpour, H. *J. Nanoparticle Res.* **2015**, *17* (5), 1.

(62) Joo, Y.; Jeon, Y.; Lee, S. U.; Sim, J. H.; Ryu, J.; Lee, S.; Lee, H.; Sohn, D. *J. Phys. Chem. C* **2012**, *116* (34), 18230.

(63) Shahamati Fard, F.; Akbari, S.; Pajootan, E.; Arami, M. *Desalin. Water Treat.* **2016**, 1.

(64) Tian, X.; Wang, W.; Wang, Y.; Komarneni, S.; Yang, C. *Microporous Mesoporous Mater.* **2015**, *207*, 46.

(65) Cavallaro, G.; Lazzara, G.; Massaro, M.; Milioto, S.; Noto, R.; Parisi, F.; Riela, S. *J. Phys. Chem. C* **2015**, *119* (16), 8944.

(66) Naumenko, E. A.; Guryanov, I. D.; Yendluri, R.; Lvov, Y. M.; Fakhrullin, R. F. *Nanoscale* **2016**, *8* (13), 7257.

(67) Long, Z.; Zhang, J.; Shen, Y.; Zhou, C.; Liu, M. *Mater. Sci. Eng. C* **2017**, *81*, 224.

(68) Miller, C. A.; Neogi, P. *Interfacial Phenomena Equilibrium and Dynamic Effects*, 17th ed.; Marcel Dekker, I., Ed.; New York, 1985.

(69) Massaro, M.; Riela, S.; Lo Meo, P.; Noto, R.; Cavallaro, G.; Milioto, S.; Lazzara, G. *J. Mater. Chem. B* **2014**, *2* (44), 7732.

(70) Lazzara, G.; Milioto, S. *Polym. Degrad. Stab.* **2010**, *95* (4), 610.

(71) Sing, K. S. W. *Pure and Applied Chemistry*. 1985, p 603.

(72) Jalalvandi, E.; Cabral, J.; Hanton, L. R.; Moratti, S. C. *Mater. Sci. Eng. C* **2016**, *69*, 144.

(73) Cavallaro, G.; Lazzara, G.; Milioto, S. *Langmuir* **2011**, *27* (3), 1158.

(74) Liu, M.; Guo, B.; Du, M.; Lei, Y.; Jia, D. *J. Polym. Res.* **2008**, *15* (3), 205.

(75) Cavallaro, G.; Lazzara, G.; Milioto, S. *J. Phys. Chem. C* **2012**, *116* (41), 21932.

(76) Germain, P.; Létoffé, J. M.; Merlin, M. P.; Buschmann, H. J. *Thermochim. Acta* **1998**, *315* (2), 87.

(77) Assaf, K. I.; Nau, W. M. *Chem. Soc. Rev.* **2015**, *44* (2), 394.

(78) Ni, X.-L.; Xiao, X.; Cong, H.; Zhu, Q.-J.; Xue, S.-F.; Tao, Z. *Acc. Chem. Res.* **2014**, *47* (4), 1386.

(79) Guilbaud, J.-B.; Baker, H.; Clark, B. C.; Meehan, E.; Khimyak, Y. Z. *J. Pharm. Sci.* **2010**, *99* (6), 2697.

(80) Wawer, I.; Cichowlas, A. A.; Nartowska, J. *Solid State Nucl. Magn. Reson.* **2001**, *20* (1–2), 35.

(81) Cavallaro, G.; Lazzara, G.; Milioto, S.; Parisi, F.; Sanzillo, V. *ACS Appl. Mater. Interfaces* **2014**, *6* (1), 606.

Chapter 5

Drug Delivery Systems Based on Halloysite Nanotubes

5. Drug Delivery

There are several advantages in the use of nanotechnology and one of this regard the medical field. First of all, a nanosystem is on the same scale as large biomolecules, such as proteins and antibodies, but is smaller than cells. Furthermore, nanometer-sized materials have particular properties like optics, electronics, magnetic and biological that can be modified changing the dimensions, the shape, the chemical composition, the chemical characteristics of the surface of the nanosystem.[1,2] Therefore nanotechnology, is suitable for medical application, where can be design a potentially infinite series of systems which can be used to transport therapeutic or diagnostic agents through biological barriers, to facilitate access to molecules, to mediate molecular interactions and detect with high sensitivity and yield the molecular changes.

In this context drug delivery systems, especially in nano-size dimension, are ideally intended to increase the effectiveness therapeutic of drugs compared to traditional dosage methods. They can perform multiple tasks such as maintaining constant the concentrations of the biological molecules in the site of action, minimize the side effects, protecting the drug from degradation and regulate the kinetic release[3] by local conditions or as a result of particular external stimulation, such as a change of pH.

There are several categories of this systems that can be used as modulator of the release of drugs including polymeric nanoparticles, micellar systems,[4] liposomes, dendrimers, cyclodextrins,[5] biocompatible polymers, gold nanoparticles, silica or iron conjugate oxides.[6] Among the polymer drug carrier systems is important the action of chitosan, a natural polymer derived from chitin deacetylation, which can control the release capacity of drugs through the mucosa.[7] Another interesting examples are the so called "multilayer nanoshells", consisting of a nucleus of oxide of silicon covered with a thin veil of gold, that are able to respond to radiations of certain wavelengths converting light into heat and selectively destroying cancer cells, not involving the healthy ones close to them.[8]

The interaction of the drugs with the carrier can take place in many ways, from a simple mixing to a more complex process influenced by different chemical factors, such as electrostatic interactions, cation exchange, hydrophobic affinity, hydrogen bonding and van der Waals forces, but also physical ones like the solvent, pH, temperature and so on.

For drug carrier proposes the use of porous materials has received considerable attention, thanks to the chemical stability and their adaptable surface reactivity. These characteristics allow to obtain porous materials with various properties for the loading,

encapsulation and controlled release of different drugs like calcium silicates,[9,10] silicon dioxide,[9] hydroxylapatite,[11] and zeolites.[12,13]

Among all of the possible carrier materials, clay minerals are one of many possibilities but with the advantage of being a natural and quite inexpensive source. It is well-known the remarkable ability of clay nanoparticles to interact with drugs or other biological molecules for their delivery, and also their capacity to interact with polymers to enhance mechanical properties as seen in the development of polymer-clay nanocomposites.[14] They already have been used as active ingredients, where clays are applied orally as antacids, gastrointestinal protectors, and antidiarrhoeics, but also in cosmetic creams, powders, and emulsions.[15] Furthermore, modern pharmaceutics employ clays as excipients acting variously as lubricants, diluents, flavor correctors, emulsifiers, rheological agents, and drug delivery modifiers.[16]

In this scenario, all kind of nanoclays were used and tested as vector for drugs transportation in physiological environment. The research group of M. Kharaziha[17], for example, focus their attention on Laponite nanoplates as a platform for the release of anionic dexamethasone (DEX), investigating the effects of pH on the adsorption kinetics of DEX in order to determine the optimal pH for maximized encapsulation. It shows that the drug tend to be encapsulated into the interlayer space of the clay (Figure 51) through an intercalation process and higher loading efficiency (95.10± 0.80 wt%) than other system based on different types of clays.[18]
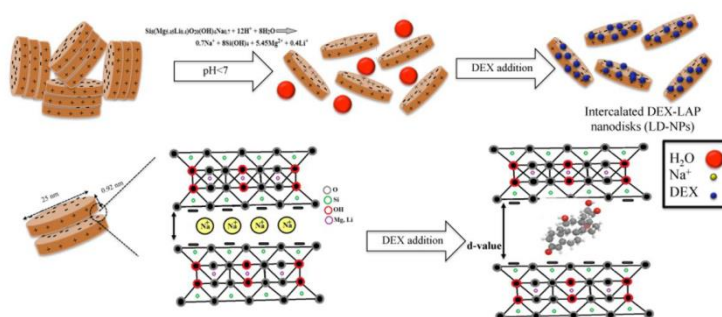
Figure 51: The schematic illustrating the intercalation of DEX into LAP nanoplates at pH=3

To select the best carrier for a drug interaction there are many features to be considered. For example, the interaction of proteins with nanoparticles or nanotubes are quite interesting to investigate, to evaluate the morphologic modification and so the possibility of biological's activities modifications.[19,20] In light of this concern Bramanti *et al.*[21] have studied the surface interactions between clays and bovine serum albumin (BSA), as model protein, by Fourier Transform Infrared Spectroscopy (FTIR) for a better

understanding of the role of clay morphology on protein conformation, comparing at the same time two type of clays, kaolin and HNT. Their evidences show a different behavior of the protein in the interaction with the clays, leading to the fact that the curvature and nanostructure of the carrier have an important role and so must be taken in consideration in the formulation of clays drug delivery system.

5.1. Halloysite Nanotubes in as Systems for Drug Delivery

An ideal carrier with multiple advantages can be represented by halloysite nanotubes, considering being, as explained in other chapters, a biocompatible and non-cytotoxic material and consequently a perfect match for developing biomedical applications.

Despite halloysite mineral was discovered more than 100 years ago, the application has been started the last decades, after the possibility to have it in pure form.[22]

There are many studies concerning the biocompatibility of halloysite that has been shown that it is non-toxic to cells and,[23,24] more in particular, in the case of cells mammary has been found that this nanoclay is less harmful than the common kitchen.[25] Besides, Halloysite tubes may have an appropriate dimension for macrophage removal from living organisms.[22,26]

Furthermore, an important feature that makes HNT a remarkable and useful vector for drugs is the unique tubular morphology with a different charge density. This particularity can be exploited in many ways allowing HNT to be used as a carrier for molecules with different chemical composition. The application of HNT for encapsulation and release of biologically active molecules and drugs was first demonstrated by Price *et al.*[27]

The negatively charged lumen corresponds to c.a. 10% by volume of the tubes, but this value can be easy increase to 30-40% by acid treatment.[28] The unique structure helps, also, the sustained release of molecules from the lumen.[29]

The inner surface of halloysite has been used as container for the loading of lipase, and the union of these with chitosan was used to fabricate an enzymatic membrane that highlights a good catalytic lipid decomposition, stability, and reusability, allowing at the same time to adsorb also cationic lysozyme in the external surface, obtaining a potential synergic effect of the dual enzyme composite.[30]

An alternative approach can be made leading to a selective interaction with the external surface. Polymer as poly(N-isopropylacrylamide) (PNIPAAM) have been grafting onto the outer sheets of halloysite nanotubes to obtain a thermoresponsive drug carrier for

curcumin delivery (Figure 52a), proving by *in vitro* tests simulations that the hybrid system allows a targeted release of the drug, preventing its degradation in gastrointestinal's pH conditions.[31] Beside the supramolecular interaction, a direct chemical grafting can be obtained to achieve a nanocarriers with specific properties as have been noticed with HNT-cur prodrug system (Figure 52b). In this case the release of the drug covalently linked to the carrier has a dual stimuli-responsive, influenced by glutathione concentration or pH conditions.[32] It is also possible to go beyond the simple loading of a drug on the clay, given by the advantage of the tubular structure of the material that allows a double fictionalization in both external and inner surface with more than one potential drug, obtaining a pro-drug system with a synergic effect.[33]

More complex hybrid system have to be synthesized with multivalent glycocluster like cyclodextrin, provide a multivalent and advanced composite system with two cavities available for encapsulation of different active species.[34,35]
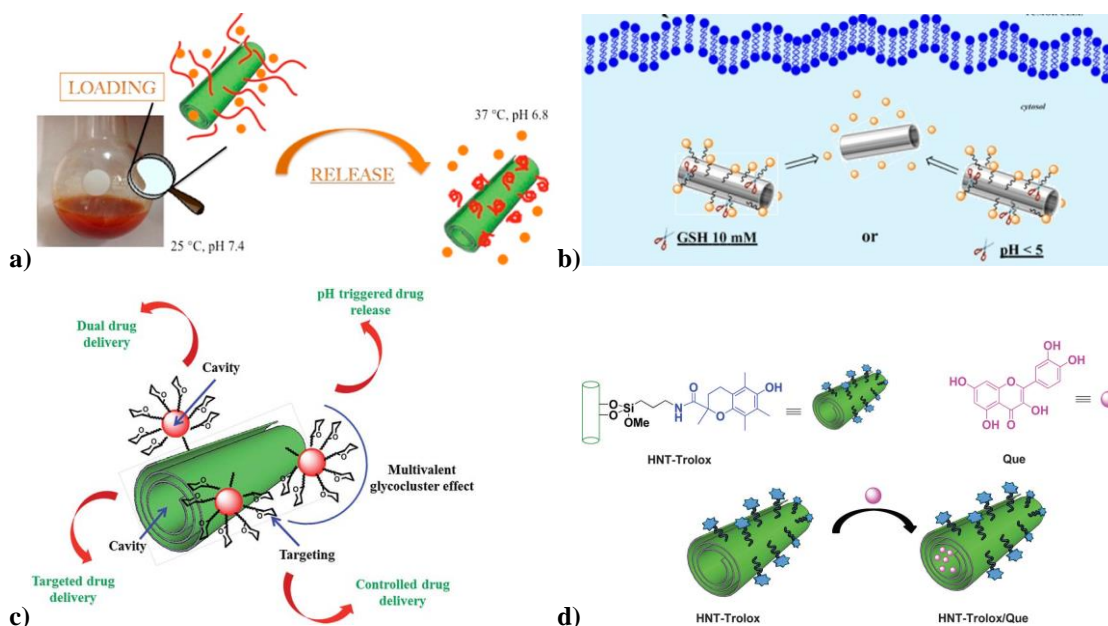
Figure 52. a) Representation of HNT-PNIPAM for Curcumin delivery **b)** HNT-Grafted Curcumin Pro-Drug system **c)** Drug Delivery system based on HNT **d)** Representation of synergic nanoantioxidant system based on HNT.

5.2. *Development and characterization of co-loaded curcumin/triazole- halloysite systems and evaluation of their potential anticancer activity*

Phenolic compounds originated from one of the main class of secondary metabolites in plants, are natural phytochemicals mostly deriving from phenylalanine, which are widely present in food and nutraceuticals.[36] Among them, curcumin and its derivatives have been extensively studied and evaluated for their biological activity. Curcumin [bis(4-hydroxy-3-methoxy-phenyl)-1,6-heptadiene- 3,5-dione] is a natural phenolic compound isolated as a yellow pigment from the dried rhizome of Curcuma longa, a plant that is widely cultivated in tropical areas of Asia and Central America, commonly used as a spice, as a food colorant, and even as a food preservative.

Figure 53. Curcumin powder.

Several studies, also, report that it is an agent possessing a wide variety of biological and pharmacological activities, including anti-proliferation,[37] anti-apoptosis,[36] anti-angiogenesis[38] and inhibition of cell invasion and metastasis.[39] Successful application of this compound is hampered, however, by the occurrence of some disadvantageous properties. Being hydrophobic in nature, curcumin is sparingly soluble in water (ca. 0.6 mg/mL). Moreover, it degrades rapidly under neutral or alkaline conditions, with a half-life shorter than 10 min in phosphate buffer solution at pH 7.2.[40] As a result, its bioavailability is poor, particularly after oral or topical administration.[41] Therefore, a carefully designed carrier could significantly facilitate curcumin delivery and broaden the range of its possible pharmaceutical applications. Nanoscale drug delivery systems are an innovative approach for overcoming the aforementioned problems. Previous attempts at encapsulating curcumin in liposomes, phospholipid complexes, or other nanoparticle-based technologies have been reported, showing an improvement in water dispersibility and a longer circulation.[42–44] A possible nanosized delivery system is constituted by naturally available clay halloysite nanotubes (HNT).

The incorporation of curcumin in HNT formed a stable, strongly colored dispersion. Color indicates a homogeneous distribution of curcumin in the aqueous medium. The interaction between **p-HNT** or **11a-b** compounds with curcumin was evaluated by DLS measurements and *Uv–vis* spectroscopy.

In order to highlight the interactions of **11a-b** with curcumin the diffusion dynamic of the modified nanotubes was studied as a function of the curcumin concentration in the mixed methanol/ water solvent.

The volume ratio water/methanol was fixed at 9:1 which is the best compromise between curcumin solubility and the stability of functionalized HNT dispersions. The concentration dependence of the diffusion coefficient was negligible (Figure 54) and therefore average values of $(3.0\pm1.0)\times10^{-13}$ m^2 s^{-1} and $(6.0\pm3.0)\times10^{-13}$ m^2 s^{-1} were calculated for **11a** and **11b**, respectively. These results show a significant slowdown of both functionalized HNT nanoparticles in the presence of curcumin, indicating that the interaction favors the aggregation or networking of the nanotubes.
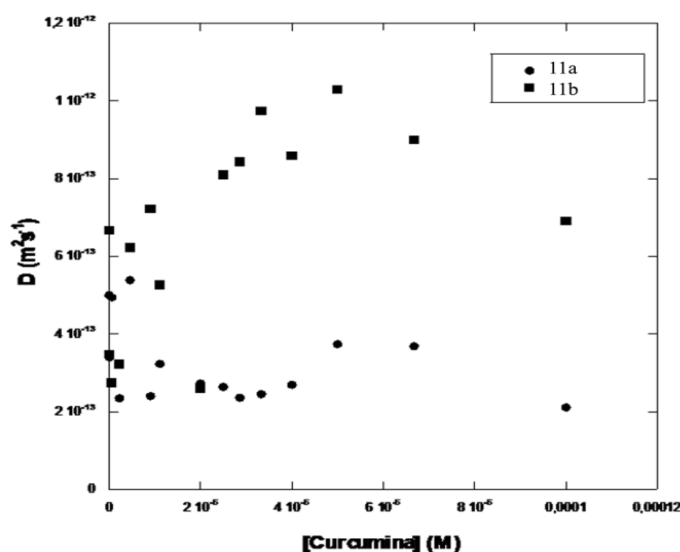
Figure 54. Diffusion coefficient variation by changing the concentration of **11a-b**/Curc complexs.

Considering the results obtained from DLS measurements, mentioned above, we recorded the *UV–vis* spectra of dispersion of **p-HNT**/curcumin both in buffer pH 8 solution/ methanol 9:1 mixture ($_{max}$ = 360 nm) and a water/methanol 9:1 mixture (λ_{max} = 425 nm), at 25 °C and at a fixed concentration of curcumin (1×10^{-4} M) in the presence of increasing amounts of **p-HNT** ($0–1.8\times10^{-3}$ g/mL). The occurrence of the interaction was evaluated by measuring the absorbance at the maximum absorption wavelength of the curcumin in each mixed solvent. Typical trends are depicted in Figure 55. Two different behaviors were observed depending on the medium solvent used. In the buffer

solution/methanol mixture absorbances (recorded at 360 nm) decrease on increasing of **p-HNT** concentration. Moreover, after interaction with **p-HNT**, the complex **p-HNT**/curcumin has a peak at the same absorption wavelength as free curcumin. These findings suggest that curcumin has been successfully encapsulated into the HNT lumen. Similar results are reported in literature for the encapsulation of curcumin within poly(amidoamine) dendrimers.[45]
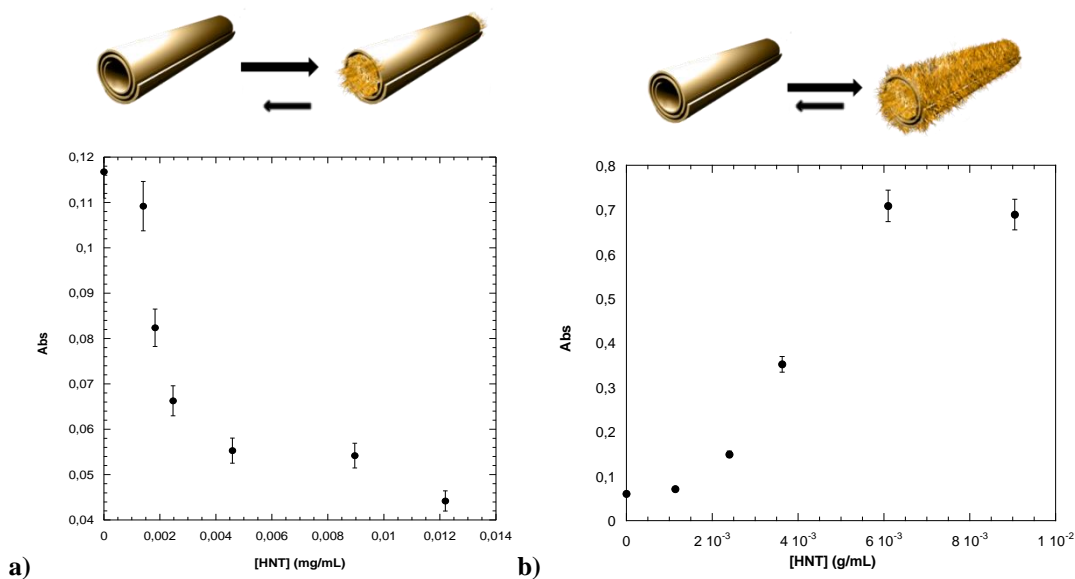
Figure 55. Trend of absorbance value of curcumin as a function of HNT concentration in **a)** blend pH 8/MeOH 9:1; **b)** blend H_2O/MeOH 9:1.

In the neutral H_2O/MeOH 9:1 mixture two absorbance maxima, at 260 and 425 nm were observed. The absorbance values at 425 nm decrease on increasing the amounts of **p-HNT**. By contrast, absorbances at 260 nm increase up to a **p-HNT** concentration of ca. 6×10^{-3} g/mL, and then reach a plateau at larger concentrations (Figure 55b). These trends could indicate that two different equilibria occur in solution, i.e. the loading of curcumin into the lumen of **p-HNT** and its adsorption onto **p-HNT** external surface.

Similarly, we recorded the *UV–vis* spectra of **11a-b**/Curcumin in mixed water/methanol 9:1 solvent, at 25 °C and a fixed concentration of curcumin (1×10^{-4} M) in the presence of varying amounts of compounds **11a-b** ($0–9\times10^{-4}$ g/mL). According to the previous observations, also, in this case, we remarked two different behaviors. We observed an initial decrease of the absorbance value and then an increase in increasing the **11a-b** concentrations (Figure 56a). As previously mentioned, we have hypothesized the coexistence of two different "curcumin species", one encapsulated and the other adsorbed onto external surfaces, of **11a**. The initial decrease could be due to the encapsulation of curcumin in the **11a** lumen, whereas the subsequent increase in the absorbances may be

attributed to the formation of an adsorbed complex. The introduction of a positive charge onto the external surface of **11a-b** makes the curcumin being preferentially adsorbed onto the external surface, by means of more effective π–π and cation–π interactions. Unfortunately, in the latter case, we could not obtain any data for the absorbance value at 260 nm because of the concomitant occurrence of the absorption band of the triazolium moieties present onto the **11a-b** surfaces.

a)   b)
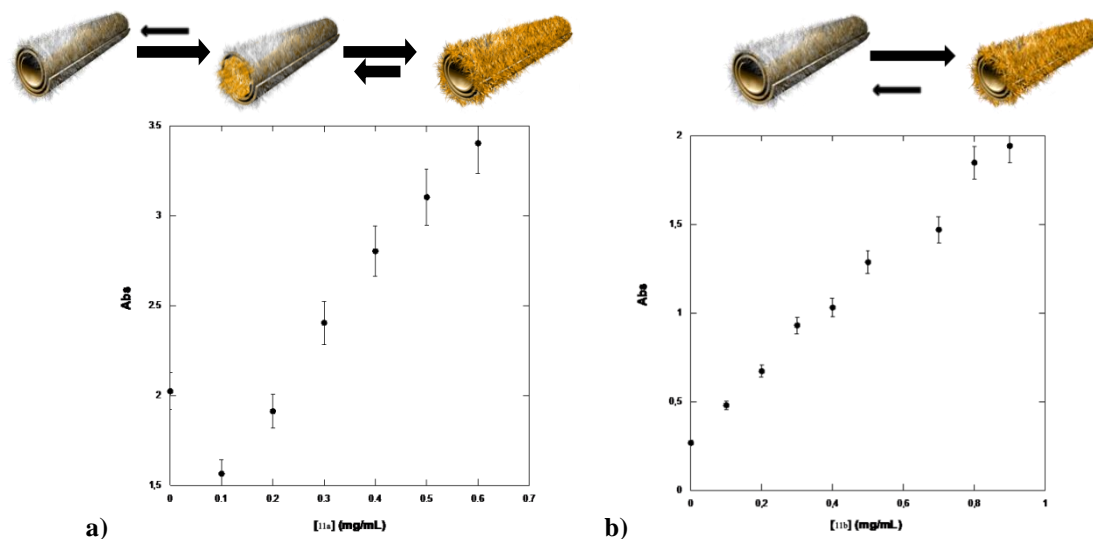
Figure 56. Trend of absorbance value as a function of concentration of **a)** compound **11a**; **b)** compound **11b**.

Figure 56b shows the variation of absorbance of curcumin as a function of **11b** concentration. In this case, no saturation trend is observed. We have supposed that the external functionalization that has longer side alkyl chain length, contributes to the adsorption of curcumin on the external surface and so we, probably, have only one equilibrium in solution.

        To verify the actual co-existence of the two different species the solid complexes **p-HNT**/curcumin (**19**) and functionalized HNT /Curcumin were prepared. **20a** and **20b** respectively from **11a** and **b**. Loading of curcumin was made with two different procedure depending on the **p-HNT** or functionalized HNT used. According to literature,[27] we performed loading procedure from aqueous solvent containing methanol, which provided higher solubility for the drug. Loading of the **p-HNT** with curcumin was based on vacuum cycling of halloysite suspension in saturated solution containing curcumin, as it was described earlier.[46,47] This cycle was repeated more times in order to get highest efficiency of loading. After loading**, 19** complex was washed in order to remove curcumin did not interact with **p-HNT**. Contrariwise for **20a-b**, nanotubes were left (0.2 mg/mL) under

constant stirring, at room temperature, in mixed water/methanol 9:1 solvent with a concentration of 10^{-5} M of curcumin. The subsequent investigations, in both cases, were conducted on the dry solid previously filtered from the dispersion, washed with water and dried for one night at 60 °C.

The obtained materials were imaged by SEM (Figure 57) and it turned out that in the submicron range the typical tubular shape is preserved in all cases while modified HNT and **p-HNT** loaded with curcumin showed a very different morphology in a larger length scale. In particular, **20a-b** did not show any peculiar organization while **19** presented a fiber-like structure. Each fiber was ca. 8 μm large in diameter and several millimeters long. The presence of HNT within the fiber with the nanoparticles distributed without an apparent orientation was observed (Figure 57c).
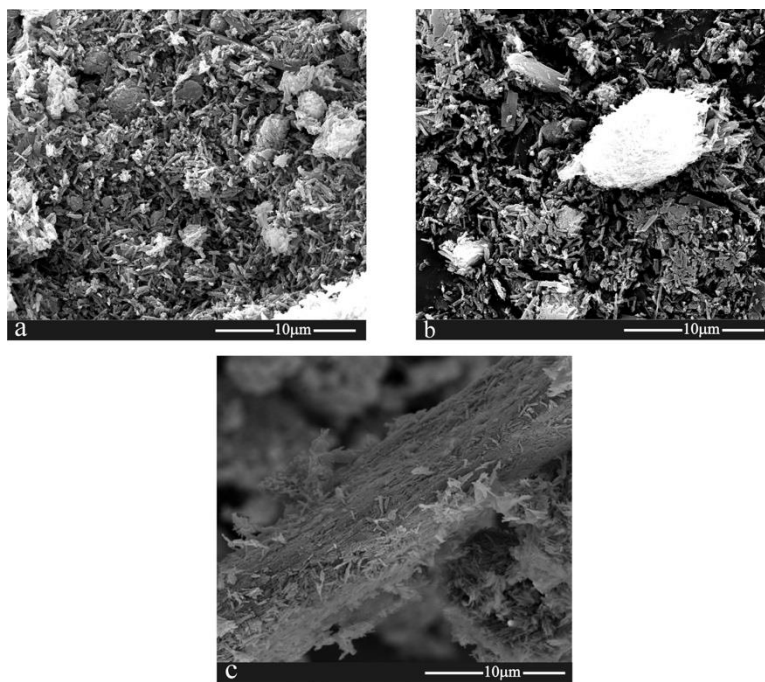
Figure 57. SEM immages of **a) 20a**; **b) 20b**; **c) 19**.

TGA experiments endowed to estimate the amount of curcumin in the solid materials. This was determined by comparing the residual mass at 400 °C of each sample and resulted to be as large as 1.5, 11.0 and 12.5 wt% for **p-HNT**, **11a** and **11b** respectively. Besides the high loading obtained, it is very interesting to observe from TGA data that the degradation temperature of the organic moieties is dependent on the investigated system. In particular, the curcumin encapsulated in **p-HNT** shows a higher degradation temperature (536 °C) as compared to the pure compound (323 °C). This striking enhancement of the thermal stability can be due to encapsulation of the degradation

products into the nanotube lumen.[48,49] It is intriguing to notice that loaded **20a-b** showed two differential degradation peaks for curcumin (401 and 320 °C for **20a**; 570 and 320 °C for **20b**), which can be attributed to the molecules at the outer surface and incorporated into the cavity. By comparing the data for loaded HNT and functionalized HNT one, can assume that incorporated curcumin is present in the functionalized HNT and that the more hydrophobic modification generates a preferential interaction of the curcumin with the outer surface. The latter findings are in agreement with the *UV–vis* results.
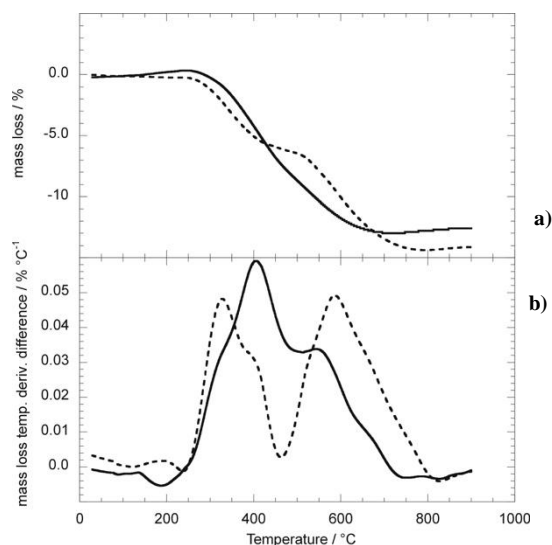
Figure 58. Thermogravimetric curves and differential Thermogravimetric curves of **a) 20a** complex; **b) 20b** complex.

With the aim to use the hybrid complexes as drug carrier, it is crucial to study how the biological molecules can be released from the carrier. Controlled release is an attainable and desirable characteristic of a drug carrier. The factors affecting the drug release rate rely on the structure of the matrix where the drug is contained and the chemical properties associated with both the clay and the drug. The drug release is also diffusion controlled as the drug can travel through the pores of halloysite. The most desirable release profile would show a constant release rate with time.[23] pH is a key factor influencing the oral drug delivery. It is known that pH is about 1.2–2.0 in stomach, about 7.0 in small intestine and as high as 8 in the distal part.[50]

For this purpose the curcumin release from each carrier was studied in three different media that mimic the physiological conditions, namely HCl 0.1 N (pH 1); and phosphate buffers pH 5 and 8.

In Figure 59 extended release profile of curcumin from **19** and **20a-b** is elucidated as a function of time, at 37 °C under mechanical stirring. The release of curcumin at pH 1 from compound **20b** reaches a plateau after 150 min, an initial burst is observed within 100

min followed by a prolonged release. The obtained result is outstanding because it is well known that curcumin suffers from chemical instability in the gastrointestinal tract. Release profiles obtained at pH 5 and pH 8 showed in both cases only a small amount of curcumin released from the systems. The same conclusions can be drawn for compound **20a-b**.
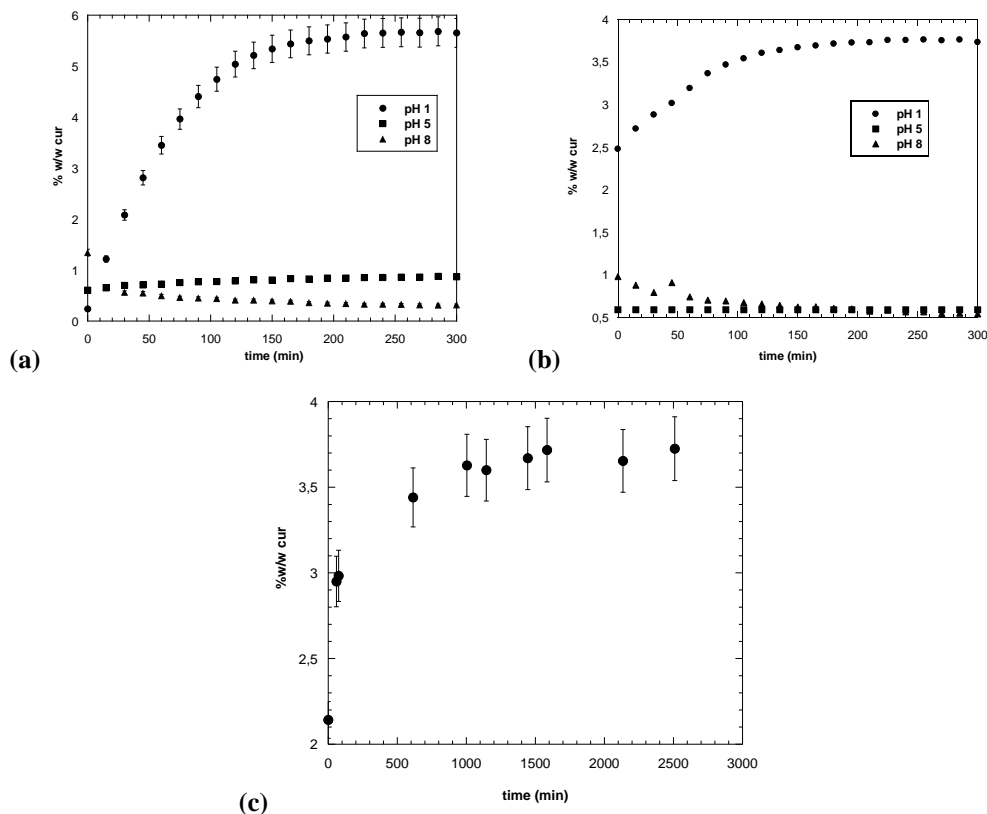
Figure 59. Percentage of released curcumin as a function of the time by **a) 20a**; **b) 20b**; **c) 19**.

As it can be seen there are significant difference for the release in different pH conditions, which can be explained as follows. A first factor to keep into account is the different solubility as a function of pH. Indeed, curcumin molecules ($pKa_1 = 8.38$, $pKa_2 = 9.88$ and $pKa_3 = 10.51$) can exist as cationic, neutral or anionic species in acidic, neutral or alkaline solution, respectively.[51] Therefore, curcumin can be easily migrated out of the carrier at pH 1 in its cationic form, resulting in a higher release as compared with that at pH 5.0 and 8.0. The interaction of curcumin and **11a-b** is another reason for the difference in drug release behavior. In acidic solution both functionalized HNT and curcumin are positively charged; therefore, electrostatic repulsions may also accelerate the release of drug from the **20b**. In the case of **19**, the release of curcumin at pH 1 showed a similar behavior than the release, at the same pH, from **20a-b**. The release of curcumin from **19** can be considered the phase of desorption of the previously adsorbed drug molecules from a cylindrical matrix.[52,53] In this solid/liquid interface process will be involved different

simple interface processes leading to the transport of the drug from the solid to the liquid phase. These simple processes may be governed by diffusion and, in our particular case, are due to the desorption of the drug adsorbed on the external HNT surface. To better understand the release mechanism of curcumin from the different carriers, we analyzed the experimental data obtained for **20b** with the following equations: first-order (4) and the Power law (5):

$$F_t = 1 - e^{-kt} \qquad\qquad \text{\textit{Equation 4}}$$

$$F_t = kt^n \qquad\qquad \text{\textit{Equation 5}}$$

where Ft is the drug release fraction at time *t*, *k* is the release constant of the respective equations, *t* is the release time and n is the characteristic diffusion exponent. The correlation coefficient for Equation 5, either for the release from **p-HNT** and functionalized HNT, is higher than the Power fit equation, so the release mode of curcumin, in both cases, follows the first-order kinetics (Table 9).

Table 9. Kinetic parameters obtained from the not linear regression of release data.

	First order		**Power fit**	
	$k\ (min^{-1})$	R^2	$k\ (min^{-1})$	R^2
19	0.0118±0.0017	0.975	0.207±0.084	0.952
20a	0.0156±0.0004	0.997	0.116±0.038	0.918

Finally, the antiproliferative activity of the supramolecular complexes **19** towards different tumoral hepatic or thyroid cell lines was investigated.

In order to validate the efficiency of **19** and **20a** on cell viability, we tested a panel of 7 tumor cell lines, namely 8505C, BCPAP, C643, SW1736, HA22T/VGH, Hep3B, and HepG2. We performed MTT and MTS tests in order to verify if the complexes are able to exert antitumoral action. Cell viability was estimated at 24, 48 and 72 h under different curcumin concentrations (in the 1–100 mM range). It was observed that cell viability decreases in a concentration and time dependent way. The inhibition efficiency of the complex increased when the incubation time was prolonged from 24 to 72 h, the **20a** displayed significantly stronger anticancer activity than free curcumin. In Figure 5.10 data regarding the antitumor effects of curcumin and its derivatives on the cell lines of hepatocarcinoma HA22T/VGH, anaplastic thyroid SW1736 and papillary thyroid BCPAP after 72 h of incubation are shown; the results obtained from treatment with **11a** are reported for useful comparison.
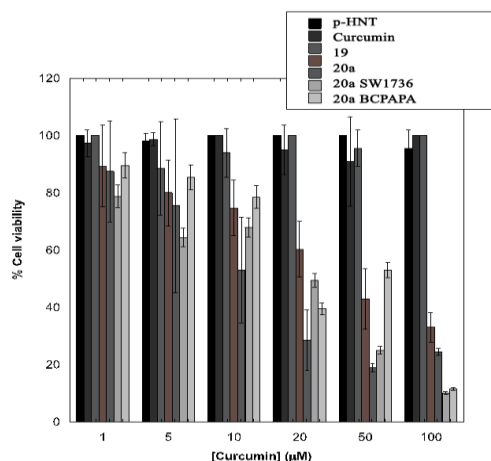
Figure 60. Antiproliferative activity of HNT, curcumin, **19**, **20a** on HA22T/VGH, SW1736 and BCPAP cell lines.

The survival rates of the various tumor cells incubated with **p-HNT** at each concentration were found in the range of 96–100%, indicating they have no effect on cell viability of the tumor cell lines under the concentration conditions investigated. This result is not surprising because it is well known that HNT materials have no cytotoxic effects[38] whereas **11a**, as it can be noticed from Figure 60, exerts variable cytotoxic effects against the different cell lines with IC_{50} of 40.0 ± 14.6 mM. This different behavior could be due to the introduction of triazolium salts onto the carrier, that it is known to possess very interesting biological activities, in particular, antitumoral effect.[54] It is known that nanoparticles enter cells through an internalization mechanism that presumably involves an endocytosis process, whereby **11a** could be uptake into the cytosol by endosomes.[55] Free curcumin has no effect on cell viability, probably due to its rapid metabolism and systemic elimination, which limits its clinical application.[41] No cytotoxic effects for the several cell lines in the presence of the complex **19** were observed. In our opinion the availability of curcumin encapsulated in the halloysite lumen is low, so it is not released in these conditions. Similar results were obtained by Leporatti *et al*. for resveratrol.[23] The **20a** shows, at each concentration, a significantly higher cytotoxicity than free curcumin. In particular, the concentration of **20a** which caused 50% inhibition of cell growth was 11.0 ± 6.4 mM for HA22T/VGH, 23.0 ± 8.6 mM for SW1736 and 23.1 ± 10.6 mM for BCPAP respectively. This increase in the cytotoxicity of **20a** compared with free curcumin was probably due to the possibility of enhanced cellular uptake via endocytic process combined with enhanced aqueous solubility of **20a**. The increase in the cytotoxicity of **20a** with respect to **19** can be explained as follows: (i) **20a** has the largest curcumin loading; (ii) in

the case of **20a** is inside and outside the nanotubes, and therefore the drug can be released quickly from the carrier. Figure 61 shows the amount of curcumin that is embedded in the HA22T/VGH cells after treatment with free curcumin, **19** and **20a**.
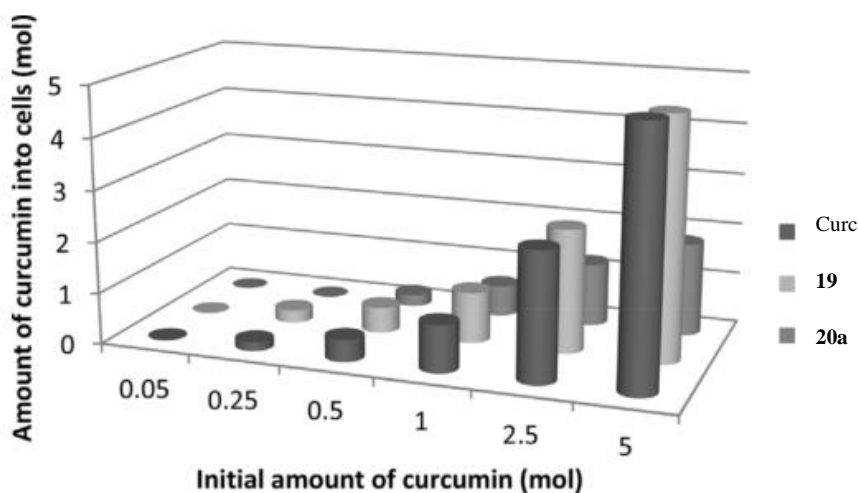
Figure 61. Graphical representation of curcumin amount (mol) into the cells as a function of initial amount of curcumin (mol) for HA22T/VGH cell line.

Despite free curcumin enters almost totally in the cells, it has no effect on cell viability probably because it is rapidly degraded as a consequence of its instability in the culture medium.[56] On the contrary when cells were treated with **20a**, we observe that curcumin enters in the cells until the concentration reaches the IC_{50} value. This may indicate that it is necessary a low amount of drug to exert a therapeutic activity. Based on the cytotoxicity assays, we summarized the IC50 values for **20a** against each cell lines after an incubation time of 72 h (Table 10). It was found that the complex is active against several tumor cell lines. It is noteworthy that **20a** is extremely effective toward both differentiated and undifferentiated tumor cell lines. This observation results particularly important on considering that at present there is no antitumoral chemiotherapic drug against anaplastic thyroid cancer (ATC) and survival of patients is less than 1 year. Moreover, for resistant cell lines, such as the hepatic cancer HA22T/VGH cell, curcumin was usually administered in combination with other chemiotherapic agents to achieve synergistic antitumor effect.[57,58]

Table 10. IC$_{50}$ values of **20a** complex on different cells line.

Complexes	Sickness	Cellular lines	IC$_{50}$ (μM)
	Anaplastic thyroid carcinoma	8505C	14 ± 7
	Papillary thyroid carcinoma	BCPAP	23 ± 11
	Anaplastic thyroid carcinoma	SW1736	23 ± 9
20a	Anaplastic thyroid carcinoma	C643	5 ± 1
	Hepatocellular carcinoma	HA22T/VGH	11 ± 7
	Hepatocellular carcinoma	HepG2	15 ± 6
	Hepatocellular carcinoma	Hep3B	3.7 ± 0.9

5.3. Pharmaceutical properties of supramolecular assembly of co-loaded cardanol/triazole-halloysite systems

Cardanol, also known as m-pentadecenyl phenol, is recovered from agricultural waste cashew nut shell liquid (CNSL) and has been considered one of the most promising natural resources of phenolic compounds, because it is a possible substitute for other commercial phenolic compounds but with many advantages such as its sustainability, nontoxicity, low cost, abundant yield, inedible property, and biodegradability.

The presence of a long aliphatic chain attached to the meta position of the phenolic ring confers exclusive properties to cardanol derivatives, such as high solubility in nonpolar environments and good processability. Furthermore, the chemical and chemical-physical properties, in particular, were attributable to the double bonds present in the long lateral chain, which are not easily reproducible by synthesis, are suitable for several application.

From a chemical point of view, cardanol oil is a rich mixture of non-isoprenoic phenolic compounds that can be processed to obtain a wide variety of nanomaterials such as nanotubes, nanofibres, gels, and surfactants. Among the phenolic secondary metabolites that are present in the shell of the walnut, the most abundant is anacardial acid followed by cardanol, cardol, and 2-methyl cardol. For example, these compounds are used in the treatment of abscesses as they are lethal to Gram-positive bacteria; as biocides against mollusks,[59] as anti-tumoral[60,61] and antimicrobials.[62,63]

Recently Suo *et al.*[64] have been extracted five new phenolic compounds and three molecules already known as cardol, and anacardic acid from the cashew. Hemshekhar *et al.*[65], instead, studied the pharmacological role of anacardial acid and its derivatives.

In particular, the ability of anacardial acid and its derivatives to inhibit the enzyme group histone acetyltransferase has been widely highlighted, also conferring the anti-carcinogenic activity by inducing cytotoxicity on many cell lines. In more detail, anti-carcinogenic activity is due to its ability to interact with the genetic pathways that regulate cell apoptosis. Although anacardial acid does not interact directly with DNA but acts by blocking the expression of a gene product that is expressed in carcinogenic cells to avoid the apoptotic process. Anacardial acid binds some transcription factors that activate the expression of the complex inhibitor cell apoptosis complex, thus avoiding uncontrolled cell proliferation typical of carcinogenic masses.[66]

Reverse-phase HPLC was used in order to investigate the supramolecular interaction between pristine or modified HNT and cardanol. HPLC equipped with Diode-Array/UV detector offers the remarkable advantage to record in real time the *UV–vis* spectrum of the chromatographic eluate (in the range 200–600 nm), and therefore it allows the simultaneous monitoring of different species/analytes.

According to previous reports, pure cardanol,[67] showed three peaks in its HPLC chromatogram, corresponding to 3-[8(Z),11(Z),14-pentadecatrienyl] phenol (79.20%), 3-[8(Z),11(Z)-pentadecadienyl] phenol (0.01%) and 3-[8(Z)-penta-decadecenyl] phenol (20.79%) with retention times (r.t.) of 2.84, 4.21 and 7.70 min respectively, recorded at 210 nm. The most abundant component displayed two bands in its UV spectrum, the first one at 210 nm and the second one, less intense, at 269 nm ca. No peaks were observed in the chromatogram related to **p-HNT** since this material shows no UV absorption. By the contrast, the **11a** exhibits a peak at r.t. 5.45 min and a UV spectrum with an absorption band at 220 nm, attributable to the triazole rings present on the outer surface of the HNT tubes (Figure 62).
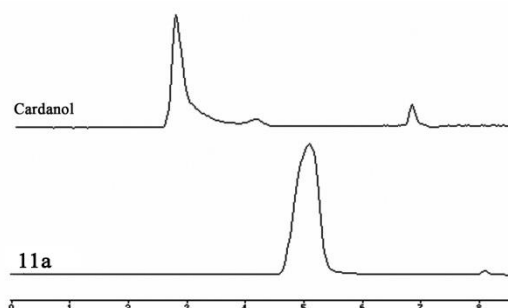
Figure 62. Chromatograms of pure cardanol and compound **11a** recorded at 210 nm.

Figure 63, shows the titration of a fixed cardanol concentration (1×10^{-4} M) with increasing amounts of **p-HNT** (ranging from 0 to 14 mg). In Figure 5.13 in particular, all

peaks in the reported chromatograms, monitored at 210 nm, are related to the supernatant solution after deposition of a white solid. The chromatograms exhibit a decrease in the intensity of the cardanol peak (r.t. 2.84 min), on increasing amounts of **p-HNT**. This finding suggests that the formation of HNT/Cardanol complex occurs (**21**).
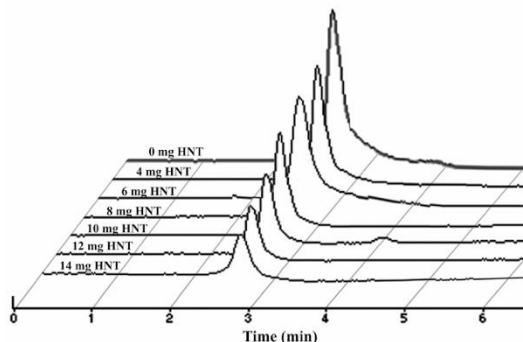
Figure 63. Variation in intensity of the chromatographic peak as a function of HNT concentration

In order to identify the possible presence of **21** complex, we changed the experimental conditions by modifying eluent and reducing flow (eluent: MeOH/H_2O 90:10 v/v; flow0.8 mL/min) and we recorded chromatogram of the dispersions after sonication, monitored at 269 nm (Figure 64). The free cardanol showed a peak at r.t. of 6.93 min, while on increasing of the amount of **p-HNT** new peak appeared, at lower r.t. (5.70 min) with a concomitant hypsochromic shift of the absorption band of cardanol from 269 to 240 nm (Figure 64a). This shift can be attributed to the formation of a complex between cardanol and **p-HNT**, where the biological molecule is adsorbed onto the HNT surface, in agreement with the TGA and SEM evidence discussed afterward. The reduction of cardanol retention time may be explained considering that the absorption of cardanol onto the **p-HNT** surface causes a less extensive interaction between the stationary phase and the biological molecule. A quantitative analysis of the HPLC results, endowing the evaluation of free and adsorbed cardanol, is shown in Figure 64b. The amount of complex, recorded at 240 nm, increases on increasing the **p-HNT** concentration approaching a plateau.
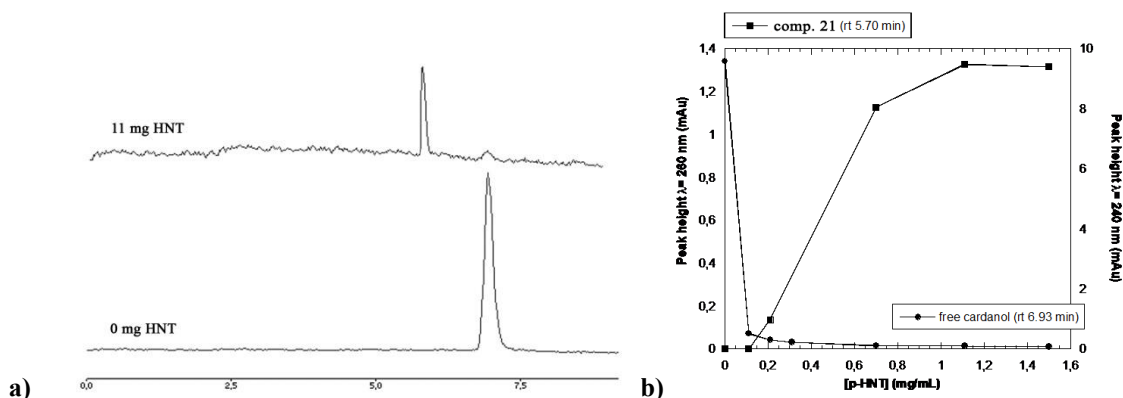
Figure 64. a) chromatograms for cardanol and the **21**; **b)** variation of the intensity of the chromatographic peak of the **21** and cardanol as a function of the concentration of HNT

HPLC measurements resulted advantageous to highlight the strong interaction occurring in functionalized HNT/Cardanol supramolecular complexes. A different behavior was observed respect to **p-HNT**; indeed at **11a** concentration larger than 0.4 mg/mL, surprisingly, no free cardanol was detected. Under the experimental conditions adopted (eluent: MeOH/H_2O 98:2 v/v; flow 1 mL/min), the **11a**/Card dispersion after sonication, displays a chromatogram (monitored at $\lambda = 210$ nm) with a peak at a 5.11 min r.t.; on the other hand, in the chromatogram recorded at 269 nm, two different peaks were observed at 4.94 and 5.23 min r.t.s., respectively. In particular, the *UV* spectrum of the peak at 5.23 min r.t. showed two absorption bands, the first at 220 nm and a second one, less intense at 269 nm, typical of cardanol molecule (Figure 65a), therefore, the second peak could be the evidence of the complex functionalized HNT/Cardanol **22a** and **22b** respectively from **11a** and **11b**. The quantitative analysis of complex is shown in Figure 65b. A very rapid increase in the intensity of the chromatographic peak is observed with a small amount of **11a**, less than 0.4 mg/mL, then a plateau is reached. Therefore, strong interaction occurs even at low **11a** concentration. This fact could be due to the supramolecular aggregation between cardanol and triazole moiety by $\pi-\pi$ and van der Waals interactions and hydrogen bonding.
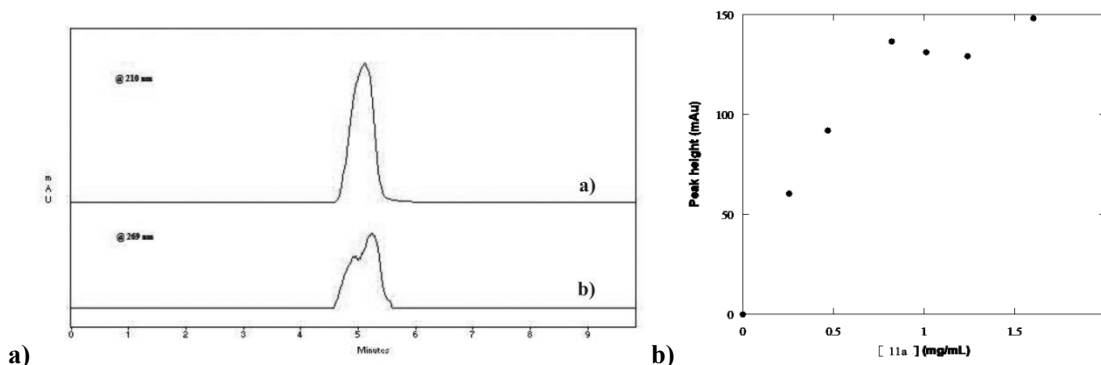
Figure 65. a) chromatogram of complex **22a**; **b)** variation of the intensity of the chromatographic peak relative to the complex as a function of the concentration of **11a**.

The stability of **11a** dispersions in the presence of variable amounts of cardanol was investigated by dynamic light scattering. Within the experimental errors, the obtained diffusion coefficients are independent of concentration and therefore the average values of 4.2×10^{-13} and 3.2×10^{-13} m^2 s^{-1} were calculated for **22a-b**, respectively. These values are ca. half those expected considering the characteristic lengths of the nanotubes (9.4×10^{-13} m^2 s^{-1}). Such a decrease can be ascribed to both a partial aggregation of nanotubes or a slowing down of the diffusion due to the adsorption of cardanol at the outer surface of **11a**. Also in this case, similarly to the complex **19**, the solid complex **22a** were prepared.

The dried complexes of cardanol with **p-HNT** and **22a-b** were investigated by thermogravimetric analysis. Figure 66 shows the thermoanalytical curves of the complexes to which the curve for **p-HNT** and **11a-b**, respectively, were subtracted. This procedure allows us to evidence the cardanol presence even though several degradation processes are present in the composite materials. The obtained curves show a single mass loss step occurring in a temperature range (from 200 °C to 260 °C) comparable to that measured for free cardanol (Fig. 66) and consistent with the compound evaporation.[68] Given that the boiling point of cardanol in the composite is unaltered, we can hypothesize that it is adsorbed at the outer nanotubes surfaces. The amount of loaded cardanol determined from the mass loss differences are ca. 5 wt% and 10 wt% for **p-HNT** and **11a**, respectively. Namely, the HNT functionalization doubled the cardanol loading efficiency regardless of the alkylic chain nature linked to the triazole moiety. These findings agree with the HPLC results and take into account for the strong hydrophobic interactions between the outer surface of **11a** and cardanol. Interestingly we observed a peculiar aging effect on the **21** complex. In particular, the thermoanalytical curve profile for the material obtained after 20 days of stirring showed two well resolved mass loss steps at ca. 200 °C and 350 °C (Figure 66a). The first step is consistent with the presence of adsorbed cardanol, while the second

mass loss process can be related to cardanol strongly interacting with the **p-HNT** lumen or interlayers.
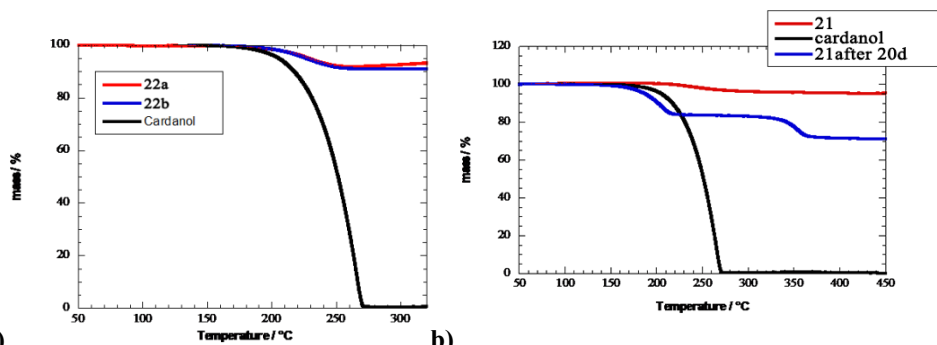
Figure 66. Thermoanalytical curves of **a) 22a-b** complexes and **b) 21** complexes in comparison with free cardanol.

Going further, based on geometrical consideration on the **p-HNT** size,[28] the loading amount of 10.2% estimated from the mass loss at 350 °C indicates a complete filling of the **p-HNT** cavity. These results prove that the incorporation of cardanol is a very slow process. To highlight the cardanol site into the solid complexes, contact angle (θ) experiments were performed. In general, the θ value of water onto a solid substrate depends on both chemical composition and surface roughness. In our case, pellets were obtained by pressing the dry powder at 104 kg cm^{-2} in order to ensure a smooth surface providing a θ value straightforwardly related to the surface composition and hydrophobicity. As Figure 67 shows, θ is nearly constant within the experiment time and it is strongly altered by the presence of cardanol. These trends indicate that both water adsorption and spreading are negligible and therefore an average value of u can be calculated from the data in Figure 67 and in particular 42.5±0.3° and 75±2° is obtained for **11a** and **22a**, respectively. The increase of θ value is consistent with the hydrophobic nature of cardanol and its adsorption at the outer surface of the nanotubes.
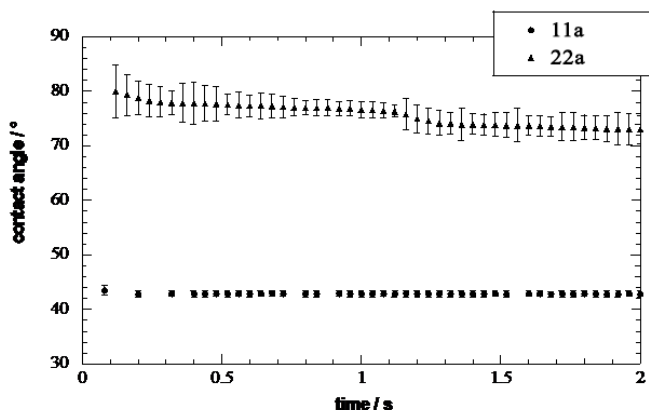
Figure 67. Contact angle as a function of time for **11a** and **22a** complex.

A similar conclusion can be drawn for **p-HNT** and **21**. The surface morphology of **21** and **22-a-b** was imaged by SEM. It clearly appears that the tubular shape of the halloysite is maintained after the surface modification and cardanol adsorption. A careful look at the images evidenced the empty cavity of the nanoclay (Figure 68a) with an average inner radius of 17 nm and an outer radius of 70 nm. The presence of the hollow cavities and the smooth outer surface of the nanotubes confirms that the cardanol adsorption occurs at the external surface (Figure 68b and 68c).
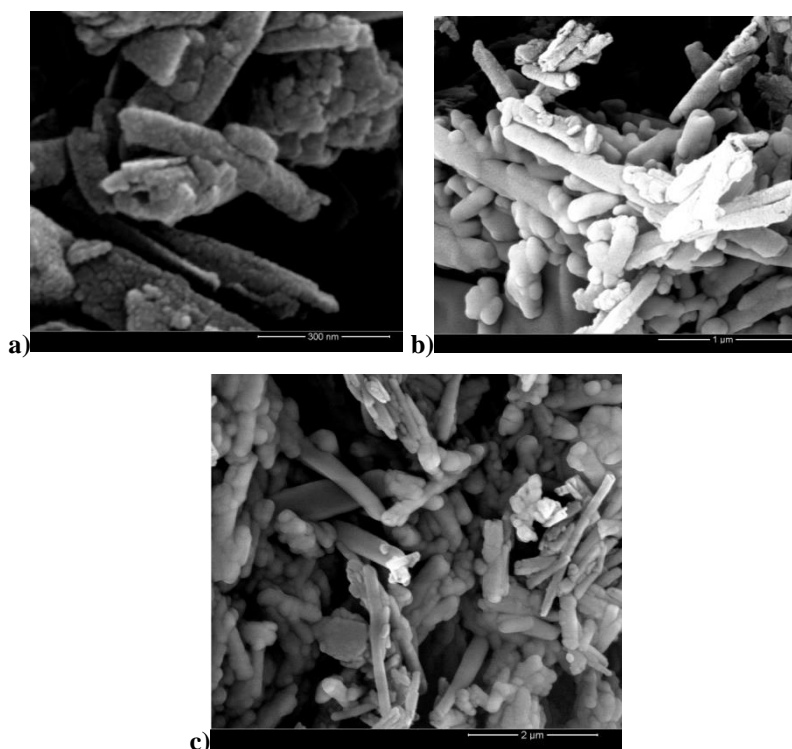
Figure 68. SEM images of **a)** compound **21**; **b)** compound **22a**; **c)** complex **22b**.

Finally, FT-IR spectra of cardanol **11a** and **22a** complex were recorded at room temperature in a spectral region between 4000 and 400 cm^{-1} to further confirm the interaction of cardanol with the outer surface of HNT (Figure 69). **11a** spectrum (Curve b) exhibits, in addition to the characteristic stretching bands of pristine halloysite,[69] the stretching bands of triazolium moiety (Chapter 4). In the spectrum of pure cardanol (Curve c), the broad band at ca. 3300 cm^{-1} is attributed to —OH stretching vibration, the bands at 2957, 2917 and 2850 cm^{-1} correspond to asymmetric and symmetric stretching of the methyl and methylene groups and the bands between 1587 and 900 cm^{-1} derive from stretching and bending of aromatic ring and C—O stretching vibration. All these characteristic bands are present in the spectrum of **22a** (Curve a), which provides direct evidence for the successful loading of cardanol on **11a** surface. Based on the unaltered

frequency of stretching bands of the OH of the inner-surface Al–OH groups, and stretching bands of cardanol, led to conclude that cardanol has been adsorbed only on the external surface of **11a**.
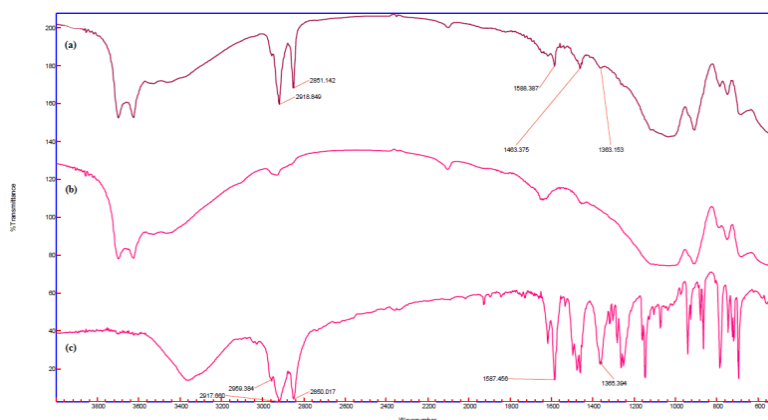
Figure 69. FT-IR spectrum of cardanol, compound **11a** and the complex **22a**.

Also in this, the kinetic *in vitro* release of cardanol from HNT carrier was investigates by means of the dialysis method at 37 °C, under mechanical stirring in physiological media, namely pH 1, 6 and 7.4.

In Figure 70 extended release profile of cardanol from **11a**, in three different pH solution, was elucidated. pH is a key factor influencing the oral drug delivery. It is known that pH is about 1.2– 2.0 in stomach, about 7.0 in small intestine and as high as 8 in the distal part.[50]
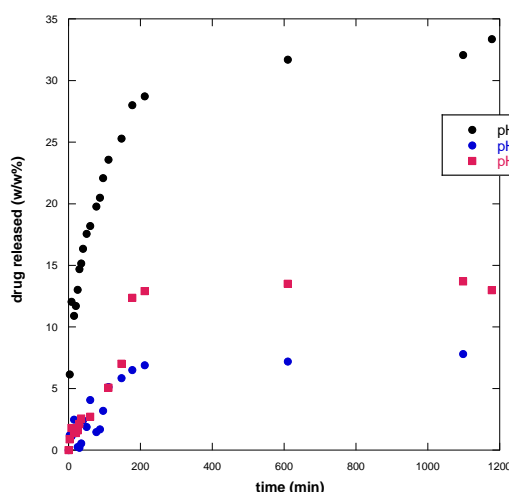
Figure 70. Variation of the release of cardanol from **22a** with pH in the release medium.

The release of cardanol at pH 1 from compound **11a** reaches a plateau after about 250 min, an initial burst is observed within 200 min followed by a prolonged release. Release profiles obtained at pH 6 and pH 7.4 showed a similar behavior than pH 1 but, in both

cases, a smallest amount of cardanol was released from the systems. In order to further study the release behavior of cardanol from **11a** in different pH solution, the in vitro release data were fitted to various models to analyze the kinetics and the release mechanism of cardanol. The experimental data were analyzed using the first-order equation, (*Eq.6*),[70] double exponential model (DEM) (*Eq.7*),[71] Higuchi's square root model (*Eq.8*)[72] and the Power law (*Eq.9*)[73,74] to elucidate the release kinetics of cardanol. The used equations are following listed:

$$F_t = 1 - e^{-kt}$$
Equation 6

$$F_t = F_e^{'}(1 - e^{-k't}) + F_e^{''}(1 - e^{-k''t})$$
Equation 7

$$F_t = kt^{1/2}$$
Equation 8

$$F_t = kt^{n}$$
Equation 9

where F_t is the drug release fraction at time t, k is the release constant of the respective equations, t is the release time and n is the characteristic diffusion exponent. The correlation coefficient (R^2) for Equation 6. is above 0.97 at different pH solution and it is higher than the other kinetics equations (Table 11), suggesting that the release mode of cardanol follows the first-order kinetics. Because cardanol is only adsorbed on HNT outer surface, the overall release process is due to only one desorption step.

Table 11. Kinetic parameters for the release of cardanol

pH	First Order		DEM			Higuchi		Power Fit	
	k_d (min^{-1})	R^2	k_d' (min^{-1})	k_d'' (min^{-1})	R^2	k_d (min^{-1})	R^2	k_d (min^{-1})	R^2
1	0.0088	0.983	0.07	0.0077	0.955	1.88	0.977	7.356	0.899
6	0.0015	0.977	0.0048	0.0045	0.834	0.142	0.959	0.225	0.960
7.4	0.0022	0.985	0.0035	0.0034	0.922	0.431	0.802	0.351	0.969

The same conclusions could be done for the cardanol release from **p-HNT** (Figure 71). Also in this case, the release mode of cardanol follows the first-order kinetics (k_d = 0.00033±0.00002 min^{-1}; R^2 = 0.994).
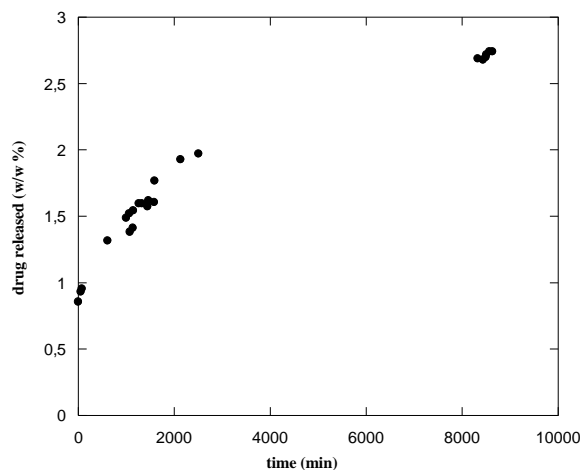
Figure 71. Amount of cardanol released from **21** at pH 1

In order to validate the efficiency of **21** and **22a-b** on cell viability, we tested a panel of 3 tumor cell lines, namely HA22T/VGH, Hep3B, and HepG2. We performed MTS test in order to verify if the complexes are able to exert a cytotoxic action. Cell viability was estimated at 72 h under different cardanol concentrations (in the 1–100 mM range). It was observed that cell viability decreases in a concentration and time dependent way. The effects of Cardanol, **22a** and **22b** complexes on the relative cell viability of Hep3B, HepG2, and HA22T/ VGH cell lines are shown in Figure 72.

 It is remarkable to note that there was no significant reduction in cell viability following incubation with various concentrations of **p-HNT** with all types of cells, indicating that the pristine halloysite carriers had no toxic effects on the cells. When the cells were incubated with f-HNT, on the contrary, we observed a little cytotoxicity against the several cell lines. This is not surprising because we have developed a new system with triazole, which is known to possess biological activity. Free cardanol has no effect on cell viability, probably due to its low solubility in physiological medium, which limits its clinical application.

No cytotoxic effects for the several cell lines in the presence of the complex **19** were observed. The **22a** and **22b** complexes show, at each concentration, a significantly higher cytotoxicity than free cardanol and **21**. The concentrations of **22a** and **22b** which caused 50% inhibition of cell growth are reported in Table 12 for all cell lines. This increase in cytotoxicity compared with free cardanol and **21** complex suggests that the introduction of triazole exerts a synergic effect with cardanol and could improve the permeability of cells in a concentration dependent manner combined with enhanced

aqueous solubility of **22a** and **21b**. In effect, a cationic surface promotes the interaction between the nanoparticles and the cells and hence increases the rate and extent of internalization.[75] The internalization mechanism presumably involves an endocytosis process, whereby **11a-b** could be uptaken into the cytosol by endosomes.[55]
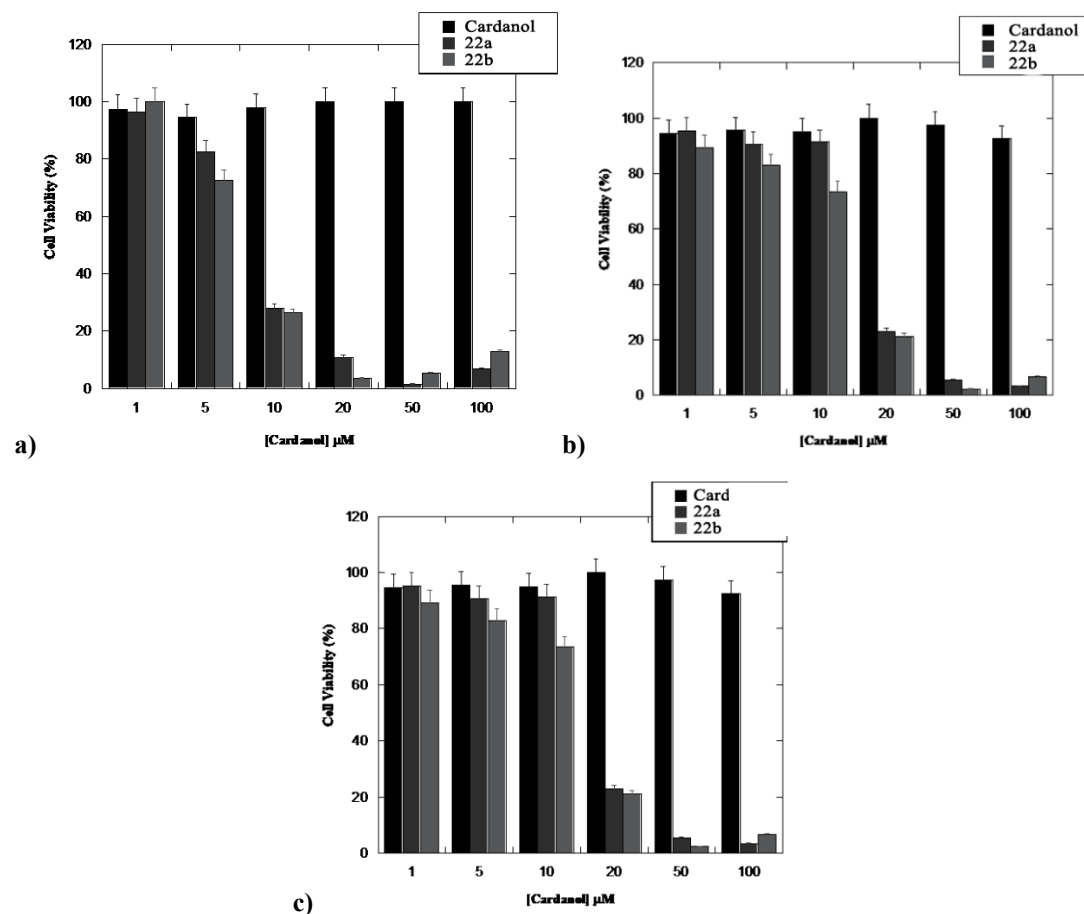
Figure 72. Cytotoxic effects of cardanol, **22a** and **22b** on **a)** hep3B; **b)** hepG2 and **c)** HA22T/VGH cells determined by MTS assay.

Table 12. IC50 of **22a** and **22b** for the three cell lines.

Complex	Cell line	IC$_{50}$ (µM)
22a	HA22T/VGH	18 ± 6
	Hep3b	8 ± 1
	HepG2	27 ± 5
22b	HA22T/VGH	17 ± 7
	Hep3b	7 ± 3
	HepG2	25 ± 12

5.4. *Multicavity halloysite–amphiphilic cyclodextrin hybrids for co-delivery of natural drugs*

The novel hybrid based on HNTs covalently linked to amphiphilic-cyclodextrin units (Compound **5**) results promising as a carrier for biologically active molecules, since it possesses two cavities, the halloysite lumen and the hydrophobic cyclodextrin cavity. The advantages of multifunctional nanocarriers with the presence of two cavities, indeed, offers the remarkable possibility for a simultaneous encapsulation of one or more drug molecules with different physicochemical properties, followed by a different path release in agreement with the cavity that interacts with the drugs. Therefore, in order to employ the new system as a drug carrier, it is studied its simultaneous interaction with two molecules, namely quercetin and silibinin, that possess different sizes and shapes.

Co-delivery has attracted more and more attention because it is known that compared to conventional single-agent treatment, multi-agent therapy can promote synergism of different drugs, increases therapeutic target selectivity, and overcomes drug resistance through distinct mechanisms of action.[76–78]

Furthermore, polyphenolic compounds, like silibinin and quercetin, that are ubiquitously distributed in plants have attracted considerable interest due to their wide variety of biochemical and pharmacological properties.[79,80] Unfortunately, their concentration in the blood circulation is likely to be low because they are sparingly soluble in water and chemically unstable in physiological medium.[81–83]

Before to start the study about the interaction of the two drugs with the hybrid halloysite-cyclodextrin, it is noteworthy to study the interaction of the two flavonoids with the pristine components. Experimental investigations performed by means of *UV-vis* and HPLC highlighted that silibinin did not interact with the cyclodextrin cavity, in contrast, it was encapsulated into the pristine HNT lumen as found by *UV-vis* spectroscopy and TGA.

Similarly to that done with curcumin, the *UV–vis* spectra of dispersion of **p-HNT**/Silibinin in aqueous solution, at 25 °C and at a fixed concentration of silibinin (1×10^{-4} M) in the presence of increasing amounts of **p-HNT** (0–1×10-3 g/mL) were recorded. The occurrence of the interaction was evaluated by measuring the absorbance at the maximum absorption wavelength of the silibinin (325 nm). Typical trends are depicted in Figure 73.
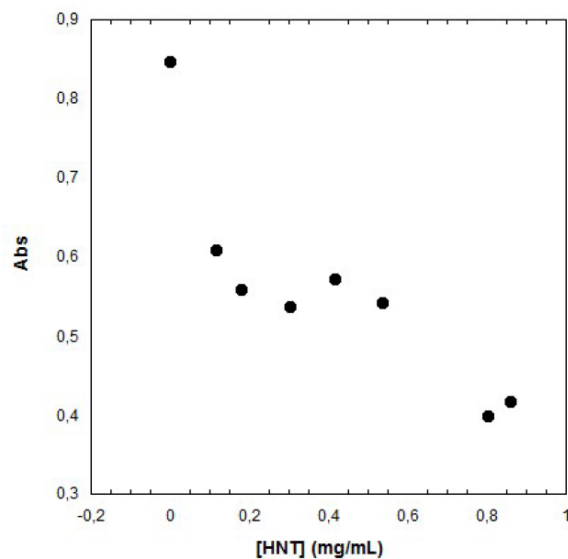
Figure 73. Trend of the absorbance of the silibinin (1×10^{-4} M) as a function of **p-HNT** concentration (0–1×10^{-3} g/mL).

The absorbance value decreases with increasing of **p-HNT** concentration. Moreover, after interaction with **p-HNT**, the **p-HNT**/Silibinin complex **23** has a peak at the same absorption wavelength as free silibinin. These findings suggest that silibinin has been successfully encapsulated into the HNT lumen.

It is interesting to observe from TGA data that the silibinin encapsulated in **p-HNT** shows a higher degradation temperature (314 °C) as compared to the pure compound (294 °C). This striking enhancement of the thermal stability can be due to encapsulation of the degradation products into the nanotube lumen (Figure 74).
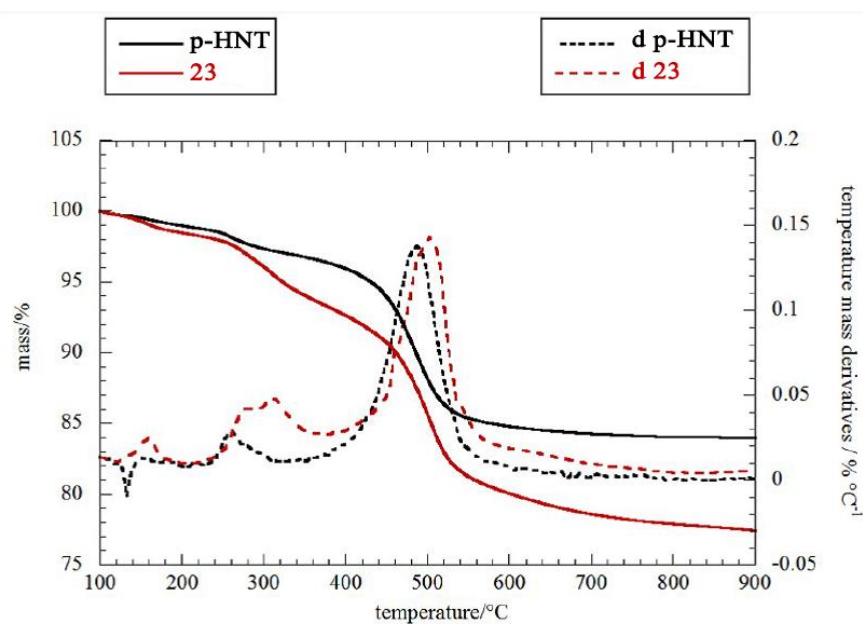
Figure 74. Thermoanalytical curves for **p-HNT** and **23** complex.

It is reported that native β–CD is efficient in including quercetin.[84] In order to verify that the CD modification does not hinder the quercetin inclusion, supramolecular interactions with amphiphilic CDs (having the same substitution pattern of **5a**) have been studied. The formation of 1:2 quercetin/amph-CD complexes has been demonstrated by isothermal titration calorimetry (ITC) and *UV-vis* spectroscopy. The ITC data provided the equilibrium constant and the enthalpy change for the quercetin–amph-CD inclusion complex formation by assuming the equilibria:

$$CD + Que \overset{K_1}{\underset{\leftarrow}{\rightarrow}} CD - Que$$

$$CD - Que + CD \overset{K_2}{\underset{\leftarrow}{\rightarrow}} CD - Que - CD$$
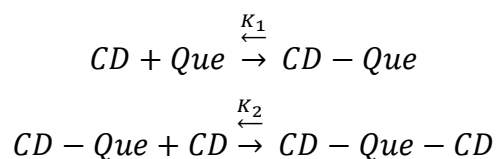
And the procedure reported elsewhere.[85]

It was found $\beta = K_1 \times K_2 = (6.3 \pm 0.3) \times 10^5 \ M^{-2}$ and $\Delta H_{ic} = 7.1 \pm 0.3 \ kJ \ mol^{-1}$, according to *UV-vis* results ($\beta = (9 \pm 2) \times 10^5 \ M^{-2}$).
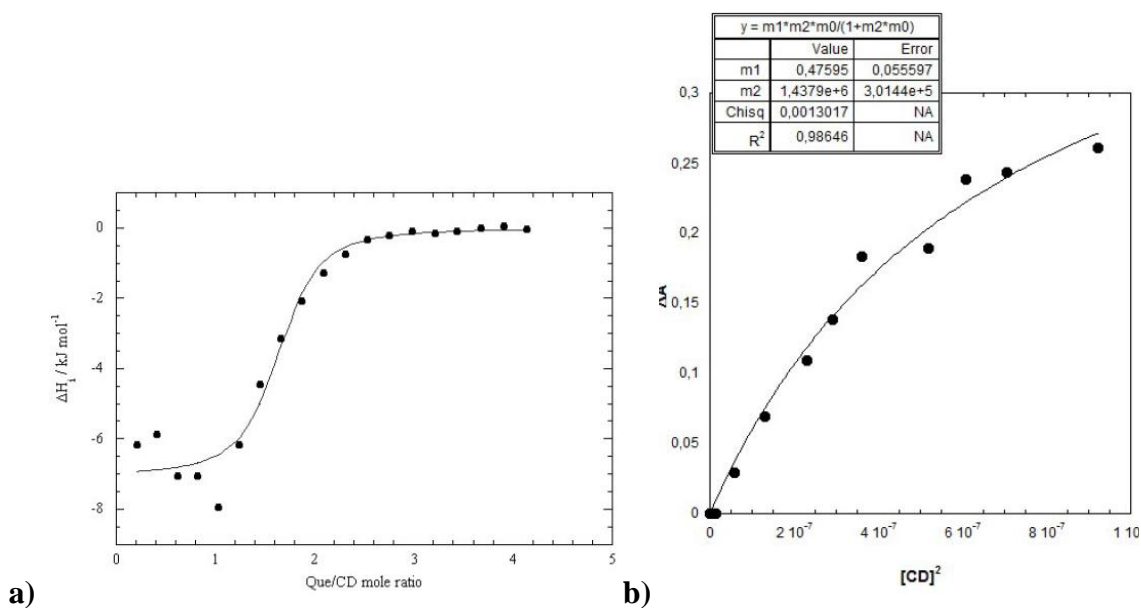
Figure 75. a) ITC titration curve; **b)** Curve fitting analysis of *UV-vis* spectral titration of quercetin with amph-CD in phosphate buffer solution at pH 6.9.

Furthermore, fluorescence titration showed that this molecule also interacts with pristine HNTs. In Figure 76 is shown the trend of the fluorescence intensity of quercetin at 540 nm, as a function of pristine HNT concentration (0-1.5 mg/L). The emission of quercetin, related to the supernatant solution, decreases on increasing of **p-HNT** concentration (Figure 76a). Moreover, after interaction with **p-HNT**, the **p-HNT**/Quercetine (**24**) has a peak at the same emission wavelength as free quercetin. These

117

findings suggest that quercetin has been successfully encapsulated into the HNT lumen, as we have previously reported for curcumin.
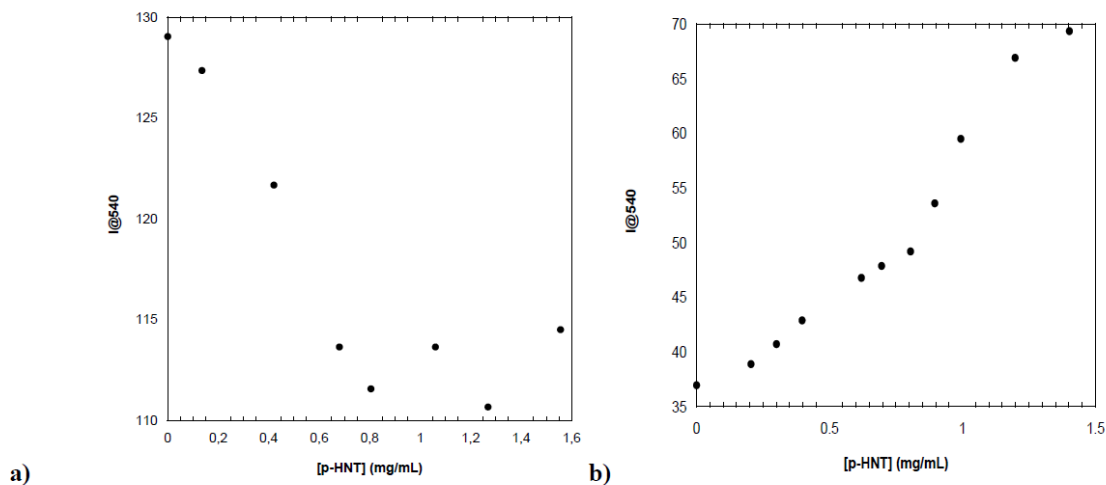
Figure 76. Trends of the fluorescence intensity of quercetin, recorded at 540 nm, as a function of **p-HNT** concentration (0-1-5 mg/mL) related to a) supernatant solution; b) dispersions after sonication.

Recording the fluorescence intensity of the dispersions after sonication, we obtained the trend shown in Figure 76b. in this case as a consequence of the more hydrophobic inner HNT surface than the surrounding medium, we observed an increase in the emission of quercetin on increasing of HNT concentration.

It was demonstrated that in the presence of HNT–cyclodextrin hybrids, curcumin, a biological molecule with a similar structure to quercetin, interacts preferentially with the cyclodextrin cavity.[35] On the ground of this evidence, we studied the interaction of **5a** with silibinin and quercetin by HPLC and fluorescence spectroscopy. According to previous reports,[86] pure silibinin showed two peaks in the HPLC chromatogram, corresponding to the diastereoisomers silibinin A and B, with retention times (rt) of 2.67 and 3.53 minutes, respectively (eluent MeOH/H_2O 90:10 v/v, flow 1 mL min^{-1}). The most abundant component displayed two bands in the UV spectrum, the first one at 280 nm and the second one, less intense, at ca. 320 nm. Pure quercetin showed one peak in the chromatogram at rt of 3.38 min and it showed an UV spectrum with two bands at 250 and 370 nm. No peaks were observed in the chromatogram related to **5a** because this material showed no UV absorption. Titration of fixed concentrations of silibinin and quercetin with **5a** (0–1.8 mg mL^{-1}) gave chromatograms (eluent MeOH/H_2O 90:10 v/v, flow 1 mL min^{-1}) which illustrated an unresolved broad peak at the range between 3.00 and 3.50 min, and presented a UV spectrum showing the same absorption maxima of silibinin. However, with the increasing amount of **5a,** the UV spectrum displays a drastic change in the intensity of the signal at 320 nm (Figure 77).
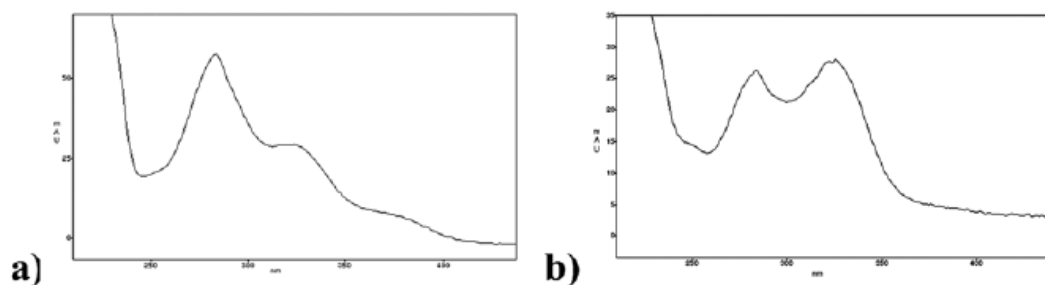
Figure 77: *Uv-vis* spectra of a) silibinin and b) **5a**-silibinin complex

It is known that dihydroflavonols show two major absorption bands: band I (300–400 nm) and band II (240–280 nm).25 Band I originates due to the light absorption of the A + C rings and corresponds to a π–π* transition; band II is due to the absorption of the B ring. Therefore, because in our systems we have hypothesized that silibinin interacts with **5a** lumen, the different UV electronic absorption behavior may be attributed to specific Sil–**5a** interactions in the form of hydrogen bonds and/or hydrophobic effects that involve phenolic OH groups of A rings. Similar results were obtained by Angelico *et al*. for the encapsulation of silibinin into liposomes.[87] Being that silibinin in aqueous medium does not show emission, the interaction of quercetin and **5a**, in contrast, was studied by means of fluorescence spectroscopy. The trend of fluorescence intensity of quercetin (1×10^{-4} M), recorded at 540 nm, with the increasing amount of **5a** (0–1.5 mg mL^{-1}) is reported in Figure 78. This trend, related to the supernatant of the dispersions, is close to that obtained in the presence of crude amph-CD. Based on this finding and on the strong interaction evidenced by ITC and *UV-vis* between Que and amph-CD, one may hypothesize that quercetin interacts preferentially with the cyclodextrin cavity (Figure 78). Similarly, curcumin, a hydrophobic drug, was selectively encapsulated into the CD instead of the hydrophilic HNT cavity.11 Loading silibinin into **5a** (compound **25**) was carried out by vacuum cycling of a **5a** suspension in a saturated silibinin solution. This cycle was repeated several times in order to obtain the highest loading efficiency. After loading, the **25** complex was washed in order to remove the free silibinin. **25** was suspended again in water and then to this dispersion a saturated solution of quercetin was added. Subsequent investigations were conducted on the dry solid filtered from the dispersion (**26**), washed with water and dried overnight at 60 °C.
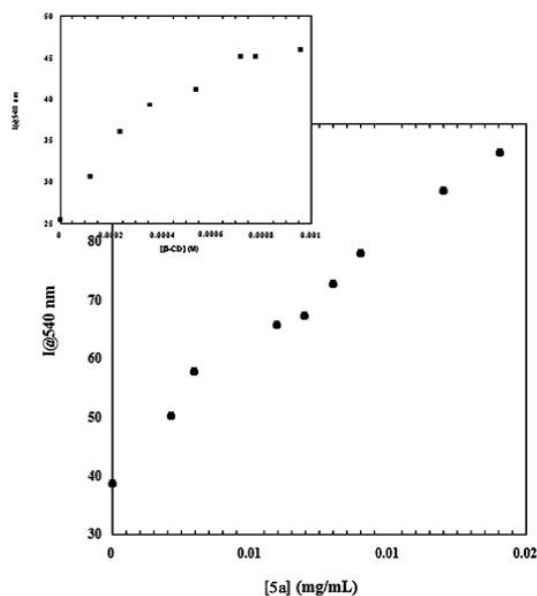
Figure 78. Trend of the fluorescence intensity of quercetin, recorded at 540 nm, as a function of **5a** concentration (0–1.8 mg mL^{-1}) in the presence of a fixed amount of silibinin (1×10^{-4} M); the inset shows the fluorescence intensity of quercetin in the presence of increasing amounts of β-CD.

The composite solids **25** and **26** were characterized by TGA (Figure 79). The thermoanalytical curves clearly show the successful loading of the drugs at each step. Given that both silibinin and quercetin degraded with a null residual at 900 °C, we calculated that compound **5a** can incorporate 6.1 wt% of silibinin and 2.2 wt% of quercetin. These results prove that the modified HNTs with a double cavity are efficient as nanocontainers for the co-delivery of two biologically active molecules.
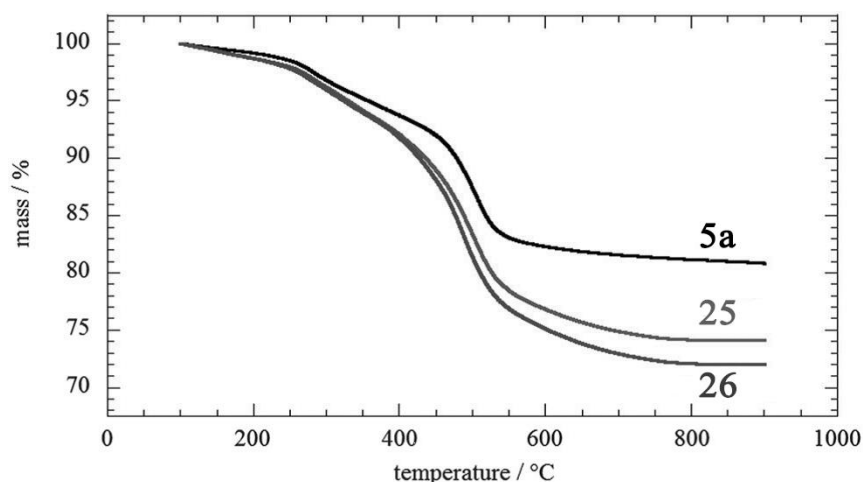
Figure 79. Thermoanalytical curves for **5a** before and after drug loading.

In Figure 80, an extended release profile of silibinin and quercetin from **5a**, in two different pH solutions, is shown. The release of silibinin at pH 1 from compound **3a** reaches a plateau after 400 min, and an initial burst is observed within 200 min followed by a prolonged release. The release profile obtained for quercetin showed a similar

behavior to silibinin, but in this case, a very low amount of molecule was released from the system (Figure 80a). These results could be explained as follows. In acidic solution both **5a** and silibinin are positively charged; therefore, electrostatic repulsions may also accelerate the release of the drug from **5a**. In the case of quercetin, it was reported that the retention efficiency of Que on β-CD is dependent on the pH, in particular, it was larger in acidic solution than in neutral and basic media.[88] Therefore, the small amount of quercetin released from **5a** at pH 1 could be explained on the basis of strong interaction of the molecules and the CD cavity in acidic medium. In physiological medium, we observed that both molecules were released from the system; also, in this case, quercetin was released in a smaller amount than silibinin. The different release in a neutral medium could be explained by taking into account that flavonoids are in their neutral form in a pH range between 4 and 6; therefore at physiological pH they could be partially dissociated and so more soluble in aqueous medium. To better understand the release behavior of silibinin and quercetin in different pH situations, the in vitro release data were fitted to various models to analyze the kinetics and the release mechanism of both molecules. The experimental data were analyzed using the zero-order and first-order equation, the double exponential model (DEM) and the Power law, to elucidate the release kinetics of silibinin at pH 1 and 7.4 and of quercetin at pH 7.4. It was found that the release mode of silibinin in acidic solution follows the double exponential model. According to the literature,[89] the DEM describes a mechanism consisting of two parallel reactions involving two spectroscopically distinguishable species. In our particular case, we observed the release of silibinin and the simultaneous, even if it is very low, the release of quercetin ($k = 0.007\pm0.001$ min^{-1} and $k_0 = 0.064\pm0.006$ min^{-1}). In physiological medium, the release mode of silibinin and quercetin follows, in both cases, the first-order kinetics ($k = 0.0017\pm0.0001$ min^{-1} and 0.0007 ± 0.0001 min^{-1}, for silibinin and quercetin, respectively). Desorption of silibinin and quercetin from **26** can be described as the desorption of the molecules encapsulated into the HNT lumen and into the β-CD cavity, respectively.
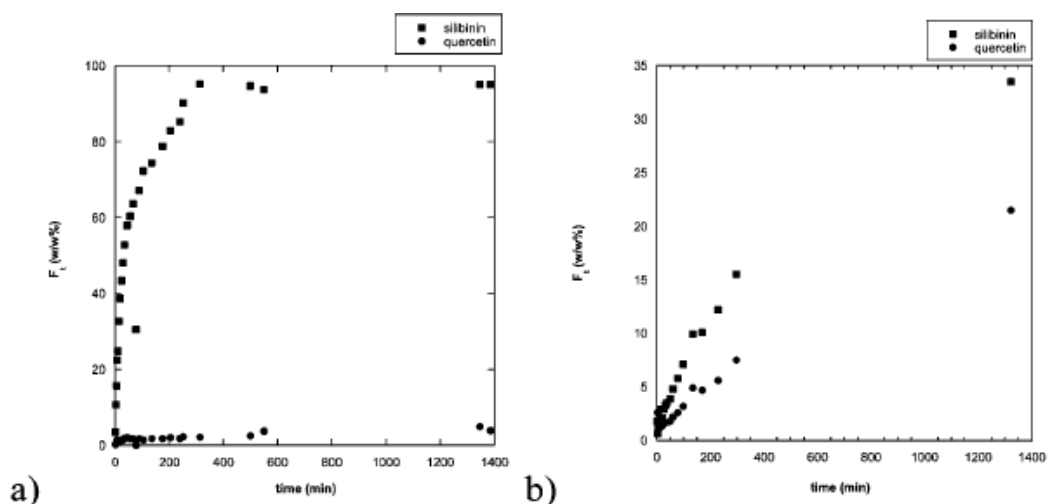
Figure 80. Amount of silibinin and quercetin released from **5a** in (a) 0.1 M HCl solution; (b) pH 7.4 phosphate buffer.

The potential anti-proliferative *in vitro* activity of the **26** complex was tested on an anaplastic thyroid cancer cell line: 8505C by means of MTS tests. The survival rates of the tumor cells incubated with **5a** at each concentration were found in the range of 96–100%, indicating that they have no effect on the cell viability of the tumor cell lines under the concentration conditions investigated. Free quercetin and silibinin have no effect on cell viability, probably due to their rapid metabolism, systemic elimination, and insolubility in physiological medium. In contrast, the cell line showed a dose dependent cytotoxic profile when subjected to the treatment of **26** (Figure 81). In particular, the concentration of **26** which caused 50% inhibition of cell growth was 27.6±6.1 mM. Compared to the free drugs, the HNT nanoparticles significantly improved the cellular cytotoxicity and exhibited the obviously synergistic effect by the co-delivery of two different anticancer drugs, silibinin, and quercetin.
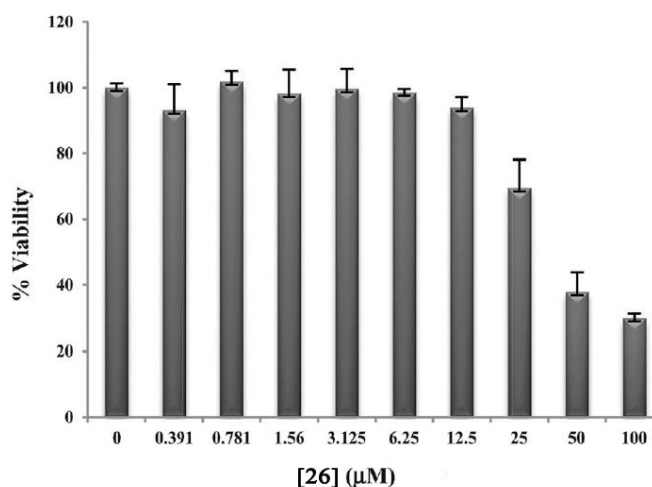
Figure 81. MTS test for the cell viability of 8505C cells cultured for 72h in the presence of **26**.

In the light of the potential application of **26** as the novel therapeutic treatment, several tests have been carried out in vitro to evaluate their uptake and localization into 8505C thyroid cancer cell lines. Indeed, for the internalization of nanoparticles by tumor cells it is essential to liberate therapeutic agents into the cytosol where most therapeutic agents accumulate and exhibit the effect. For this purpose, we analyzed, by means of fluorescence microscopy, the interaction between cells and the carrier. Fluorescence microscopy data revealed that **5a** showed a high propensity to cross cell membranes resulting in a massive cell uptake, as highlighted by the fluorescence emission localized in the cytoplasm. In particular, halloysite nanoparticles penetrate into the cells and concentrate around the cell nucleus from the observation of the silibinin fluorescence signal (green) within cells (Figure 82). The results suggested that the **26** complexes could be effectively transported into living cells.
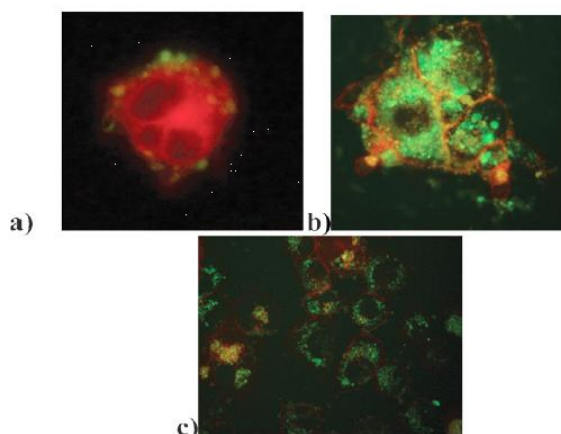
Figure 82. Fluorescence microscopy images of the **5a** uptake by 8505C. 8505C cell membrane (red)with co-localised **5a** (green) outside nuclei at **a)** 1h and (**b** and **c**) 24h.

5.5. Halloysite-cyclodextrin nanosponges as efficient carrier systems for antifungine drugs

Over the past two decades, urogenital infections have become a major public health concern affecting pre-menopausal women worldwide.[90] The most common recurring infection is due to opportunistic fungal pathogen responsible of Candidiasis. Specifically, Candidiasis is caused by the invasion of the tissues by a microbiota naturally occurring in the humans, in particular on the skin, mouth, throat, stomach, colon, rectum and vagina. The fungus that caused Candidiasis may belong to 150 different species and among them the most involved are: C. *albicans*, C. *glabrata*, C. *parapsilosis*, C. *tropicalis* and C. *krusei*. This disease often occurs in immunocompromised individuals, such as people

subjected to treatment with certain medications, for example, antibiotics, or such as people with pathological states, such as diabetes, AIDS or cancer. It was found that more than 25% of the world's population suffers of a form of mycoses.[91]

Clotrimazole is one of the most important drugs used for the treatment of Candidiasis both oral and vaginal.[92] Generally, this drug is administered by means of several dosage forms such as ovules and cream for vaginal treatment or inserts, lotion, and solutions for the oral one. Unfortunately, clotrimazole suffers from low aqueous solubility (~0.5 mg/L) and a short plasma half-life (3–6 h),[92–96] which, in combination with hepatic toxicity and neurologic disorders,[97] make the pharmacological application of CLT very difficult. Therefore, the development of new delivery systems for this drug is the major concern as far as is concerned the preparation of novel formulations for Candidosis treatment. In the years some studies have been focused on the development of systems able to overcome the CLT low solubility, improving its bioavailability. Clotrimazole molecules were successfully incorporated in mucoadhesive gels, liposomes and niosomes,[98] microemulsions,[99] microemulsion-based gels[96] and inclusion complexes with β-cyclodextrin.[100]

The HNT-CD nanosponges hybrid were employed for loading and release of clotrimazole and, with the final goal to apply the nanomaterials for Candidosis treatment. The nanosponges were further modified with cysteamine hydrochloride molecules, that allow the introduction of a positive charge that should be crucial for improve mucohadesivity.

HNT-CD compound **3** was reacted with an excess of cysteamine hydrochloride by irradiation with UV light, from the Hg lamp, using methanol as solvent, in quartz vials at room temperature under an argon atmosphere. After 18 h, the solid was filtered off, washed several times with MeOH and CH_2Cl_2 and dried at 80 °C overnight (Scheme 9).
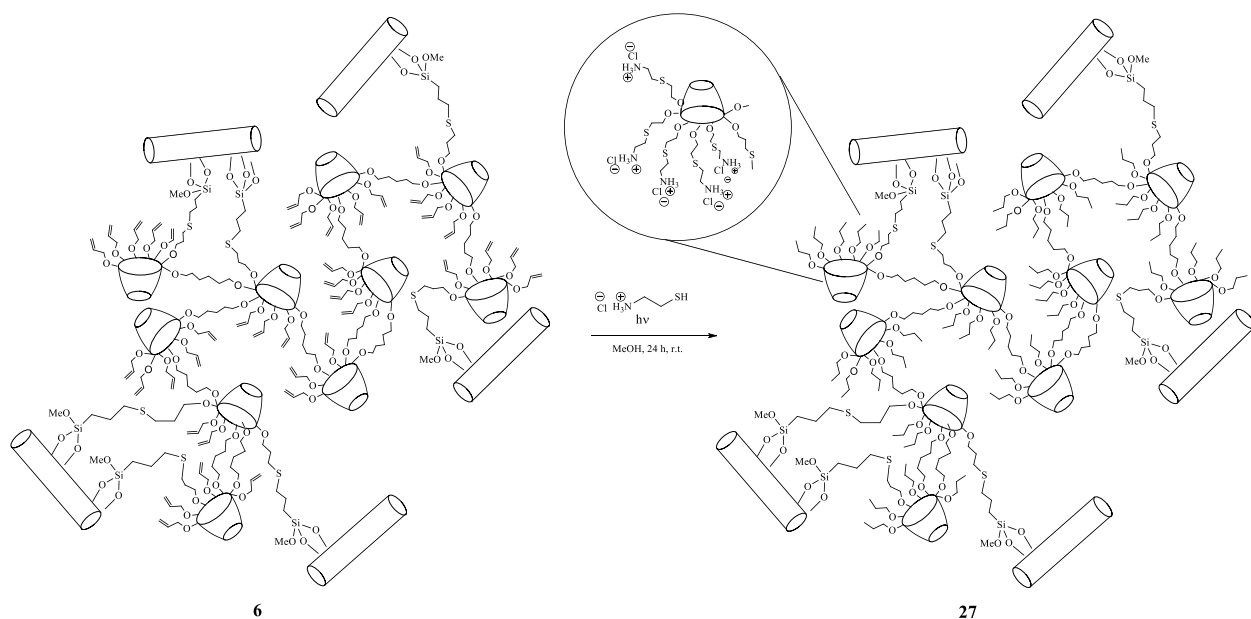
Scheme 9. Schematic representation of the synthesis of compound **27**

The obtained nanomaterial was analyzed by TGA in order to evaluate the percentage of the loading, that was ca. 1 wt%. By comparing the thermogravimetric analysis of compound **27** and **3** it is observed that the cysteamine moieties are degraded in the temperature range between 200 to 250 °C being the first degradation step of the hybrid material (Figure 83).
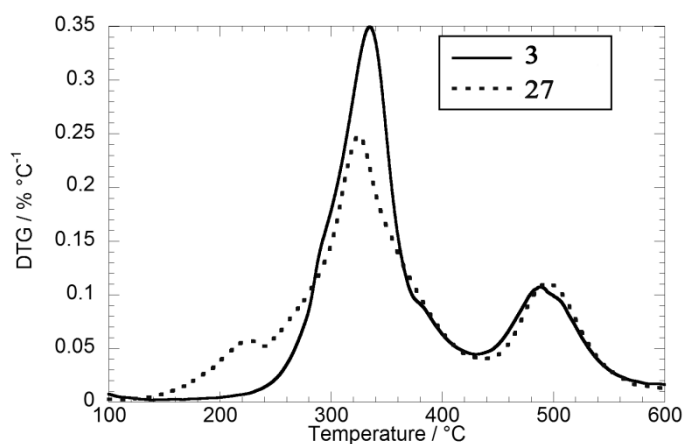
Figure 83. DTG of compound **3** and compound **27.**

Compared to pristine **p-HNT**, the **3** and **27** nanomaterials exhibit the vibration bands for C−H stretching of methylene groups around 2980 cm^{-1} and a broad and wide band around 3000 cm^{-1} due to the −OH groups of cyclodextrin (Figure 84). These findings provide evidence for the presence of organic moieties in the new material. After reaction

with cysteamine, new signals appeared in the FT-IR spectrum of the final nanomaterial. In particular is clearly evident the band at ca. 1740 cm^{-1} that corresponds to the vibration stretching band of NH_3^+ groups. The presence of protonated amine group generates an alteration of the HNT surface charge. Namely, the ζ-potential value of -19 mV observed for pristine HNT is moved to **-**13.30 mV for compound **17**.
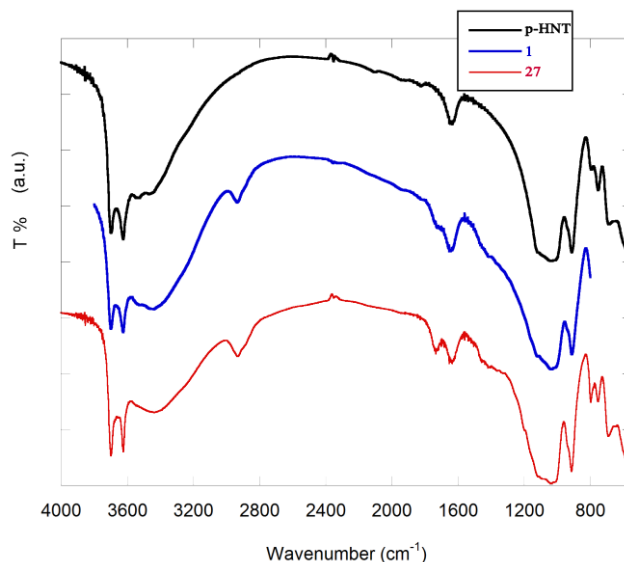
Figure 84. FT-IR spectra of **p-HNT**, compound **1** and compound **27**.

As far as is concerned the interaction of clotrimazole with the nanosponge, as it was seen before, first of all, preliminary studies were performed in order to investigate on the interaction of the clotrimazole drug with the single component of the organic/inorganic component of the hybrid (compound **27**). The interaction with cyclodextrin moiety was studied in solid state by means of differential scanning calorimetry and in aqueous solution by *UV-vis* measurements.

The DSC technique can be used as a tool to evidence the inclusion of molecules into the CD cavities.[101] Accordingly, the melting peak of a give substance disappears when the inclusion complex with CD is formed because the crystallinity is lost. Clotrimazole shows a melting peak in the DSC trace at 148.6 °C with an enthalpy of melting (ΔH_m) of 193 kJ mol^{-1}. From the DSC data on solid CD/clotrimazole mixtures, the fraction of drug not forming inclusion complex can be obtained from the crystallinity degree as $X_{FREE}=\Delta H_{mix}/\Delta H_m$, being ΔH_{mix} the measured enthalpy per mole of clotrimazole in the mixture, provided that CD does not exhibit any signal in this temperature domain. Figure 85 shows the X_{FREE} values as a function of the CD: Clotrimazole mole ratios for solid mixtures prepared by drying out under vacuum overnight an aqueous solution after equilibration for one week under stirring. It should be noted that an excess of clotrimazole

which possesses a certain crystallinity is always present being not included into the CD cavity even in large excess of CD. This results clearly indicates that the complex formation is not quantitative but an equilibrium between encapsulated and free drug is present. Time dependence of the inclusion phenomenon was investigated by stirring the aqueous CD+clotrimazole mixture (at CD: Clotrimazole mole ratios of 2.8) for different times before vacuum drying. The X_{FREE} vs time results show a relatively slow inclusion kinetics, which takes 3000 min to reach a constant inclusion fraction.
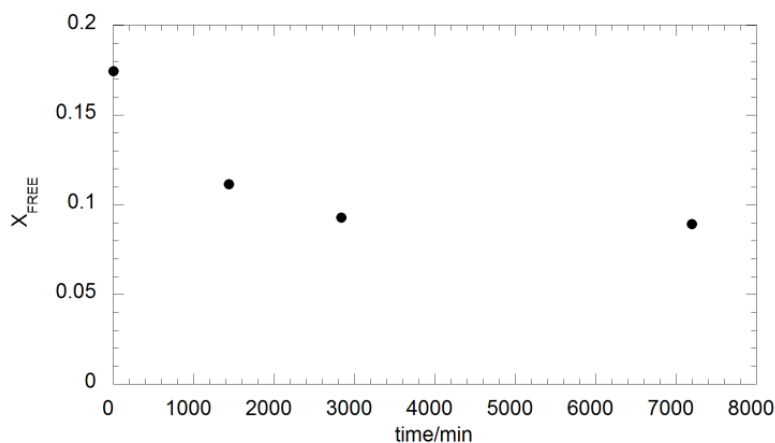
Figure 85. Plot of the X_{FREE} vs time.

UV-vis experiments showed that the clotrimazole molecule interacts with the hydrophobic cyclodextrin cavity, forming 1:1 and 2:1 complexes with a binding constant of $(7\pm1)\cdot10^6\,M^{-2}$.

Halloysite presents a positively charged inner lumen and negative charge on its external surface. Therefore, in order to deep investigate the mechanism involves in clotrimazole adsorption into the clay we studied the interaction of the drug at different pH values, i.e. pH 1.0 and 7.4. These values were chosen since clotrimazole possesses a pK_a value of 5.83, so the drug could be present in its cationic or neutral form. In Figure 87 is reported the equilibrium amount of drug adsorbed into the clay (Qe, mol g^{-1}) as a function of the equilibrium clotrimazole concentration in solution (Ce, mol L^{-1}) at pH 1.0 and 7.4.
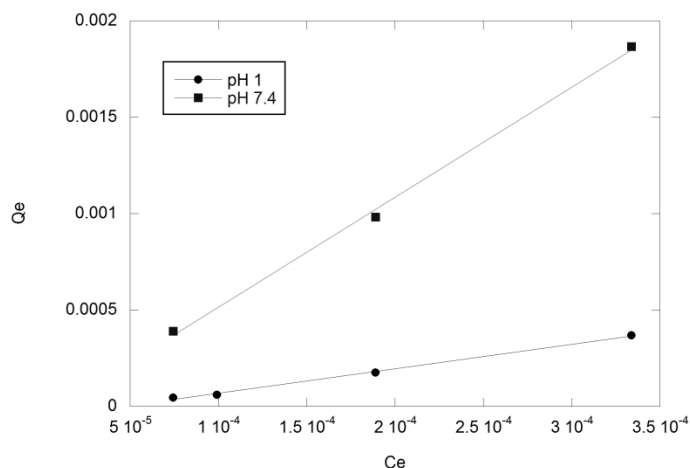
Figure 86. Adsorption isotherms of CLT on compound **27** in HCl 0.1N and phosphate buffer pH 7.4.

The adsorption data were analyzed by the Freundlich model. The obtained results are reported in Table 13; as it shown the clotrimazole adsorption is better in acidic medium than physiological conditions.

Table 13. Parameters of Freundlich isotherm model for CLT adsorption on compound **2**.

	$Q_e = K_F C_e^{1/n}$		
pH	**K_F** **(mol g^{-1} (mol L^{-1})$^{1/n}$)**	***n***	**R^2**
1.0	25±12	1.39±0.06	0.998
7.4	0.07±0.06	0.4±0.1	0.926

The loading of clotrimazole into compound **27** was carried out by mixing the hybrid compound with a methanolic highly-concentrated clotrimazole solution. Then, the obtained suspension was stirred and kept under vacuum for 3-5 min resulting in light fizzling, which indicated that air is removed from the tubes.[102] Once that the vacuum was removed, solution entered into lumen and the loaded compound condensed within the tube. This procedure was repeated 2–3 times to improve the loading efficiency. After loading, the obtained complex **28** was washed with water in order to remove free drug (Scheme 10).
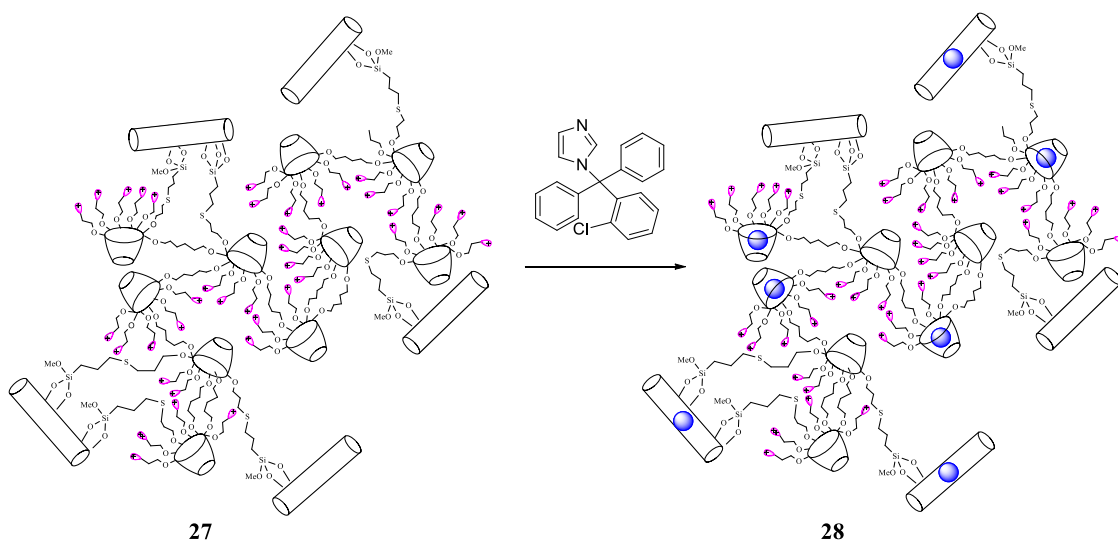
Scheme 10. Schematic representation of the CLT loading on compound **27** in order to obtain **28.**

The hybrid **28** was characterized by TGA (Figure 87). After the subtraction of the signal from the hybrid 2, the DTG profile corresponds to that of pristine drug. The corresponding 5.4 % CLT loading was obtained from TGA.
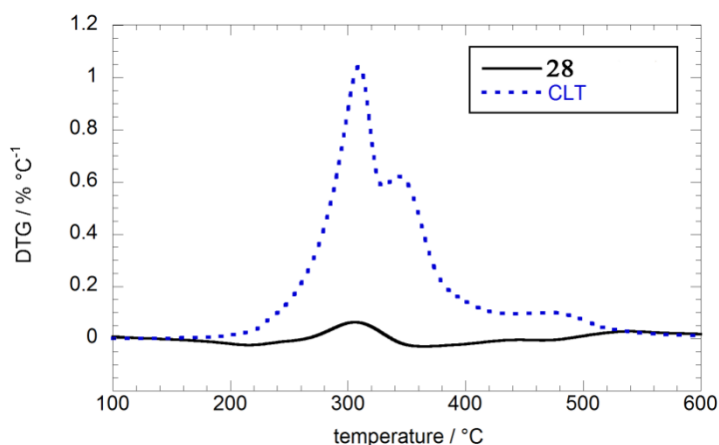
Figure 87. Differential thermogravimetric curves of CLT and hybrid **28** after hybrid **27** signal subtraction.

Finally, the release of clotrimazole loaded in **27** was evaluated by the dialysis bag method using conditions designed to mimic physiological conditions (phosphate buffer pH 7.4) and the obtained kinetic data are shown in Figure 88. The release of clotrimazole was found to be slow and sustained with ~60% drug released after 150 min while the clotrimazole molecules encapsulated into pristine HNT lumen showed a complete release after 30 min only. Therefore, the introduction of cyclodextrin moieties was crucial to obtain a sustained release of the antifungine within time. Although the conditions adopted in the *in vitro* release test do not represent all aspects of the physiological conditions; the experimental data collected suggest that the halloysite hybrid could promote a prolonged

release of clotrimazole in the buccal region, which could benefit antifungal therapy. Since no *burst* release of drug was noted, it is possible to conclude that the totality clotrimazole is encapsulated in both HNT lumen and cyclodextrin cavity, further confirming that the drug molecules are not physically adsorbed on HNT surface.

The kinetic data obtained were analyzed by the Korsmeyer-Peppas model in order to deep investigate the release behavior of clotrimazole. The results showed that the data are well fitted by this model (R^2=0.979) with a $k = 4.3 \pm 1.1$ min^{-1} and $n = 0.55 \pm 0.5$, indicating that the release of clotrimazole from the hybrid is governed by Fickian diffusion mechanism.
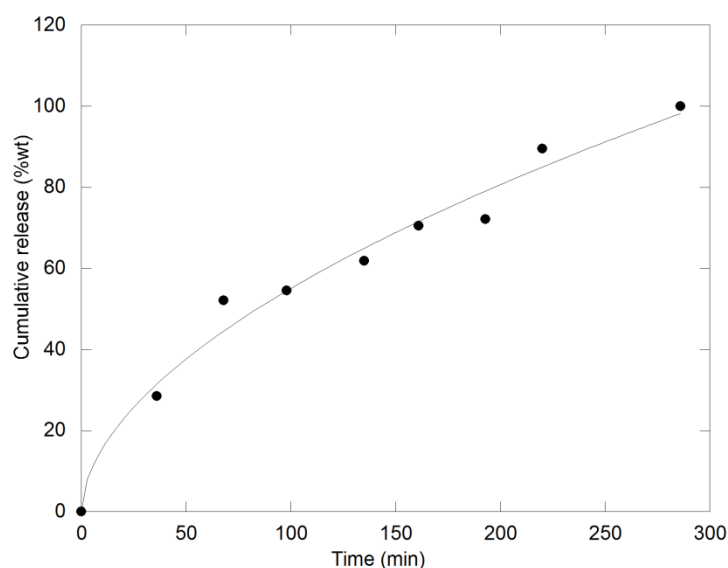
Figure 88. Amount of CLT released from **28** in pH 7.4 phosphate buffer/Tween$^{®}$20 1% solution.

References

(1) Xia, Y.; Xiong, Y.; Lim, B.; Skrabalak, S. E. *Angew. Chemie Int. Ed.* **2009**, *48* (1), 60.

(2) Peer, D.; Karp, J. M.; Hong, S.; Farokhzad, O. C.; Margalit, R.; Langer, R. *Nat. Nanotechnol.* **2007**, *2* (12), 751.

(3) Aguzzi, C.; Viseras, C.; Cerezo, P.; Salcedo, I.; Sánchez-Espejo, R.; Valenzuela, C. *Colloids Surfaces B Biointerfaces* **2013**, *105*, 75.

(4) Steichen, S. D.; Caldorera-Moore, M.; Peppas, N. A. *Eur. J. Pharm. Sci.* **2013**, *48* (3), 416.

(5) Zeng, J.; Huang, H.; Liu, S.; Xu, H.; Huang, J.; Yu, J. *Colloids Surfaces B Biointerfaces* **2013**, *105*, 120.

(6) Huma, F.; Akhter, Z.; Zafar-Uz-Zaman, M.; Yasin, T. *J. Appl. Polym. Sci.* **2013**, *128* (1), 444.

(7) Pal, K.; Behera, B.; Roy, S.; Sekhar Ray, S.; Thakur, G. *Soft Mater.* **2013**, *11* (2), 125.

(8) Ma, Y.; Liang, X.; Tong, S.; Bao, G.; Ren, Q.; Dai, Z. *Adv. Funct. Mater.* **2013**, *23* (7), 815.

(9) Ito, Y.; Arai, H.; Uchino, K.; Iwasaki, K.; Shibata, N.; Takada, K. *Int. J. Pharm.* **2005**, *289* (1–2), 69.

(10) Jain, S. K.; Awasthi, A. M.; Jain, N. K.; Agrawal, G. P. *J. Control. Release* **2005**, *107* (2), 300.

(11) Mizushima, Y.; Ikoma, T.; Tanaka, J.; Hoshi, K.; Ishihara, T.; Ogawa, Y.; Ueno, A. *J. Control. Release* **2006**, *110* (2), 260.

(12) Martucci, A.; Pasti, L.; Marchetti, N.; Cavazzini, A.; Dondi, F.; Alberti, A. *Microporous Mesoporous Mater.* **2012**, *148* (1), 174.

(13) Horcajada, P.; Márquez-Alvarez, C.; Rámila, A.; Pérez-Pariente, J.; Vallet-Regí, M. *Solid State Sci.* **2006**, *8* (12), 1459.

(14) Dawson, J. I.; Oreffo, R. O. C. *Adv. Mater.* **2013**, *25* (30), 4069.

(15) Carretero, M. I.; Pozo, M. *Appl. Clay Sci.* **2010**, *47* (3–4), 171.

(16) Carretero, M. I.; Pozo, M. *Appl. Clay Sci.* **2009**, *46* (1), 73.

(17) Roozbahani, M.; Kharaziha, M.; Emadi, R. *Int. J. Pharm.* **2017**, *518* (1–2), 312.

(18) Jain, S.; Datta, M. *Appl. Clay Sci.* **2015**, *104*, 182.

(19) Bouhekka, A.; Bürgi, T. *Appl. Surf. Sci.* **2012**, *261*, 369.

(20) Huang, G.; Chen, S.; Liang, H.; Wang, X.; Gao, J. *Appl. Clay Sci.* **2013**, *80–81*, 433.

(21) Della Porta, V.; Bramanti, E.; Campanella, B.; Tiné, M. R.; Duce, C. *RSC Adv.* **2016**, *6* (76), 72386.

(22) Lvov, Y.; Wang, W.; Zhang, L.; Fakhrullin, R. *Adv. Mater.* **2016**, *28* (6), 1227.

(23) Vergaro, V.; Abdullayev, E.; Lvov, Y. M.; Zeitoun, A.; Cingolani, R.; Rinaldi, R.; Leporatti, S. *Biomacromolecules* **2010**, *11* (3), 820.

(24) Maisanaba, S.; Pichardo, S.; Puerto, M.; Gutiérrez-Praena, D.; Cameán, A. M.; Jos, A. *Environ. Res.* **2015**, *138*, 233.

(25) Lvov, Y.; Abdullayev, E. *Prog. Polym. Sci.* **2013**, *38* (10–11), 1690.

(26) Lvov, Y.; Abdullayev, E. *Prog. Polym. Sci.* **2013**, *38*, 1690.

(27) VEERABADRAN, N. G.; PRICE, R. R.; LVOV, Y. M. *Nano* **2007**, *2* (2), 115.

(28) Abdullayev, E.; Joshi, A.; Wei, W.; Zhao, Y.; Lvov, Y. *ACS Nano* **2012**, *6* (8), 7216.

(29) Lvov, Y.; Aerov, A.; Fakhrullin, R. *Adv. Colloid Interface Sci.* **2014**, *207* (1), 189.

(30) Sun, J.; Yendluri, R.; Liu, K.; Guo, Y.; Lvov, Y.; Yan, X. *Phys. Chem. Chem. Phys.* **2017**, *19* (1), 562.

(31) Cavallaro, G.; Lazzara, G.; Massaro, M.; Milioto, S.; Noto, R.; Parisi, F.; Riela, S. *J. Phys. Chem. C* **2015**, *119* (16), 8944.

(32) Massaro, M.; Amorati, R.; Cavallaro, G.; Guernelli, S.; Lazzara, G.; Milioto, S.; Noto, R.; Poma, P.; Riela, S. *Colloids Surfaces B Biointerfaces* **2016**, *140*, 505.

(33) Massaro, M.; Riela, S.; Guernelli, S.; Parisi, F.; Lazzara, G.; Baschieri, A.; Valgimigli, L.; Amorati, R. *J. Mater. Chem. B* **2016**, *4* (13), 2229.

(34) Massaro, M.; Riela, S.; Baiamonte, C.; Blanco, J. L. J.; Giordano, C.; Lo Meo, P.; Milioto, S.; Noto, R.; Parisi, F.; Pizzolanti, G.; Lazzara, G. *RSC Adv.* **2016**, *6* (91), 87935.

(35) Massaro, M.; Riela, S.; Lo Meo, P.; Noto, R.; Cavallaro, G.; Milioto, S.; Lazzara, G. *J. Mater. Chem. B* **2014**, *2* (44), 7732.

(36) Aggarwal, M.; Jain, R.; Mishra, A. P.; Kulkarni, P. G.; Vyas, C.; Sharma, R.; Gupta, M. *J. Astrophys. Astron.* **2008**, *29* (1–2), 195.

(37) Choi, H.; Chun, Y.-S.; Kim, S.-W.; Kim, M.-S.; Park, J.-W. *Mol. Pharmacol.* **2006**, *70* (5), 1664.

(38) Lai, X.; Agarwal, M.; Lvov, Y. M.; Pachpande, C.; Varahramyan, K.; Witzmann, F. A. *J. Appl. Toxicol.* **2013**, n/a.

(39) Chen, H.-W.; Lee, J.-Y.; Huang, J.-Y.; Wang, C.-C.; Chen, W.-J.; Su, S.-F.; Huang, C.-W.; Ho, C.-C.; Chen, J. J. W.; Tsai, M.-F.; Yu, S.-L.; Yang, P.-C. *Cancer Res.* **2008**, *68* (18), 7428.

(40) Kurien, B. T.; Singh, A.; Matsumoto, H.; Scofield, R. H. *Assay Drug Dev. Technol.* **2007**, *5* (4), 567.

(41) Anand, P.; Kunnumakkara, A. B.; Newman, R. A.; Aggarwal, B. B. *Mol. Pharm.* **2007**, *4* (6), 807.

(42) Tang, H.; Murphy, C. J.; Zhang, B.; Shen, Y.; Sui, M.; Van Kirk, E. A.; Feng, X.; Murdoch, W. J. *Nanomedicine* **2010**, *5* (6), 855.

(43) Duan, J.; Zhang, Y.; Han, S.; Chen, Y.; Li, B.; Liao, M.; Chen, W.; Deng, X.; Zhao, J.; Huang, B. *Int. J. Pharm.* **2010**, *400* (1–2), 211.

(44) Kim, T. N.; Park, M. S.; Lim, K. Il; Yang, S. J.; Yoo, H. J.; Kang, H. J.; Song, W.; Seo, J. A.; Kim, S. G.; Kim, N. H.; Baik, S. H.; Choi, D. S.; Choi, K. M. *Diabetes Res. Clin. Pract.* **2011**, *93* (2), 285.

(45) Wang, L.; Xu, X.; Zhang, Y.; Zhang, Y.; Zhu, Y.; Shi, J.; Sun, Y.; Huang, Q. *J. Mater. Sci. Mater. Med.* **2013**, *24* (9), 2137.

(46) R. Price, B. P. G. Y. L. R. *J. Microencapsul.* **2001**, *18* (6), 713.

(47) Abdullayev, E.; Price, R.; Shchukin, D.; Lvov, Y. *ACS Appl. Mater. Interfaces* **2009**, *1* (7), 1437.

(48) Cavallaro, G.; Lazzara, G.; Milioto, S. *Langmuir* **2011**, *27* (3), 1158.

(49) Du, M.; Guo, B.; Jia, D. *Polym. Int.* **2010**, n/a.

(50) Shargel, L.; Yu, A. B. C. *Applied Biopharmaceutics & Pharmacokinetics*, 7th ed.; McGraw Hill: New York, 2012.

(51) Bernabé-Pineda, M.; Ramírez-Silva, M. T.; Romero-Romo, M.; González-Vergara, E.; Rojas-Hernández, A. *Spectrochim. Acta Part A Mol. Biomol. Spectrosc.* **2004**, *60* (5), 1091.

(52) Korsmeyer, R. W.; Gurny, R.; Doelker, E.; Buri, P.; Peppas, N. A. *Int. J. Pharm.* **1983**, *15* (1), 25.

(53) Dash, S.; Murthy, P. N.; Nath, L.; Chowdhury, P. *Acta Pol. Pharm.* 67 (3), 217.

(54) Pokhodylo, N. *Sci. Pharm.* **2013**, *81* (3), 663.

(55) Zhang, S.; Li, J.; Lykotrafitis, G.; Bao, G.; Suresh, S. *Adv. Mater.* **2009**, *21* (4), 419.

(56) Wang, L.-P.; Wang, Y.-P.; Pei, X.-W.; Peng, B. *React. Funct. Polym.* **2008**, *68* (2), 649.

(57) Ganta, S.; Amiji, M. *Mol. Pharm.* **2009**, *6* (3), 928.

(58) Notarbartolo, M.; Poma, P.; Perri, D.; Dusonchet, L.; Cervello, M.; D'Alessandro, N. *Cancer Lett.* **2005**, *224* (1), 53.

(59) Kubo, I.; Komatsu, S.; Ochi, M. *J. Agric. Food Chem.* **1986**, *34* (6), 970.

(60) Chandregowda, V.; Kush, A.; Reddy, G. C. *Eur. J. Med. Chem.* **2009**, *44* (6), 2711.

(61) Kubo, I.; Ochi, M.; Vieira, P. C.; Komatsu, S. *J. Agric. Food Chem.* **1993**, *41* (6), 1012.

(62) Himejima, M.; Kubo, I. *J. Agric. Food Chem.* **1991**, *39* (2), 418.

(63) Muroi, H.; Kubo, I. *J. Agric. Food Chem.* **1993**, *41* (10), 1780.

(64) Suo, M.; Isao, H.; Ishida, Y.; Shimano, Y.; Bi, C.; Kato, H.; Takano, F.; Ohta, T. *J. Nat. Med.* **2012**, *66* (1), 133.

(65) Hemshekhar, M.; Sebastin Santhosh, M.; Kemparaju, K.; Girish, K. S. *Basic Clin. Pharmacol. Toxicol.* **2012**, *110* (2), 122.

(66) Sung, B.; Pandey, M. K.; Ahn, K. S.; Yi, T.; Chaturvedi, M. M.; Liu, M.; Aggarwal, B. B. *Blood* **2008**, *111* (10), 4880.

(67) Mahata, D.; Mandal, S. M.; Bharti, R.; Gupta, V. K.; Mandal, M.; Nag, A.; Nando, G. B. *Int. J. Biol. Macromol.* **2014**, *69*, 5.

(68) IZZO, P. T.; DAWSON, C. R. *J. Org. Chem.* **1950**, *15* (4), 707.

(69) Yuan, P.; Southon, P. D.; Liu, Z.; Green, M. E. R.; Hook, J. M.; Antill, S. J.; Kepert, C. J. *J. Phys. Chem. C* **2008**, *112* (40), 15742.

(70) Gibaldi, M.; Feldman, S. *J. Pharm. Sci.* **1967**, *56* (10), 1238.

(71) Wilczak, A.; Keinath, T. M. *Water Environment Research*. Water Environment Federation pp 238–244.

(72) Higuchi, T. *J. Pharm. Sci.* **1963**, *52* (12), 1145.

(73) Ritger, P. L.; Peppas, N. A. *J. Control. Release* **1987**, *5* (1), 23.

(74) Siepmann, J. *Adv. Drug Deliv. Rev.* **2001**, *48* (2–3), 139.

(75) Shenoy, D. B.; Amiji, M. M. *Int. J. Pharm.* **2005**, *293* (1–2), 261.

(76) Poon, C.; He, C.; Liu, D.; Lu, K.; Lin, W. *J. Control. Release* **2015**, *201*, 90.

(77) Wang, H.; Wu, Y.; Zhao, R.; Nie, G. *Adv. Mater.* **2013**, *25* (11), 1616.

(78) Lehár, J.; Krueger, A. S.; Avery, W.; Heilbut, A. M.; Johansen, L. M.; Price, E. R.; Rickles, R. J.; Short III, G. F.; Staunton, J. E.; Jin, X.; Lee, M. S.; Zimmermann, G. R.; Borisy, A. A. *Nat. Biotechnol.* **2009**, *27* (7), 659.

(79) Huang, W.-Y.; Cai, Y.-Z.; Zhang, Y. *Nutr. Cancer* **2009**, *62* (1), 1.

(80) Birjees Bukhari, S.; Memon, S.; Mahroof Tahir, M.; Bhanger, M. I. *J. Mol. Struct.* **2008**, *892* (1–3), 39.

(81) Kumari, A.; Yadav, S. K.; Pakade, Y. B.; Singh, B.; Yadav, S. C. *Colloids Surfaces B Biointerfaces* **2010**, *80* (2), 184.

(82) Zheng, Y.; Haworth, I. S.; Zuo, Z.; Chow, M. S. S.; Chow, A. H. L. *J. Pharm. Sci.* **2005**, *94* (5), 1079.

(83) Wei, Y.; Ye, X.; Shang, X.; Peng, X.; Bao, Q.; Liu, M.; Guo, M.; Li, F. *Colloids Surfaces A Physicochem. Eng. Asp.* **2012**, *396*, 22.

(84) Jullian, C.; Moyano, L.; Yañez, C.; Olea-Azar, C. *Spectrochim. Acta Part A Mol. Biomol. Spectrosc.* **2007**, *67* (1), 230.

(85) De Lisi, R.; Lazzara, G.; Milioto, S. *Phys. Chem. Chem. Phys.* **2011**, *13* (27), 12571.

(86) Liu, H.; Du, Z.; Yuan, Q. *J. Chromatogr. B* **2009**, *877* (32), 4159.

(87) Angelico, R.; Ceglie, A.; Sacco, P.; Colafemmina, G.; Ripoli, M.; Mangia, A. *Int. J. Pharm.* **2014**, *471* (1–2), 173.

(88) Zhu, X.; Ping, W. *Spectrochim. Acta Part A Mol. Biomol. Spectrosc.* **2014**, *132*, 38.

(89) Calabrese, I.; Cavallaro, G.; Scialabba, C.; Licciardi, M.; Merli, M.; Sciascia, L.; Turco Liveri, M. L. *Int. J. Pharm.* **2013**,

457 (1), 224.

(90)   Kennedy, M. A.; Sobel, J. D. *Curr. Infect. Dis. Rep.* **2010**, *12* (6), 465.

(91)   Wady, A. F.; Machado, A. L.; Zucolotto, V.; Zamperini, C. A.; Berni, E.; Vergani, C. E. *J. Appl. Microbiol.* **2012**, *112* (6), 1163.

(92)   Esposito, E.; Ravani, L.; Contado, C.; Costenaro, A.; Drechsler, M.; Rossi, D.; Menegatti, E.; Grandini, A.; Cortesi, R. *Mater. Sci. Eng. C* **2013**, *33* (1), 411.

(93)   Ravani, L.; Esposito, E.; Bories, C.; Moal, V. L.-L.; Loiseau, P. M.; Djabourov, M.; Cortesi, R.; Bouchemal, K. *Int. J. Pharm.* **2013**, *454* (2), 695.

(94)   Hrabálek, A.; Doležal, P.; Vávrová, K.; Zbytovská, J.; Holas, T.; Klimentová, J.; Novotný, J. *Pharm. Res.* **2006**, *23* (5), 912.

(95)   Loftsson, T.; Hreinsdôttir, D. *AAPS PharmSciTech* **2006**, *7* (1), E29.

(96)   Bachhav, Y. G.; Patravale, V. B. *AAPS PharmSciTech* **2009**, *10* (2), 476.

(97)   Yong, C. S.; Li, D. X.; Prabagar, B.; Park, B. C.; Yi, S. J.; Yoo, B. K.; Lyoo, W. S.; Woo, J. S.; Rhee, J. D.; Kim, J. A.; Choi, H. G. *Pharmazie* **2007**, *62* (10), 756.

(98)   Ning, M.; Gu, Z.; Pan, H.; Yu, H.; Xiao, K. *Indian J. Exp. Biol.* **2005**, *43* (2), 150.

(99)   Hashem, F. M.; Shaker, D. S.; Ghorab, M. K.; Nasr, M.; Ismail, A. *AAPS PharmSciTech* **2011**, *12* (3), 879.

(100) Prabagar, B.; Yoo, B.-K.; Woo, J.-S.; Kim, J.-A.; Rhee, J.-D.; Piao, M. G.; Choi, H.-G.; Yong, C. S. *Arch. Pharm. Res.* **2007**, *30* (2), 249.

(101) Lazzara, G.; Milioto, S. *J. Phys. Chem. B* **2008**, *112* (38), 11887.

(102) Tully, J.; Yendluri, R.; Lvov, Y. *Biomacromolecules* **2016**, *17* (2), 615.

Chapter 6

Halloysite Nanotubes

as Support for

Metal-Based Catalysts

6. *Halloysite Nanotubes in catalysis applications*

Since its introduction to the chemical industry by J. Roebuch in 1746, catalysis has played an important role in chemical research. Nowadays, approximately 85–90% of the products of the chemical industry are made in catalytic processes. In particular, due to disadvantages presented by the traditionally employed homogenous catalysts, much attention is devoted to the development of heterogeneous catalysts based on metal nanoparticles (NPs). The benefits of the use of metal-NPs as catalysts in the chemical industry are related to the increasing selectivity and activity of catalysts by controlling pore size and particle characteristics. Unfortunately, metal-nanoparticles have a tendency to agglomerate, forming large particles with low catalyst efficiency. To prevent the aggregation of metal-NPs during the catalyst's synthesis process or a catalytic reaction, they are usually dispersed but are preferably anchored to high surface-area and robust supports, so the reactant molecules can reach as many surface atoms of the metal as possible. When NPs are dispersed on high surface-area supports, their interactions with the support surfaces become important in determining their catalytic performances.[1]

Many efforts have been devoted to the synthesis of various supports for metal nanoparticles based on silica, alumina, zeolites, organic polymers, dendrimers, fullerenes and so on.[2–6]

Halloysite nanotubes possess several advantages, including high stability, resistance against organic solvents, and ease of disposal or reusability. In comparison to platy clays such as montmorillonite, kaolin and LAPONITE® that are stacked in larger crystallites, halloysite does not need exfoliation and thus has a large surface area without any additional material treatment. All these features provide the metal nanoparticles supported on halloysite nanotubes with several advantages for their industrial application.

The most widely used method for supported metal nanoparticles involves the halloysite external surface modification with suitable functionality, able to interact with the metal salts, followed by reduction in order to obtain metal nanoparticles. Otherwise, it is possible to immobilize metal nanoparticles on the HNT surface by physical adsorption or self-assembly. In this context, Fe, Co, Ni, and Pd were adsorbed on the halloysite surface, leading to hybrid nanomaterials.[7,8] TiO_2 nanoparticles were bound to the nanotube surface though silane linkage.[9] Ag nanoparticles were successfully immobilized on halloysite by dispersing the nanomaterial in an aqueous solution of precursor $AgNO_3$ and followed by a reduction reaction in the presence of reductants such as $NaBH_4$ or polyols.[10]

Since nanoparticles loaded into the HNT lumen are expected to be more stable than those supported on the external surface, it is interesting to design metal–halloysite hybrids where metal nanoparticles are located inside the tubes (Figure 89).[11] In this way, it is also possible to avoid metal aggregation. Ouyang *et al.* reported the preparation of Ag NPs/HNTs composites under vacuum conditions.[11] With this method, the solution of silver acetate fills the lumen of HNTs under vacuum and it is subsequently transformed to Ag NPs by a pyrolytic process.

In another work, Ag nanoparticles were loaded into the HNT lumen by exploiting the different charges between the external surface and the inner one. This method considers the electrostatic interactions between N-acetyl-L-cysteine-modified Ag NPs and the positively charged HNT lumen. The Ag NPs loaded into the lumen of HNTs possess excellent structural stability due to the irreversible electrostatic interaction.[12]

Similarly, Cu–Ni NPs were loaded into the halloysite internal surface by means of a ligand-assisted reduction of Cu^{2+} and Ni^{2+}-cations, followed by annealing. Specifically, Cu–Ni NPs were encapsulated in the HNT lumen by co-reduction of $CuCl_2$ and $NiCl_2$ in aqueous ethanol. In order to better disperse the cationic metals ions onto the alumina surface, sodium citrate was used as a cation-delivery ligand, exploiting, also, in this case, electrostatic interactions. The cations were finally converted to the required Cu–Ni NPs by treatment with hydrazine at 80 °C.[12]

A different strategy to fill the HNT lumen with CuO was reported, where inorganic reverse micelles were developed using alkyltrimethylammonium bromide surfactants adsorbed at the outer HNTs surface. The as-prepared reverse inorganic micelles generated water-in-oil emulsions, and copper sulphate aqueous solution was entrapped in the lumen. After calcination, uniform CuO distribution in the HNTs lumen was observed.[13]
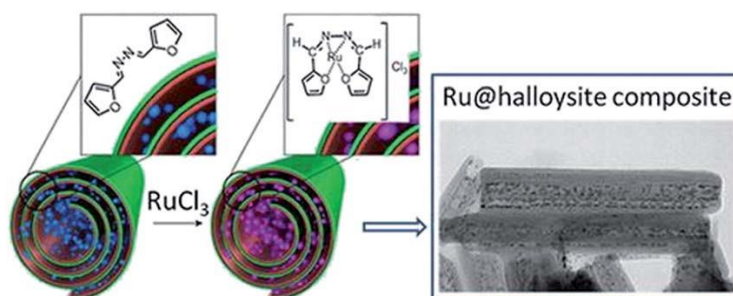
Figure 89. Schematic representation of the synthesis of Ru nanoparticles inside the HNT lumen.

To the light of the above halloysite properties and due to the fact that this nanomaterial shows superior activity with regards to others support, during my PhD I

have also focused the attention on the development of novel support for immobilization of metal nanoparticles. In particular my efforts were developed to design and characterize novel hybrid based on halloysite for the immobilization of palladium, gold, cobalt, and iron magnetite nanoparticles.

For the efficient immobilization of PdNPs, were investigated two different systems based on halloysite covalently functionalized with triazolium salts, in order to obtain the so-called "Supported Ionic Liquid Phase" (SILP). Nanoparticles immobilized on SILP were already investigated and they have shown high capacity to stabilize palladium; in this context, for example, Gruttadauria *et al.* described a new kind of material constituted by a highly cross-linked imidazolium on the surface of silica gel. The multi-layered imidazolium salt frameworks permitted the immobilization of palladium in high loading (10 wt%).

To test the catalytic activity of the palladium stabilized on halloysite nanomaterials, it was chosen the Suzuki-Miyaura coupling reaction. This reaction is one of the most valuable synthetic routes for the preparation of symmetric and asymmetric biaryls, which are important skeletons in the structures of biologically active compounds,[14] agrochemicals, pharmaceuticals, [15–17] polymers,[18] ligands[19] and functional materials.[18] The key advantages of the Suzuki–Miyaura cross-coupling are: (i) the mild conditions under which it is conducted; (ii) the high tolerance toward functional groups, (iii) the commercial availability and stability of boronic acids to heat, oxygen and water; and (iv) the ease of handling and separation of boron-containing by-products from the reaction mixtures.[20]

Similarly to palladium nanoparticles, the gold ones (AuNPs) have attracted enormous attention in the field of chemical synthesis due to their unique stability, selectivity, and catalytic activities for transformation reactions. However, their high surface energy due to the large surface-to-volume ratio and high collision frequency associated with their greater mobility cause serious stability problems, such as a tendency to aggregate, changes in shape and damage to their surface states during catalytic reactions, and eventual loss of their initial activity and selectivity. To avoid their aggregation during the reaction and hence the deactivation, and also to facilitate their separation and recovery from the reaction solution, AuNPs can be anchored to solid support. Up to now, for the best of our knowledge, few papers reported the immobilization of gold nanoparticles on functionalized halloysite, so, the second part of this chapter deals on the preparation and characterization of novel systems HNT/Au.

Another interesting metal for catalytic applications is the cobalt. Co and its oxide are widely used catalysts showing very high potential application and attractive perspective. The study of these metallic nanomaterials associated to the peculiar characteristics of halloysite gives us the possibility to find out a new family of supported metal catalysts with high application possibilities and large interest.

6.1. Suzuki–Miyaura catalyst based on Pd nanoparticles supported on halloysite nanotubes.

The first generation heterogeneous catalyst HNT/Pd, compound **29,** was synthesized in two consecutive steps: first, by anion exchange reaction of compound **11a** from X^- to $PdCl_4^{2-}$; second, the solid crude material obtained was recovered by filtration and, the Pd(II) was reduced to Pd^0 with $NaBH_4$ in ethanol (Scheme 11).

11a   **29**
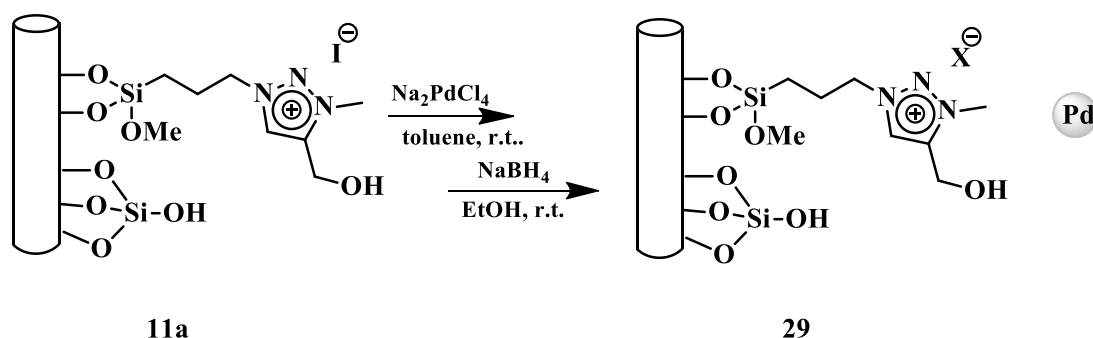
Scheme 11. Schematic representation of the immobilization of PdNPs on compound **11a.**

Following this procedure, a HNT-IL catalyst with 5.3 wt% Pd was obtained as determined by energy-dispersive X-ray measurements (EDX). This loading was greater than the one obtained for HNT-imidazolium salt confirming the good ability, to act as stabilizer for palladium nanoparticles, showed by triazolium salts.[21]

The catalyst was used in the Suzuki–Miyaura reaction between phenylboronic acid and a set of aryl halyde under experimental conditions previously adopted for imidazolium catalyst;[22] i.e. in a mixture ethanol/water (1:1) at 120 °C in the presence of K_2CO_3 as base (Table 14). All the reactions were run for 10 min. The catalyst was used in 0.1 mol% loading. Conversions were high, ranging from 25% to 99%; in all case, no byproducts were detected and the conversions reported in Table 14 correspond to yields. Full conversions were achieved when aryl bromides and iodides were employed (entries 1 and 7, respectively), while

less reactive aryl chloride (entry 9) gave lower yield. Longer times of irradiation led to the degradation of compounds.

Table 14. Suzuki reaction between phenyl boronic acid and several aryl halyde under microwave irradiations.
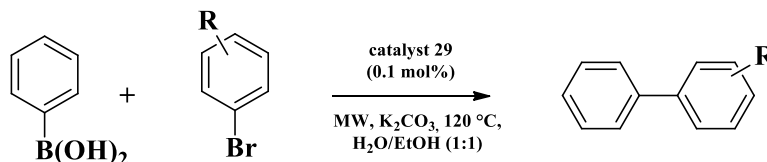
Entry	Ar-X	Conversion (%)[a]
1	4-bromoacetophenone	>99
2	3-bromoacetophenone	65
3	4-bromobenzaldehyde	>99
5	4-bromoanisole	83
6	3-bromoanisole	95
7	4-bromoaniline	58
8	4-iodoacetophenone	>99
9	4-iodoanisole	>99
10	4-clorobenzaldehyde	25

[a]Determined by ^{1}H-NMR.

The next step was the recycling study of the catalytic material. Because of the very small amount of catalyst used (1 mg), we carried out recycling investigations using catalyst at 1 mol% in the reaction between phenylboronic acid and 3-bromoanisole (Table 15).

Table 15. Recycling test.
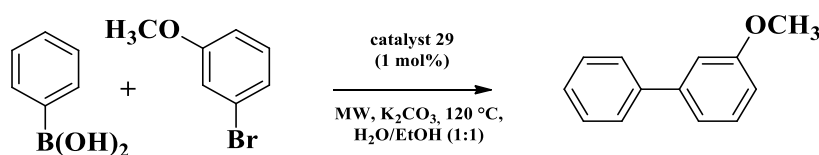
Entry	Run	Conversion (%)[a]
1	1	94
2	2	86
3	3	85
4	4	27

[a]Determined by ^{1}H-NMR.

The catalyst was recovered by centrifugation and was reused in the same reaction in four cycles. Under the above conditions, catalyst afforded biphenyl-3-anisole in 94–85 % yield in three cycles, after that we observed a decrease in the yield. Atomic absorption

spectroscopy (AAS) analysis of the washings after three cycles showed that 1.3% of palladium was released into solution during the course of a reaction. These results were different from that reported for HNT-imidazolium catalyst;[22] probably because the thermal stability of 1,2,3-triazolium salts (200–300 °C), is lower than that of 1,3-dialkyl imidazolium based ionic liquids (generally, T_d >300 °C).[23] Therefore the triazolium could have a lower stability in the experimental conditions of Suzuki reaction under microwave irradiation.

The loss of activity after three cycles could be ascribed to the thermal decomposition of triazolium salts on HNT surface and due to that we observed a greater Pd leaching.

In the light of these results, in order to improve the catalytic activity of HNT-IL, we designed a second generation HNT-triazole catalyst, based on the halloysite functionalized with dicationic triazolium salts (compound **17**). Dicationic ionic liquids, indeed, have high thermal stability, higher than that normally characterizing the corresponding monocationic; therefore, in terms of designing ionic liquids for specific applications, the dicationic ionic liquids open up the possibility to develop a new system with resistance to high temperature.[23] Furthermore, for an application as support catalyst in the Suzuki reaction, the new support was designed with an aromatic linker to allow $\pi-\pi$ interactions between catalyst and substrates and, therefore, facilitate the cross-coupling reaction. Such material, being high loaded (or multilayered) ionic liquid-like material, could be capable of stabilizing a higher amount of catalytically active Pd species.[2] Such an approach could furnish a catalytic material to be used in a low weight% compared to the substrates. This is certainly useful for large-scale applications.

Loading of palladium on the ditriazolium salts functionalized halloysite was performed as previously described for first generation catalyst. Compound **30** with 6.3 wt% Pd was obtained as determined by EDX measurements.

The introduction of two triazole rings and a linker between them, onto the support could change system's properties, so in order to optimize reaction conditions such as reaction temperature, time and amount of palladium catalyst, we performed several test reactions. To find the best conditions, the reaction between 3-bromoanisole and phenylboronic acid was chosen as model reaction, for which influences of different parameters were examined to obtain the best possible combination. The parameters included solvent, reaction time and catalyst concentration. Since it is known that an important parameter is represented by the reaction medium, the first step was a solvent study. Six reaction media were examined, namely EtOH/H_2O 1:1, ethanol, toluene, acetonitrile, 1,4 dioxane and water (Table 16). Organic solvents (entries 1-4) gave low yield for the reaction.

Table 16. Optimization of experimental conditions for Suzuki cross-coupling reaction under microwave irradiation.
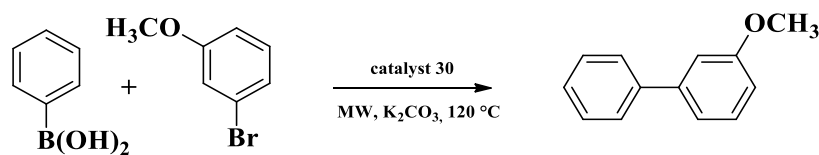
Entry	Solvent	Time (min)	Pd (mol%)	Conversion (%)[a]
Solvent effect				
1	Acetonitrile	10	1	18
2	1,4 Dioxane	10	1	20
3	EtOH	10	1	25
4	Toluene	10	1	43
5	H_2O/EtOH (1:1)	10	1	78
6	H_2O	10	1	96
Time effect				
7	H_2O	5	1	89
8	H_2O	15	1	80
Pd loading				
9	H_2O	10	0.1	>99

[a]Determined by ^{1}H-NMR

However, when we adopted the organic/aqueous co-solvent, an increasing in the yield was observed (entry 5). Surprisingly, high yield was obtained when we used as solvent pure water. Next the effect of reaction times on the Suzuki reaction in H_2O, were examined. The best experimental conditions were obtained with an irradiation time of 10 min; indeed, with longer times, conversions decreased (Table 16, entry 8). To estimate the effects of the amount of Pd catalyst on the conversion reaction, we performed an additional reaction with 0.1 mol% catalyst, resulting in quantitative conversion (entry 9). **30** was used in the Suzuki–Miyaura reaction between phenylboronic acid and a set of aryl halide in water at 120 °C in the presence of K_2CO_3 as base. All the reactions were run for 10 min. **30** was used in 0.1 mol% loading. The results were summarized in Table 17. Conversions were high with yields up to 99% in the case of anisole derivatives, on the contrary, other substrates gave lower yields in water but we observed an increasing in conversion in a mixture water/ethanol (1:1), The merit of the co-solvent may be attributed to the good solubility of the organic reactants and the inorganic base. In this case, yields were similar to those obtained with **29**.

Table 17. Suzuki cross-coupling reaction of phenylboronic acid with various aryl halides under optimized reaction conditions under microwave irradiation.
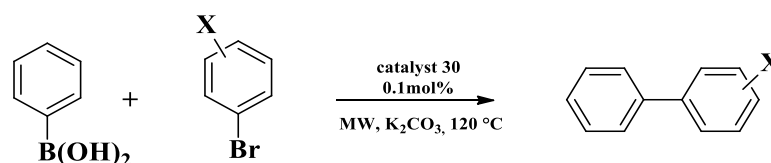
Entry	Ar-X	Conv. (%)[a] H$_2$O	Conv. (%)[a] H$_2$O/EtOH (1:1)
1	3-bromoanisole	>99	
2	4-bromoanisole	>99	
3	3-bromoacetophenone	25	65
4	4-bromoacetophenone	49	
5	3-bromobenzaldheyde	39	
6	4-bromobenzaldheyde	58	85
7	4-bromoanisole	>99	
8	1-bromo-4-nitrobenzene	25	
9	1-bromo-2,4,6-triisopropylbenzene	<5	
10	3-iodoanisole	>99	
11	4-iodoanisole	>99	
12	4-chlorobenzaldheyde	<5	

[a]Determined by ^{1}H-NMR

The excellent conversions obtained for anisole derivatives could be due to a synergic effect of ethereal alkyl chains or aromatic rings, present in the catalyst support and microwave irradiation on cross-coupling of anisole in water. This indicates that the electron- richness of the support promoted the ability for oxidative addition,[24] which is a crucial step in enhancing the catalytic activity of catalyst in the Suzuki coupling reaction.

The next step was the recycling study of the catalytic materials 2. Also in this case, recycling investigations were carried out using catalyst 2 at 1 mol% in the reaction between phenylboronic acid and 3-bromoanisole (Table 18). Catalyst was recovered by centrifugation and was reused in the same reaction in five cycles. Under the above conditions, catalyst 2 afforded biphenyl-3-anisole in 99-90 % in five cycles.

Table 18. Recycling investigation.

Entry	Cycle	Conversion (%)[a]
1	1	>99
2	2	>99
3	3	>99
4	4	90
5	5	90

[a]Determined by ^{1}H-NMR

In order to determine the degree of leaching of the metal from heterogeneous catalyst, the catalyst was recovered by centrifugation after the reaction was completed and the palladium content of the supernatant was determined by AAS. It was shown that less than 0.01% of the total amount of the original palladium species was lost into solution during the course of a reaction, therefore the leaching level was negligible, which was also confirmed by the excellent recoverability and reusability of this heterogeneous catalyst. The low leaching in Pd catalysts immobilized on to gel- supported ionic-liquid phase has been ascribed to a 'release and catch' mechanism.[25–28] It has been proposed that during Suzuki coupling palladium is dissolved in solution (leaching), then after completion of the process palladium is redeposited on to the support and its full and efficient recovery can be achieved if the redeposition is complete at the end of the reaction.[25] It is worth noting that the enhanced catalytic performance of **30** can be also due to the thermal stability of this support. This hypothesis was confirmed by FT-IR spectroscopy. The spectrum of the catalyst was not altered by the catalytic process (Figure 90).
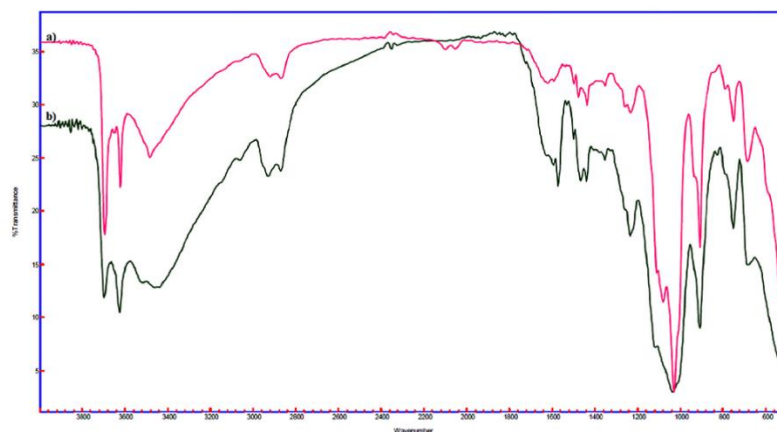
Figure 90. FT-IR spectra of HNT-IL **30** catalyst **a)** before and **b)** after five consecutive runs.

6.2. Gold nanoparticles supported on functionalized halloysite as catalyst for reduction reaction

Since thiols are widely employed as an anchoring group for gold nanoparticles due to the strong Au-thiol bond,[29] the first step for the synthesis of HNT/Au nanocatalyst was the modification of the halloysite nanotubes with thiol-terminated organosilane following the procedure reported in Chapter 4 (Scheme 12). In the second step the immobilization of gold nanoparticles on thiol functionalized halloysite (compound **1**) was carried out in an aqueous medium at room temperature. The formation of the AuNPs was achieved by simply adding an aqueous solution of HAuCl$_4$ to an aqueous dispersion of HNT-SH, followed by reduction with NaBH$_4$ in methanol. During the reduction reaction the solution color changes from yellow to brown. The dispersion was then filtered in order to remove the supernatant solution, which was colorless, suggesting the absence of free AuNPs and finally it was dried under vacuum.

For comparison another preparation method was adopted. Citrate-stabilized AuNPs were first synthesized by the classic citrate reduction method;[30] then the HNT-SH was used to attach the AuNPS on the halloysite surface by ligand exchange reaction between citrate-stabilized AuNPs and the HNT-SH nanomaterial.[31]
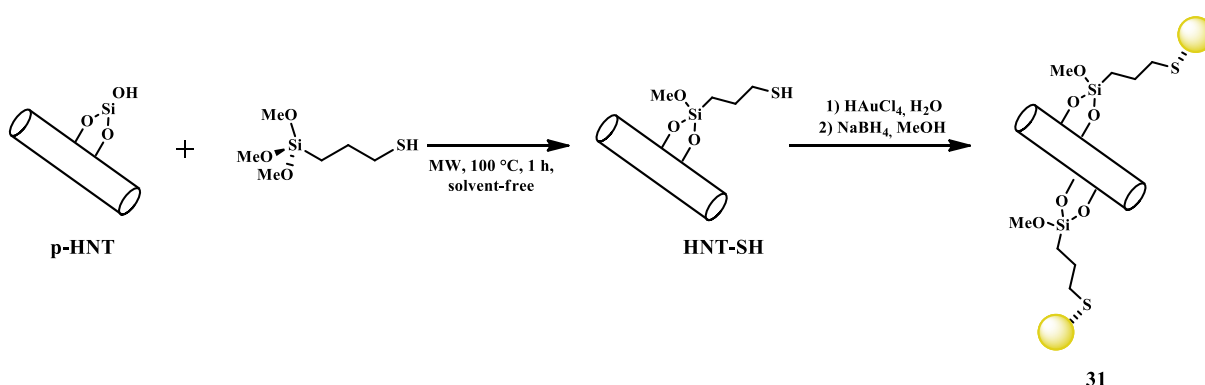
Scheme 12. Schematic representation of the synthesis of compound **31**.

The content of gold nanoparticles, on the solid halloysite support, was determined by Inductively Coupled Plasma-Optical Emission Spectrometry (ICP-OES) and was estimated as 6.6 wt%. As shown in the energy-disperse X-ray (EDS) pattern and elemental mapping, the weak but evenly distributed signals from Au further confirmed the well dispersion of gold nanoparticles in the sample (Figure 91a). This well dispersion of Au was suggested to be related to the even distribution of thiol groups on halloysite. Furthermore, EDS measurements confirmed the successful functionalization highlighting the presence of sulfur in the structure of the nanomaterial deriving from the covalently grafted organosilane. SEM micrographs

(Figure 91b) showed that the characteristic lengths and the tubular shape of HNTs were preserved in the catalyst **31**.

The morphology of HNT/Au nanomaterial was investigated by TEM microscopy. The gold nanoparticles presented a spherical shape and were found to be mainly attached on the support surface. The **31** material showed quite a uniform distribution of AuNPs with an average diameter of 4.2 ± 1.5 nm (Figure 92a-b), thus the gold nanoparticles are well distributed on halloysite surface without any aggregation. In addition, TEM images confirm the feasibility of the preparation method. The size of gold nanoparticles, indeed, is highly dependent on the way they are prepared. In the case of using the citrate stabilization, the obtained AuNPs are not so uniform in size. The average size of the AuNPs is about 35.6 ± 4.8 nm (Figure 92c-d). Therefore, it is possible to conclude that the adopting the $NaBH_4$ reduction method allows to obtain nanoparticles with small sizes and better dispersion on halloysite surface.
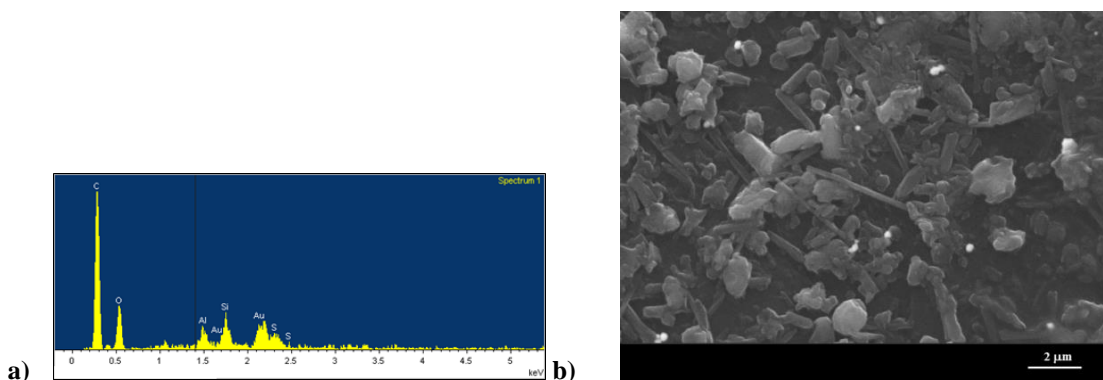
Figure 91. (a) EDX pattern and (b) SEM images of **31**.
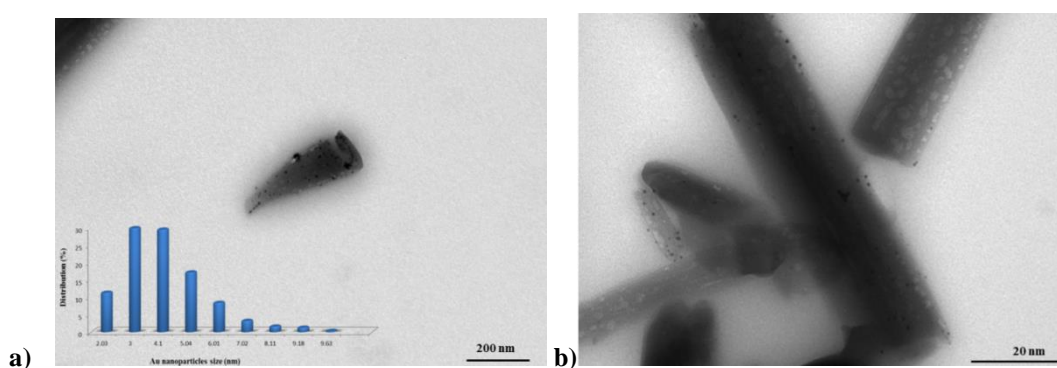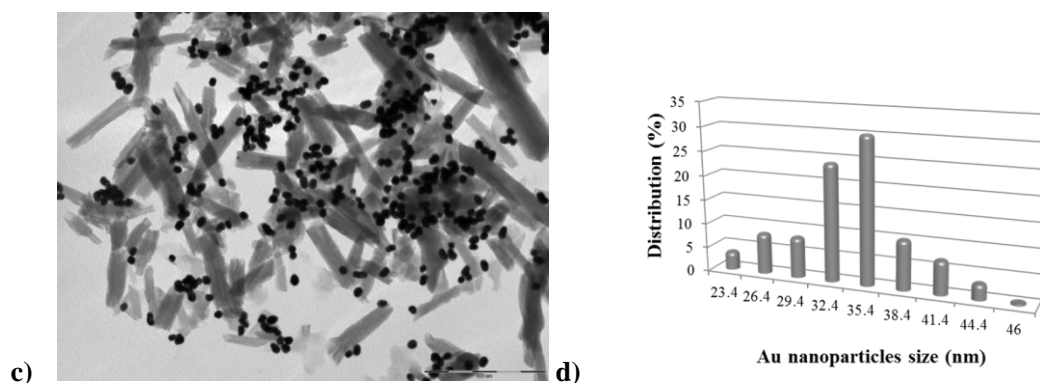
Figure 92. TEM images of the **31**; the inset shows AuNPs size distribution (n = 308).

6.2.1. Catalytic Activity of HNT/Au nanomaterial 31

To evaluate the catalytic performance of the HNT/Au hybrid nanomaterial obtained, we chose the reduction of 4-nitrophenol (4-NP) by $NaBH_4$ that is the most often used reaction to test the catalytic activity of metal nanoparticles in aqueous solution.[32] The interest in this reaction is mainly due to the fact that 4-NP is a common reactant in pharmaceuticals and can be a hazardous by-product that is inhibitory and toxic in nature, whereas 4-aminophenol (4-AP) is used for black-and-white films and for the production of acetaminophen.

The $NaBH_4$ mediated reduction of 4-NP is thermodynamically feasible (since E_0 for 4-NP/4-AP is -0.76 V and for H_3BO_3/BH_4^- -1.33 V *vs* NHE) but kinetically restricted due to the large potential difference between donor (BH_4^-) and acceptor (4-NP) species with decreases the feasibility of this reaction. The gold nanoparticles, with the suitable redox potential help to overcome the kinetic barrier by facilitating relay of electrons from donor to acceptor species.[33]

Furthermore, this reaction can be easily monitored by *UV-vis* spectroscopy and since one of the reactant ($NaBH_4$) is in large excess, its concentration can be considered constant during the reaction[34,35] and therefore, it is possible to determine the apparent rate constant k_{app} from the slope of the linear correlation of $\ln(A/A_0)$ with time t.

The aqueous solution of 4-NP is faint yellow and it changes into yellow-green with the addition of $NaBH_4$ due to the formation of 4-nitrophenolate ions; as a consequence the maximum absorption peak of 4-NP aqueous solution located at 317 nm shifted to 396 nm after the addition of $NaBH_4$. Without the addition of AuNPs, no reaction was observed. A similar result can be found for the 4-NP/$NaBH_4$ aqueous solution in the presence of HNT-SH. These results suggest that 4-NP cannot be reduced by $NaBH_4$ in absence of AuNPs and that the HNT-SH is not able to exert any catalytic activity. Pristine Au nanoparticles did not show any relevant catalytic activity. On the contrary, with the addition of the catalytic nanomaterial

31, the solution color faded from yellow-green to transparent with time, and small bubbles were continuously released from the surface of the catalyst, which indicates the occurrence of the reduction reaction in the system.

The catalytic activity of **31** in the reducing reaction of 4-NP mainly depends on AuNPs size. The obtained results indicate that the catalytic reduction reaction using the smallest AuNPs (4.2 ± 1.5 nm) is the fastest, in which the reduction reaction comes to completeness within 7 min, while when the AuNPs size increases the catalytic efficiency decreases and the reaction time become longer. Therefore for further studies we decide to investigate only the catalytic performance of the catalyst. First of all we investigated the influence of $NaBH_4$ concentration on the reduction reaction. The typical time dependent *UV−vis* spectra of 4-NP reduction are shown in Figure 93. At low $NaBH_4$ concentration, e.g., 9 mM, the absorbance intensity at 400 nm decreases slowly with reaction time and a new peak at 300 nm appears simultaneously, corresponding to the characteristic absorption of 4-AP. The reducing reaction is rather slow and only 30% of 4-NP was reduced after 1 h (Figure 93a). On the other hand, the increasing of $NaBH_4$ (25 mM) concentration led to an increase in the reaction rate and the 4-NP was completely reduced after only 6 min (Figure 93b).
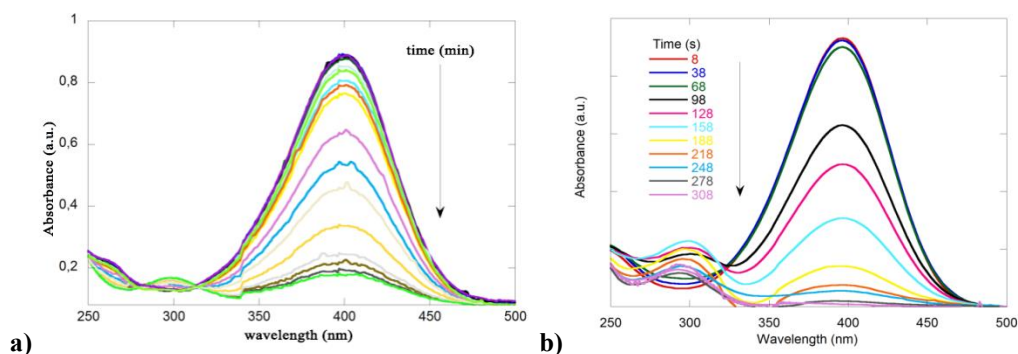
Figure 93. Time dependent UV−vis spectra of the reduction of 4-NP at $NaBH_4$ concentration of **a)** 9 and **b)** 25 mM. The concentrations of 4-NP and AuNPs were 0.050 mM and 0.0286 μg/mL, respectively.

As above mentioned, the k_{app} (s^{-1}) was estimated by the linear fitting of the experimental results and the obtained data are listed in Table 19. As expected the results indicate that k_{app} depends on $NaBH_4$ concentration in the system.

Table 19. Reduction of 4-NP at different $NaBH_4$ concentrations.[a]
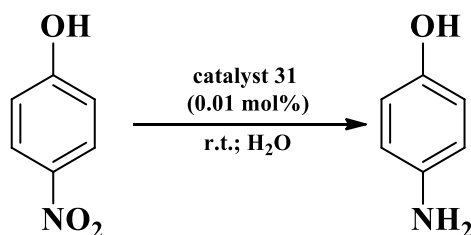
Entry	[NaBH$_4$] (mM)	k_{app} (s^{-1})
1[a]	9	0.00012
2[a]	17	0.00047
3[b]	25	0.00630
4[b]	50	0.01150

[a]Reaction conditions: 0.1 mmM of 4-NP.
[b]Reaction conditions: 0.050 mM of 4-NP and **2** ng mL^{-1} of AuNPs (30 µL of 0.001 mg/mL dispersion).

Since the reduction of 4-NP is strictly depended on the amount of AuNPs introduced in the system we performed an additional study varying the amount of the catalyst (Table 20). Surprisingly, in this case an increase of the catalyst amount led to a decrease in the reaction rate (Figure 94a, Table 20, entry 1).

a)   b)
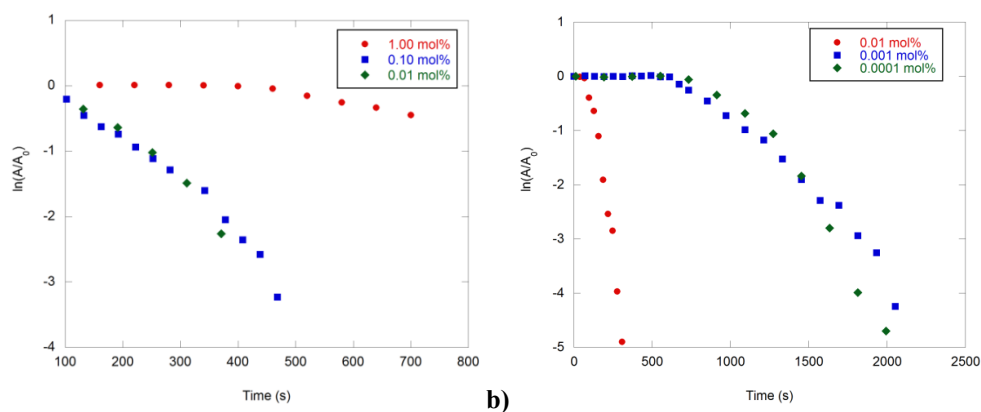
Figure 94. Plot of ln(A/A$_0$) *versus* time at different nanocatalyst concentration. The concentrations of 4-NP and NaBH$_4$ were 0.050 mM and **a)** 25 mM **b)** 50 mM, respectively.

Table 20. Reduction of 4-NP at different catalyst concentration.[a]
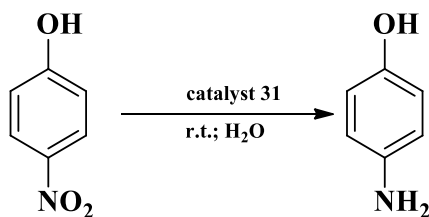
Entry	Au mol%	k_{app} (s^{-1})	TOF (h^{-1})
1	1.01	0.0016	125
2	0.11	0.0069	7,470
3	0.05	0.0068	12,740
4	0.01	0.0063	97,040

[a]Reaction conditions: 0.050 mM of 4-NP and 25 mM of NaBH$_4$.

To further estimate the catalytic efficiency of the new hybrid obtained we calculated the apparent turnover frequency (TOFa) values[36] defined as:

$$TOF_a = \frac{n_p}{n_c \cdot t} \qquad \qquad Equation\ 10$$

where n_p and n_c are the moles of the product molecules and the catalyst during time t, respectively. The obtained results are reported in Table 20.

To deep investigate the catalytic process and to understand this apparently anomalous behavior the colloidal stability of the catalyst in water was investigated by ζ-potential and dynamic light scattering (DLS). ζ-potential data clearly show that, as expected, the –SH surface functionalization of HNT did not alter the surface charge of the nanotubes (Table 21). On the other hand, **31** hybrid system showed a change in the ζ-potential in the direction of a reduction of negative site at the outer HNT surface (Table 21). This effect agrees with the Au linkage to –SH moiety and indicates that the **31** system presents a reduction of its colloidal stability due to electrostatic repulsions. The hydrodynamic radius obtained by DLS experiments provided a clear understanding of the aggregation behavior of the nanoparticles in water as a function of their concentration. Figure 94 shows the trend of the apparent hydrodynamic radius with the catalyst concentration in water. In the dilute regime the obtained size corresponds to that of HNT-SH (dotted line in Figure 95) as the nanomaterials does not undergo to aggregation in the solvent media. Increasing the concentration generates a larger apparent hydrodynamic radius that indicates aggregation among particles with a consequent reduction of the active surface available for the catalytic process. In other words,

due to aggregation one obtains greater particles size and therefore the catalytic active sites accessible to the reactants are reduced and generating worse catalytic performances.
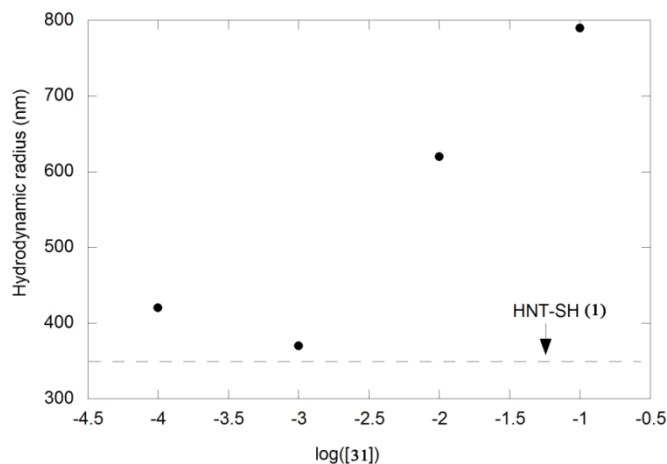
Figure 95. Trend of the apparent hydrodynamic radius with **31** concentration in water (the dotted line represents the apparent hydrodynamic radius of **31** in the same conditions).

Table 21. ζ-potential and DLS data for the nanomaterials investigated at different concentrations.

	Catalyst (mg mL^{-1})	Hydrodynamic radius (nm)	ζ-Potential (mV)
p-HNT	/		37.6±1.4
1	/	175	36.9±1.6
31	0.0001	210	20.6±1.6
31	0.001	185	20.3±1.6
31	0.01	310	20.5±1.6
31	0.1	395	26±2

To the light of the above results we tried to further improve the catalytic performance of the **31**. In particular we performed some additional catalytic tests increasing the amount of NaBH$_4$ to 50 mM and varying the catalyst amount from 0.01 to 0.0001 mol%. The obtained results are collected in Figure 95 and Table 22. The data confirm the DLS results; indeed in an aqueous dilute regime, no aggregation of nanoparticles was observed and the reaction rate depends only on the amount of catalyst.

As it is possible to observe from Figure 95, when the amount of catalyst is very low, there is no change in the absorbance of 4-NP within the first seconds, and therefore the reaction proceeds with an initial induction period (t_0). During this period, the **31** does not seem to participate in the reduction reaction, and the catalysis reaction is paralyzed until the induction period is finished.[37,38] After this t$_0$, the reduction starts and the absorbance of 4-NP decreases at a fast speed. This induction period is normally observed in most of the catalytic reductions involving 4-NP and it is related to the diffusion time required for the adsorption of the

reactants onto the catalyst surfaces before initiation of the reaction. At higher catalyst concentration, probably the adsorption of the 4-NP on the halloysite surface was fast and no induction period is observed. When the catalyst concentration is low, the adsorption of 4-NP needs more time, since less active sites were available and we observed an induction period of several seconds.

Table 22. Reduction of 4-NP at different catalyst concentration.[a]

Entry	Au mol%	k_{app} (s^{-1})	TOF (h^{-1})
1	0.01	0.0115	145,160
2	0.001	0.0048	186,340
3	0.0001	0.0018	2,204,530

[a]Reaction conditions: 0.050 mM of 4-NP and 50 mM of NaBH$_4$.

When catalyst loading was further decreased down to 0.001 mol%, the 4-NP was successfully reduced to 4-aminophenol in a few minutes (entry 2) with an apparent turnover frequency (TOF$_a$) of 186,340 h^{-1}. Further improvement has been obtained by decreasing the amount of gold nanoparticles. Just 0.0001 mol% of HNT/Au (1.97×10^{-8} mg of AuNPs) is sufficient to quantitatively yield the amino derivative in 27 min with a k_{app} value of 0.0018 s^{-1} (entry 3). In such a way, a remarkable TOF$_a$ value of 2,204,530 h^{-1} was achieved. To the best of our knowledge, this value is the highest reported for AuNPs immobilized on a solid support (Table 23).

Table 23. Reduction of 4-NP over different Au nanocatalysts.

Support	AuNPs size (nm)	k_{app} (s^{-1})	TOF$_a$ (h^{-1})	Ref.
PMMA	6.9	7.2×10^{-3}	88.6	[39]
CNs	10-30	2.1×10^{-3}	109	[36]
Chitosan	3.1	1.2×10^{-2}	50.4	[40]
AOBC	10.6 ± 2.9	4.5×10^{-3}	1198	[41]
CSNFs	5	5.9×10^{-3}	563	[42]
NCC-G$^{AT}_0$	3.5	2.8×10^{-3}	608	[43]
SBA-15	2.3	1.7×10^{-2}	[a]	[44]
NC	5.7	3.6×10^{-3}	1185[b]	[32]
Glucan	8	1.9×10^{-3}	5922	[45]
HNT	4.2 ± 1.5	1.8×10^{-3}	2,204,530	

[a]No data available [b]Calculated as the rate constant divided by the amount of gold on the support.

These interesting results could be explained by a synergistic effect between halloysite and AuNPs in the hybrid nanomaterial. In fact, the hollow nanotubular structure of halloysite with high specific surface areas and considerable adsorption ability, promotes the diffusion of the reactants and the adsorption rate. Besides, the surface chemical structures of rolling silica tetrahedral layers and alumina octahedral layers with a higher conduction band edge in halloysite, may modulate interfacial electron transfer dynamics. On the basis of these evidences we proposed a reaction mechanism as follow.

The catalytic reaction on the AuNP surface has been hypothesized to follow a Langmuir−Hinshelwood mechanism,[31,38] where both BH_4^- and 4-NP initially adsorb on the nanoparticle surface where the BH_4^- adsorption transfers a surface-hydrogen species to the surface of the particles.[46] Halloysite could significantly attract the negatively charged nitrophenolate and BH_4^- ions through electrostatic interaction, resulting in their enrichment on HNT/Au surface. Thus borohydride ions could be easily adsorbed onto the surface of gold nanoparticles to react and transfer electrons to the them. Therefore, electrons leave the gold nanoparticles and end up with an electron enriched region at the interface of gold nanoparticles and halloysite support. The existence of the surplus electrons added to the HNT surface facilitates the uptake of electrons by the adsorbed 4-nitrophenol molecules, which leads to the reduction of 4-nitrophenol into the 4-aminophenol (Figure 96).
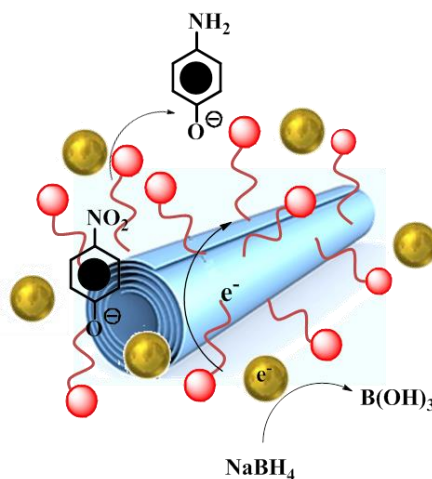
Figure 96. Cartoon representation of the catalytic mechanism proposed.

To study the recyclability of **31**, the same catalyst was used to perform the same reduction reaction for the consecutive runs. After each catalytic cycle, the catalyst (5 mg) was centrifuged, washed several time with water and dried for the next cycle of catalysis. The catalyst exhibits high activity in the same reaction time (30 min) after running for 10 cycles without presumably leaching of gold nanoparticles (Figure 97). Such results indicate that the presence of thiol functionalized halloysite as support for gold, was sufficient to stabilize the

catalytic nanoparticles by preventing their aggregation, producing a good catalyst with high activity and stability.
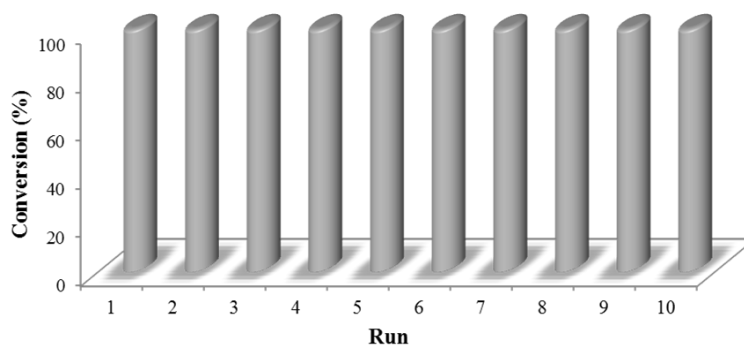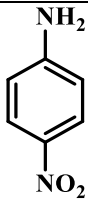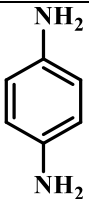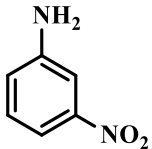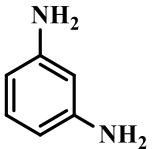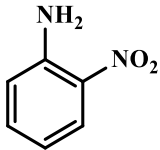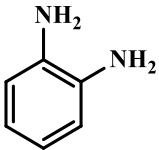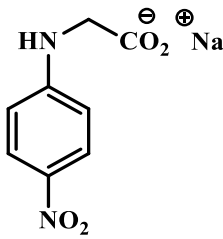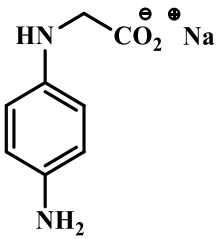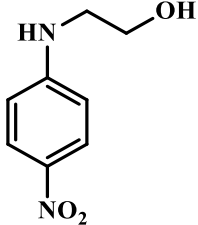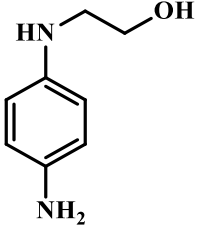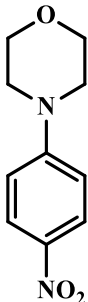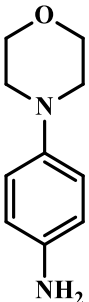
Figure 97. Recycling tests of catalyst **31** nanocatalyst.

Hence, the applicability of the reaction has been checked on a set of nitroarene derivatives having either electron-donating or electron-withdrawing groups in different positions respect to the nitro group (Table 24). To achieve this scope we choose to run the reactions in the presence of 0.1 mol% of catalyst with 50 mM of $NaBH_4$ to clearly monitor the conversion efficiency of the reaction. It is seems clearly that the presence of a strong electrondonating substituent at the para position with respect to the reacting nitro group, is an important requirement for the reaction to occur (entries 1, 4, 5, 6). In particular, 4-nitroaniline (entry 1) and 4-(4-nitrophenyl)morpholine (entry 6) are more reactive than other nitroaniline derivatives, while the methyl 2-((4-nitrophenyl)amino)acetate (entry 8) is not reactive at all. The presence of substituent in meta or orto position with respect to nitro group significantly reduces the reaction rate. The N-substituted derivative (entry 7) shows less reactivity than the correspondent nitroaniline compound (entry 4); despite alkyl substituents on the N atom should enhance the overall electrondonating character of the group. Furthermore, it was observed that the presence of a negative charge on the ancillary chain bound to the N atom (entries 4 and 7), disadvantages the reduction reaction. This probably reflects a more difficult approach of the anionic reducing agent to the nitroarene-catalyst.[47]

Table 24. Reduction of various nitroarenes using the HNT/Au catalyst.[a]

Entry	Substrate	Product	Time (min)	k_{app} (s^{-1})	TOF$_a$ (h^{-1})
1			144	4.2×10^{-4}	416
2			252	1.0×10^{-4}	238
3			1175	2.1×10^{-5}	54
4			600	2.66×10^{-5}	100
5			638	7.6×10^{-5}	86
6			223	1.3×10^{-4}	270

7			240	7.8×10^{-5}	124[b]
8			/	/	/
9			1000	9.2×10^{-6}	71[c]
10			540	1.1×10^{-5}	856[b]

[a] Reaction condition: nitroarene 0.1 mM, 0.1 mol% of HNT/Au catalyst (0.0197 µg of AuNPs), 0.50 mM of NaBH$_4$.

[b] The absorbance value reaches a plateau after that the reaction does not continue.

[c] The reduction reaction was stopped after 1000 min.

We finally focused the attention on the use of flow technology as an alternative efficient stirring method able to preserve the efficiency of a heterogeneous catalytic system, simplify its recovery and reuse.[3]

In particular, the reduction reaction takes place inside a glass tube column using a mixture of sand impregnated with 1 wt% of the **31**, as stationary phase and water as mobile phase. The column was connected, by using the appropriate tubes and valves, to a peristaltic pump. Sand was added as inert support to both improve the flowability of the overall system and minimize the amount of catalyst in the column (Figure 98). The reaction mixture was injected in the column at a 1.0 mL min^{-1} flow rate for 30 minutes. In these conditions in the collected fraction we observed that the 70% of 4-NP was reduced. The column has been running for one month and it still works well without any loss in catalytic activity confirming the good recyclability of the catalyst.
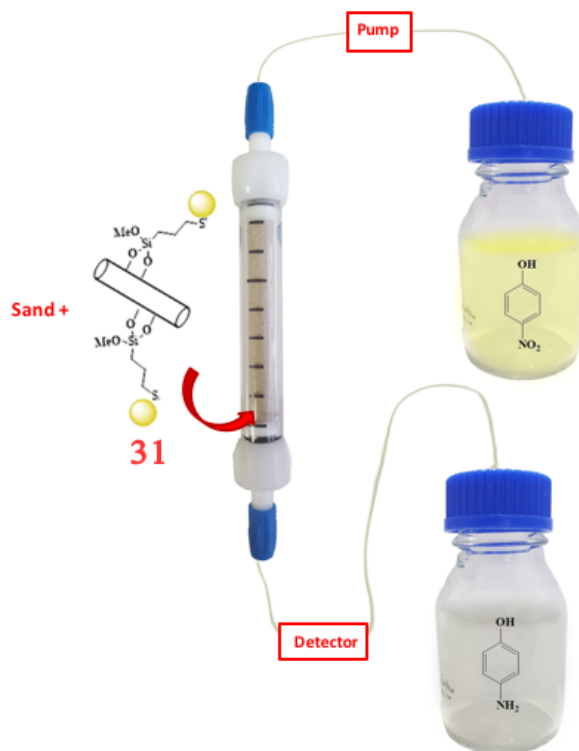
Figure 98. Flow system for **31** catalytic tests.

6.3. Cobalt Nanoparticles on Halloysite Nanotubes, Morphology, Properties and Preliminary Study on Catalytic Activity

In the last years, nanomaterial based on Cobalt nanoparticles (CoNPs) and its oxide, have been widely used as catalysts. Due to the fact that Co nanoparticles present a relatively slow spontaneous oxidation in air, and tunable oxidation process in the presence of other gases,[48–50] CoNPs and Co_2O_3 composites have been used for VOC emissions abatement by oxidation reactions,[51–53] CO and CO_2 conversion,[50,54] and other reactions as Fischer–Tropsch.[55–57]

The Fischer-Tropsch process is an important industrial synthesis that allows to hydrocarbons of different types starting from gaseous reactants such as carbon monoxide and hydrogen. For the realization of this process, different types of metal catalysts are used and studied, such as cobalt and its oxides, ruthenium and iron. Some of these, or their mixtures, are particularly appreciated since they can selective produce alkyl derivatives with different length and different molecular chains. In this context, nanoparticles as Ru, Fe, Co, Rh, Ni, Ir, Pt and Pd, respectively, show a decreasing of the molecular average weight of hydrocarbons produced by Fischer-Tropsch.

In particular, the Ru nanoparticles, followed by iron, nickel, and cobalt, are the most active metals for the hydrogenation of carbon monoxide and, more important they are, among

the plethora of metal nanoparticles, the only ones which possess the characteristics for commercial production applications.

In practical application, catalysts based on Ni produce too much methane. Ruthenium is too expensive and not enough abundant for large-scale industry applications.

Cobalt and iron were the first proposed metal catalyst for syngas conversion, by Fischer-Tropsch process, and both have been used in the industry for hydrocarbon synthesis. Cobalt, though more expensive, are more resistant to deactivation, and are more active when the feedstock is natural gas.

An important parameter is also the dispersion of the catalyst that is able to influence the distribution of the products.[57]

The catalytic performance of Fischer-Tropsch catalysts are strongly depended on the methods of catalyst preparation. The metal particles are usually supported on high surface area supports such as alumina, silica, or zeolites. The goal of active phase deposition is to spread cobalt onto porous support, and usually, as far as is concern the use of Cobalt-supported catalysts, they are prepared by impregnation. This consists in the deposition of a solution of the metal precursors on a dry support.

The impregnation method is based on very simple idea, but the fundamental phenomena underlying impregnation and drying are extremely complex, this this makes reproducibility very difficult.[58]

Recently several catalysts based on halloysite have been studied for application in the field of fuels. For example, an halloysite catalyst functionalized by NiO and CoO was obtained in order to have the hydro-cracking of heavy petroleum residues obtained by vacuum distillation.[59]

Other halloysite based catalysts, containing nano cobalt and copper particles, were tested for the on degradative capacity of toluene.[60] A catalyst of Co-halloysite were, also, prepared by double-solvent and wet-impregnation methods.[57]

Zhao *et al.* synthesized, via a one-pot solvothermal method, Co particles anchored outside and at the inner surface of the HNTs, using amine functional halloysite nanotubes as support materials. The obtained composites show good catalytic activity to generate H_2 gas by hydrolysis of $NaBH_4$ solution, increased by higher dispersion of the Co particles and lower Co content and with the ability to be used for several times without loss in the catalytic activity.[61]

Halloysite nanotubes modified with 3-aminopropyltriethoxysilane (**32**) have demonstrated the ability to efficiently absorb cobalt ions from waste water solutions.[62]

During the period at the Lousiana Institute of Technology, under the supervision of Prof. Y. Lvov, I performed some experiment in order to prepare and test some catalytic materials based on Co nanoparticles and halloysite nanotubes. Different materials were developed based on Co nanoparticles supported on pristine and modified halloysite.

The functionalization of halloysite was achieved by the covalent grafting of 3-aminopropyl trimethoxysilane on the external surface of HNT. The experimental procedure reported for this synthesis is shown in Scheme 13 and followed the synthetic route reported in Chapter 4 for the synthesis of compound **8**.
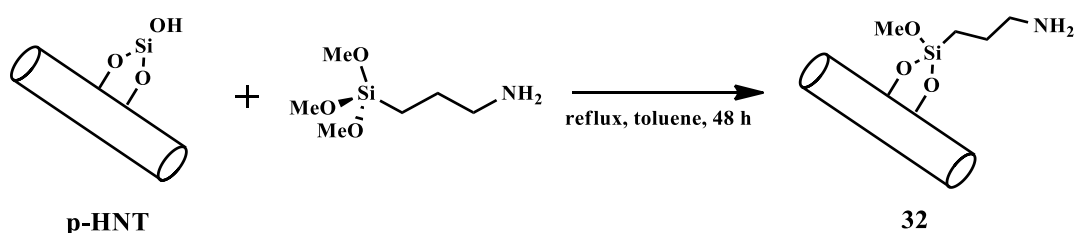
Scheme 13. Schematic representation of the synthesis of compound **32**.

Following this procedure a loading of 2.5 wt% of the organic portion on halloysite surface was obtained, as estimated by TG analysis. The successful functionalization was also confirmed by contact angle measurements. The contact angle, in water, of compound **32** is $61.2\pm1.3°$ greater than that of pristine HNT ($21.9 \pm1.3°$). The increased value could be due to the introduction of an alkyl chain on the halloysite external surface and therefore an hydrophobization of the system.

6.3.1 Thermal decomposition HNT-Co Synthesis

Thermal decomposition is one of the most common techniques to obtain supported metal nanoparticles starting from different salts. Organic ligands, in particular, under appropriate heating, are removed, living the metals adsorbed on the supporting material.

Generally, Co^{2+} ions are immobilized on a support by electrostatic interactions between the ions and the supports. The common porous material such as alumina, silica, and titania have different points of zero charge, and, for this reason, the operative pH is crucial in order to obtain an homogenous distribution of the ions on the support. Another factor that affects the distribution of the metal on the support are the reduction conditions. Indeed, these are indispensable for obtaining cobalt metal particles from the decomposition of cobalt salts.

After initial physical adsorption, the metal ions interact with the active surface sites such as surface oxygen, hydroxyl groups and amino, or others grafted groups. Thermal decomposition, can also provide to the oxidization of supported metal complex to cobalt oxides.[58]

In order to obtain cobalt nanoparticles supported on halloysite nanotubes materials by thermal degradation, different experiment were performed by mixing the reactants in different proportions. The experimental procedure adopted involves the impregnation of the nanotubes through many sonication-drying cycles. Generally, a small amount of a saturated solution of Cobalt(II) acetylacetonate (Co(II) acac) in acetone is added dropwise on HNT nanomaterials (in different, followed by a sonication treatment for 5 minutes and finally dried, under air, at 80 °C. The entire procedure was repeated until all the salt was added.

The mixture was finally calcined, under N_2 flow, with a heating rate of 10 °C·min^{-1} from room temperature to 300 °C or 370°C, maintained at that temperature for 1.5 h and then slowly cooled down. The maximum temperature and the heating time were chosen from TGA data of the precursor. Indeed these values allow to obtain the complete disappearance of the organic ligand but not to give thermal degradation of the halloysite. The best experimental results were obtained by mixing 1:1 in weight of Co(II) acac (23 wt% of Co in the metal salt) and HNT or the compound **32**. The obtained compounds are listed in Table 25.

Table 25. Summary of HNT/Cobalt samples.

	1:1 by wt. HNT/ Co(II) acac	1:1 by wt. HNT/Co
p-HNT	Compound **33a**	Compound **34a**
32	Compound **33b**	Compound **34b**

From thermogravimetric analysis of the precursors of **33a** and **33b** results one loss in weight of approximately 30% from 100 °C to 300 °C due to the organic ligand.

It is noteworthy the appearing of a splitting of the characteristic HNT loss mass at 500 °C, generally attributed to the loss of interstate water, Figure 99.[63]

It is known that some small molecules could be intercalated in the interlayers space, changing the distance between the layers and the chemical neighborhood of the water molecules present.[64] The split of the weight loss can be due to the partial intercalation of molecules or small molecular systems. After heating the nanomaterial at 300 °C, the TGA showed that the thermograms of the compound was similarly to that of **p-HNT** with only one difference; the characteristic mass loss relative to the halloysite in this latter case, showed a degradation temperature lower of c.a. 10 °C with respect to **p-HNT**. It is important to note

that after thermal degradation, the relative loss in weight due to the grafted amino silane disappears too. It means that all of the obtained materials, after calcination, showed the feature of pristine halloysite and the metal. Therefore the use of modified halloysite for the synthesis of Co nanoparticles supported on HNT is necessary to ensure a better loading of the metal salt on the solid support.
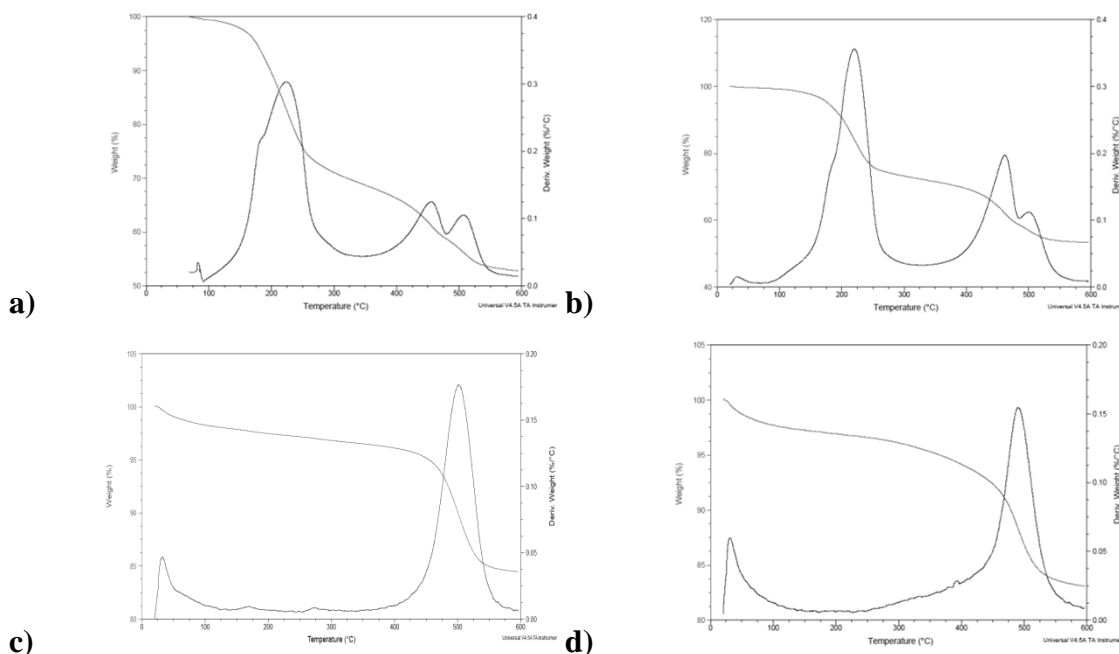
Figure 99. Thermograms of **a)** precursor compound **33a**, **b)** precursor compound **33b**, **c) p-HNT**, **d)** compound **33b**.

The percentage of cobalt nanoparticles present on HNT was estimated by EDX analysis showing 16.9 ± 2.8% for **33a** and 18.1 ± 4.1% for **33b** respectively, as expected by stoichiometric consideratins.

In order to estimate the properties of the new materials, the surface area and the porosity for the future catalytic applications, gas adsorption-desorption measures were performed.

Table 26. Specific Surface Area and porosity analysis.

	Surface Area[a] m^2/g	Pore Volume[b] cc/g	Pore Radius[b] $Å$
p-HNT	20.88	0.1885	33.355
33a	27.81	0.2225	20.821
33b	40.36	0.9055	not available

a) Determinate by BET theory; b) Determinate by BJH theory

As shown in Table 26, the new materials have increased value of surface area and total pore volume. These parameters are very important in the catalytic applications of materials, because, an increased active surface means a more active catalyst.

TEM and SEM micrographs of the final samples show that the characteristic lengths and the tubular shape of HNT were preserved. From statistical analysis it was found that the metal nanoparticles possess a mean diameter size of 5 nm. Surprisingly, the SEM micrograph of compounds **33b** shows the presence of some cluster of cobalt nanoparticles present also into the inner surface of a semi-unwound sheet of the tubes (Figure **100a, b**). For the best of my knowledge this represents the first case ever reported. Although TEM imagines show, in the case of compound **33b**, the homogeneous coating of the halloysite tubes with particles both on the external surface and in the interlayer of the tubes, XRD analysis has confirmed that no modification in interlayer distance occurred.
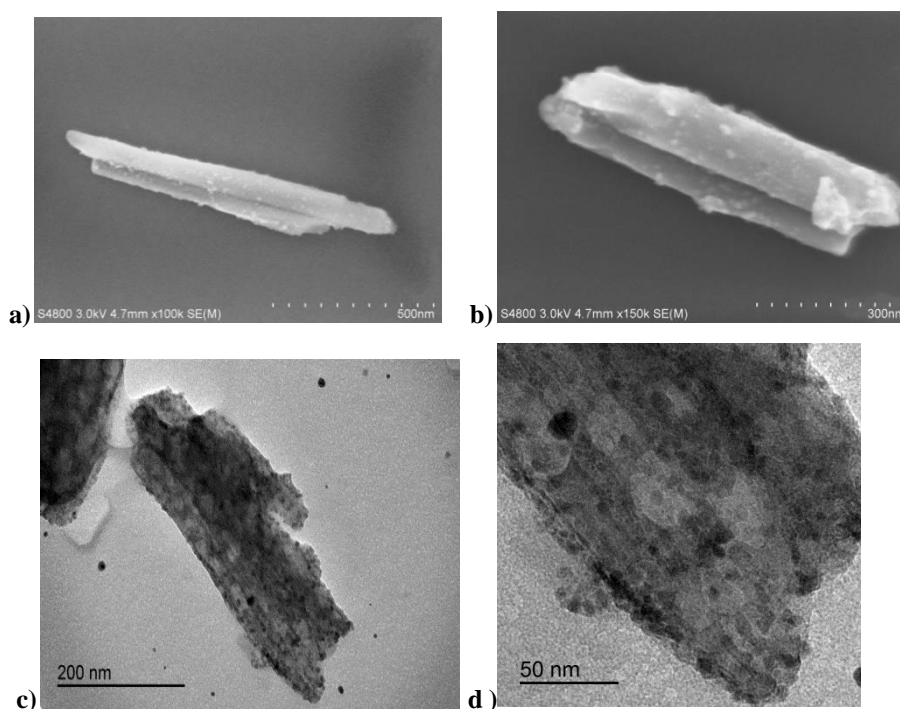
Figure 100. a, b) SEM micrographs of compound **33a**, **c,d)** TEM micrographs of compound **33a**

Th experimental procedure described above was also used to obtain two materials with a 50 wt% of cobalt (compounds **34a** and **34b**, respectively). The thermogravimetric analysis shows that both materials present a wide mass loss of approximately 43% from 100 °C to 370 °C due to degradation of the organic ligand. In this case it is noteworthy that these mass losses did not occur at one temperature, but, as it is possible to note in Differential thermal analysis curves, different relative maxima are present. In addition, the typical mass loss of HNT undergoes a drastic shift from 500 °C to 460 °C in both samples. The thermograms registered after calcination shows that the mass loss of HNT still presents a degradation temperature of 460 °C.
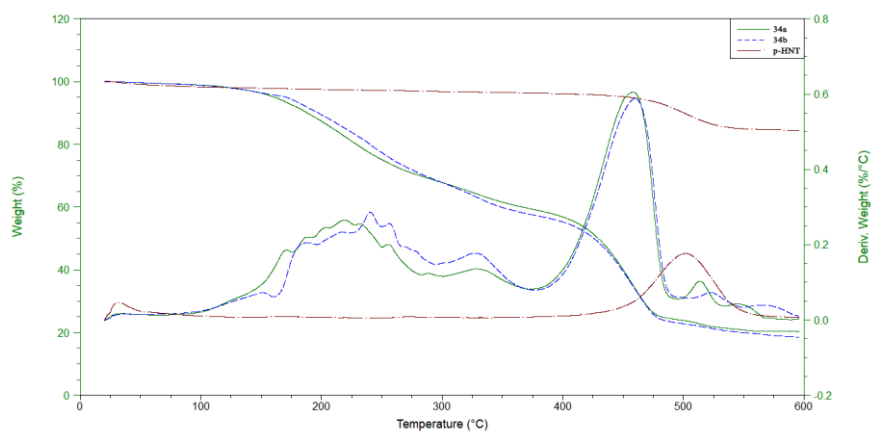
Figure 101. Thermograms of precursor compound **34a**, **34b** and **p-HNT**.

SEM and TEM micrographs show that the tubular structure in unaltered, but is possible to note how the particles completely coating the tubes and are clustered each other forming different dimension aggregation close and far from the tubes.
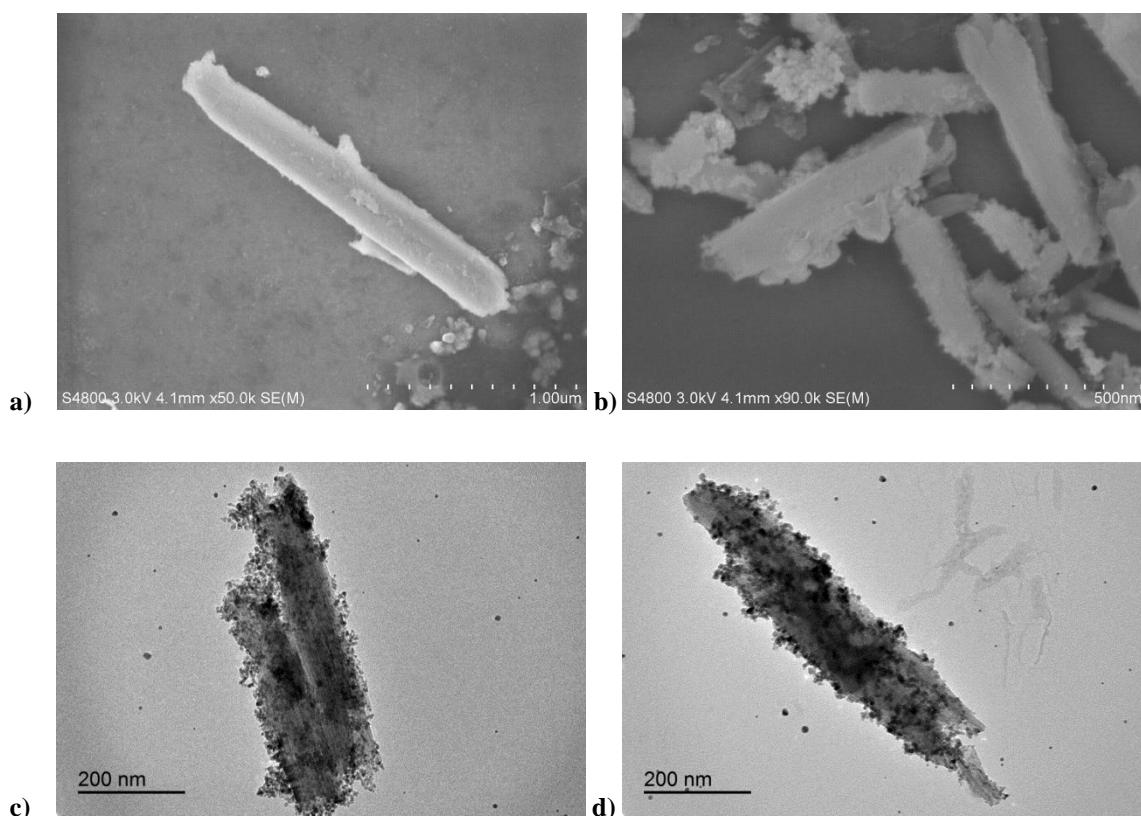
Figure 102. a, b) SEM micrographs of compound **34a**, **c,d)** TEM micrographs of compound **34a**.
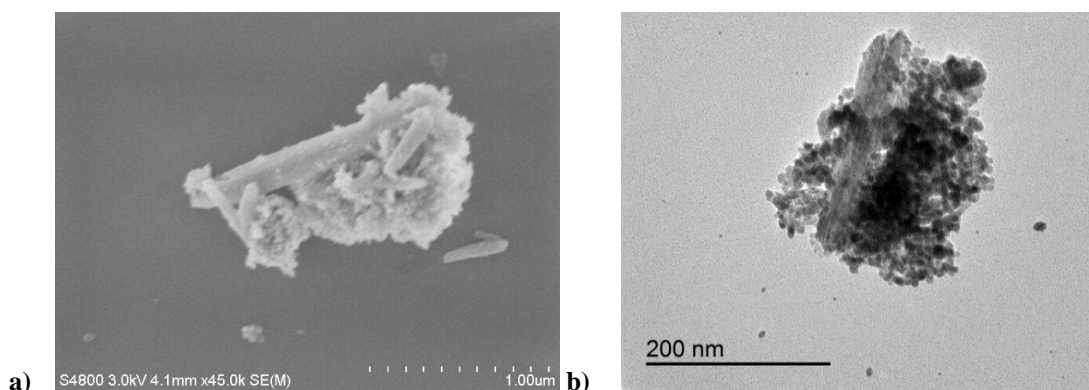
Figure 103. a, b) SEM and TEM micrographs of compound **34b**.

In this case it was not possible to calculate the percentage of the metal nanoparticles immobilized on the support by means EDX measurements since the sample was inhomogeneous in composition with the nanoparticles forming a thick layer on the tubes. For the same reasons, gas adsorption-desorption measurements showed a significant decreasing of the porosity.

Co nanoparticles have shown good ability on the catalytic reduction 4-nitrophenol and the H_2 generation from $NaBH_4$.[61,65] therefore in order to test the catalytic activity of the obtained materials in the nitrophenol reduction mediated by $NaBH_4$, compound **33b** was chosen as model.

Preliminary studies were performed to test the influence of the concentration of Co in the reduction reaction. The obtained results are reported in Table 27. As it is possible to note, as expected, the value of k_{app} decreases proportionally to the Co present. The catalyst based on HNT showed goods catalytic activity despite the introduction of a very low amount of $NaBH_4$.

Table 27: TOF and k_{app} values at different at ratio of catalyst and substrate

Entry	% molCo/mol 4-NP	$NaBH_4$/4-NP	TOF (h^{-1})	kapp (s^{-1})
1	25.5	1.8	80.7	1.29E-2
2	8.5	1.8	177	7.0E-3
3	4.2	1.8	157	4.0E-3
4	0.8	1.8	123	3.0E-4

Moreover the TOF value, increases with the decreasing of catalyst and finally decreases at lower concentration of Co.

Subsequently, keeping the concentration of catalyst constant, the influence of $NaBH_4$ concentration in the reaction was investigated. As reported in Table 28, in this case we observed. The values of k_{app} are, for the investigated ranges, almost unchanged. The value of TOF, on the other hand, rapidly decreasing. More accurate tests aimed at assessing the catalytic effectiveness of the system are currently underway.

Table 28. TOF and K_{app} values at different at ratio of $NaBH_4$.

Entry	% molCo/mol4NP	NaBH$_4$/4NP	TOF (h^{-1})	k_{app} (s^{-1})
1	4.2	1.8	157	4.0E-3
2	4.2	1.1	94.1	3.2E-3
3	4.2	0.7	58.8E	2.1E-3

6.3.2 Chemical reduction synthesis for HNT-Co materials.

Afterwards we investigated a different reduction method to obtain metal nanoparticles. In this context the chemical reduction using $NaBH_4$ is a common way to prepare metal nanoparticles. [66]

$$2Co^{2+} + BH_4^- + 2H_2O \rightarrow 2Co_{(s)} + 2H_{2(g)} + 4H^+ + BO_2^-$$

During the reduction process is possible to observe a vigorous bubbling due to the H_2 formation that accompanies particle formation. The reaction could be drive also to the formation of some Co_2B species.[67]

Exploiting the ability of $-NH_2$ groups to bind cobalt ions, compound **32** was used as starting material to synthetize systems with potential catalytic activities based on HNT and cobalt.

Compound **32** was, in a first attempt, washed several time with a 0.1 M NaOH aqueous solution, which allows the deprotonation of eventually present amine groups and, at the same time, increases the negative charges on the outer surface of the halloysite. Therefore, this preliminary treatment could be beneficial in order to increase the potential binding sites on the HNT/Co catalyst. The obtained activate material was then dispersed in a acetone solution of Co(II) acac and stirred, at room temperature, for a reaction time of 24 h. The material was then washed several times with water and dried at 60 °C overnight.

Finally, the pink powder obtained was reduced by adding dropwise an aqueous solution of $NaBH_4$ to give the compound **35a**.

It is interesting to note that, adopting this experimental procedure, pristine halloysite cannot support any Co nanoparticles. The obtained catalyst was characterized by several techniques. From TGA data was not possible to observe any differences I the thermograms compared to that of the precursor **32**.

The morphology of the material was investigated by means of SEM investigations; as it is possible to note from Figure 104, also in this case the tubular structure of HNT was preserved after functionalization. The percent loading of the metal nanoparticles in the catalyst, estimated by EDX analysis, is of 10 wt%.
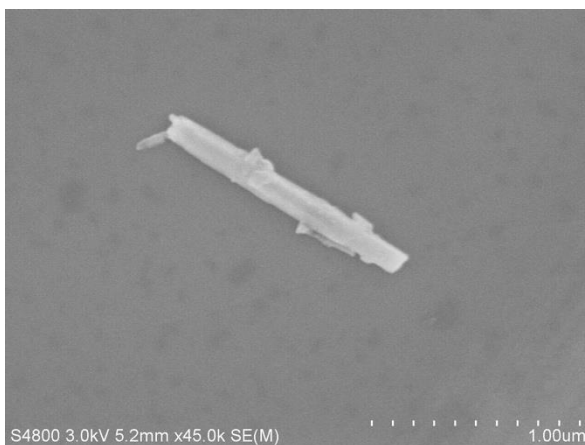
Figure 104. SEM micrograph of compound **21a**.

In order to further improve the nanoparticles loading on the support another synthetic approach was performed. In details compound **32** was refluxed in the presence of the Co(II) acac salt solution and then reduced. Unfortunately, the material so obtained (compound **35b**) showed only the 2.3±0.1 wt% of loading and the presence of metal clusters on the HNT surface as highlighted from TEM image (Figure 105). Therefore this material is not further investigated.
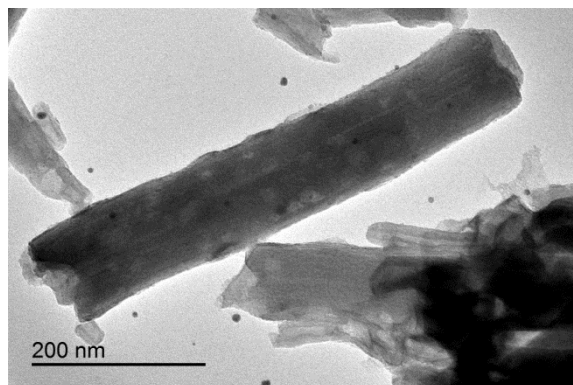
Figure 105. TEM micrograph of compound **35b**.

6.3.3 One step preparation and catalytic ability preliminary tests

As previously mentioned, NaBH$_4$ is also used as reducing agent in the catalytic reduction of 4-NP. To the best of our experiences, up to now, there is not any report of simultaneous production and catalytic activity of metal nanoparticles on halloysite, therefore we performed an additional synthetic pathway where the metal was reduced *in situ* during the reduction reaction of 4-NP by NaBH$_4$, chosen as model.

To achieve this objective, first of all, the Co(II) acac salt was immobilized on **p-HNT** surface (compound **36**). The successful loading was confirmed by SEM investigations which show the presence of completely coated tubes, due to the coating layer of salt's crystals.
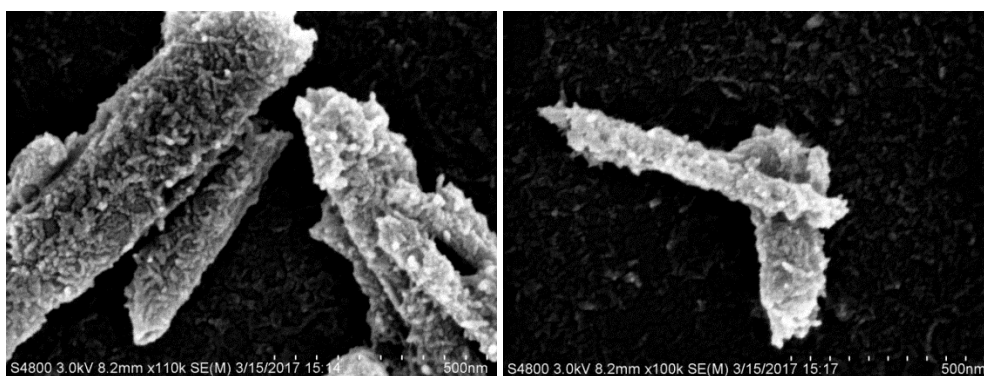
Figure 106. SEM micrographs of compound **36**.

The presence of salt was also proved by FTIR spectra. In Figure 107 are reported the FT-IR spectra of pristine HNT and compound **36**.

As it is possible to note, the FT-IR spectrum of compound **36** shows the presence of additional IR bands related to the vibration stretching bands of the Co(II) acetylacetonate salt in the HNT.
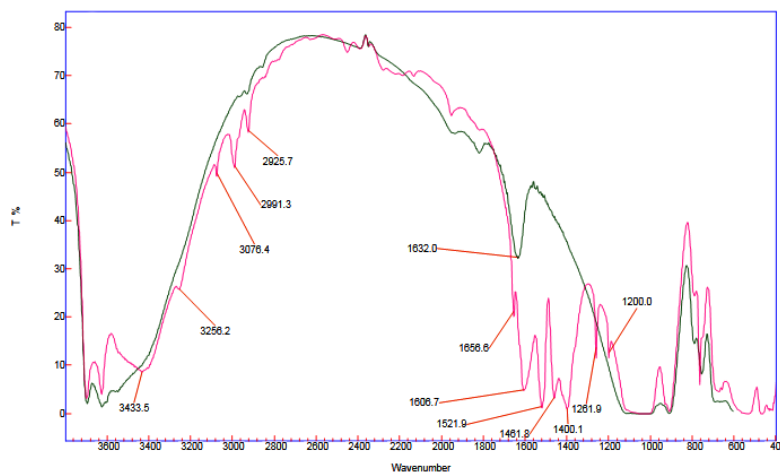
Figure 107. IR spectrum of **36** (purple) and **p-HNT** (green).

The percentage of Co in the sample is, estimated by EDX, 11.5 %wt%.

To gain some information about the rate of the reduction of the Co salt in the presence of NaBH$_4$ some UV-*vis* measurements were carried out.

The aqueous solution of compound **36** (0.1 mg mL^{-1}) shows an absorption maximum at ca. 290 nm, attributed to the singlet $\pi \rightarrow \pi^*$ transition[68] which disappears in the presence of NaBH$_4$ within time (Figure 108).
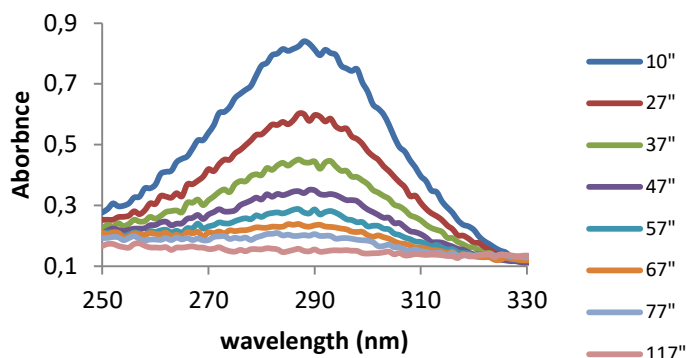
Figure 108. UV spectra of **36** 0.05 mg/mL dispersion in DI water (9.7E-5 M in Co) and NaBH$_4$ 2.5E-2 M at different times at 20°C.

Figure 109 shows the trend of the absorbance at 290 nm as a function of time.

From the fitting of experimental data, it was possible to obtain the k_{app} of the process, that is of $3.73 \times 10^{-2}\,\text{s}^{-1}$.
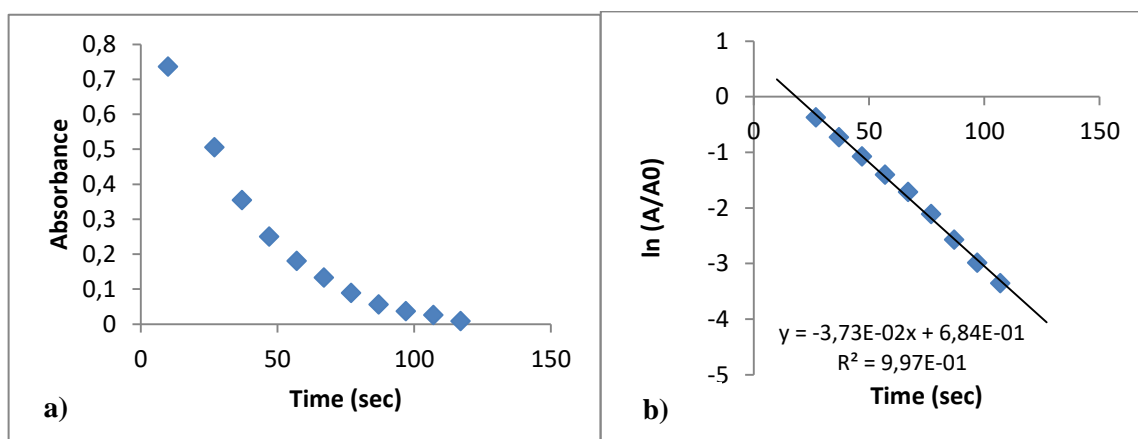
Figure 109. a) Absorbance at 290 nm as a function of time **b)** ln (A/A0) at 290 nm as a function of time

As far as is concern the 4-NP reduction, preliminary studies showed that the reaction did not occur both in absence of NaBH$_4$ and compound **36** (Figure 110). In this latter case a wide

absorption band around 300 nm was also observed, due to the presence of the metal salt in the HNT support.
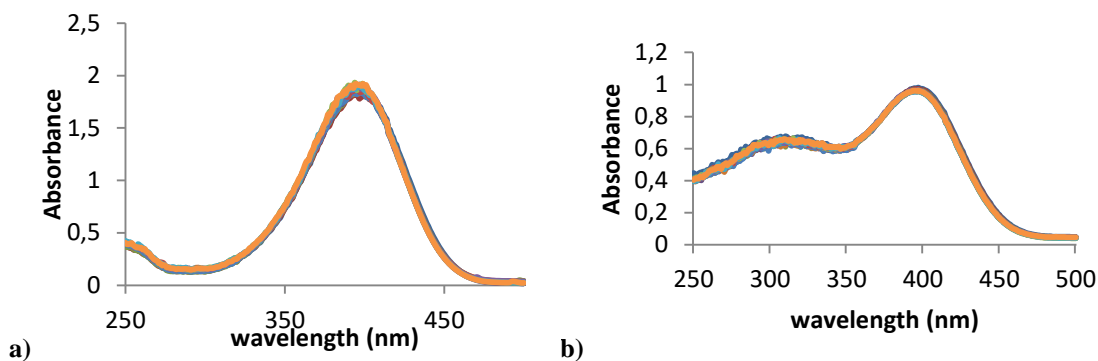
Figure 110: **a)** Spectra of 4-NP and NaBH$_4$ solution at different times; **b)** Spectra of **20** and 4-NP solution at different times

First of all, the catalytic reduction of 4-NP in the presence of NaBH$_4$ and **36** was investigated by varying the concentration of Co. Indeed, the high catalytic efficiency with low metal loading is one of the important goals of a good catalyst. The trend of the absorbance of 4-NP as a function of time is shown in Figure 111.
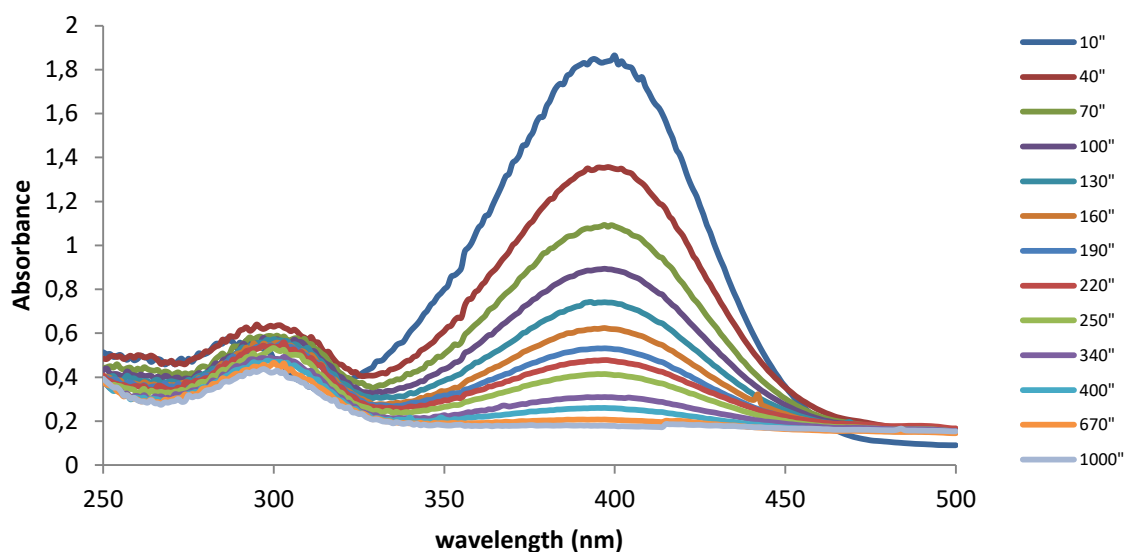
Figure 111. Spectra of **36** (97% w/w), NaBH$_4$ and 4-NP solution at different times.
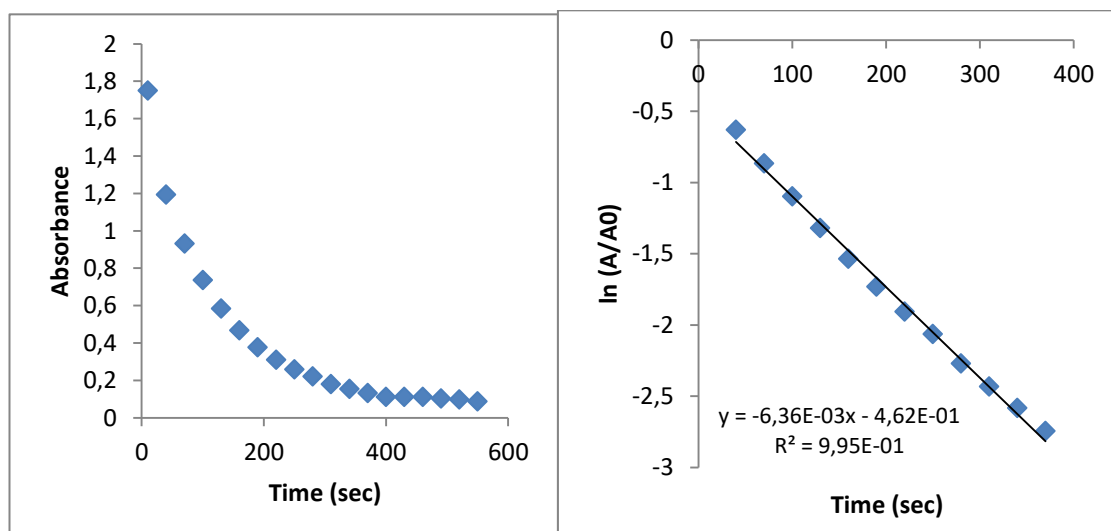
Figure 112. a) Absorbance at 396 nm as a function of time **b)** ln (A/A0) at 396 nm as a function of time

From the plot of ln (A/A$_0$) (Figure 112), it was possible to find out the k_{app} of the process that is 6.4×10^{-3} s^{-1}, ten times smaller than that observed in the case of the only catalyst.

The experiment was repeated to find out if the catalyst and the 4NP reactions could influence each other. At first were added the dispersion of **36** and NaBH$_4$, after 2 minutes was added the solution of 4NP. The reduction proceeds, as previously observed, and the value of k_{app} is the same of the "one step" experiment.

The experiments were repeated varying the ratio of catalyst and substrate. The obtained k_{app} are reported in Table 29.
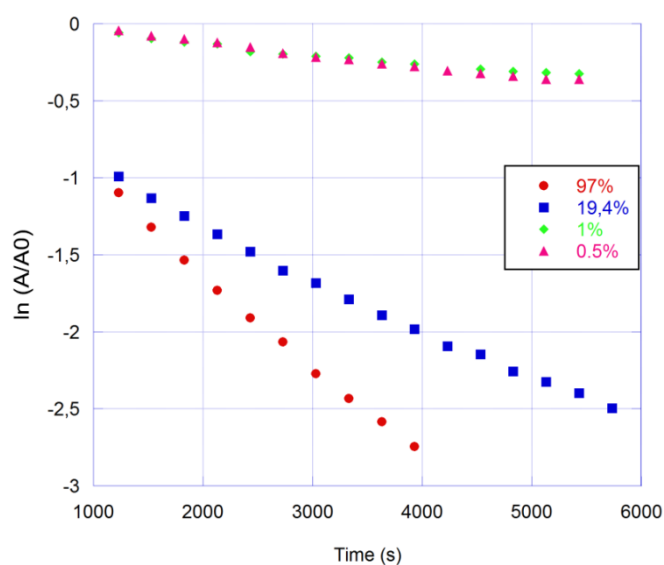
Figure 113. ln (A/A0) at 396 nm as a function of time at ratio of catalyst and substrate

Table 29. k_{app} values at different at ratio of catalyst and substrate

% mol Co/ mol 4NP	k_{app}	R^2
97	6.4 E - 3	0.995
19.4	3.3 E - 4	0.993
1	6.3 E - 5	0.973
0.5	7.9 E - 5	0.987

Table 30. TOF and k_{app} values at different at ratio of $NaBH_4$.

% molCo/mol4NP	$NaBH_4$/4NP	TOF (h^{-1})	k_{app} (s^{-1})
97.2	250	1.19E+01	6.4 E - 3
19.4	250	1.45E+01	3.3 E - 4
1.0	250	8.17E+01	6.3 E - 5
0.5	250	4.93E+01	7.9 E - 5

As it is possible to observe the k_{app} value decreases with the decreasing of catalyst concentration as expected. Indeed, less cobalt nanoparticles are present, less active surface sites are available for the reaction with 4-NP.

6.4 Metal nanoparticles supported on Halloysite Nanotubes for self-assembly and auto repair systems.

As mentioned in the introduction of this chapter, in the last years there has been an increasing interest from the scientific community towards the synthesis of organized systems on nanometric scale. This was more highlighted tanks to the 2016 Nobel Prize awarded to Prof. J. Sauvage, J. Stoddart and B. Feringa.

Self-assembly is one of the most important phenomena that is exploited for the establishment of structures organized at the nanometric level.

In the bottom-up building, the materials and devices are made by autoaggregation of molecular building blocks drove by chemical bonds and supramolecular interactions.

Molecular systems tend to organize themselves *via* self-assembly to form macro molecules systems, as proteins than cellular organelles, tissue and so on until living being. These systems have high efficiency and exceptional properties as the self-replication and the self-repeating.

A big challenge for the scientist of present and future is the building of analogs artificial system. This is a long way, but, some materials with attractive self-organizing and self-repairing ability are real. More steps are done in artificial molecular machines direction build, making real the dream of Feynman to have nanometric motors and machines.

Recently, some system based on halloysite nanotubes have shown abilities to organizing them self in ordinate structures. It has been observed that a drop of dispersion of halloysite nanotubes, loaded with molecules able to increase, in absolute value, the value of ζ-potential if left to dry, presents at the edges a "coffee-ring" in which the nanotubes are arranged according to an arrangement oriented.[69]

Analogous behaviors were observed if an appropriate dispersion of HNT is it is placed on a metallic sphere and let dry[70] or in special glass capillary system in case of HNT loaded with polystyrene sulfonate.[71]

A highly oriented layer of halloysite on polyacrylonitrile porous membrane has also studied for molecular separation, absorption, and biomedical applications.[72]

By selective functionalization of halloysite lumen by click reaction, was possible to obtain halloysite organized fibers.[73]

Similar phenomena have been also find out in carbon nanotubes systems and modified magnetic particles with surfactants under specific stimuli, observing high degrees of fiber organization and in some cases interesting properties such as auto repair ability.[74–76]

Based on the above finding, during my PhD, I also focused my attention on the development of organized nanosystems based on halloysite and ferrite nanoparticles.

The materials obtained by refluxing the pristine halloysite in the presence of Fe(II) and Fe(III) respectively, showed a ferromagnetic behavior (Figure 114d) and a percent loading of nanoparticles onto the HNT of 5 wt% as estimated by TGA (**37**).

The material shows values of apparent hydrodynamic radius and ζ–potential close to that of pristine HNT.

The morphology of the HNT/ferrite nanomaterial was imagined by SEM.

SEM images (Figures 114a-c) show that the HNT are coated with ferrite nanoparticles with an inhomogeneous distribution.
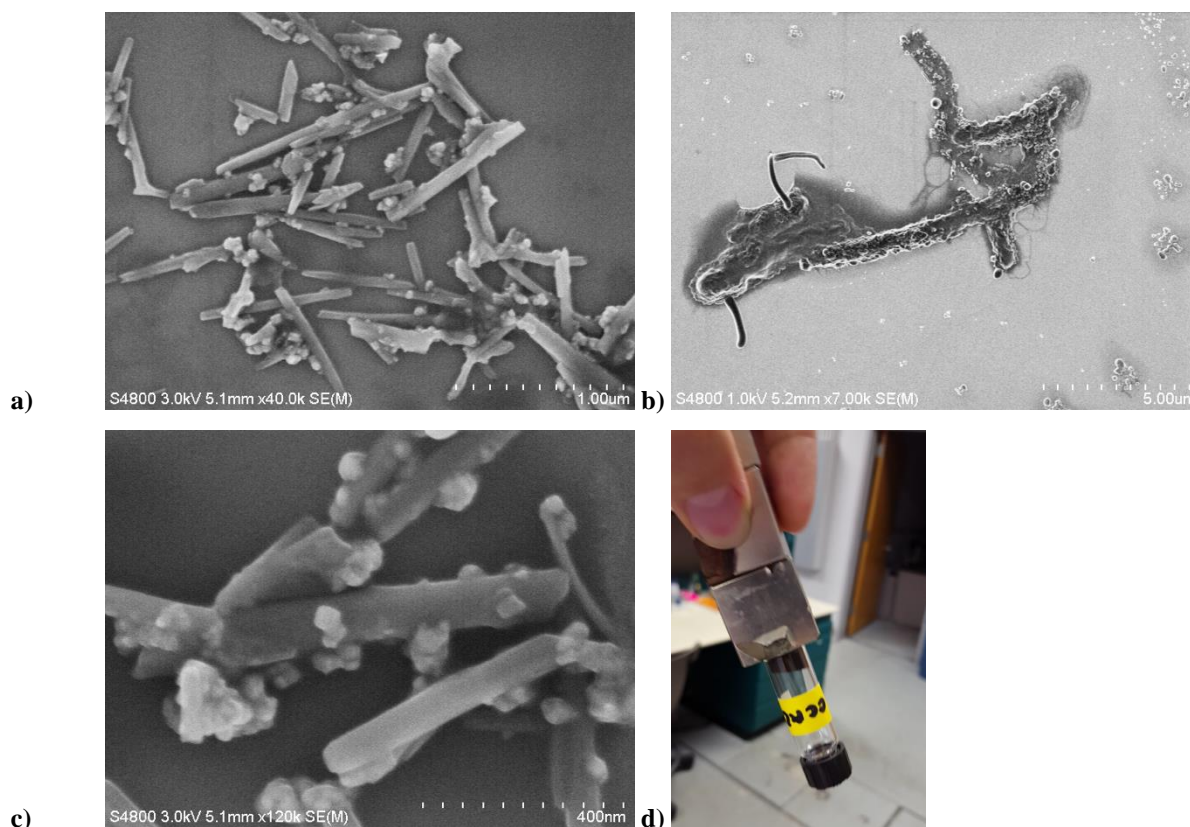
Figure 114. a-c) SEM micrographs of **37 d)** Ferromagnetic behavior of **37** powder.

To increase the aqueous colloidal stability of the obtained nanomaterials, they were loaded with the 3 wt% of sodium alginate. **38** This polymer, indeed, is able to increase the colloidal stability of nanomaterials as a consequence of the increase in its ζ potential value. In addition, alginate can form interconnected structure among its chain, by simple adding calcium ions.

A dispersion 0.1% mg/mL of **38** was dropped on different silica waffles and dry at RT under a specific position of the magnet. On the spot, after dry, was dropped a 1M CaCl$_2$ solution, dry, washed with water and dry again before checking.

The homemade system is able to give several preliminary information about the responding ability of the materials to external stimuli.

Macroscopically is possible to note how a solution placed on a silica waffle and subjected to a magnetic field shows the formation of a fibrous cluster.

These remain after the removing of the magnetic field and can be blocked by adding of Calcium Chloride.

The fibers have, also, auto repairing ability, indeed, after a perturbation the system is able to come back to the original conformation (Figure 115).
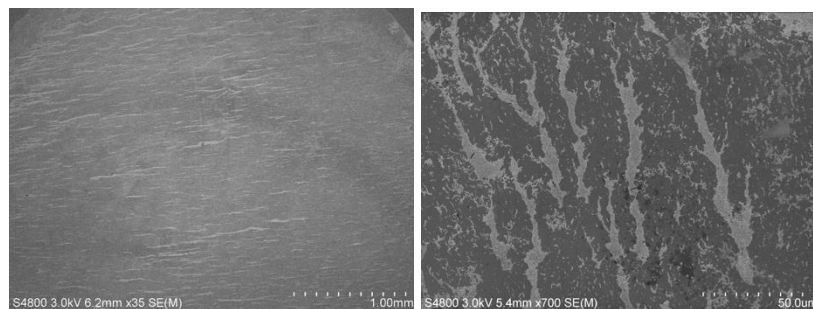
Figure 115. Fibrous aggregations.

Dropping the solution is also possible to observe how the shape of the drop is stretched, presenting a "new type" of "coffee rings" which presents a radially organization with respect to the drop center (Figure 116).
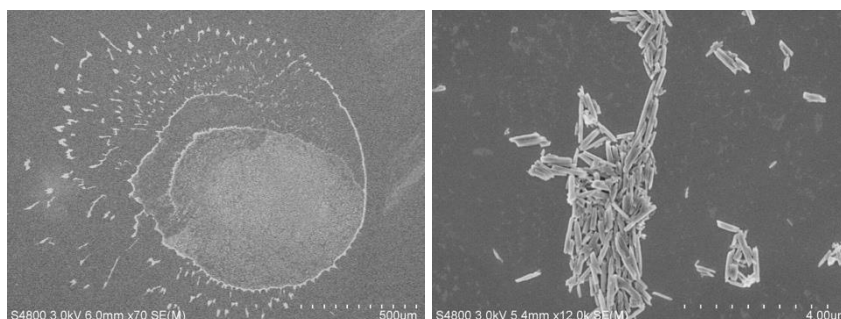
Figure 116. "coffee rings" at different magnifications.

Combining magnetic and capillarity forces by the use of silica microchannels, it is possible to obtain interesting organized structures as shown in Figure 117.

Unfortunately, the system is not able to retain the iron particles that therefore leave the tubes forming a different kind of fibrous structures.
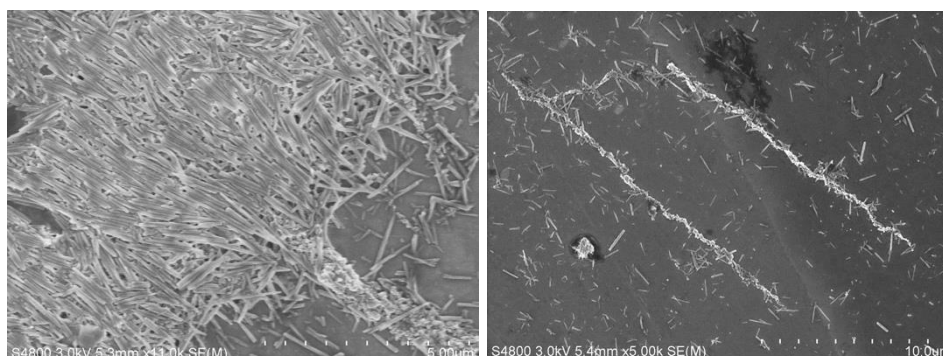
Figure 117. fibrous structures obtained by Combining magnetic and capillarity

References

1   J. Liu, *ACS Catal.*, 2017, **7**, 34–59.

2   C. Pavia, E. Ballerini, L. A. Bivona, F. Giacalone, C. Aprile, L. Vaccaro and M. Gruttadauria, *Adv. Synth. Catal.*, 2013, **355**, 2007–2018.

3   C. Petrucci, G. Strappaveccia, F. Giacalone, M. Gruttadauria, F. Pizzo and L. Vaccaro, *ACS Sustain. Chem. Eng.*, 2014, **2**, 2813–2819.

4   X. Liu, D. Gregurec, J. Irigoyen, A. Martinez, S. Moya, R. Ciganda, P. Hermange, J. Ruiz and D. Astruc, *Nat. Commun.*, 2016, **7**, 13152.

5   A. Fihri, M. Bouhrara, B. Nekoueishahraki, J.-M. Basset and V. Polshettiwar, *Chem. Soc. Rev.*, 2011, **40**, 5181.

6   A. M. P. Salvo, V. La Parola, L. F. Liotta, F. Giacalone and M. Gruttadauria, *Chempluschem*, 2016, **81**, 471–476.

7   Y. Zhang, X. He, J. Ouyang and H. Yang, *Sci. Rep.*, 2013, **3**, 2948.

8   Y. Fu and L. Zhang, *J. Solid State Chem.*, 2005, **178**, 3595–3600.

9   R. Wang, G. Jiang, Y. Ding, Y. Wang, X. Sun, X. Wang and W. Chen, *ACS Appl. Mater. Interfaces*, 2011, **3**, 4154–4158.

10   P. Liu and M. Zhao, *Appl. Surf. Sci.*, 2009, **255**, 3989–3993.

11   V. A. Vinokurov, A. V. Stavitskaya, Y. A. Chudakov, E. V. Ivanov, L. K. Shrestha, K. Ariga, Y. A. Darrat and Y. M. Lvov, *Sci. Technol. Adv. Mater.*, 2017, **18**, 147–151.

12   J. Ouyang, B. Guo, L. Fu, H. Yang, Y. Hu, A. Tang, H. Long, Y. Jin, J. Chen and J. Jiang, *Mater. Des.*, 2016, **110**, 169–178.

13   N. M. Sanchez-Ballester, G. V Ramesh, T. Tanabe, E. Koudelkova, J. Liu, L. K. Shrestha, Y. Lvov, J. P. Hill, K. Ariga and H. Abe, *J. Mater. Chem. A*, 2015, **3**, 6614–6619.

14   R. Capdeville, E. Buchdunger, J. Zimmermann and A. Matter, *Nat. Rev. Drug Discov.*, 2002, **1**, 493–502.

15   K. L. McPhail, D. E. A. Rivett, D. E. Lack and M. T. Davies-Coleman, *Tetrahedron*, 2000, **56**, 9391–9396.

16   S. S. Moleele, J. P. Michael and C. B. De Koning, *Tetrahedron*, 2006, **62**, 2831–2844.

17   Y. Q. Long, X. H. Jiang, R. Dayam, T. Sanchez, R. Shoemaker, S. Sei and N. Neamati, *J. Med. Chem.*, 2004, **47**, 2561–2573.

18   M. Kertesz, C. H. Choi and S. Yang, *Chem. Rev.*, 2005, 105, 3448–3481.

19   S. Kaye, J. M. Fox, F. A. Hicks and S. L. Buchwald, *Adv. Synth. Catal.*, 2001, 343, 789–794.

20   D. G. Hall, *Boronic Acids: Preparation and Applications in Organic Synthesis and Medicine*, Wiley-VCH Verlag GmbH & Co. KGaA, Weinheim, FRG, 2006.

21   G. Zhang, Y. Wang, X. Wen, C. Ding and Y. Li, *Chem. Commun.*, 2012, **48**, 2979.

22   M. Massaro, S. Riela, G. Cavallaro, M. Gruttadauria, S. Milioto, R. Noto and G. Lazzara, *J. Organomet. Chem.*, 2014, **749**, 410–415.

23   S. Sanghi, E. Willett, C. Versek, M. Tuominen and E. B. Coughlin, *RSC Adv.*, 2012, **2**, 848–853.

24   H.-J. Cho, S. Jung, S. Kong, S.-J. Park, S.-M. Lee and Y.-S. Lee, *Adv. Synth. Catal.*, 2014, **356**, 1056–1064.

25   K. Köhler, R. G. Heidenreich, S. S. Soomro and S. S. Pröckl, *Adv. Synth. Catal.*, 2008, **350**, 2930–2936.

26   Z. Niu, Q. Peng, Z. Zhuang, W. He and Y. Li, *Chem. - A Eur. J.*, 2012, **18**, 9813–9817.

27   F. Zhao, M. Shirai, Y. Ikushima and M. Arai, *J. Mol. Catal. A Chem.*, 2002, **180**, 211–219.

28   M. I. Burguete, E. García-Verdugo, I. Garcia-Villar, F. Gelat, P. Licence, S. V Luis and V. Sans, *J. Catal.*, 2010, **269**, 150–160.

29   S. M. Ansar, R. Haputhanthri, B. Edmonds, D. Liu, L. Yu, A. Sygula and D. Zhang, *J. Phys. Chem. C*, 2011, **115**, 653–660.

30   R. G. Freeman, M. B. Hommer, K. C. Grabar, M. A. Jackson and M. J. Natan, *J. Phys. Chem.*, 1996, **100**, 718–724.

31   S. M. Ansar and C. L. Kitchens, *ACS Catal.*, 2016, **6**, 5553–5560.

32   Y.-T. Liao, J. E. Chen, Y. Isida, T. Yonezawa, W.-C. Chang, S. M. Alshehri, Y. Yamauchi and K. C. W. Wu, *ChemCatChem*, 2016, **8**, 502–509.

33   W. Yan, C. Chen, L. Wang, D. Zhang, A.-J. Li, Z. Yao and L.-Y. Shi, *Carbohydr. Polym.*, 2016, **140**, 66–73.

34   K. Hayakawa, T. Yoshimura and K. Esumi, *Langmuir*, 2003, **19**, 5517–5521.

35   J. Zeng, Q. Zhang, J. Chen and Y. Xia, *Nano Lett.*, 2010, **10**, 30–35.

36   X. Wu, C. Lu, Z. Zhou, G. Yuan, R. Xiong and X. Zhang, *Environ. Sci. Nano*, 2014, **1**, 71–79.

37   X. Zhou, W. Xu, G. Liu, D. Panda and P. Chen, *J. Am. Chem. Soc.*, 2010, **132**, 138–146.

38   S. Wunder, Y. Lu, M. Albrecht and M. Ballauff, *ACS Catal.*, 2011, **1**, 908–916.

39   K. Kuroda, T. Ishida and M. Haruta, *J. Mol. Catal. A Chem.*, 2009, **298**, 7–11.

40   Y.-C. Chang and D.-H. Chen, *J. Hazard. Mater.*, 2009, **165**, 664–669.

41   M. Chen, H. Kang, Y. Gong, J. Guo, H. Zhang and R. Liu, *ACS Appl. Mater. Interfaces*, 2015, **7**, 21717–21726.

42   H. Koga, E. Tokunaga, M. Hidaka, Y. Umemura, T. Saito, A. Isogai and T. Kitaoka, *Chem. Commun.*, 2010, **46**, 8567–8569.

43   A. Herreros-López, C. Hadad, L. Yate, A. A. Alshatwi, N. Vicentini, T. Carofiglio and M. Prato, *European J. Org. Chem.*, 2016, **2016**, 3186–3192.

44   A. T. Miah, S. K. Bharadwaj and P. Saikia, *Powder Technol.*, 2017, **315**, 147–156.

45   I. K. Sen, K. Maity and S. S. Islam, *Carbohydr. Polym.*, 2013, **91**, 518–528.

46   M. Li and G. Chen, *Nanoscale*, 2013, **5**, 11919–11927.

47   M. Russo, F. Armetta, S. Riela, D. Chillura Martino, P. Lo Meo and R. Noto, *J. Mol. Catal. A Chem.*, 2015, **408**, 250–261.

48   M. Salavati-Niasari, Z. Fereshteh and F. Davar, *Polyhedron*, 2009, **28**, 1065–1068.

49   T. C. Rojas, J. C. Sánchez-López, M. J. Sayagués, E. P. Reddy, A. Caballero and A. Fernández, *J. Mater. Chem.*, 1999, **9**, 1011–1017.

50   S. Gao, Y. Lin, X. Jiao, Y. Sun, Q. Luo, W. Zhang, D. Li, J. Yang and Y. Xie, *Nature*, 2016, **529**, 68–71.

51   F. Wyrwalski, J.-F. Lamonier, S. Siffert, L. Gengembre and A. Aboukaïs, *Catal. Today*, 2007, **119**, 332–337.

52   C. Ma, Z. Mu, C. He, P. Li, J. Li and Z. Hao, *J. Environ. Sci.*, 2011, **23**, 2078–2086.

53   M. H. Castaño, R. Molina and S. Moreno, *J. Mol. Catal. A Chem.*, 2013, **370**, 167–174.

54   X. Xie, Y. Li, Z.-Q. Liu, M. Haruta and W. Shen, *Nature*, 2009, **458**, 746–749.

55   A. Nakhaei Pour and M. Housaindokht, *Catal. Letters*, 2013, **143**, 1328–1338.

56   X. Long, Z. T. Liu, Z. W. Liu, X. Li and K. Fujimoto, *Catal. Letters*, 2009, **131**, 388–392.

57   S. Chen, J. Li, Y. Zhang, D. Zhang and J. Zhu, *J. Nat. Gas Chem.*, 2012, **21**, 426–430.

58   A. Y. Khodakov, W. Chu and P. Fongarland, *Chem. Rev.*, 2007, **107**, 1692–1744.

59   V. M. Abbasov, H. C. Ibrahimov, G. S. Mukhtarova and E. Abdullayev, *Fuel*, 2016, **184**, 555–558.

60   A. M. Carrillo and J. G. Carriazo, *Appl. Catal. B Environ.*, 2015, **164**, 443–452.

61   D. Zhao, Z. Cheng and Z. Nan, *Mater. Chem. Phys.*, 2016, **183**, 615–621.

62   X. Wang, Y. Chen, W. Zhang, W. He, J. Wang and B. Chen, *Korean J. Chem. Eng.*, 2016, **33**, 3504–3510.

63   P. Yuan, D. Tan and F. Annabi-Bergaya, *Appl. Clay Sci.*, 2015, **112–113**, 75–93.

64   R. L. Frost and J. Kristof, *Clays Clay Miner.*, 1997, **45**, 551–563.

65   H. Ma, H. Wang, T. Wu and C. Na, *Appl. Catal. B Environ.*, 2016, **180**, 471–479.

66   M. Massaro, S. Riela, G. Cavallaro, C. G. Colletti, S. Milioto, R. Noto, F. Parisi and G. Lazzara, *J. Mol. Catal. A Chem.*, 2015, **408**, 12–19.

67   L. Jianming, D. B. Dreisinger and W. C. Cooper, *Hydrometallurgy*, 1997, 45, 305–322.

68   M. M. Nolasco, P. M. Vaz, P. D. Vaz, R. A. S. Ferreira, P. P. Lima and L. D. Carlos, *J. Coord. Chem.*, 2014, **67**, 4076–4089.

69   Y. Zhao, G. Cavallaro and Y. Lvov, *J. Colloid Interface Sci.*, 2015, **440**, 68–77.

70   M. Liu, Z. Huo, T. Liu, Y. Shen, R. He and C. Zhou, *Langmuir*, 2017, **33**, 3088–3098.

71   M. Liu, R. He, J. Yang, W. Zhao and C. Zhou, *ACS Appl. Mater. Interfaces*, 2016, **8**, 7709–7719.

72   L. Qin, Y. Zhao, J. Liu, J. Hou, Y. Zhang, J. Wang, J. Zhu, B. Zhang, Y. Lvov and B. Van Der Bruggen, *ACS Appl. Mater. Interfaces*, 2016, **8**, 34914–34923.

73   F. Arcudi, G. Cavallaro, G. Lazzara, M. Massaro, S. Milioto, R. Noto and S. Riela, *J. Phys. Chem. C*, 2014, **118**, 15095–15101.

74   B. Bharti, A.-L. Fameau, M. Rubinstein and O. D. Velev, *Nat. Mater.*, 2015, **14**, 1104–1109.

75   B. Bharti and O. D. Velev, *Langmuir*, 2015, **31**, 7897–7908.

76   S. Kumar, H. Kaur, H. Kaur, I. Kaur, K. Dharamvir and L. M. Bharadwaj, *J. Mater. Sci.*, 2012, **47**, 1489–1496.

Chapter 7

Modified Halloysite Nanotubes for Pollutant Removal

7.   *Halloysite for pollutant renovation*

Dyes are extensively used in several fields such as the plastic, textile, cosmetic and paper industries; therefore the possibility to discharge them in the environment, without a preliminary treatment, represents one of the major concerns, since it may cause various serious environmental problems, such as disturbance of aquatic photosynthesis and damage of the ecosystem. In addition, organic contaminants, including pharmaceuticals and organochlorine pesticides, are, also, an environmental concern because of their potential impact on aquatic organisms and capacity to bioaccumulate in the food chain.[1–4] Therefore, the development and evaluation of new materials for the sorption of organic contaminants still remain in the focus of innovative applications in water, air and soil treatment. Numerous approaches have developed cheaper and more effective materials especially composed of natural compounds like chitosan,[5,6] starch,[7] zeolites[8] or clay.[9]

In this context, halloysite nanotubes, modified or not, present superior removal capacity for organic contaminant from contaminated wastewater. Recently, a number of studies on removal of cationic, neutral and anionic dyes from aqueous solution onto natural HNTs have been reported.[10–15] These works were based on the adsorption mechanisms including physical and chemisorption, site geometry, etc. and showed moderate adsorption capacity (26–113.46 mg·g^{-1}) and reusability.

Not covalent functionalization of both HNT lumen by selective adsorption of anionic and cationic surfactants as sodium dodecanoate and decyltrimethylammonium bromide was, also, reported (Figure 118). It is demonstrated that the adsorption of anionic surfactant into the HNTs lumen increases the net negative charge of the nanotubes enhancing the electrostatic repulsions and consequently the dispersion stability. On the contrary, the cationic surfactant addition enhances the precipitation of the nanomaterial. The functionalization of HNT lumen with sodium alkanoate, in addition, generates a nanohybrid with a hydrophobic lumen. Due to this structure, this material behaves like a sponge to entrap hydrophobic compounds.[16]
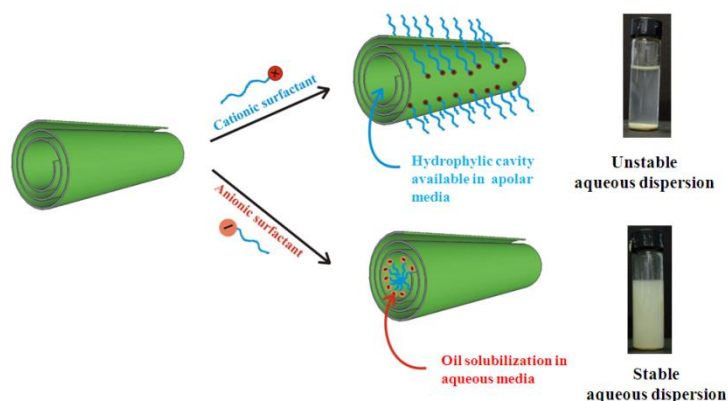
Figure 118. Illustration of the hybrid surfactant/HNTs materials.

Good adsorbent to dye based on alginate beads reinforced with HNT, with excellent physical and chemical properties, were obtained by Liu *et al.* This new system showed high removal efficiency of methylene blue (above 90%) even after 10 successive adsorption-desorption cycles.[17]

The modification of HNT external surface with silane, such as APTES, improves the dispersibility of the HNT in an organic system. In a recent work, Yang *et al.* functionalized the HNT (f-HNT) surface both with APTES and Fe_3O_4.[18] The magnetic modified halloysite was used as reinforcing agent of a supramolecular gel (Figure 119). The authors found that the introduction of only 4 wt% of f-HNT remarkable increases the compressive strength of the reinforced supramolecular gel composite from 19 kPa to 28 kPa. The magnetic supramolecular gel composite obtained was used as adsorbent for organic dyes exhibiting an excellent adsorption capability.
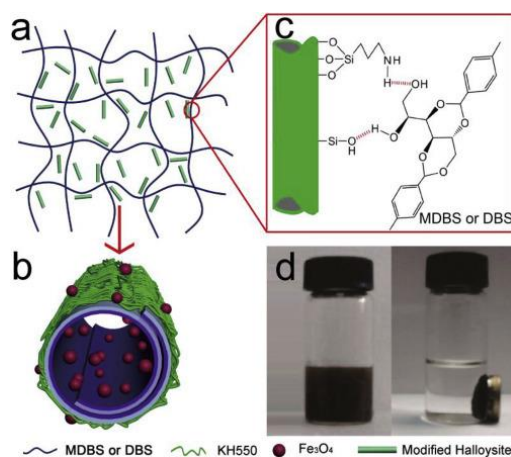
Figure 119. Schematic illustration of the preparation of magnetic supramolecular gels containing hydrophobically modified HNTs loaded with Fe_3O_4 NPs.

Li, Yao *et al.*,[19] reported the immobilization of $LaFeO_3$, one of the most important perovskite-type semiconductor, on HNTs surface via facile sol-gel method. The catalytic

performances towards degradation of antibiotics are evaluated under visible light using chlortetracycline as drug model. The decomposition studies revealed that pristine halloysite possesses no photocatalytic activity, whereas, after irradiation of chlortetracycline in the presence of the pure $LaFeO_3$, the 74% of the drug was degraded within 90 min. On the contrary, the degradation rate increases up to 87 % when $LaFeO_3$/HNTs are used as catalyst. For similar purpose, graphitic carbon nitride (g-C_3N_4) which possesses high thermal and chemical stability and suitable band gap was combined with halloysite and ZnO via a facile calcination method, in order to obtain promising nanocomposite photocatalyst for degradation of pollutant.[20]

Phenol-based pesticides represent one class of important organic pollutant. They are widely used for agricultural purposes and are considered as one of the most important endocrine disrupting chemicals present in the environment. For example, nonylphenol compounds, are stable in water and exhibit aquatic toxicity and estrogenic activity even at very low concentrations, therefore the development of adsorbent for these compounds is crucial. In this context, HNTs were employed as base materials to prepare some special adsorbents for adsorption/degradation of phenol-based pollutants.

A photocatalyst based on HNTs was prepared by Huo *et al.* combining CdS with the nanotube by hydrothermal synthesis method.[21] This material was used as core to fabricate a novel thermal-responsive surface molecularly imprinted photocatalyst, where the shell was created by introducing a thermo-responsive polymer such as poly-N-(isopropyl acrylamide).[22] The imprinted polymer layer provides the photocatalyst molecular recognition ability to form the selective photo-degradation of the target pollutant and, thanks to this, it might be used for the treatment and disposal dues of antibiotics from wastewater. Szczubiałka *et al.*[23] synthetized a hybrid photosensitizer by the incorporation of Rose Bengal into HNTs for the photodegradation of phenol-based pesticide. The photosensitizer was found to be efficient for singlet oxygen generation and combine adsorption ability with photocatalytic properties.

Other work reports on HRP immobilized on biohybrid HNTs-Chitosan through cross-linking by glutaraldehyde that was used to remove chemicals, in particular phenols, from wastewater. It exhibited overall high removal efficiency and removal rate, which demonstrates that the HRP immobilized on HNTs-Chitosan systems could be promising in wastewater treatment (Figure 120).[24]
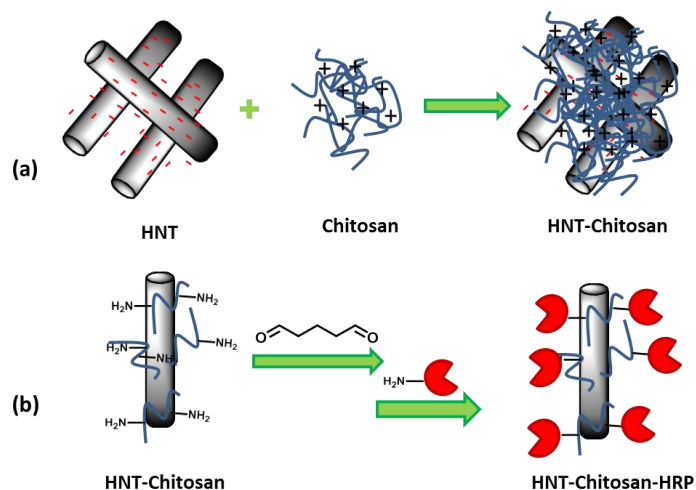
Figure 120. Schematic illustration of (a) the preparation of chitosan–halloysite hybrid nanotubes and (b) the immobilization of horseradish peroxidase.

In this chapter, I am going to describe an overview of the recent progress achieved on the development of HNT hybrids for application in the environmental field, as adsorbent for several pollutants. Covalent and not covalent functionalized HNTs hybrids were exploited. In details the hybrid nanosponge (HNT-CD) was successfully applied in removal of organic dyes; while the supramolecular complex between halloysite and cucurbit[8]uril was used for the adsorption of volatile organic compounds, such as pyrene and toluene, both in gas and in liquid phase.

7.1. Halloysite–Cyclodextrin Nanosponges for Enhanced Dyes Adsorption

The HNT-CD hybrid (compound **6**) was employed as adsorbent material for organic dyes. To achieve this goal, first of all, the adsorption capacity of the new hybrid nanomaterials was evaluated by adsorption isotherm experiments using rhodamine B (RB) as dye model.

In Figure 121 is reported the equilibrium amount of dye adsorbed into the clay (Q_e, mol·g^{-1}) as a function of the equilibrium dye concentration in solution (C_e, mol·L^{-1}). First of all, it can be observed that the amount of adsorbed dye increases on increasing the equilibrium dye concentration and it is considerably lower at the higher pH (Figure 121). This could be explained as follow: HNT presents a negative outer surface in a wide pH range, therefore, in acidic pH media an electrostatic attraction between the negatively

charged nanosponge hybrid and positively charged RB would take place; on the contrary for pH values up to 7.4, RB mainly exists in zwitterion forms forming dimmers[25] which are unable to interact with the HNT surfaces and therefore the dye can be encapsulated mainly into CD cavities decreasing the adsorption efficiency.
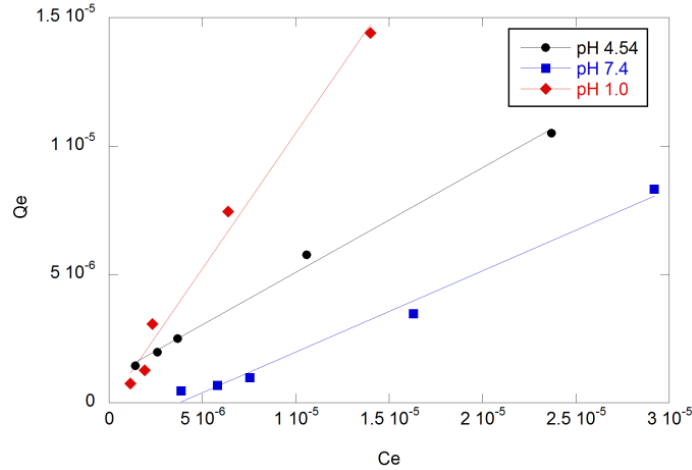
Figure 121. Adsorption isotherms of RB on (a) HNT-CD nanosponge hybrid in HCl 0.1 N, acetate buffer pH 4.54 and phosphate buffer pH 7.4.

Both the Langmuir and the Freundlich models were used to analyze the experimental data. The obtained results are reported in Table 31. The models are expressed as follows:

$$Q_e = \frac{KQ_mC_e}{1+KC_e}$$

Equation 11

where Q_e (mol g^{-1}) is the quantity of adsorbed RB at equilibrium; C_e (mol L^{-1}) is the concentration of RB in solution at equilibrium; Q_m (mol g^{-1}) is a constant standing for the maximum monolayer adsorption capacity of adsorbent. K_L is a constant corresponding to the affinity of adsorbent towards adsorbate. The Langmuir isotherm model assumes that the adsorption occurs on a homogenous surface and no interaction happens between adsorbates on the plane of surface.

On the contrary, the Freundlich isotherm is valid for multilayer adsorption that adsorption takes place on heterogeneous surfaces accompanied by interactions between adsorbed molecules.

$$Q_e = K_F C_e^{1/n}$$

Equation 12

where C_e is the equilibrium concentration of dye solution (mg L^{-1}), Q_e is the equilibrium capacity of dye on the adsorbent (mg g^{-1}), K_F is a Freundlich constant related to adsorption capacity (L g^{-1}). The other Freundlich constant *n* is a measure of the deviation from

linearity of the adsorption and used to verify types of adsorption. In the Freundlich isotherm model, the value of *n* indicates the type of isotherm. When *n* is equal to unity, the adsorption is linear. Further, *n* below unity indicates that adsorption is a chemical process; whereas, *n* above unity is associated with a favorable adsorption and a physical process.

As it is possible to note the adsorption data are better fitted by the Freundlich model suggesting the heterogeneity of the polymer and multi-molecular layer adsorption. The value of *n* is larger than 1 in acidic solution, which indicates the favorable nature of adsorption and a physical process; while the *n* value less than 1 obtained in a neutral medium indicates that the adsorption bond becomes weak; unfavorable adsorption takes place, as a result of the decrease in adsorption capacity.[26]

For comparison, we studied the adsorption of RB on pristine HNT (**p-HNT**). In all cases, we observed a decrease in the RB adsorption efficiency with respect to **6**. In addition, the adsorption data are better fitted by Langmuir model at pH 7.4; furthermore both models are not applicable for data at pH 4.54.

Table 31. Parameters of Langmuir and Freundlich isotherm models for RB adsorption on HNT-CDs nanosponges hybrids.

pH		Langmuir $Q_e = \frac{K_L Q_m C_e}{1+K_L C_e}$			Freundlich $Q_e = K_F C_e^{1/n}$		
		Q_m (mol g^{-1})	K_L (L mol^{-1})	R^2	K_F (mol g^{-1} (mol L^{-1})$^{1/n}$)	n	R^2
1.00	HNT-CDs (20%)	$(2.7\pm1.5)\times10^{-5}$	$(7\pm6)\times10^5$	0.965	0.08±0.06	1.3±0.1	0.996
	HNT-CDs (40%)	$(2.0\pm0.1)\times10^{-5}$	$(3\pm2)\times10^5$	0.964	0.3±0.1	1.01±0.03	0.977
4.54	HNT-CDs (20%)	$(2.5\pm0.4)\times10^{-5}$	$(3\pm1)\times10^5$	0.994	0.05±0.01	1.26±0.05	0.997
	HNT-CDs (40%)	$(6\pm4)\times10^{-5}$	$(8\pm6)\times10^4$	0.991	0.10±0.06	1.13±0.07	0.994
7.40	HNT-CDs (20%)	na	na	na	86±40	0.65±0.02	0.999
	HNT-CDs (40%)	na	na	na	2.2±1.9	0.80±0.05	0.994

[na]Langmuir model is not successful.

To well-understand the adsorption mechanisms, kinetics of Rhodamine B adsorption onto **6**, in the best pH conditions, were investigated (Figure 122). It was found that the adsorption amount increases rapidly in first 100 min, and then slows down until the sorption reached equilibrium. The beginning rapid adsorption of RB is due to the existence

of a large number of sorption sites on the surface of HNT-CDs nanosponge hybrids (HNT and CDs cavities, interstitial channels). As the surface active sites are occupied, the adsorption rates slow down and finally reached the adsorption equilibrium.

a)   **b)**
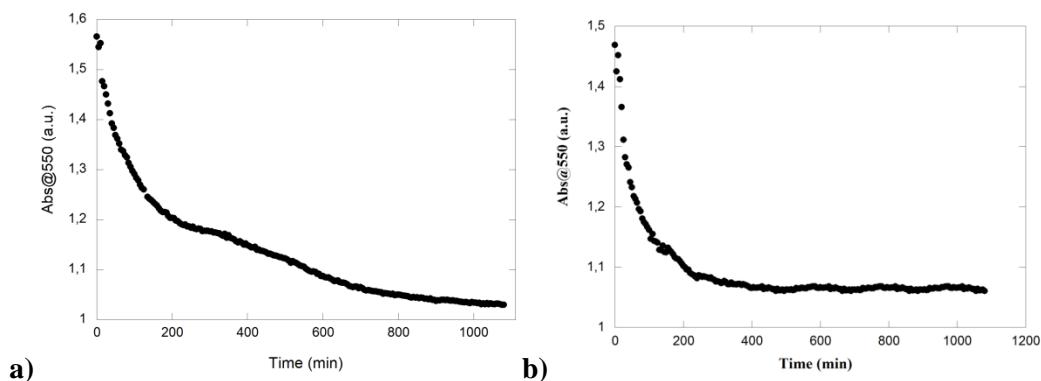
Figure 122. Kinetic adsorption of RB on **6 a)** (20%); **b)** (40%) in acetate buffer pH 4.54.

Table 32. Adsorption kinetic parameters of RB onto **6** nanosponges hybrids.

First-order $Q_T = Q_e \cdot \left(1 - e^{k_1 t}\right)$			Second-order $Q_T = Q_e \cdot \left(\dfrac{Q_e kt}{1 + Q_e kt}\right)$			Weber-Morris $Q_T = kt^{1/2} + C$	
Q_e	k_1	R^2	Q_e	k_2	R^2	k_{IPD}	R^2
$(5.27\pm0.01)\times10^{-6}$	0.024 ± 0.001	0.565	$(5.51\pm0.02)\times10^{-6}$	$(8.32\pm0.03)\times10^{4}$	0.903	$(2.59\pm0.08)\times10^{-9}$	0.874
$(5.27\pm0.01)\times10^{-6}$	0.100 ± 0.006	0.399	$(5.37\pm0.01)\times10^{-6}$	$(3.5\pm0.1)\times10^{5}$	0.844	$(2.6\pm0.2)\times10^{-8}$	0.556

The kinetic data were fitted by first-order, second-order, intraparticle diffusion models and double exponential (DEM) (Tables 32 and 33). It was found that the experimental data are better fitted by DEM model (Table 33). According to the literature, the DEM mode describes a process where the adsorbent offers two different types of adsorption sites.[27] Therefore, it could be possible that rapid adsorption equilibration occurs within a few minutes onto HNT external surface, whereas on inner cyclodextrin core, adsorption is more slowly.

Table 33. Adsorption kinetic parameters of RB onto HNT-CDs nanosponge hybrids.

	DEM $Q_T = Q_e' \cdot \left(1 - e^{k't}\right) + Q_e'' \cdot \left(1 - e^{k''t}\right)$				
	Q_e' $(10^{-6}\,M)$	k' (min^{-1})	Q_e'' $(10^{-6}\,M)$	k'' (min^{-1})	R^2
20%	3.91 ± 0.02	0.083 ± 0.003	1.61 ± 0.02	$(3.4\pm0.01)\times10^{-3}$	0.994
40%	3.73 ± 0.02	0.8 ± 0.1	1.61 ± 0.02	$(1.35\pm0.03)\times10^{-2}$	0.981

Finally, in order to determine the effect of temperature on RB adsorption, experiments were conducted at 277, 298, 310 and 331 K, respectively (Figure 123). The adsorption

process was favorable at lower temperature and RB molecules were orderly adsorbed on the surface of **6** and into CD cavities. The thermodynamic parameters were calculated by means of the van't Hoff equation and listed in Table 34. The obtained data further confirm that the material shows better adsorption efficiency in acidic medium with respect to the neutral one.
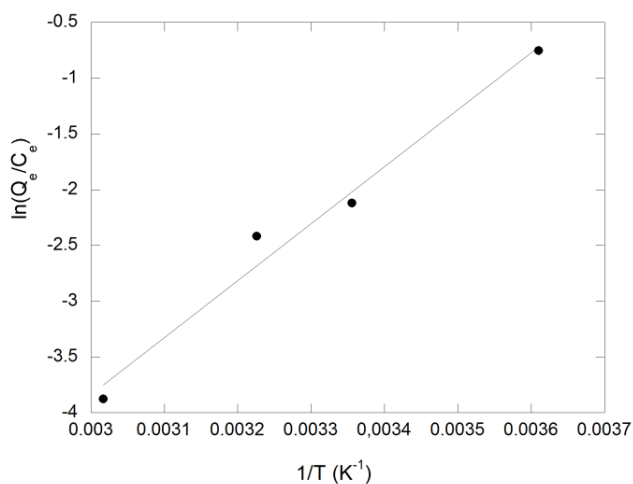
Figure 123. Temperature-dependent adsorption of RB on **6**.

Table 34. Thermodynamic parameters at different temperatures.

pH	T (K)	$\Delta G^{\circ\ a}$ (KJ mol^{-1})	ΔH (KJ mol^{-1})	ΔS (J mol^{-1})
	277	-88.31		
4.54	298	-87.37	-100.71	-44.76
	310	-86.83		
	331	-85.89		
7.40	277	1.87	-37.19	-141

^{a}Obtained from Langmuir model.

In order to evaluate the performance of the obtained HNT-CD hybrid polymers **6**, additional adsorption experiments were performed to determine the adsorption capacity of the hybrid for six cationic and anionic dyes (Figure 124a), under different pH values, namely 1.0, 4.54 and 7.4 (Figure 124b). In general, the synthesized materials show higher adsorption capacity than **p-HNT** (Figure 125 and Table 35) as a consequence of the introduction of CD moieties and the formation of network.

(a)

Methylene Blue   Toluidine Blue   Congo Rubin

Rhodamine B   Methyl Orange   Bromocresol Green

(b)
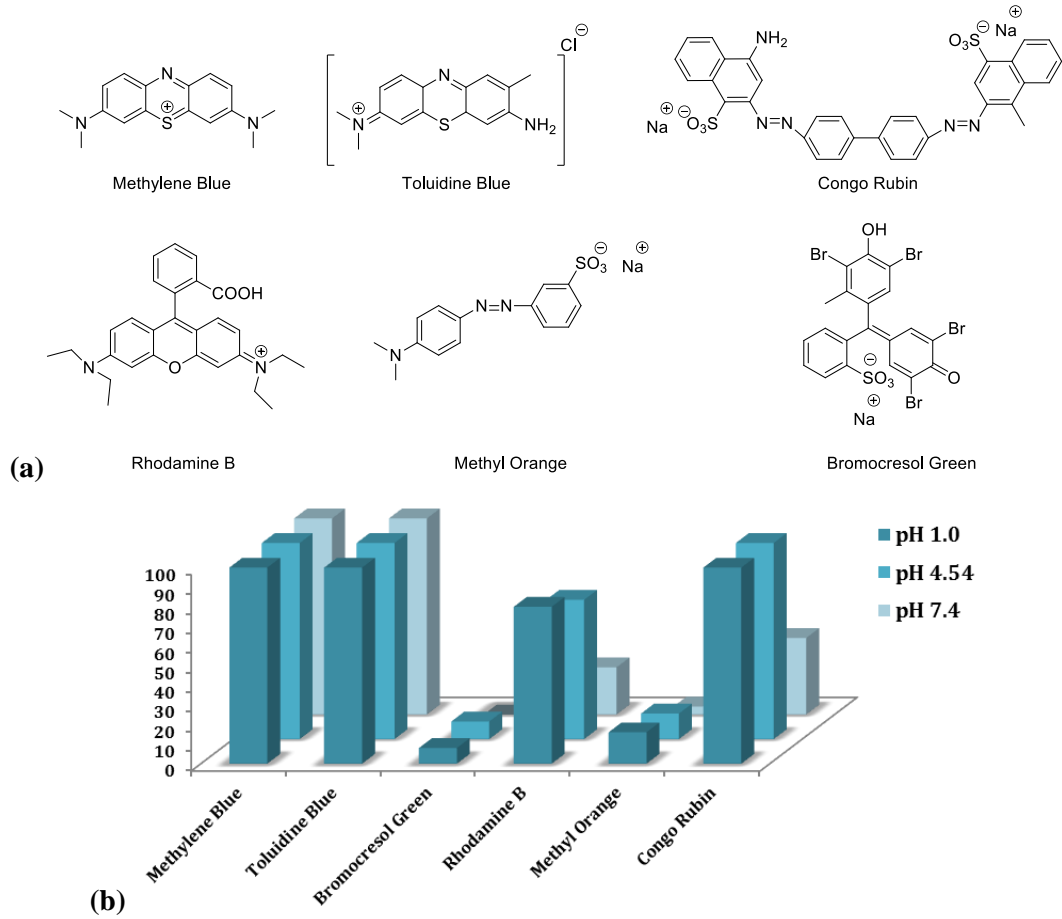
Figure 124. Cationic and anionic dyes investigated; (b) adsorption capacities of **6** for the different dyes at pH 1, 4.54 and 7.4.
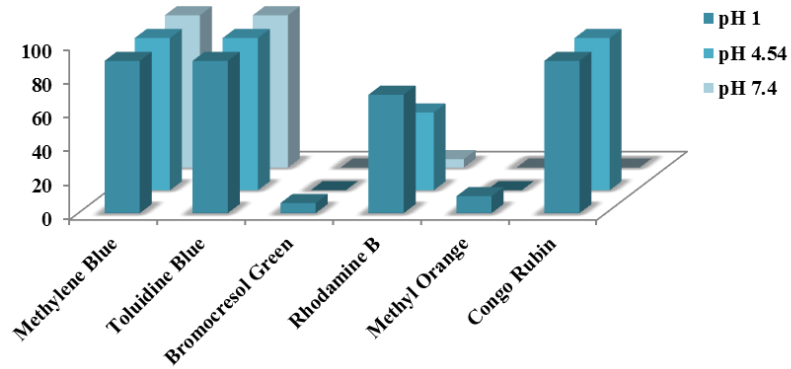
Figure 125. Adsorption capacities of **p-HNT** for the different dyes at pH 1.0, 4.54 and 7.4.

Table 35. Comparison between the adsorption performances of pristine HNT and HNT-CD (40%) hybrid.

Organic Dye	Compound 6			HNT		
	pH 1	pH 4.54	pH 7.4	pH 1	pH 4.54	pH 7.4
Methylene Blue	100	100	100	90	90	90
Toluidine Blue	100	100	100	90	90	90
Bromocresol Green	8	9	0	6	0	0
Rhodamine B	80	71	24	70	46	5
Methyl Orange	16	13	4	10	0	0
Congo Rubin	100	100	39	90	90	0

It was found that **6**, in all pH values investigated, showed high adsorption capacity for cationic dyes. In particular methylene blue (MB) and toluidine blue (TB) are quantitatively adsorbed, while only 70% of RB is adsorbed at the best pH value. These differences could be due to the small steric hindrance of MB and TB with respect to RB.

Anionic dyes are poorly adsorbed from the polymer, probably due to the presence of electrostatic repulsions between the negatively charged halloysite external surface and the dyes. The small amount of these dye adsorbed could selectively interact with positively charged HNT lumen. However, in these cases, the best adsorption is obtained at pH 4.54. The anionic dyes, indeed, turns from a neutral to a largely delocalized anionic form at around pH 4, therefore they can interact with the nanomaterial in their partly cationic form.[28]

Surprisingly, the nanomaterial showed good adsorption capacity for the anionic dye congo rubin (CR) at acidic pH values. This could be explained by a difference in binding mechanism of halloysite to the anionic dyes and a strong interaction between CR and HNT.[13] In addition, the formation of inclusion complexes between CR and β-CD occurs.[29] At lower pH, the sulfonate ions of CR can be neutralized and the complexing effect between neutral CR and the cavity of β-CD is strengthened, thereby promoting adsorption of CR.

The obtained results show that **6** could be used as a good nano-adsorbent for selective adsorption of cationic dyes with respect to the anionic ones in a wide pH range. For comparison in Table 36 are reported the adsorption capacities of MB on **6** and that obtained with other adsorbents.

Table 36. Adsorption capacities of MB for some adsorbent.

Adsorbent	Adsorption capacity (mg g^{-1})	Ref.
p-HNT	84.32	10
Titania	5.98	30
Zeolite	16.37	31
NaOH-treated kaolin	20.49	32
Titanate nanotubes	133.30	33
β-cyclodextrin cross-linked by citric acid	105.00	34
6	226	

The results demonstrated that the HNT-CD hybrid nanosponges could be employed as promising adsorbents for removal of organic dyes from wastewater.

7.2. Halloysite/Cucurbit[8]uril hybrid as efficient nanosponge for volatile organic compounds adsorption

A different system, the one obtained by the noncovalent functionalization of both halloysite surfaces with the cucurbit[8]uril (CB[8]) supramolecule was employed for organic volatile compounds removal. In particular, toluene was chosen as model and its amount (W_{oil}) captured by the solid nanohybrids as a function of time was determined. For a comparison purpose, the adsorption ability of pristine components (HNT and CB[8]) was investigated. All the results are reported in Table 37.

It is noteworthy that the hybrid nanomaterial exhibits a strong enhancement of capability in capturing toluene gas compared to the pristine HNT. At a given time, the adsorbed amount is larger for the nanohybrids; for instance, after 2 h, the toluene amount captured by the nanohybrid is ca. 50 times larger than that of pristine HNT; such a difference reduces to ca. 4 after 20 h. On the contrary, the pristine CB[8] shows a better capture ability compared to the nanohybrids so that it would appear that the new nanomaterial fails in the application within this topic. Indeed, to obtain straightforward insights on the entrapping ability of the new hybrid we calculated the W_{oil} on the basis of the rule of mixtures by using the W_{oil} data for pristine HNT and CB[8] and considering that the hybrid contains 25 wt% of the CB[8]. As the computed values indicate, the new nanomaterial presents very good capacity of complexing toluene from the gas phase at any time.

Table 37. Capture Ability of Vapor Toluene by Adsorbents at 25 °C.

	18	**HNT**	**CB[8]**
Time (h)	*Woil*	*Woil*	*Woil*
2	18.0±0.2a); 72.0±0.8b) 5.6c)	0.37±0.01	21.1±0.3
3	36.9±0.4a) 147.6±1.6b) ;6.9c)	1.38±0.04	23.3±0.4
20	38.6±0.4a); 154.4±1.6b) 17.3c)	10.7±0.1	37.3±0.4

W_{oil}, mg toluene/g adsorbent; [a] experimental value; [b] experimental value expressed as mg toluene/gCB[8] in the hybrid [c] calculated value according to the rule of mixtures.

The entrapped oil vapor into the cavity of CB[8] molecules allows to the formation of inclusion complexes controlled by weak interactions. Based on thermodynamic properties for the inclusion of gases into cucurbit[6]uril[35] one expects that the guests might be released upon temperature increase. Therefore, the reversible binding of gases may be exploited to remove them with the consequent reuse of the nanohybrids for the same purposes.

Adsorption experiments in liquid phase evidenced that the presence of CB[8] onto the nanoclay surfaces significantly improves the HNT removal ability towards toluene dissolved in water. From these measurements the partition coefficient of toluene (*P*) in aqueous dispersions of pristine and modified HNT. *P* was calculated as follow:

$$P = \frac{C_{ads}}{C_w}$$

Equation 13

where C_{ads} is the concentration of toluene adsorbed onto the nanomaterials surface, while C_w is the toluene concentration in the aqueous phase.

We observed that *P* for modified HNT is three times larger with respect to that calculated for pristine HNT. Particularly, *P* values are 215±8 and 72±5 for compound **18** and HNT, respectively. These results indicate that the modified nanotubes possess a larger affinity toward toluene because of the presence of hydrophobic domains (composed by CB[8] molecules). On the other hand, the lower adsorption ability of the pristine nanotubes agrees with the HNT hydrophilic nature. The mechanism of interactions between compound **18** and hydrocarbons was clearly evidenced by fluorescence spectroscopy experiments, which were carried out by using pyrene as a fluorescent probe. Figure 126 illustrates the fluorescence emission spectra of saturated aqueous solutions of pyrene in the presence of both pristine and functionalized HNT.

Interestingly, compound **18** induces a significant enhancement of the pyrene fluorescence intensity with respect to that observed in water. As reported[36] for the adsorption of pyrene onto cucurbit[6]uril cavity, the changes in the fluorescence emission can be attributed to both the complex formation and the hydrophobic interactions. Accordingly, the fluorescence intensity of pyrene is slightly affected by pristine HNT (Figure 126), which possesses a hydrophilic nature. Furthermore, the influence of HNT on I_1/I_3 ratio is negligible being that the ratios are 1.78 and 1.74 for pyrene in water and in HNT aqueous dispersion, respectively (Figure 126). On the contrary, Figure 127 shows that I_1/I_3 ratio monotonically decreases with the compound **18** concentration approaching a constant value, which indicates the saturation of the hydrophobic domains.
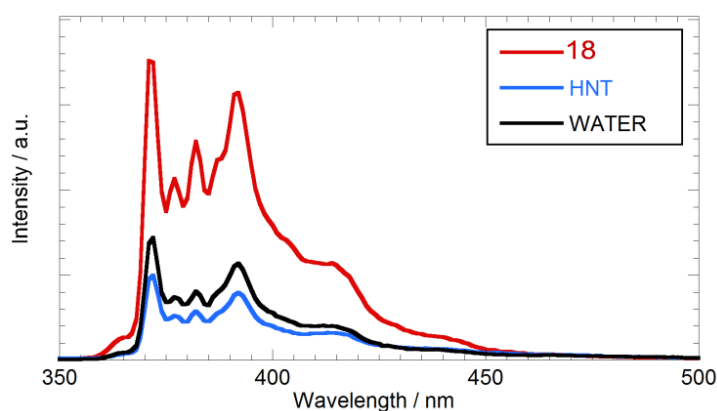
Figure 126. Emission fluorescence spectra of aqueous pyrene solution (5×10^{-7} mol dm^{-3}) in the presence of HNT and compound **18**.The concentrations of pristine and functionalized HNT are 0.31 g dm^{-3} and 0.27 g dm^{-3}, respectively. For comparison, the emission fluorescence spectrum of pyrene in water is reported.

A quantitative evaluation of the affinity of Pyrene to the hydrophobic domains of the compound **18** hybrid can be provided by the distribution constant of the hydrocarbon between the water and the CB[8] hydrophobic lumen (K_{Pyr}) using the following approach:[37]

$$\frac{I_1}{I_3} = \left(\frac{I_1}{I_3}\right)_w \cdot \chi_{Pyr,w} + \left(\frac{I_1}{I_3}\right)_L \cdot \left(1 - \chi_{Pyr,w}\right) \qquad Equation 14$$

where $\chi_{Pyr,w}$ is the fraction of Pyrene in the aqueous phase, while $(I_1/I_3)_w$ and $(I_1/I_3)_L$ are the Pyrene emission fluorescence signal in water and in the CB[8] hydrophobic lumen, respectively. K_{Pyr} is related to $\chi_{Pyr,w}$ as

$$\chi_{N,w} = \frac{1}{\left(1 + K_{Pyr} \cdot c_{HNT/CB[8]}\right)} \qquad Equation 15$$

where $c_{HNT/CB[8]}$ is the concentration of the functionalized HNT expressed as g dm^{-3}.

Equations 4 and 5 were successfully applied to the I_1/I_3 vs $c_{HNT/CB[8]}$ trend (Figure 127) yielding K_{Pyr} value of 17 ± 2 dm^3 g^{-1}. Being that the interactions between the hydrocarbon and HNT surfaces are negligible, K_{Pyr} allowed us to calculate the constant of the complex formation between CB[8] and Pyrene, which is $(2.3\pm0.3)\times10^5$ dm^3 mol^{-1}. This value is consistent with guest-host complex stoichiometry of 1:1.[38]
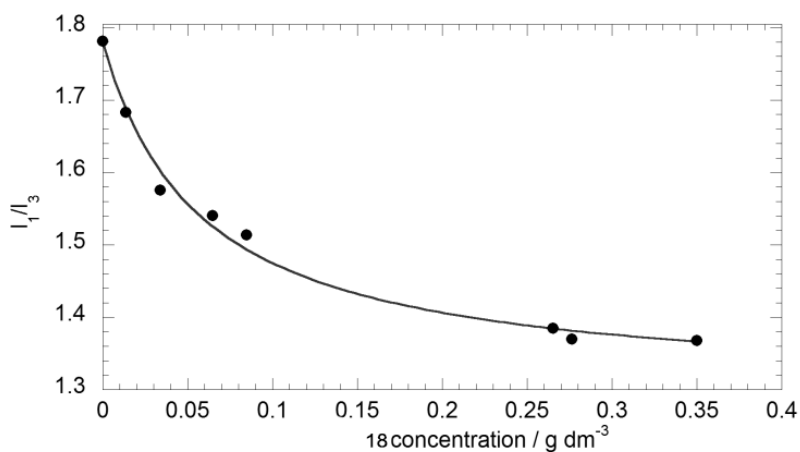
Figure 127. I_1/I_3 ratio for pyrene fluorescence spectra in aqueous dispersions of compound **18** as a function of the hybrid concentration. Lines are the best fits according to equations 7.4 and 7.5.

References

(1) Nakata, H.; Kawazoe, M.; Arizono, K.; Abe, S.; Kitano, T.; Shimada, H.; Li, W.; Ding, X. *Arch. Environ. Contam. Toxicol.* **2002**, *43* (4), 473.

(2) Loganathan, B.; Phillips, M.; Mowery, H.; Jones-Lepp, T. L. *Chemosphere* **2009**, *75* (1), 70.

(3) Kümmerer, K. *Annu. Rev. Environ. Resour.* **2010**, *35* (1), 57.

(4) Santos, L. H. M. L. M.; Araújo, A. N.; Fachini, A.; Pena, A.; Delerue-Matos, C.; Montenegro, M. C. B. S. M. *J. Hazard. Mater.* **2010**, *175* (1), 45.

(5) Xie, J.; Li, C.; Chi, L.; Wu, D. *Fuel* **2013**, *103*, 480.

(6) Ding, Y.; Zhao, Y.; Tao, X.; Zheng, Y.-Z.; Chen, J.-F. *Polymer (Guildf).* **2009**, *50* (13), 2841.

(7) Kohli, D.; Garg, S.; Jana, A. . *Indian Chem. Eng.* **2012**, *54* (3), 210.

(8) Perego, C.; Bagatin, R.; Tagliabue, M.; Vignola, R. *Microporous Mesoporous Mater.* **2013**, *166*, 37.

(9) Barreca, S.; Orecchio, S.; Pace, A. *Appl. Clay Sci.* **2014**, *99*, 220.

(10) Zhao, M.; Liu, P. *Microporous Mesoporous Mater.* **2008**, *112* (1–3), 419.

(11) Liu, R.; Zhang, B.; Mei, D.; Zhang, H.; Liu, J. *Desalination* **2011**, *268* (1–3), 111.

(12) Kiani, G.; Dostali, M.; Rostami, A.; Khataee, A. R. *Appl. Clay Sci.* **2011**, *54* (1), 34.

(13) Chen, H.; Zhao, J.; Wu, J.; Yan, H. *RSC Adv.* **2014**, *4* (30), 15389.

(14) Zhao, Y.; Abdullayev, E.; Vasiliev, A.; Lvov, Y. *J. Colloid Interface Sci.* **2013**, *406*, 121.

(15) Luo, P.; Zhao, Y.; Zhang, B.; Liu, J.; Yang, Y.; Liu, J. *Water Res.* **2010**, *44* (5), 1489.

(16) Cavallaro, G.; Lazzara, G.; Milioto, S. *J. Phys. Chem. C* **2012**, *116* (41), 21932.

(17) Liu, L.; Wan, Y.; Xie, Y.; Zhai, R.; Zhang, B.; Liu, J. *Chem. Eng. J.* **2012**, *187*, 210.

(18) Zeng, X.; Sun, Z.; Wang, H.; Wang, Q.; Yang, Y. *Compos. Sci. Technol.* **2016**, *122*, 149.

(19) Li, X.; Zhu, W.; Yan, X.; Lu, X.; Yao, C.; Ni, C. *Appl. Phys. A* **2016**, *122* (8), 723.

(20) Li, X.; Yao, C.; Lu, X.; Hu, Z.; Yin, Y.; Ni, C. *Appl. Clay Sci.* **2015**, *104*, 74.

(21) Xing, W.; Ni, L.; Liu, X.; Luo, Y.; Lu, Z.; Yan, Y.; Huo, P. *Desalin. Water Treat.* **2015**, *53* (3), 794.

(22) Xing, W.; Ni, L.; Liu, X.; Luo, Y.; Lu, Z.; Yan, Y.; Huo, P. *RSC Adv.* **2013**, *3* (48), 26334.

(23) Bielska, D.; Karewicz, A.; Lachowicz, T.; Berent, K.; Szczubiałka, K.; Nowakowska, M. *Chem. Eng. J.* **2015**, *262*, 125.

(24) Zhai, R.; Zhang, B.; Wan, Y.; Li, C.; Wang, J.; Liu, J. *Chem. Eng. J.* **2013**, *214*, 304.

(25) Yang, C.; Wu, S.; Cheng, J.; Chen, Y.

J. Alloys Compd. **2016**, *687*, 804.

(26)   Gereli, G.; Seki, Y.; Murat Kuşoğlu, İ.;
         Yurdakoç, K. *J. Colloid Interface Sci.*
         2006, *299* (1), 155.

(27)   Qiu, H.; Lv, L.; Pan, B.; Zhang, Q.;
         Zhang, W.; Zhang, Q. *J. Zhejiang Univ.*
         A **2009**, *10* (5), 716.

(28)   Russo, M.; Saladino, M. L.; Chillura
         Martino, D.; Lo Meo, P.; Noto, R. *RSC*
         Adv. **2016**, *6* (55), 49941.

(29)   Yu, L.; Xue, W.; Cui, L.; Xing, W.;
         Cao, X.; Li, H. *Int. J. Biol. Macromol.*
         2014, *64*, 233.

(30)   Fetterolf, M. L.; Patel, H. V.; Jennings,
         J. M. *J. Chem. Eng. Data* **2003**, *48* (4),
         831.

(31)   Han, R.; Zhang, J.; Han, P.; Wang, Y.;
         Zhao, Z.; Tang, M. *Chem. Eng. J.* **2009**,
         145 (3), 496.

(32)   Ghosh, D.; Bhattacharyya, K. G. *Appl.*
         Clay Sci. **2002**, *20* (6), 295.

(33)   Xiong, L.; Yang, Y.; Mai, J.; Sun, W.;
         Zhang, C.; Wei, D.; Chen, Q.; Ni, J.
         Chem. Eng. J. **2010**, *156* (2), 313.

(34)   Zhao, D.; Zhao, L.; Zhu, C.-S.; Huang,
         W.-Q.; Hu, J.-L. *J. Incl. Phenom.*
         Macrocycl. Chem. **2009**, *63* (3–4), 195.

(35)   Sousa e Silva, F. C.; de Lima, S. M.;
         Demets, G. J.-F. *RSC Adv.* **2014**, *4*
         (102), 58796.

(36)   Sueldo Occello, V. N.; Veglia, A. V.
         Anal. Chim. Acta **2011**, *689* (1), 97.

(37)   Lazzara, G.; Milioto, S.; Gradzielski,
         M. *Phys. Chem. Chem. Phys.* **2006**, *8*
         (19), 2299.

(38)   Barrow, S. J.; Kasera, S.; Rowland, M.
         J.; del Barrio, J.; Scherman, O. A.
         Chem. Rev. **2015**, *115* (22), 12320.

Chapter 8

Conclusions

1. Conclusions

Halloysite is a biocompatible, no toxic and abundantly available at low cost naturally formed tubule material of nanometric dimensions. The different inside/outside chemical composition allows the selective modification of both surfaces and also the selective loadings and release of molecules. Due to these characteristics, HNTs are suitable for development of hybrid sustainable materials with prospective industrial applications in wastewater remediation, green packaging, drug delivery and so on.

The functionalization of the halloysite external surface with organic moieties, such as mono and di-cationic triazolium salts, allowed to obtain the so-called supported ionic liquids that have been successfully used as stabilizer for palladium nanoparticles. The catalytic performances of these materials were tested in the Suzuki reaction between phenyl boronic acid and several aryl halides leading to the formation of the corresponding biaryls in good yields using microwave irradiations and the sole water as solvent. The use of microwaves has led many advantages, first of all, it was possible to perform that reaction which with conventional heating did not occur. These findings highlighted a synergistic effect between the metal nanoparticles and the specific tubular structure of halloysite. In addition, the "dicationic system" showed to be active for at least five cycles without leaching of the metal.

The catalytic performances of the Au nanomaterial supported on HNT were tested in the reduction reaction by varying the $NaBH_4$ and catalyst concentrations. The collected data show that the apparent kinetic constant increases with increasing of $NaBH_4$ concentration, on the contrary, surprisingly, it decreases with increasing the amount of the catalyst due to the aggregation between nanoparticles with consequently worse catalytic performances. In an aqueous dilute regime, no aggregation of nanoparticles was observed and the reaction rate depends only on the amount of catalyst.

The applicability of the reaction has been checked on a set of nitroarene derivatives showing that the reaction is promoted by the presence of electron donating group in *para* position with respect to the reaction center. The catalyst was used without loss in its catalytic activity for at least ten cycles.

The catalytic performances of HNT-Au were outstanding, reaching remarkable TOF values. To the best of our knowledge, this value probably represents the highest value ever reported for the reduction of similar system.

Also, a prototype of a flow system based on gold nanoparticles supported on thiol functionalized HNT for the reduction of 4-NP to 4-AP was developed.

Amino-functionalized halloysite was employed for the immobilization of Co nanoparticles and the catalytic performance of the new catalyst obtained was preliminarily

tested in the reduction of 4-nitrophenol by $NaBH_4$ obtaining high catalytic efficiency in particular at low $NaBH_4$ concentrations.

On the same reaction, one step reduction-action system has been tested.

Ferrite – sodium alginate loaded halloysite has been used on self-repairing and auto assembly systems. The micrometric and nanometric structures have been imagined by SEM showing some degree of organized structures.

The use of functionalized halloysite resulted advantageous also for application in the drug carrier. In particular, the triazolium modified halloysite, a kind of prodrug, was used for the loading and sustained release of two molecules with important biological activities, curcumin and cardanol respectively. Each characterization showed that depending on the molecules it was possible to obtain different halloysite hybrids, in particular in the case of curcumin, it arranges itself both inside and outside the tube while cardanol interacts preferentially with the external surface of halloysite.

These systems have the advantage of high drug encapsulation efficiency, as well as controlled and sustained release capabilities; moreover, the triazole moiety, into the HNT surface, was found to have a synergic effect with curcumin, which makes functionalized HNT an ideal carrier for anti-cancer therapies as confirmed by MTT and MTS assays.

The cardanol release from the carrier occurs in ca. 6 h and the released amount, as well as the kinetic parameters, are strongly influenced by the pH. Cytotoxicity experiments on several cell lines proved that cardanol is a promising anticancer and that the use of chemically modified nanotubes exercises synergic effects likely improving the permeability of cells to cardanol.

The introduction of a second cavity onto halloysite external surface, as cyclodextrin macromolecules, allowed to obtain multicavity systems which possess the characteristic both of halloysite and cyclodextrin and therefore can simultaneously interact with potential drugs such as silibinin and quercetin. Physico-chemical characterization of the halloysite hybrids showed that the silibinin interacts only with the halloysite lumen whereas quercetin with both cavities. The kinetic release of the two molecules from the multicavity system was also carried out. The interaction between cells and the carrier, analyzed by fluorescence microscopy, revealed cytoplasm specific uptake ability.

The same synthetic pathway was employed for the synthesis of halloysite nanosponges hybrids that showed the presence of two cavities, in particular as aforementioned, the cyclodextrin cavity and the halloysite inner lumen and additional channels formed by the presence of a hyper-reticulated network. This system was promising for environmental purposes, indeed it showed great capacity to adsorb contaminants such as organic dyes.

The halloysite nanosponge hybrids were also used as carrier for clotrimazole, an antifungine drug, in order to obtain novel systems for the treatment of oral Candidosis. Adsorption isotherm showed that the clotrimazole better interacts with both halloysite and cyclodextrin in acidic medium; furthermore, by means of kinetic investigations, it is possible to conclude that such a system can effectively release in a sustained manner over the time.

The non-covalent functionalization of the halloysite surfaces was exploited for the synthesis of halloysite cucurbit[8]uril hybrids. In this system, the cucurbituril interacts with both the external surface and the lumen as highlighted by several techniques. Solid state variable contact time, cross polarization, magic angle spinning NMR experiments evidenced that the cucurbit[8]uril distribution in the halloysite is driven by the specific interaction with HNT inner aluminol surface that is richness in hydrogen bond donating groups.

The new hybrid was used once again for the removal of organic contaminants such as toluene and pyrene both in gas and liquid phases.

Chapter 9

Experimental Details

9. *Experimental details*

9.1. *Material and methods*

Cardanol was provided by Prof. Attanasi, University of Urbino.

The 3-azidopropyltrimethoxysilane **7** was synthesized as previously reported[1].

Methylene blue, toluidine blue, methyl orange and congo rubin were purchased from Merck company, bromocresol green and rhodamine B were purchased from Carlo Erba; all dyes were used without further purification.

All reagents were purchased from Sigma-Aldrich and used without further purification.

Halloysite was purchased from Sigma-Aldrich and used without further purification. Halloysite has an average tube diameter of 50 nm and inner lumen diameter of 15 nm. Typical specific surface area is 65 m^2 g^{-1}; pore volume of ~1.25 cm^3 g^{-1}; refractive index 1.54 and specific gravity 2.53 g cm^{-3}.

Halloysite used for the synthesis of HNT-CD hybrid nanosponge (compound **6**) is the Matauri Bay halloysite from Northland, New Zealand, supplied by Imerys Tableware, New Zealand.

Microwave-assisted syntheses were carried out with a CEM DISCOVER monomode system in a closed vessel.

Thermogravimetric analyses were performed on a Q5000 IR apparatus (TGA Instruments) under a nitrogen flow of 25 cm^3 min^{-1} for the sample and 10 cm^3 min^{-1} for the balance. The weight of each sample was ca. 10 mg. Measurements were carried out by heating the sample from room temperature up to 900 °C at a rate of 10 °C min^{-1}.

IR spectra (KBr) were recorded with an Agilent Technologies Cary 630 FT-IR spectrometer. Specimens for these measurements were prepared by mixing 5 mg of the sample powder with 100 mg of KBr.

ζ-potential and dynamic light scattering (DLS) measurements were taken by using microelectrophoretic ZetaPlus Potential Analyzer (Brookhaven Instruments) at 25.0±0.1 °C.

Halloysite-cyclodextrin nanosponges (compound **6**) were imagined by Scanning Electron Microscope 22 (Hitachi S4800 FE-SEM). The halloysite samples were coated with 1 nm gold by Cressington 23 Sputter Coater (208HR) before the imaging.

For TEM observation the samples were prepared using a drop of suspension solution on formvar-coated copper grid (400 mesh) and allowing the drop to dry completely in a

vacuum desiccator. The TEM images of the samples were obtained using a Philips TEM CM 100 transmission electron microscope at accelerating voltage = 80 kV.

The dispersion was agitated in an orbital shaker (VWR) at a constant speed of 250 rpm.

The specific surface area and pore sites distribution were made by N_2 adsorption/desorption Nova 2200 Quantachrome Instruments analyzer.

UV-vis measurements were performed using a Beckmann DU 650 spectrometer.

^{13}C $\{^1H\}$ CP-MAS NMR spectra were obtained at room temperature through a Bruker Avance II 400 MHz (9.4 T) spectrometer operating at 100.63 MHz for the ^{13}C nucleus and 400 MHz for ^1H. $^1H \rightarrow ^{13}C$ Cross Polarization Magic Angle Spinning (CP/MAS) NMR experiments were carried out at MAS rate of 10 kHz using zirconia rotors of 2.5 mm in diameter and with KEL-F caps. The ^1H 90° pulse was 2.5 μs, 300 scans, a contact time of 1.5 ms and a repetition delay of 3 s. The optimization of the Hartmann-Hahn condition was obtained using an adamantane sample. The cross polarization time (T_{CH}) values for the carbonyl carbon were obtained through variable contact time (VCT) experiments. The contact times used in the (VCT) experiments were 0.05, 0.1, 0.2, 0.3, 0.4, 0.5, 0.6, 0.8, 1.0, 1.2, 1.5, 2.0, 2.5, 3.0, 3.5, 4.0, 4.5, 5.0, 6.0 and 7.0 ms.

Dynamic light scattering (DLS) experiments were done by means of a Zetasizer NANO-ZS (Malvern Instruments). The field-time autocorrelation functions were well described by a single decay, which provides the decay rate (Γ) of the diffusive mode. For the translational motion, the collective diffusion coefficient at a given concentration is $D_t = \Gamma/q^2$ where q is the scattering vector given by $4\pi n \lambda^{-1} \sin(\theta/2)$ being n the water refractive index, λ the wavelength (632.8 nm) and θ the scattering angle (173°). The concentration of the compound **18** aqueous dispersion was 10^{-3} wt %.

Differential scanning calorimetry was performed by using a differential scanning calorimeter TA Instrument DSC (2920 CE). The calorimeter was calibrated using indium as standard. Each sample (2–3 mg) was heated according to a temperature program of 10 °C min^{-1} in the temperature range comprised between 10 and 500 °C.

The microscope ESEM FEI QUANTA 200F, with EDX probe, was used to study the morphology of HNT hybrid. Before each experiment, the sample was coated with gold in argon by means of an Edwards Sputter Coater S150A to avoid charging under electron beam.

^1H-NMR spectra were recorded at 250 MHz in CDCl$_3$ solutions at room temperature on a Bruker Avance II 300 MHz spectrometer.

Solid state ^{13}C and ^{29}Si NMR spectra were obtained at room temperature through a Bruker Avance II 400 MHz (9.4 T) spectrometer.

Fluorescence investigations were carried out by using pyrene as a fluorescent probe, which is sensitive to the nature of its microenvironment.[2] The emission spectrum consists mainly of five bands. The ratio between the intensity of the first (at 373 nm) and that of the third (at 384 nm) vibrational band (I_1/I_3) strongly depends on the medium polarity: it is ca. 1.8 in aqueous media and it ranges between 1.2 and 0.8 in hydrophobic media. The steady-state pyrene fluorescence spectra of the air equilibrated samples were registered with a Fluoromax 4 (Jobin-Yvon) spectrofluorometer (right angle geometry, 1 cm × 1 cm quartz cell) at 25.0 ± 0.1 °C. The excitation wavelength was 333 nm and the emission spectra were recorded from 350 to 500 nm. The widths of slits were set at 1.5 and 1 nm for excitation and emission, respectively. The dispersions for these measurements were prepared as described in the following. Known aliquots of a solution of pyrene in acetone were carefully added into dark flasks by a Hamilton microsyringe. After solvent evaporation, the aqueous dispersions of the investigated materials were added and equilibrated at room temperature for approximately 3 days under vigorous stirring. For all of the dispersions, the final concentration of pyrene was 5×10^{-7} mol dm^{-3}, which is its solubility in water. The concentrations of pristine and functionalized HNT are 0.31 g dm^{-3} and 0.27 g dm^{-3}, respectively.

Contact angle measurements were performed by using an optical contact angle apparatus (OCA 20, Data Physics Instruments) equipped with a video measuring system having a high-resolution CCD camera and a high-performance digitizing adapter. SCA 20 software (Data Physics Instruments) was used for data acquisition. To obtain a tablet, the powder like material was pressed under 104 kg cm^{-2} for 10 min. The contact angle of water, in air, was measured by the sessile drop method. The water droplet volume was 10.0±0.5 mL. The temperature was set at 25.0±0.1 °C for the support and the injecting syringe as well. Images were collected 25 times per second. From the data analysis the contact angle, the volume and the contact area of the drop were calculated. The volume of the droplet was constant within the time of the experiment.

The chromatographic measurements were performed using a Shimadzu Class VP (Shimadzu, Japan) which consists of a pump (LC-10AD VP Shimadzu), an injection valve equipped with a 20 mL injection loop, an *UV-vis* Diode-Array (SPD-M10A VP) and an acquisition data software Class-VP. After optimization of chromatographic conditions, the separation was carried out in a C_{18} column (Discovery Supelco, 25 cm×4.6 mm, 5 μm).

The mobile phase consisted of methanol/water 90:10 v/v, at room temperature, flow 1 mL min^{-1}.

The ITC experiments were carried out at 25 °C by means of a nano-ITC200 calorimeter (MicroCal). An amount of approximately 40 mL of quercetin solution (2 mmol dm^{-3}) was injected into the thermally equilibrated ITC cell (202 mL) filled with the CD solution (0.1 mmol dm^{-3}). The solvent was phosphate buffer (pH = 6.9)/MeOH 6:4. The heat effect was measured after each addition of 2 mL and corrected by dilution effects.

The dispersions were sonicated using an ultrasound bath VWR Ultrasonic Cleaner (power 200 W and frequency 75 MHz).

Inductively Coupled Plasma-Optical Emission Spectrometry (ICP-OES) analyses were carried out with an Optima 2100, Perkin Elmer, equipped with an autosampler model AS-90. Analyses were conducted using a calibration curve, obtained by dilution (range: 0–10 ppm) of palladium standard solution for ICP-OES analyses. The operative wavelengths were 340.458 and 363.470 nm.

Steady-state fluorescence spectra were acquired using a JASCO FP-777W spectrofluorimeter. Excitation and emission slits were 1.5 and 3 nm, respectively, the excitation wavelength was 372 nm and the emission interval was between 300 and 750 nm.

9.1.1. Kinetic release

The release of biological molecules from the HNT carriers was done as follows: 25 mg of the sample was dispersed in 1mL of dissolution medium and transferred into a dialysis membrane (Medicell International Ltd MWCO 12-14000 with a diameter of 21.5 mm). Subsequently, the membrane was put in a round bottom flask containing 10 mL of the release medium at 37 °C and stirred. Different media (0.1 M HCl, phosphate buffer pH 6.0, 7.4 and 8.0 respectively) were considered in order to evaluate the influence of pH on the release behavior of the drug. At fixed time, 1 mL of the release medium has been withdrawn and analyzed by *UV-vis* (at the appropriate absorption wavelength). To keep constant the volume of the release medium, 1 mL of fresh solution has been used to replace the collected one. The biological molecules concentrations in the solution were determined by *UV-vis* spectrophotometry using the Lambert-Beer law. Total amounts of drug released (Ft) were calculated as follows:

$$F_t = V_m C_t + \sum_{i=0}^{t-1} V_a C_i \qquad\qquad Equation\ 16$$

where V_m and C_t are the volume and the concentration of the drug at time t. V_a is the volume of the sample withdrawn and C_i is the drug concentration at time i (i < t).

9.1.2. Cell culture

The human papillary thyroid carcinoma cell line BCPAP and the human anaplastic thyroid carcinoma cell lines SW1736 and C643 were kindly provided by Prof. F Frasca, University of Catania. BCPAP were cultured in RPMI 1640 (PAA), supplemented with 10% FBS, 5% penicillin-streptomycin, and 5% glutamine. SW1736 and C643 cell line was cultured in DMEM (PAA), supplemented with 10% FBS, 5% penicillin-streptomycin, and 5% glutamine cultures were maintained in 5% CO_2 at 37 °C in a humidified incubator.

8505c anaplastic thyroid cancer cells (ECAC Sigma-Aldrich) were grown in RPMI1640 (Sigma-Aldrich) supplemented with 10% FCS (Sigma-Aldrich), 2 mM L-glutamine and penicillin-streptomycin and incubated at 37 °C in 5% CO_2 and 100% humidity.

HA22T/VGH, HepG2, and Hep3B are a poorly differentiated hepatoma cell lines which contain HBV integrants. It was cultured in Roswell Park Memorial Institute (RPMI) 1640 (HyClone Europe Ltd., Cramlington, UK) supplemented with 10% heat-inactivated fetal calf serum, 2 mM L-glutamine, 1 mM sodium pyruvate, 100 units/mL penicillin and 100 mg/mL streptomycin (all reagents were from HyClone Europe) in a humidified atmosphere at 37 °C in 5% CO_2. Cells having a narrow range of passage number were used for all experiments.

9.1.3. MTT assay for curcumin

Cell proliferation was assessed by colorimetric assay using 3-(4,5-Dimethylthiazol-2-yl)-2,5-diphenyltetrazolium bromide (MTT). Cells were plated in 96-well plate at a density of 5×10^3 cells/well and cultured up to 24, 48 and 72h in the presence of HNT/Curc or **10a**/Curc. At the end of the incubation period the cells were incubated for 4h at 37 °C with MTT; then the medium was removed and the cells were treated with DMSO for 5 min. Absorbance was read at 550 nm in a Multiskan FC microplate reader (Thermo Fisher Scientific). Protocol to determine the amount of curcumin embedded into cells. The amount of drug embedded into cells (C_{cell}) was determined by the following equation:

$$C_{cell} = C_i - C_f \hspace{3cm} Equation\ 17$$

where C_i is the concentration of curcumin associated to halloysite and C_f is the drug concentration in the supernatant after incubation, respectively. The curcumin content in the supernatant was determined spectrophotometrically at 445 nm referring to a standard calibration curve.

9.1.4. MTS assay for cardanol

The cells were seeded at 2×10^4 cells/well onto 96-well plates and then incubated overnight. At time 0, medium was replaced with fresh complete medium and cardanol, **11a-b** and **22a-b** thereof were added in concentrations as indicated. At the end of treatment,16 mL of a commercial solution (obtained from Promega Corporation, Madison, WI, USA) containing 3-(4,5-dimethylthiazol-2-yl)- 5-(3-carboxy methoxyphenyl)-2-(4-sulphophenyl)-2H-tetrazolium (MTS) and phenazine ethosulfate were added. The plates were incubated for 2h in a humidified atmosphere at 37 °C in 5% CO_2. The bioreduction of the MTS dye was assessed by measuring the absorbance of each well at 490 nm. Cytotoxicity was expressed as a percentage of the absorbance measured in the control cells.

9.1.5. MTS assay for silibinin and quercetin

Tumoral cells were plated at 1500 cells per well in triplicate in a 96-well plate. After 24h of incubation, HNT/drug suspension was added ranging from 100 mM to 0.391 mM. After 72h of incubation the plate was washed with sterile PBS, to avoid color interference from the HNT compound. 20 mL of the CellTiter 96 AQueous One Solution (Promega, Milan) was added, and the plate was incubated for 4 hours at 37 °C. The absorbance at 490 nm was recorded using a plate reader (Multiskant TC Microplate Photometer, Thermo SCIENTIFIC, Milan). The results were expressed as % of viability with respect to the control cells that were not treated. IC_{50} was calculated by Global Optimization using Simulated Annealing Software (GOSA-fit).

9.1.6. Fluorescence microscopy

8505c cells were seeded in a Nunc Lab-Tek Chamber Slide at a density of 300 000 cells per slide in RPMI culture medium and incubated under standard conditions. After 24h HNT complex was added at 10 mM and incubated for 1h and 24h, respectively. Slides were then extensively washed with PBS-containing Ca and Mg and counterstained with Evans Blue in PBS at 0.005%. Slides were observed using a Zeiss Axiophot fluorescence microscope with a FITC filter equipped with a Nikon DS-Fi1 CCD-camera.

9.1.7. Swelling properties

Water sorption capacity of HNT-CDs nanosponge hybrid was determined gravimetrically. The nanomaterial with determined weight was immersed for 1 h in distilled water at room temperature until swelling equilibrium was reached. After this time

water was removed and the nanomaterial weighted using analytical balance. Water excess was removed using filter paper prior weighting. The swelling ratio (SR) was calculated using the equation:

$$SR\,(\%) = \frac{(W_s - W_d)}{W_d} \cdot 100 \qquad\qquad \textit{Equation 18}$$

where W_s and W_d are the weights of the hybrid at the swelled and the dry state, respectively. Experimental data were expressed as the mean ± standard deviation (SD) for *n*=3.

9.1.8. Batch adsorption experiments

All adsorption experiments were conducted on sealed vessels containing 5.0 mg of HNT-CDs hybrid and 2 mL of RB solution (2×10^{-5} M) in HCl 0.1 N, acetate buffer pH 4.24 and phosphate buffer pH 7.4 at 277, 298, 310 and 331 K, respectively. The obtained dispersion were vigorously vortexed and shaken in a thermostatic shaker with a shaking of 200 rpm at 25 °C. The supernatant were obtained by centrifugation for detecting RB concentration via *UV-vis* spectrophotometer at the maximum absorption wavelength of 550 nm. The removal efficiency (RE (%)) was calculated by:

$$RE\,(\%) = \frac{(C_0 - C_e)}{C_0} \times 100 \qquad\qquad \textit{Equation 19}$$

where C_0 and C_e are initial and equilibrium concentrations of RB (M), respectively.

9.1.9. Adsorption isotherms

The adsorption isotherms of HNT-CDs hybrids were obtained by weighing 5 mg of HNT-CDs nanosponge in the presence of RB solution in a concentration range of 5×10^{-6} - 7.5×10^{-5} M, in HCl 0.1 N, acetate (0.01 M) buffer pH 4.54 and phosphate buffer pH 7.4, and shaken in a thermostated shaker with a shaking of 200 rpm for 12 h to reach equilibrium at 298 K. The equilibrium adsorption capacity Q_e (mol g^{-1}) was calculated by the following equation:

$$Q_e = \frac{(C_0 - C_e) \cdot V}{M} \qquad\qquad \textit{Equation 20}$$

where C_0 and C_e are initial and equilibrium concentrations of RB (M), respectively, M is the weight of HNTs (g) and V is the volume of RB solution (L).

9.1.10. Adsorption kinetics

The batch experiments were carried out for investigating the adsorption kinetics of RB onto HNT-CDs nanosponge hybrid at room temperature in acetate buffer (0.01 M) pH 4.54. For all experiments, HNT-CDs nanosponge hybrid (5 mg) was added to 2 mL solution of RB (2.5×10^{-5} M). The amount of RB adsorbed at time t (Q_t, mol g^{-1}) was calculated by the following equation:

$$Q_t = \frac{(C_0 - C_t) \cdot V}{M}$$

Equation 21

where C_0 and C_t are initial and t time concentrations of RB (M), respectively, M is the weight of HNTs (g) and V is the volume of RB solution (L).

9.1.11. Adsorption experiments of toluene in vapor phase

The adsorption capacity of pristine HNT and CB[8] as well as the compound **18** powders towards toluene in vapor phase was studied as in the following. Each adsorbant was equilibrated in a desiccator saturated with toluene vapors at 22.0 ± 0.1 °C. The amount of adsorbed toluene was determined through gravimetric method.

9.1.12. Adsorption experiments of toluene in liquid phase

The ability of pristine HNT and compound **18** hybrid to entrap toluene dissolved in water was monitored following the protocol reported for similar systems.[33] To this purpose, 0.4 g of the adsorbent material was added to 10 cm^3 of aqueous saturated solution of toluene. The dispersions were stirred and equilibrated for 1 week. The concentration of residual toluene in the aqueous phase (C_w) was determined by measuring the absorption spectra at 25.0 ± 0.1 °C within a range comprised between 190 and 600 nm using an Analytic Jena Specord S 600 BU by keeping in mind that toluene presents a peak at 261 nm.

9.1.13. Clotrimazole adsorption isotherms

The adsorption isotherms of compound **2** were obtained by weighing 5 mg of **2** in the presence of CLT solution in a concentration range of $1.25 \times 10^{-4} - 1.9 \times 10^{-5}$ M, in HCl 0.1 N and phosphate buffer pH 7.4, and shaken in a thermostated shaker with a shaking of 200 rpm for 12 h to reach equilibrium at 298 K. The equilibrium adsorption capacity Qe (mol g^{-1}) was calculated by the following equation:

$$Q_e = \frac{(C_0 - C_e) \cdot V}{M}$$

Equation 22

where C_0 and C_e are initial and equilibrium concentrations of CLT (M), respectively, M is the weight of HNTs (g) and V is the volume of CLT solution (L).

9.1.14. General procedure to obtain HNT/biological molecule dispersions

Various weighed amounts of HNT compounds (from 2 up to 14 mg) were dispersed by sonication for 5 minutes in H_2O, at an ultrasound power of 200 W and a temperature of 25 °C. 1 mL of appropriate biological molecule solution (1×10^{-4} M) in a mixture of appropriate buffer/EtOH (6:4) was added to the HNT dispersions. The final volume was 10 mL.

9.1.15. General procedure to obtain solid complexes

To a dispersion of HNT in deionized water (5 mL), 1 mL of biological molecules solution 10^{-2} M in ethanol was added. The suspension was sonicated for 5 min, at an ultrasound power of 200 W and at 25 °C and then was evacuated for 3 cycles. The suspension was left under stirring for 24 h at room temperature. After this time the powder was washed with water and then dried at 80 °C under vacuum.

For the dual loaded complexes, afterward the HNT/biological molecule solid complex was suspended again in deionized water (5 mL) and 1 mL of quercetin solution (10^{-2} M) in ethanol was, then, added. The suspension was stirred for 4 days at rt and then was filtered; the powder was washed with small amounts of water and then dried at 70 °C under vacuum overnight.

9.1.16. General procedure for spectrophotometric measurements

Measurement solutions were prepared by adding increasing volumes of the solution of heptakis-6-(tert-butyldimethylsilyl)-2-propaneoxy-2-hexanethio-β-cyclodextrins in phosphate buffer (pH 6.9) (1.2×10^{-3} M) to 100 mL of the quercetin aqueous solution into a volumetric flask. In these solutions, the concentrations of the quercetin were constant and equal to 1×10^{-5} M while the concentration of the heptakis-6-(tert-butyldimethylsilyl)-2-propaneoxy-2-hexanethio-β-cyclodextrin increased from

1.2×10^{-4} M up to 1.08×10^{-3} M. The absorbance was recorded at 370 nm and spectroscopic data were fitted using the following equation (the non-linearized version of Benesi–Hildebrand treatment):

$$CD + Que \underset{\leftarrow}{\overset{K_1}{\rightarrow}} CD - Que \qquad\qquad Equation\ 23$$

$$CD - Que + CD \overset{K_2}{\underset{\leftarrow}{\rightarrow}} CD - Que - CD \qquad \qquad \textit{Equation 24}$$
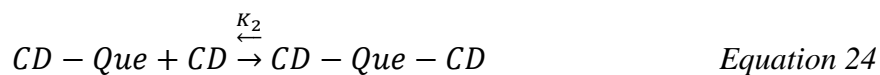
$$\Delta A = \frac{\Delta \varepsilon \cdot \beta \cdot Que \cdot [CD]^2}{1 + \beta \cdot [CD]^2} \qquad \qquad \textit{Equation 25}$$

$$\beta = K_1 \cdot K_2 \qquad \qquad \textit{Equation 26}$$

where $\Delta \varepsilon$ is the difference of the extinction molar coefficient of free and complexed quercetin, and Que and CD are the total concentration of the quercetin and the heptakis-6-(tertbutyldimethylsilyl)-2-propaneoxy-2-hexanethio-β-cyclodextrin, respectively.

9.1.17.   *Typical Procedure for the Suzuki reaction via microwave irradiations*

Catalyst, phenylboronic acid (65 mg, 0.547 mmol), K_2CO_3 (84 mg, 0.61 mmol), aryl bromide (0.55 mmol), ethanol (0.6 mL) and water (0.6 mL) or water (1.2 mL) were placed in a microwave test tube provided with a cap The mixture was inserted into microwave apparatus at a temperature of 120 °C and 14 W power, under constant stirring for 10 min; the solvent was then removed under reduced pressure and the residue was checked by ^{1}H-NMR to calculate conversion.

9.1.18.   *Recyclability of the catalysts*

Catalysts (1 mol%), phenylboronic acid (65 mg, 0.547mmol), K_2CO_3 (84 mg, 0.615mmol), 3-bromoanisole (0.55mmol), ethanol (0.6 mL) and water (0.6 mL) or water (1.2 mL) were placed in a microwave test tube provided with a cap The mixture was inserted into microwave apparatus at a temperature of 120 °C and 14 W power, under constant stirring for 10 min. The reaction mixture was then centrifuged and the liquid mixture was decanted; the residual solid was washed with CH_2Cl_2, water, and Et_2O. The catalysts were dried and reused.

9.1.19.   *General conditions for the reduction nitroarenes*

Generally, **31** aqueous suspension (different volume to reach the desired catalyst amount) was added into a mixed aqueous solution of 2 mL containing a nitroarene (0.10 mM) and $NaBH_4$ (from 8 to 50 mM) in a quartz cuvette, at room temperature. The reduction process was monitored by recording the $UV-vis$ spectra of the reaction mixture at 2 min intervals during the reaction. The reaction rate constant was determined by measuring the absorbance intensity of the initially observed peak of the substrate, as a function of time.

9.1.20. Recyclability of 31 catalyst

31 catalyst (5 mg), 4-nitrophenol (0.3 mM), and NaBH$_4$ (33 mM) were placed in a vial under constant stirring and at room temperature. After 30 min, the complete reduction was checked by measuring the absorbance intensity at 397 nm. The reaction mixture was then centrifuged and the supernatant was decanted; the residual solid was washed three times with water, **31** was dried and reused in the same reaction for ten consecutive cycles.

9.1.21. Reduction of 4-NP under flow conditions

A glass tube column with an inner diameter of 10 mm and a length of 100 mm (Supelco Omnifit Column Kit) was filled with sand (50-70 mesh) and **31** (pore volume 1.26-1.34 mL g^{-1}). The column was first eluted with water by using a peristaltic pump (LC-10AD VP Shimadzu). For evaluate the catalytic performance of the system, a mixed solution of 4-NP (0.100 mM) and NaBH$_4$ (100 mM) was injected into the column and eluted at a flow rate of 1 mL min^{-1}. The reduction 4-NP by NaBH$_4$ under the catalysis of **31** was monitored by the *UV−vis* spectra of the eluent collected. The amount of 4-NP reduced within 30 min was estimated by using a calibration curve and it was found that the system is able to reduce ca. 70% of the initial 4-NP for at least one month.

9.1.22. General conditions for the reduction 4-NP using Co catalyst

Generally, **33a** aqueous suspension (different volume to reach the desired catalyst amount) was added into a mixed aqueous solution of 2 mL containing a nitroarene (0.10 mM) and NaBH$_4$ in a quartz cuvette, at room temperature. The reduction process was monitored by recording the *UV−vis* spectra of the reaction mixture at 1 to 10 min intervals during the reaction. The reaction rate constant was determined by measuring the absorbance intensity of the initially observed peak of the substrate, as a function of time.

9.2   Syntheses

9.2.1. Synthesis of Compound 1

First, 1 g of HNT was weighted in a MW test tube provided with a cap, and 2 mL of 3-mercaptopropyl trimethoxysilane was added dropwise. The mixture was dispersed ultrasonically for 5 min at room temperature and inserted in MW apparatus at 100 °C, under constant stirring for 1h. The powder was filtered, rinsed with MeOH and dried at 80 °C overnight.

9.2.2. Synthesis of heptakis-6-(tert-butyldimethylsilyl)-2-allyloxy-β-cyclodextrin (compound 2)[3]

In a 500 mL round bottom flask NaH powder (60%, 0.790 g, 32 mmol) was weighed and under constant stirring, at 0 °C and Ar atmosphere were added 120 mL of DMF. After 10 minutes a solution of heptakis-6-(tert-butyldimethylsilyl)-β-cyclodextrin **2** (5 g, 26 mmol) in DMF (25 mL) was added dropwise. The reaction was allowed to stir at 0 °C for 30 min and then overnight at room temperature. The reaction vessel was cooled to 0 °C, and allyl bromide (1.64 mL, 18.95 mmol) was added dropwise. The reaction was then allowed to stir overnight at room temperature. The reaction was evaporated to dryness, and the residue was dissolved in CH_2Cl_2 (250 mL) and washed with water (3x150 mL) and finally with brine (150 mL). The organic layer was dried (MgSO4), filtered, and evaporated to dryness to afford a white foam. Purification by column chromatography (SiO_2, hexane/AcEt 8:1, 6:1 and 4:1) afforded a yellow foam with a yield of 25%.

^{1}H-NMR ($CDCl_3$, 300 MHz) δ: 0.04 (s, 21H, Si(C**H**$_3$)), 0.05 (s, 21H, Si(C**H**$_3$)), 0.89 (s, 63H, C(C**H**$_3$)$_3$), 3.31-3.35 (dd, 7H, **H**(2)); 3.51-3.68 (m, 21H, **H**(4), **H**(5), **H**(6a)); 3.92-4.00 (m, 14H, **H**(6b), **H**(3)); 4.21-4.27 (m, 7H, OC**H**$_A$); 4.47-4.53 (dd, 7H, OC**H**$_B$); 4.92 (d, 7H, **H**(1)); 5.21-5.35 (m, 14H, CH=C**H**$_2$); 5.90-6.03 (m, 7H, C**H**=CH$_2$).

^{13}C-NMR ($CDCl_3$, 300 MHz) δ: 5.2 (Si**C**H$_3$), -5.1 (Si**C**H$_3$), 18.3 (**C**(CH$_3$)$_3$), 25.9 (C(**C**H$_3$)$_3$), 61.7 (**C**-6), 71.6, 79.5, 82.0 (**C**-2, **C**-3, **C**-4, **C**-5), 73.2 (O**C**H$_2$), 101.1 (**C**-1), 118.2 (**C**H$_2$=CH), 134.3 (CH$_2$=**C**H).

9.2.3. Synthesis of the HNT modified by heptakis-6-(tertbutyldimethylsilyl)-2-allyloxy-*β*-cyclodextrin (compound 3)

Compound **1** (0.10 g) was weighed in a MW test tube provided with a cap and compound **2** (0.4 mmol) was added. The mixture was inserted into the MW apparatus and the temperature of 100 °C and a power of 30 W, under constant stirring, for 1h. The solid was filtered off, rinsed with CH_2Cl_2 and dried at 80 °C under vacuum.

9.2.4. Synthesis of heptakis-6-(tert-butyldimethylsilyl)-2-propaneoxy-2-hexanethio-*β*-cyclodextrins

In a quartz test tube the heptakis-6-(tert-butyldimethylsilyl)-2-allyloxy-β-cyclodextrin **2** (100 mg, 46.2 mmol, 1 eq.) and hexanethiol (0.23 mL, 1.62 mmol, 35 eq.) were dissolved in distilled 95% toluene/MeOH (the concentration of CDs was 5 mM). A stream of Ar was bubbled through the solution for 15 min to thoroughly degas it. The test tube, maintained under an atmosphere of Ar, was placed in front of a Hg lamp (265 nm) and stirred for 20 h. Following removal of solvent, the residue was washed three times with hexane and purified by chromatography (SiO_2, from 100% hexane/EtOAc to 50% hexane/EtOAc) to afford the product as a white solid (yield 82%).

^{1}H-NMR (DMSO, 300 K, 300 MHz) δ: 0.2 (42H, s), 0.88 (21H, t, J = 9.5 Hz), 0.98 (63H, s), 1.30 (28H, m), 1.42 (14H, m), 1.63 (14H, m), 1.90 (14H, m), 2.68 (14H, m), 2.79 (14H, m), 3.37 (14H, t,

J = 7.4 Hz), 3.02 (7H, dd, J = 3.0 Hz, J = 9.5 Hz), 3.54 (14H, m), 3.59 (7H, bs), 3.79 (7H, m), 3.99 (14H, m), 4.94 (7H, d, J = 3.3 Hz).

^{13}C-NMR (DMSO, 300 K, 75 MHz) δ: 4.9, 14.1, 22.7, 25.9, 28.2, 30.6, 30.8, 31.1, 33.2, 73.5, 62.5, 74.4, 74.9, 75.9, 79.7, 102.0.

9.2.5. Synthesis of compounds 5a–d

The appropriate thiol **4a–d** (1000 eq.) and compound **3** (100 mg) were dissolved in anhydrous toluene. A stream of Ar was bubbled through the solution for 15 min to thoroughly degas it. The solution, maintained under an atmosphere of Ar, was placed in front of a Hg lamp and stirred for 24 h. Following removal of solvent, the precipitate was washed with CH_2Cl_2 and dried overnight at 80 °C under vacuum.

9.2.6. Synthesis of CDs polymer

Heptakis-6-(tert-butyldimethylsilyl) 2-allyloxy-β-cyclodextrin **2** (200 mg) was weighed in a MW test tube provided with a cap and a catalytic amount of AIBN was added. The mixture was inserted in the MW apparatus at 100 °C, under constant stirring, for 1 h. Successively, the solid was filtered off, rinsed several times with CH_2Cl_2 (until the unreacted reagents were not detected by TLC) and dried at 80 °C under vacuum.

^{1}H-NMR (DMSO, 300 MHz) δ: 0.04 (s, Si(**CH$_3$**)), 0.05 (s, Si(**CH$_3$**)), 0.89 (s, C(**CH$_3$**)$_3$), 3.31-3.35 (m); 3.51-3.68 (m); 3.92-4.00 (m); 4.21-4.27 (m); 4.47-4.53 (m); 4.92 (m); 5.21-5.35 (m); 5.90-6.03 (m).

^{1}H-NMR of the CD polymer compared to the one of β-CDs shows broad signals, typical of not symmetric cyclodextrin modifications.
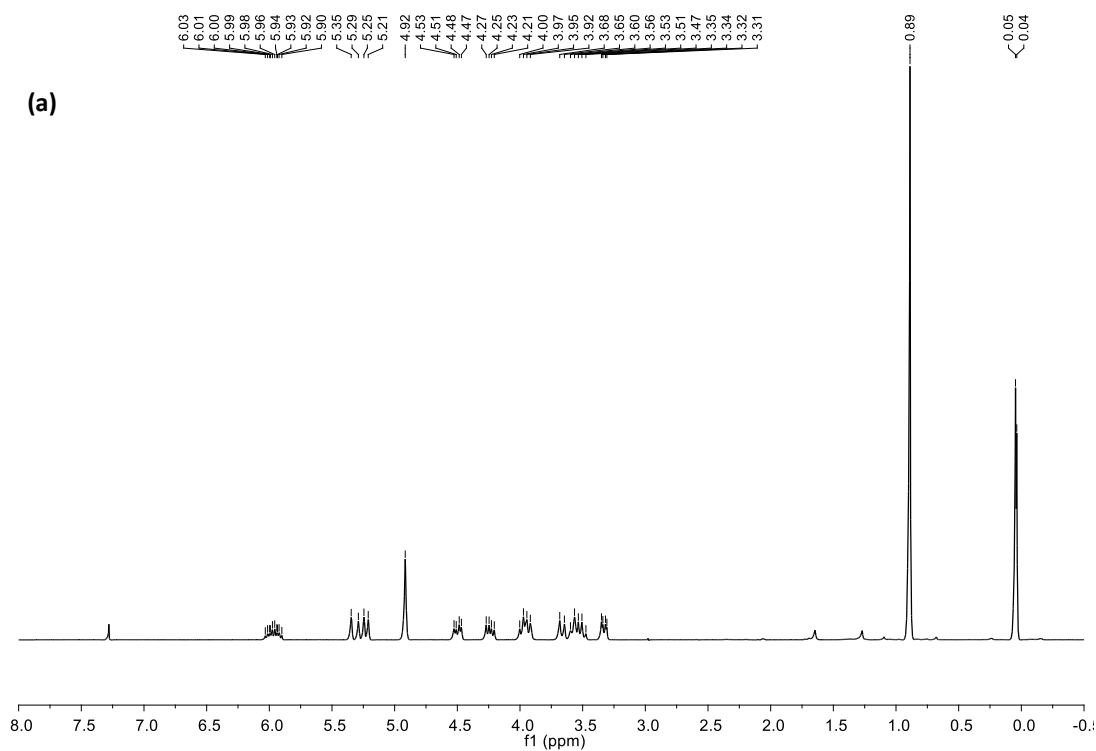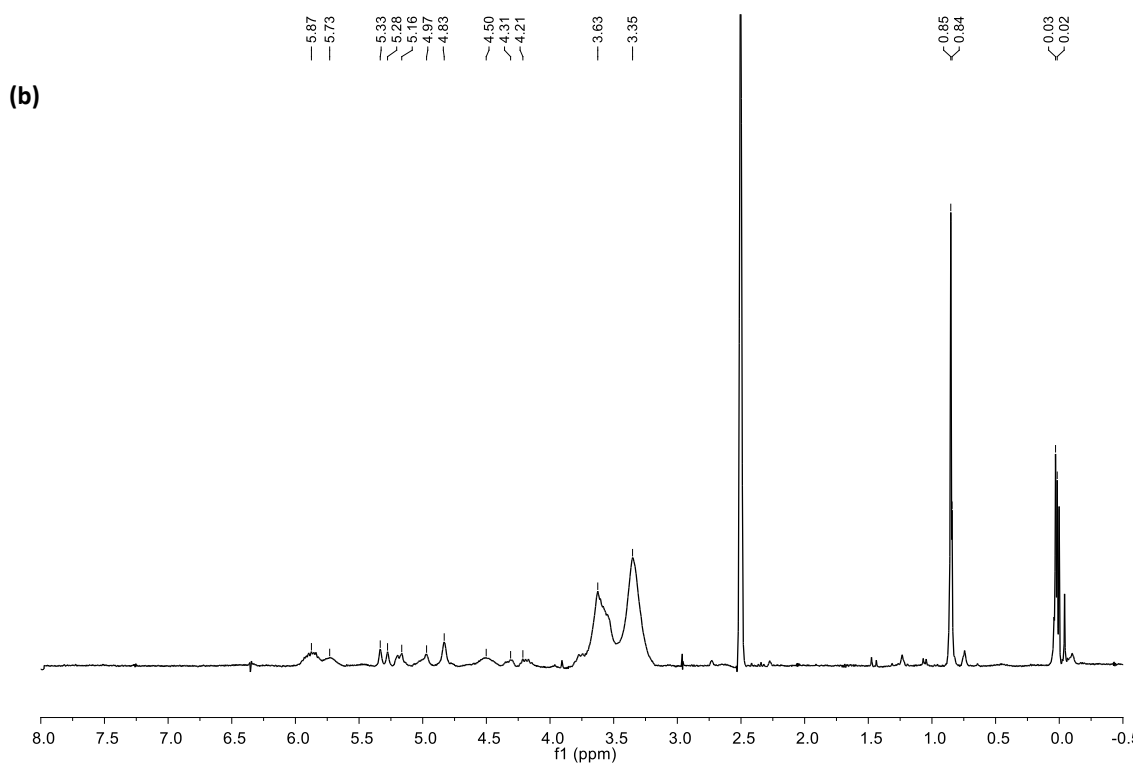
Figure 128. ^{1}H-NMR spectra of (a) β-CDs and (b) CD cross-linked polymer.

9.2.7. Synthesis of HNT-CDs nanosponge hybrids (compound 6)

Thiol-functionalized HNTs (200 mg) and heptakis-6-(tert-butyldimethylsilyl) 2-allyloxy-β-cyclodextrin **2** (200 or 300 mg) were weighed in a MW test tube provided with a cap and a catalytic amount of AIBN was added. The mixture was inserted in the MW apparatus at 100 °C, under constant stirring, for 1 h. Successively, the solid was filtered off, rinsed several times with CH_2Cl_2 and CH_3OH (until the unreacted reagents were not detected by TLC) and dried at 80 °C under vacuum.

9.2.8. Synthesis of compound 8

In a typical synthetic run, 100 mL of 3-azidopropyl trimethoxysilane **7** was dissolved in 20 mL of dry toluene and 1g of clay powder was added. The suspension was first dispersed under ultrasonic irradiation for 15 min and then refluxed for 16h under stirring. Afterwards, the crude solid filtered off, washed with several aliquots of MeOH and dried overnight at 80 °C under vacuum.

9.2.9 General synthesis of compound 10

Compound **8** (500 mg) was suspended in an H$_2$O/*t*-BuOH 1:1 mixture (4 mL) and propargyl alcohol **9** (20.7 mg, 10 eq) was added. The mixture was stirred under argon in the presence of catalytic amount of CuSO$_4$/sodium ascorbate solution (1 M, 1:10 v/v) at room temperature for 24h. After this time, the solvent was filtered off, the powder was rinsed with H$_2$O, then with MeOH and finally dried at 80 °C under vacuum.

9.2.10. General procedure for the synthesis of compounds 11a-b

Compound **10** (100 mg) was suspended in dry toluene (10 mL) and an excess of the proper iodoalkane was added. The suspension was then refluxed at 120 °C for 24h. After this time, the solid was filtered off, rinsed with CH$_2$Cl$_2$ and finally dried at 80 °C under vacuum.

9.2.11. Synthesis of 4,4-bis[2-(2-hydroxyethoxy) ethoxy]-diphenyl 13

A solution of 4,4-byphenol **12** (1 eq) in dry DMF (5.5 mL) was added to a stirred suspension of K$_2$CO$_3$ (3 eq) in dry DMF (15 mL) under argon. The mixture was stirred for 1 h at 60 °C. After this time, a solution of 2-(2-chloroethoxy)-ethanol (2.6 eq) in dry DMF(8.1 mL) was added over 30 min, and the temperature was raised to 85 °C. Stirring and heating were continued for 7 days. After cooling to room temperature, the reaction mixture was filtered and the residue was washed with DMF (20 mL). The solvent was removed in vacuo and the residue was partitioned between CH$_2$Cl$_2$ and H$_2$O with addition of NaCl. The pH was adjusted to ca. 2 with 2N HCl, and the organic phase was washed with H$_2$O, dried (MgSO$_4$), and concentrated in vacuo. The residue was purified by chromatography (Eluent: CH$_2$Cl$_2$/MeOH 25:1) and the product was obtained as a red oil in a yield of 30% (0.730 g).

^{1}H-NMR (300 MHz, CDCl$_3$) δ: 2.96 (s, 2H, O**H**); 3.46–3.55 (m, 12H, C**H**$_2$); 3.67–3.72 (m, 8H, C**H**$_2$); 4.06–4.10 (t, 4H, C**H**$_2$); 6.93–6.99 (m, 4H, C**H**); 7.23–7.32 (m, 4H, C**H**).

^{13}C NMR (300 MHz, CDCl$_3$) δ: 54.06; 62.37; 69.24; 70.36; 71.12;71.49; 73.18; 113.13; 121.28; 129.09; 132.19; 157.01.2.3.

9.2.12. Synthesis of compound 14

Compound **13** (500 mg, 1 eq) was dissolved in dry DMF (30 mL)and treated with NaH (1.12 g, 2.5 eq). After the evolution of gas ceased (~30 min), propargyl bromide (6 mL of 80% wt solution in PhMe, 6 eq) was added via a syringe. The mixture was left to stir at r.t. for 3 d. The solvent was removed in vacuo and the crude mixture was subjected to column

chromatography (CH$_2$Cl$_2$ 100%, CH$_2$Cl$_2$/AcEt1:1, AcEt 100% and AcEt/MeOH 10:1). 1 was obtained as a brown oil in a yield of 80%.

^{1}H NMR (300 MHz, CDCl$_3$) δ: 1.59 (s, 2H, **CH**); 3.48–3.53 (m, 8H,**CH$_2$**); 3.59–3.71 (m, 12H, **CH$_2$**); 4.06–4.14 (m, 4H, **CH$_2$**); 4.15–4.19(m, 4H, **CH$_2$**); 6.93–7.01 (m, 4H, **CH**); 7.25–7.31 (m, 4H, **CH**).

FT-IR (nujol): 2114 cm^{-1} stretching C≡C; 2875 cm^{-1} stretching –CH$_2$; 3282 cm$^-$^{1}stretching ≡C-H.

9.2.13. Synthesis of compound 15

Azido functionalized halloysite (compound **8**) (500 mg) was suspended in an H$_2$O/*t*-BuOH 1:1 mixture (4 mL) and compound **14** (319 mg) was added. The mixture was stirred under argon in the presence of catalytic amount of CuSO$_4$/sodium ascorbate solution (1 M, 1:10 v/v) at room temperature for 48 h. After this time, the solvent was filtered off, the powder was rinsed with H$_2$O, then with NaOH 0.1N and finally with CH$_2$Cl$_2$. The powder was then dried at 80 °C under vacuum.

9.2.14. Synthesis of compound 17

Compound **15** (500 mg) was suspended in a H$_2$O/*t*-BuOH 1:1 mixture (4 mL) and NaN$_3$ (152 mg, 2.5 eq) was added. The mixture was stirred under argon in the presence of catalytic amount of CuSO$_4$/sodium ascorbate solution (1 M, 1:10 v/v) at room temperature for 48h. After this time, the solvent was filtered off, the powder was rinsed with H$_2$O, then with NaOH 0.1N and finally with CH$_2$Cl$_2$. The powder (compound **16**) was then dried at 80 °C under vacuum. Then it was suspended in dry toluene (100 mL) and an excess of the bromobutane was added. The suspension was then refluxed at 120 °C for 24h. After this time, the solid was filtered off, rinsed with CH$_2$Cl$_2$ and finally dried at 80 °C under vacuum.

9.2.15. Typical procedure for the synthesis of the palladium catalysts 29 and 30

In a round-bottom flask were placed PdCl$_2$ (95 mg, 0.536 mmol), NaCl (626 mg, 10.72 mmol, 20 equiv.), Compound **11b** or **17** and toluene (13.6 mL). The flask was heated at 60 °C for 48h, then filtered under reduced pressure, washed with Et$_2$O and water and dried overnight under reduced pressure at room temperature. The material was suspended in ethanol (10 mL) and to this suspension a solution of NaBH$_4$ (79 mg, 2.1 mmol, 7 equiv.) in ethanol (24 mL) was added dropwise. The suspension turned black and was stirred at room

temperature for 6h, then filtered under reduced pressure, washed with water and dried overnight under reduced pressure at room temperature.

9.2.16. Synthesis of compound 27

Compound **6** (150 mg) and cysteamine hydrochloride (65 mg) were weighed in a quartz vial and 4 mL of MeOH were added. A stream of Ar was bubbled through the solution for 20 min to thoroughly degas it. The mixture, kept under an Ar atmosphere, was placed in front of am Hg lamp and stirred overnight. Successively, the solid was filtered off, rinsed several times with MeOH and dried at 80 °C under vacuum.

9.2.17. Preparation of HNT/cucurbit[8]uril supramolecular structure(compound 18)

The used procedure to prepare the **18** structure is described in the literature.[4] Briefly, aqueous saturated CB[8] solution was mixed with halloysite powder and sonicated for 15 min. Then, the obtained suspension was stirred and kept under vacuum for 3−5 min resulting in light fizzling indicating that air was removed from the nanotubes and replaced by the CB[8] saturated solution. The process was repeated three times for the most efficient loading. Successively, the sample was separated from the aqueous phase by centrifugation and free cucurbituril was isolated and recycled for further experiments. The complex compound **18** was washed several times with water and dried at 70 °C overnight under vacuum. The complex compound **18** is based on supramolecular interactions that are weaker and reversible, thus if it is used a good solvent for CB[8] these interactions will be broken and release occurs quickly both from the cavity and external surface. On this basis, water was used to control the CB[8] solubilization. We checked the remove of free CB[8] by performing TGA experiments after each washing cycle. The washing procedure was stopped when a constant loading is measured by TGA.

9.2.18. Preparation of HNT/Au 31 hybrid via NaBH₄ reduction

In a 10 mL round bottom flask were placed **1** (0.25 g), $HAuCl_4 \times 3H_2O$ (0.05 g, 0.13 mmol) and water (4 mL). The obtained dispersion was sonicated for 1 min and was stirred for 18 h at room temperature. The mixture was filtered under reduced pressure, washed with water and dried under reduced pressure at room temperature. The material was re-suspended in MeOH (4 mL) and to this dispersion $NaBH_4$ (0.03 g, 0.8 mmol), as a reducing agent, was added. The suspension was stirred at room temperature for 18 h. The

dispersion was filtered under reduced pressure, washed several times with MeOH and then dried overnight under reduced pressure at 60 °C.

9.2.19. Synthesis of compound 32

In a typical synthetic run, 3g of 3-aminopropyl trimethoxysilane was dissolved in 50 mL of toluene and 1g of halloysite powder was added. The suspension was first dispersed under ultrasonic irradiation for 10 min and then refluxed for 24h under stirring. Afterwards, the crude solid was centrifuged, washed with several aliquots of toluene and dried overnight at 60 °C.

9.2.20. Synthesis of compounds 33a and b

In a 50 mL centrifuge tube, 200 mg of HNT or **32** were weighed. Afterwards, by small aliquots (500µL), a saturated solution of Cobalt(II) acetylacetonate (200 mg) in acetone was added dropwise to the on powder. The obtained mixture was sonicated for 5 minutes and dried at 80 °C. The mixture was then crunched and calcined, under N_2 flow, with a heating rate of 10 °C·min^{-1} from room temperature to 300 °C, maintained at that temperature for 1.5 h and then slowly cooled down.

9.2.21. Synthesis of compounds 34a and b

In a 50 mL centrifuge tube, 200 mg of HNT or **32** were weighed. Afterwards, by small aliquots (500µL), a saturated solution of Cobalt(II) acetylacetonate (373 mg) in acetone was added dropwise to the on powder. The obtained mixture was sonicated for 5 minutes and dried at 80 °C. The mixture was then crunched and calcined, under N_2 flow, with a heating rate of 10 °C·min^{-1} from room temperature to 370 °C, maintained at that temperature for 1.5 h and then slowly cooled down.

9.2.22. Synthesis of compounds 35a

300 mg of **32** were dispersed in 30mL of 0.1 M NaOH aqueous solution by vortex, the collected by centrifuge and dried overnight at 60 °C.

The sample was dispersed, by ultrasonic irradiation, in 15 mL of Cobalt(II) acetylacetonate (150 mg) in acetone.

The purple dispersion was stirred 48h at RT. Collected by centrifuge was washed three times with acetone and dry at 60° some hours.

Finally, the pink powder obtained was dispersed in 15 mL of water by sonication and were added dropwise 50 mL of aqueous NaBH$_4$ (240 mg) solution.

The black moisture was stirred 24h at RT than collected by centrifuge, washed 3 times with water and dry overnight at 60 °C.

9.2.23.   Synthesis of compound 35b

150 mg of **32** and 150 mg of Cobalt(II) acetylacetonate were dispersed in 20mL of acetone, by 5 minutes of ultrasonic irradiation. The moisture was then refluxed for 24h, cooled down, collected by centrifuge and dried.

The pink powder obtained was dispersed in 5 mL of water by sonication and were added dropwise 15 mL of aqueous $NaBH_4$ (200 mg) solution.

The black moisture was stirred 24h at RT than collected by centrifuge, washed 3 times with water and dry overnight at RT under vacuum.

9.2.24.   Synthesis of compound 36

A solution of Cobalt(II) acetylacetonate in acetone (100mg in 100 mL) in 1:1 ratio to HNT, was sonicated in an ice bath for 1 hour. Then it was poured into a beaker and to it 100 mg of HNT were added. The dispersion was left at RT under gentle stirring until dry.

9.2.25.   Synthesis of compound 37

500 mg of Chinese HNT, 500 mg of $FeCl_2$ and 300 mg of $FeSo_4 .7H_2O$ were dispersed in 40mL water, by 5 minutes of ultrasonic irradiation. The moisture was then refluxed for 3h, cooled down to 50 °C and c.a. 2 mL of a 4M solution of NaOH was added until pH11.

The moisture was kept 2h at 50 °C and overnight at RT.

The black powder was collected by centrifuge and washed several times until clear supernatant.

9.2.26.   Synthesis of compound 38

50 mg of **37** were added to 6.6 g sodium alginate solution (100 mg) in 0.5 M NaCl, by 10 minutes of ultrasonic irradiation and stirring.

Tree cycles of 15 min of vacuum were performed, then stirred overnight at RT.

The powder was collected by centrifuge, washed three times with water and dried.

References

1   US4401598 A, 1983.

2   I. Wawer, A. A. Cichowlas and J. Nartowska, *Solid State Nucl. Magn. Reson.*, 2001, **20**, 35–45.

3   M. Massaro, S. Riela, P. Lo Meo, R. Noto, G. Cavallaro, S. Milioto and G. Lazzara, *J. Mater. Chem. B*, 2014, **2**, 7732–7738.

4   G. Cavallaro, G. Lazzara, S. Milioto, F. Parisi and V. Sanzillo, *ACS Appl. Mater. Interfaces*, 2014, **6**, 606–612.

Curriculum Studiorum

PUBLISHED WORKS

M. Massaro, G. Cavallaro, <u>C. G. Colletti, S.</u> Guernelli, G. Lazzara, S. Riela, S. Pieraccini, G. D'Azzo. *Halloysite nanotubes for efficient loading, stabilization and controlled release of insulin. A preliminary study for transdermal delivery, Biomacromolecules*, submitted.

M. Massaro, <u>C. G. Colletti,</u> S. Guernelli, G. Lazzara, M. Liu, R. Noto, F. Parisi, I. Pibiri, S. Riela. *Synthesis of highly uniform carbon dots using halloysite nanotubes as template, Nanoscale*, submitted.

M. Massaro, <u>C. G. Colletti,</u> B. Fiore, G. Lazzara, R. Noto, S. Guernelli, N. Zaccheroni, S. Riela. *Gold nanoparticles supported on functionalized halloysite as catalyst for reduction reaction in flow. J. Catal.*, submitted.

M. Massaro, A. Campofelice, <u>C. G. Colletti,</u> G. Lazzara, R. Noto, S. Riela. *Functionalized halloysite nanotubes: efficient carrier systems for antifungine drugs Appl. Clay Sci.*, https://doi.org/10.1016/j.clay.2018.01.005

M. Massaro, <u>C. G. Colletti,</u> G. Lazzara, S. Milioto, R. Noto and S. Riela. *Halloysite nanotubes as support for metal-based catalysts, J. Mater. Chem. A,* **2017**, *5*, 13276-13293.

M. Massaro, <u>C. G. Colletti,</u> G. Lazzara, S. Guernelli, R. Noto and S. Riela. *Synthesis and characterization of HNT-cyclodextrin nanosponges for enhanced dyes adsorption, ACS Sustain. Chem. Eng.*, **2017**, *5 (4)*, 3346–3352.

M. Massaro, S. Riela, G. Cavallaro, <u>C. G. Colletti,</u> S. Milioto, R. Noto, G. Lazzara. *Ecocompatible Halloysite/Cucurbit[8]uril Hybrid as Efficient Nanosponge for Pollutants Removal*, *ChemistrySelect* **2016**, *1*, 1773 – 1779

M. Massaro, S. Riela, G. Cavallaro, <u>C. G. Colletti,</u> S. Milioto, R. Noto, F. Parisi, G. Lazzara *Palladium supported on Halloysite-triazolium salts as catalyst for ligand free Suzuki cross-coupling in water under microwave irradiation, J. Mol. Catal.* **2015**, 408, 12-19.

M. Massaro, S. Piana, <u>C. G. Colletti,</u> R. Noto, S. Riela, C. Baiamonte, C. Giordano, G. Pizzolanti, G. Cavallaro, S. Milioto, G. Lazzara *Multicavity halloysite-amphiphilic cyclodextrin hybrids for co-delivery of natural drugs into thyroid cancer cells, J. Mater. Chem. B* **2015**, *3*, 4074-4081.

M. Massaro, <u>C. G. Colletti,</u> R. Noto, S. Riela, P. Poma, S. Guernelli, F. Parisi, S. Milioto, G. Lazzara *Pharmaceutical properties of supramolecular assembly of co-loaded cardanol/triazole-halloysite systems, Int. J. Pharm.* **2015**, *478*, 476–485.

S. Riela, M. Massaro, <u>C. G. Colletti,</u> A. Bommarito, C. Giordano, S. Milioto, R. Noto, P. Poma, G. Lazzara *Development and characterization of co-loaded curcumin/triazole-halloysite systems and evaluation of their potential anticancer activity, Int. J. Pharm.* **2014**, *475*, 613-623.

COMUNICATIONS TO CONFERENCES

Nov. 16th –18th, 2017   2nd Green conservation for cultural heritage, Palermo, Italy.
Oral Comunication: Y. Lvov, A. Joshi, G. Cavallaro, <u>C. Colletti,</u> G. Lazzara, *"Environment-Friendly Bronze Protective Coating with Natural Clay Nanotubes"*

July 17th –21th, 2017   16th international clay conference, Granada, Spain.
Poster Comunication: <u>C.G. Colletti,</u> M. Massaro, S. Riela, L. Lazzara, Y. Darrat, Y. Lvov, *"Halloysite nanotubes as support for metal nanoparticles for catalytic application"* Scientific Research Abstracts, Vol. 7, p. 162, **2017**, ISSN 2464-9147 (Online)

Febr. 9th – 10th, 2017   Workshop delle Sezioni Sicilia Calabria SCI - Messina 2016-17
Oral Comunication: <u>C. G. Colletti,</u> G. Cavallaro, S. Guernelli, G. Lazzara, M. Massaro, S. Milioto, R. Noto, S. Riela,*" Materiali ibridi a base di nanotubi di allosite per la rimozione d'inquinanti".*

July 13th – 15th, 2016   XI Spanish-Italian Simposium on Organic Chemistry (SISOC XI), Donòstia-San Sebastian
Oral Comunication: M. Massaro, G. Cavallaro, <u>C.G. Colletti</u>, G. Lazzara, S. Milioto, R. Noto, S. Riela, "*Halloysite Nanotubes as Support for Metal-Based Catalysts*".

June 17th – 19th, 2015   12th Mediterranean Conference on Calorimetry and Thermal Analysis, MEDICTA 2015, Girona, *Spain.*
Poster Communication: M. Massaro, S. Riela, <u>C.G. Colletti</u>, R. Noto, G. Cavallaro, S. Milioto, F. Parisi, G. Lazzara "*Synthesis and characterization by thermogravimetric analysis of a new drug delivery system based on halloysite nanotubes*".

June 7th – 12th, 2015   International Conference-Applied Mineralogy Advanced Materials (AMAM), Castellaneta Marina (Ta), Italia.
Oral Communication: S. Riela, <u>C.G. Colletti</u>, M. Massaro, R. Noto, G. Cavallaro, S. Milioto, F. Parisi, G. Lazzara "*Chemical modification of halloysite nanotubes for the development of smart nanomatirials*".

Dec. 1th -2th, 2014   Convegno congiunto delle Sezioni Calabria e Sicilia 2014, Palazzo Chiaramonte "Steri", Palermo.
Poster Communication: <u>C.G. Colletti</u>, S. Riela, M. Massaro, R. Noto, P. Poma, S. Guernelli, F. Parisi, S. Milioto, G. Lazzara "*Caratterizzazione e valutazione dell'attività antiproliferativa di nuovi sistemi per il drug carrier allosite- Sali triazolici/cardanolo*".

Oct. 27th – 30th, 2014   14th Sigma Aldrich Young Chemists Symposium (SAYCS), Riccione
Poster Communication: <u>C.G. Colletti</u>, S. Riela, M. Massaro, R. Noto, P. Poma, S. Guernelli, F. Parisi, S. Milioto, G. Lazzara "*Co-loaded Cardanol/triazole – halloysite system characterization of supramolecular complex and evaluation of its antiproliferative activity*".

Aug. 31th - Sep.4th, 2014   5th EuCheMS-Chemistry Congress, Istanbul
Poster Communication: S. Riela, M. Massaro, <u>C.G. Colletti</u>, A. Bommarito, C. Giordano, S. Milioto, R. Noto, P. Poma, G. Lazzara "*Synthesis and characterication of positively charged functionalized halloysite/curcumin system and evaluation of their anticancer activity*".

Aug. 31th - Sep.4th, 2014   5th EuCheMS-Chemistry Congress, Istanbul
Poster Communication: S. Riela, M. Massaro, F. Arcudi, <u>C.G. Colletti</u>, G. Lazzara, S. Milioto, R. Noto "*Synthesis and evaluation of catalytic activity in water and microwave irradiation of a new support based on HNT triazolium salts*".

Acknowledgements

A heartfelt thanks to Prof. Yuri Lvov for welcoming me to his research group, at the Louisiana Institute of Technologies, allowing me a personal and cultural growth. Thank you also for the trust and scientific and personal support you have shown me at all times.

A special thought also for all my friends and colleagues who made my visit to the USA unique.

Special thanks to the whole group of Prof. Milioto, in particular to Prof. Lazzara for their support and active collaboration.

Special thanks to Dr. Riela and Dr. Massaro for everything.

In the end, a thank you to Prof. R. Noto, example, and personal and scientific model.

"... it happens also in chemistry as in architecture that " beautiful" edifices, that is, symmetrical and simple, are also the most sturdy: in short, the same thing happens with molecules as with the cupolas of cathedrals or the arches of bridges."

Primo Levi - The Periodic Table